# Exo-C

## IMAGING NEARBY WORLDS

**EXOPLANET DIRECT IMAGING:**
**CORONAGRAPH PROBE**
**MISSION STUDY** *"Exo-C"*

THE *SCIENCE AND TECHNOLOGY DEFINITION TEAM* (STDT)
and THE Exo-C *DESIGN TEAM*

FINAL REPORT, MARCH 2015

CL#15-1197

The cost information contained in this document is of a budgetary and planning nature and is intended for informational purposes only. It does not constitute a commitment on the part of JPL and Caltech.

About the cover: The Exo-C observatory is shown in its Earth-trailing orbit, following in the path of discovery pioneered by NASA's Kepler mission. By directly imaging planets orbiting nearby stars, Exo-C will obtain spectra and color measurements that will reveal their atmospheric properties for the first time. The inset shows what Exo-C observations might find in a single day around the bright star Altair—planets analogous to Jupiter and Saturn and a dusty asteroid belt.
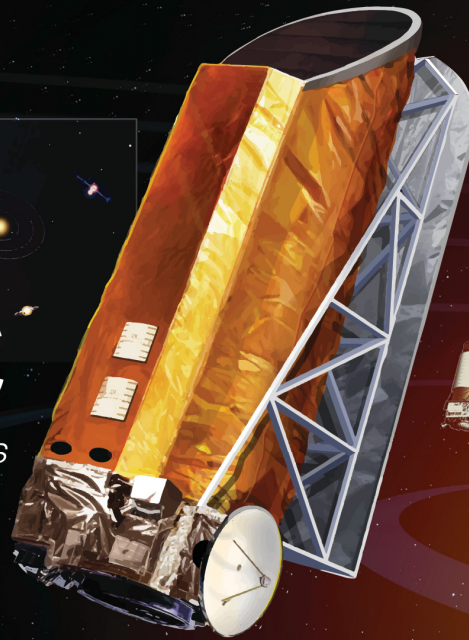
Graphic art by Joby Harris.

National Aeronautics and Space Administration

# Exo-C
## *Imaging Nearby Worlds*

www.nasa.gov

## Mission Overview

Exo-C is a mission concept study chartered in 2013 by NASA HQ. It is an agile space observatory optimally designed for direct imaging and spectroscopy of nearby planetary systems using internal coronagraphs, instruments that are close to technical readiness after a decade of laboratory work. Over its 3 year mission Exo-C will detect and characterize planets in reflected starlight, from Jupiter to super-Earth sizes and located in Saturn-like to Earth-like orbits. It will study cool planets like those in our solar system—complementing transit studies of hot, short-period planets—and serve as a technology pathfinder for future imaging of Earth-like planets.

## Mission Design

Exo-C brings together a 1.4-m aperture, precision pointing and wavefront control, internal coronagraphs, and a highly stable observatory to enable optical wavelength (0.45–1.0 μm) studies of nearby planetary systems at billion-to-one contrast. Its high contrast imaging performance will surpass that of the *Hubble Space Telescope* by a factor of 1000 and that of any other ground or space telescope now operating or under construction. The mission and hardware design are patterned after the highly successful *Kepler* mission, to achieve the same goal of delivering ground-breaking exoplanet science at an affordable cost.

## Science Objectives

- **Discovery of new planets in the Solar neighborhood:** Exo-C's multi-epoch imaging will search beyond the limits of other detection techniques around >100 nearby stars including alpha Centauri. Small mini-Neptune, super-Earth, and possibly Earth-sized planets will be detectable.
- **Characterization of known and mission-discovered planets**: Exo-C will measure the colors and spectra of at least a dozen known radial velocity planets orbiting nearby stars, and of the brightest new planets it discovers - measuring primary atmospheric constituents such as $CH_4$ and $H_2O$.
- **Structure and evolution of circumstellar disks:** Exo-C will resolve the structure of dust clouds orbiting nearby stars, tracing the gravitational effect of planets too small and remote to detect by any other means, in a sample of hundreds of exo-Kuiper belts
- **Survey of dust in habitable zones:** Exo-C's inner working angle of 0.16" at 550 nm will spatially resolve the habitable zones of up to 150 nearby stars

# Imaging

Survey **150** nearby stars for exoplanets down to super-Earth and perhaps Earth sizes
Measure **35** known & new exoplanets with multi-color photometry and astrometry
Survey **150** nearby stars for habitable zone dust
Image structure in **150** known debris disks
Image structure in **40** proto-planetary disks



Simulated Exo-C views of exoplanetary systems. *Left*: Jupiter & Saturn analogs and a 1 zodi dust belt seen in 3 colors, 12 hrs integration around the bright star Altair. *Right*: The known radial velocity planets 47 Ursa Majoris c and d would be detected in this 2 day V-band integration along with an outer dust ring.

# Spectroscopy

Measure spectra of **20** known & new exoplanets



Simulated Exo-C spectrum at R=70 of epsilon Eridani b, the nearest confirmed radial velocity planet

# Designed for Stability

Benign thermal environment in Earth-trailing orbit
Sunshade shields telescope and instrument
Active thermal control of telescope and instrument
Two stages of payload vibration isolation
Body-fixed solar array and high gain antenna
Active wavefront control to compensate for drifts
Design heritage from NASA's *Kepler* mission

# Observatory Configuration

- Solar Array/Sunshade
- SA/Sunshade Support Structure
- Barrel Structure
- Removable Lid
- Secondary Mirror Assy
- Instrument Enclosure
- Instrument Bench Assy
- Primary Mirror Assembly
- Primary Support Structure
- Radiator Panel Assembly
- Star Tracker Assembly
- Isolation Assembly
- Spacecraft Assembly
  - SC and Payload Electronics
  - Reaction Wheel Assy
  - Propulsion Assy
  - LV interface Ring Assy



6.4m
2.5m

# Exo-C Fast Facts

| Telescope | 1.4 meter unobscured Cassegrain |
|---|---|
| Mission Lifetime and Orbit | 3 years in an Earth trailing orbit |
| Spacecraft Bus | Kepler-like |
| Coronagraph Architecture | Baseline: Hybrid Lyot Coronagraph Backups: Vector Vortex and Phase-Induced Amplitude Apodization |
| Imaging Camera | 1k x1k EMCCD detector with 0.041 arcsec per pixel sampling |
| Integral Field Spectrograph | 1k x1k EMCCD with R= 70 sampling |
| Contrast | $10^{-9}$ raw, $10^{-10}$ or better post-processing |
| Contrast stability | $\leq 10^{-10}$ at the inner working angle (IWA) |
| Bandwidth | 450 to 1000 nm |
| High Contrast Field of View (radius) | Smallest IWA = 0.133" at 450 nm Largest OWA = 2.9" at 900 nm |
| Imager Full Field of View | 42" by 42" |

# Schedule



| FY15 | FY16 | FY17 | FY18 | FY19 | FY20 | FY21 | FY22 | FY23 | FY24 | FY25 |
|---|---|---|---|---|---|---|---|---|---|---|
| 2015 | 2016 | 2017 | 2018 | 2019 | 2020 | 2021 | 2022 | 2023 | 2024 | 2025 |

PRE-PHASE A   PHASE A (12 mo)   PHASE B (31 mo)   PHASE C (34 mo)   PHASE D (16 mo)   PHASE E (36 mo)

KDP-A   KDP-B   KDP-C   KDP-D   KDP-E
PLAR
Lifecycle Milestones   SRR ▽▽ MDR   SIR ▽   ORR▽   MRR
MCR   PDR ▽ 7/2   CDR ▽ 1/7   TRR ▽   Launch ★ 6/9

# Foreword

In spring 2013 the NASA Astrophysics Division chartered two exoplanet direct imaging mission studies. Both were instructed to develop a mission concept at the "probe scale," defined as a total mission cost ≤$1B FY15. Science and Technology Definition Teams (STDTs) were selected by NASA HQ. Engineering Design Teams were assembled at the Jet Propulsion Laboratory and formed the second key element of each Study Team. Each team was tasked to deliver interim and final study reports after 9 and 18 months of work. Independent cost and technical evaluations were developed by The Aerospace Corporation during the studies and provided impetus to design improvements. This document presents the final report for the internal coronagraph probe study "Exo-C."

Exo-C is NASA's first community study of a modest-aperture space telescope optimized for coronagraphic observations of exoplanetary systems. An internal coronagraph enables the mission to be carried out with a single spacecraft—a highly agile space telescope that can return to targets at multiple epochs for high-completeness planet searches and orbit determinations. It also enables a high duty cycle for high-contrast observations. This type of mission was specifically endorsed by the Electromagnetic Observations from Space panel of the *Astro2010* decadal survey.

While the Exo-C study represents the largest-scale effort to date to define this class of mission, it is by no means the first one. Over the past 25 years several individual groups have proposed missions like Exo-C numerous times to Announcements of Opportunity (AO) issued by NASA and ESA (Table F-1). Like Exo-C, these proposed missions aimed to directly image extrasolar planets and/or circumstellar disks while also serving as technology pathfinders toward an eventual flagship mission to image terrestrial planets. Members of the Exo-C Study Team participated in many of these previous efforts, as well as in the 2006 Terrestrial Planet Finder Coronagraph (TPF-C) mission study. The Exo-C study builds on this rich heritage of previous work and takes full advantage of the latest technical advances.

**Table F-1.** Historic proposals/studies of dedicated internal coronagraph space missions.

| Mission | Aperture | Year and AO | Proposal/Study Lead |
|---|---|---|---|
| CIT | 1.5 m | 1988 JPL study | R. Terrile |
| CODEX | 2.4 m | 1997 *Hubble* instrument proposal | R. Brown |
| ECLIPSE | 1.65 m | 1998 MidEx | J. Trauger |
| ECLIPSE | 1.8 m | 2000 Discovery | J. Trauger |
| ESPI | 1.5 m | 2002 MidEx | G. Melnick |
| JPF | 1.5 m | 2002 MidEx | M. Clampin |
| ECLIPSE | 1.5 m | 2004 Discovery | J. Trauger |
| EPIC | 1.5 m | 2004 Discovery | M. Clampin |
| ECLIPSE | 1.5 m | 2006 Discovery | J. Trauger |
| EPIC | 1.5 m | 2006 Discovery | M. Clampin |
| TOPS | 1.2 m | 2006 Discovery | O. Guyon |
| SEE-COAST | 1.5 m | 2007 ESA M1/M2 | J. Schneider |
| ACCESS | 1.5 m | 2008 ASMCS | J. Trauger |
| EPIC | 1.65 m | 2008 ASMCS | M. Clampin |
| PECO | 1.4 m | 2008 ASMCS | O. Guyon |
| SPICES | 1.5 m | 2010 ESA M3 | A. Boccaletti |
| EXCEDE | 0.7 m | 2011 MidEx | G. Schneider |

# Author List

## Science and Technology Definition Team

Karl Stapelfeldt.................................................................................................NASA Goddard (Chair)

Ruslan Belikov ...................................................................................................................NASA Ames

Geoffrey Bryden................................................................................................................ JPL/Caltech

Kerri Cahoy................................................................................................................................ MIT

Supriya Chakrabarti ................................................................................................... UMass Lowell

Mark Marley ......................................................................................................................NASA Ames

Michael McElwain ............................................................................................................NASA Goddard

Victoria Meadows..............................................................................................................Univ. of Washingon

Eugene Serabyn ................................................................................................................ JPL/Caltech

John Trauger....................................................................................................................... JPL/Caltech

## JPL Engineering Design Team

Frank Dekens.........................................................................................................Exo-C Design Lead

Michael Brenner..........................................................................Exo-C Design Lead up to Interim Report

Paul Brugarolas ............................................................................................. Pointing Engineer

Serge Dubovitsky................................................................................................. Flight Operations

Robert Effinger....................................................................................... Thermal and System Engineer

Casey Heeg .................................................................................................. System Engineer

Brian Hirsch ........................................................................................ Mechanical Engineer

Andy Kissil .........................................................................................Engineering Dynamics

John Krist ..............................................................................................Optical Simulations

Jared Lang.......................................................................................................... System Engineer

Joel Nissen .....................................................................................Performance System Engineer

Jeff Oseas......................................................................................... Optical Design Engineer

Christopher Pong ....................................................................................... Pointing Engineer

Marissa Rubio .........................................................................................Secretarial Support

Eric Sunada ............................................................................................... Thermal Engineer

Keith Warfield................................................................................................Probe Study Office

## With Additional Contributions by

Shawn Domagal-Goldman.....................................................................................NASA Goddard

Marc Kuchner........................................................................................................NASA Goddard

Peter Lawson....................................................................................................... JPL/Caltech

Caroline Morley…………………………………………………………...………UC Santa Cruz

Bijan Nemati...........................................................................................................JPL/Caltech

Aki Roberge ........................................................................................................NASA Goddard

Tyler Robinson…………………………………………………………………..NASA Ames

Jagmit Sandhu ..................................................................................................... JPL/Caltech

Sara Seager........................................................................................................... MIT

Steve Unwin………………………………………………………………………..JPL/Caltech

# 1    Table of Contents

# 2   Executive Summary

The Exo-C mission will be NASA's first space observatory specifically designed to perform direct imaging and spectroscopy of nearby extrasolar planets. Exo-C will open a new observational domain—imaging at very high contrast and very small angular separation—enabling the first detailed exploration of planetary systems around stars like our Sun. Exo-C brings together a 1.4-m aperture, precision wavefront control, internal coronagraphs with demonstrated technical readiness, and a highly stable spacecraft environment to enable optical wavelength (0.45–1.0 μm) studies of nearby planetary systems at billion-to-one contrast. The mission and hardware design is patterned on the highly successful Kepler mission, to achieve the same goal of delivering groundbreaking exoplanet science at low risk and at an affordable cost.

Exo-C's direct imaging will detect and characterize planets in Earth-like to Saturn-like orbits, and from Jupiter down to at least super-Earth sizes, complementing transit-based exoplanet observations, which are limited to planets that are much closer to the parent star. Exo-C's exoplanetary "Grand Tour" of our nearest stellar neighbors will provide a comprehensive survey of planetary systems more like our own, enabling a new era of comparative planetology. The high-contrast direct imaging capabilities of Exo-C also have the potential to advance many other fields of astronomy.

In the course of its 3-year mission, Exo-C will address four key science goals:

***Spectroscopy of known exoplanets:*** Exo-C will obtain photometry, astrometry and spectroscopy of about a dozen giant planets detected by radial velocity (Figure ES-1) and orbiting nearby stars. These will be the first "cool Jupiters" like our own, for which true masses and atmospheric composition will be measured. Exo-C's spectra will be sensitive to features of methane, ammonia and water in
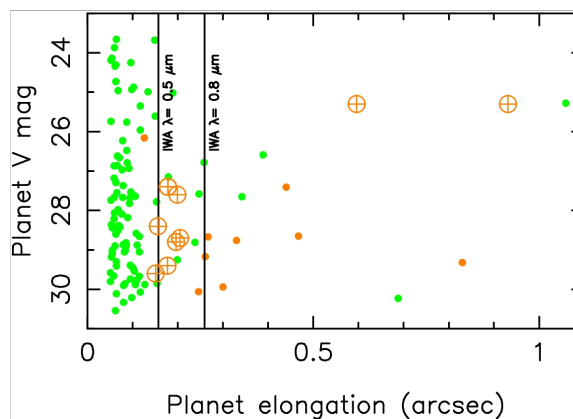


**Figure ES-1.** Separation and expected brightness for known RV planets (points) and putative HZ Earth analogs (⊕s) accessible to Exo-C. Color codes for contrast difficulty.
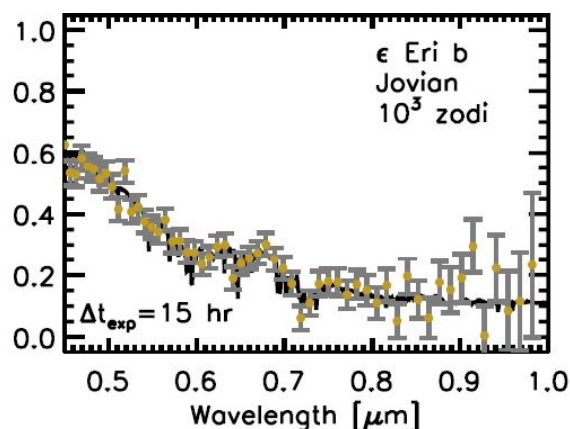


**Figure ES-2.** Simulated Exo-C spectrum of ε Eridani b, the nearest confirmed RV planet.
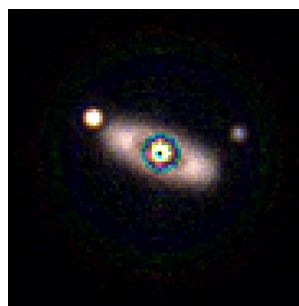


**Figure ES-3.** Hypothetical planetary system around the bright star Altair detected by Exo-C in a simulated 12 hour exposure in V, R, and I bands. Shown are Jupiter and Saturn analogs in 5 and 10 AU orbits, and a 1 zodi dust ring between 2-4 AU.

their planetary atmospheres, and spectral detections will be used to constrain relative abundances, metallicity and the depth of any cloud decks (Figure ES-2).

*Discovery and characterization of new planets in the solar neighborhood:* Exo-C's multi-epoch imaging has the capability to discover nearby planets beyond the limits of the radial velocity and transit detection techniques around at least 100 nearby stars (including α Centauri). A possible search result appears in Figure ES-3, while the discovery potential around nearby stars is shown in Figure ES-4. Searches will be made at multiple epochs for planets at contrasts down to a few×$10^{-10}$. Exo-C's contrast capability will permit detection of Jupiter-like planets with semi-major axes out to 9 AU, Neptune-like planets out to 3 AU and super-Earths out to 1 AU. With excellent telescope stability and low exo-zodi, Earth-twins could be detected around a few of the nearest stars. Spectral characterization of the brightest planet discoveries—from exo-Jupiters to any nearby Earths—will be obtained (Figure ES-1). Spectrally searching for biosignatures in the atmospheres and surfaces of Earth-like planets around the closest stars may be possible, if suitable candidate planets are found.
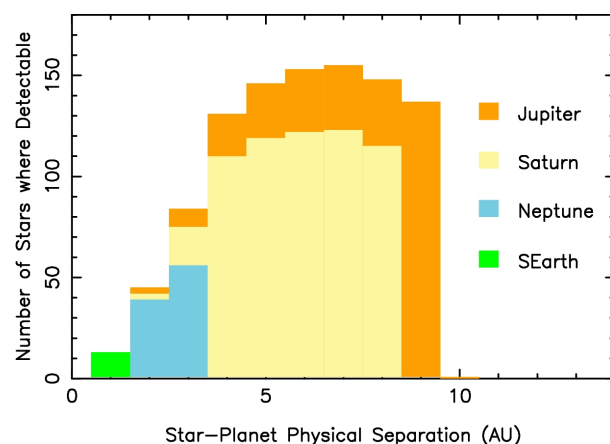


**Figure ES-4.** Exo-C exoplanetary search space among nearby stars, as a function of planet size and orbit.

*Structure and evolution of circumstellar disks:* Exo-C, with contrast 1,000 times better than that achievable with the Hubble Space Telescope (HST*)*, will resolve dust structures, tracing the gravitational effect of planets too small or remote to detect by any other means, and measuring dust properties in a large sample of exo-Kuiper belts. Exo-C will survey several hundred debris disk targets and will be capable of resolving rings, gaps, warps and asymmetries driven by planetary perturbations of circumstellar debris disks. Exo-C will be able to detect disks as tenuous as the Kuiper belt, enabling comparative studies of dust inventory and properties across stellar ages and spectral types.

*Survey of dust in habitable zones:* Exo-C's inner working angle of 0.16″ at 550 nm will spatially resolve the habitable zones of up to 200 nearby stars (70 solar type), enabling the search for dust down to levels a few times that found in our Solar System. These observations will provide crucial constraints on the background levels against which future missions will observe Earth-like exoplanets.

Exo-C is a compelling next step on NASA's exoplanet exploration path, with its basic mission concept endorsed by the Astro2010 Electromagnetic Observations from Space (EOS) panel. Exo-C will image and spectrally characterize planets and disks in reflected light. It will achieve image contrast levels that surpass those of currently operating space telescopes, the *James Webb Space Telescope (JWST),* and what can be done by groundbased Extremely Large Telescopes (ELTs) equipped with extreme adaptive optics. Exo-C will characterize cool planets in orbits at or beyond 1 AU irrespective of their orbit inclination to the line of sight, allowing equal access to all nearby stellar hosts and probing a different population than the set of hot, short period planets that may be characterized by transit spectroscopy. In addition to its compelling and unique science, Exo-C will is a scalable technology pathfinder for a future New Worlds mission capable of detecting atmospheric biosignatures on Earth analogs orbiting nearby stars.

As a dedicated and self-contained observatory for exoplanet direct imaging, Exo-C will have the mission time and pointing agility to revisit targets as often as needed.

Revisits enable candidate exoplanets to be verified by establishing common proper motion with their host star. Revisits also provide astrometric measurements needed for orbit determinations, photometric measurements of planetary phase curves, and the additional search completeness needed to maximize discovery of new planets. The Exo-C mission design will allow revisits to be scheduled as soon as a month after a previous observation. This flexibility allows quick return to a planet that proves exceptionally interesting or that requires further integration time to constrain a promising spectral feature.

Exo-C's telescope aperture, orbit, spacecraft, and lifetime are nearly identical to those of the Kepler mission, which is our cost reference. It builds on a rich heritage of exoplanet direct imaging mission concepts that have been proposed and studied by individual groups a dozen times since 1999. We highlight steps taken thus far to reduce mission cost and risk relative to previously proposed coronagraph mission concepts. These include the use of an intermediate class launch vehicle and choosing an orbit where no propulsion or mission navigation is needed after launch.

We present the design of the mission and science payload. The baseline Exo-C design is an unobscured Cassegrain telescope with a 1.4-m clear aperture, in a highly stable Earth-trailing orbit, and designed for a 3-year science mission lifetime. It carries a starlight suppression system (SSS) consisting of the following elements (in optical train order): fine-guidance and low-order wavefront sensor (FGS/LOWFS), wavefront control (WFC) system based on two large-format deformable mirrors, and a coronagraph. Two backend instruments, an imaging camera and an integral field spectrometer (IFS), receive the SSS output beam. The science instrument bench is mounted laterally on the anti-Sun side of the telescope, obviating the need for high incidence reflections that induce unwanted polarization effects and better isolating it from spacecraft disturbances.
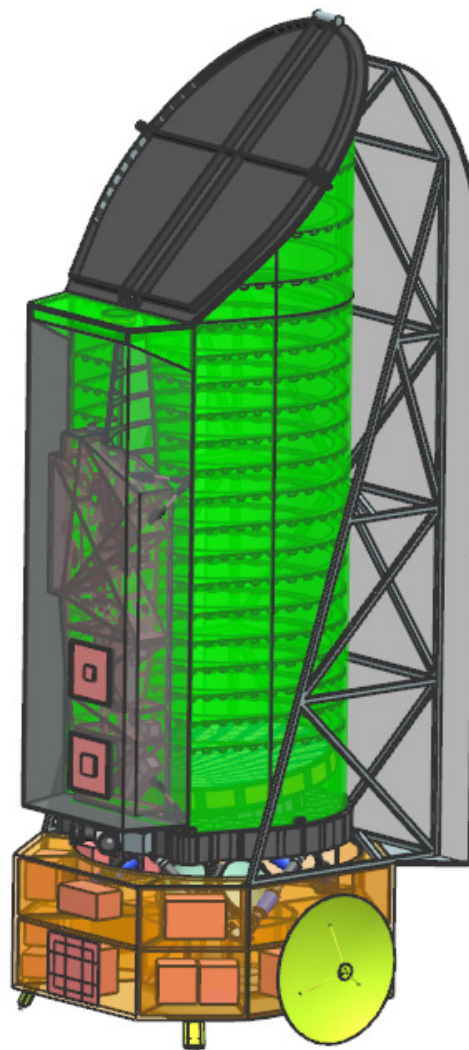


**Figure ES-5.** Visualization of the final Exo-C observatory design. A Kepler-like spacecraft hosts a telescope aperture the same as Kepler's, launched into the same orbit and with the same prime mission lifetime as Kepler.

The instrument creates a dark field with $10^{-9}$ raw contrast between radii ~2−20 $\lambda/D$ from the star. The imager fully covers this field with bandpass filters over the wavelength range 450–1000 nm. A smaller field 1.2″ in radius is covered by the IFS at spectral resolution R=70 over $\lambda$=495–1000 nm.

The telescope is designed for precision pointing and high stability. Two stages of vibration isolation are used between the reaction wheels and the science payload. The solar arrays and high-gain antenna are body-fixed, and a stiff barrel assembly is used as the telescope metering structure (Figure ES-5).

Telescope pointing is updated at a high rate using the bright science target star as a reference to drive a fine steering mirror. Spacecraft body pointing requirements are comparable to those of Kepler. Active thermal control is used for the telescope, instrument, and telescope barrel assembly—all of which are shielded from direct sunlight by a large solar panel. Modeling of the structural, thermal, and optical performance of this configuration shows that the telescope in its Earth-trailing orbit will have the high wavefront stability needed to meet Exo-C's science goals (Figure ES-6).

Exo-C builds on more than a decade of NASA technology investments and laboratory demonstrations for high contrast imaging with unobscured apertures. The AFTA/WFIRST coronagraph study continues to mature the technologies needed for Exo-C. AFTA efforts directly beneficial to Exo-C include flight qualification of deformable mirrors and low-noise detectors, development of coronagraphic masks, LOWFS design and testing, and the development of a dynamic high-contrast testbed to demonstrate coronagraph contrast performance in the presence of flight-like pointing and wavefront disturbances. A prototype high contrast IFS will soon be demonstrated under separate funding. Exo-C's
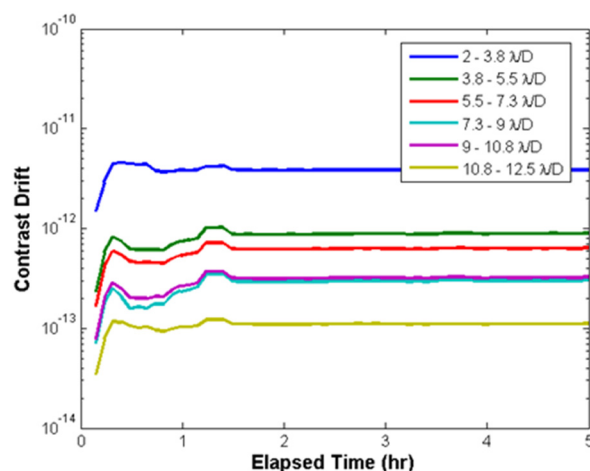


**Figure ES-6** Modeled contrast evolution in six radial zones in the coronagraphic image plane after the telescope was rolled by 30º about the line of sight. Even at the inner working angle of 2 λ/D, the contrast drift is below the $10^{-11}$ level, showing that the Exo-C design meets its stringent wavefront stability requirements.

remaining technology requirements beyond these existing efforts are 1) testbed time with an unobscured pupil and 2) coronagraph-specific mask or beamshaping technology developments to demonstrate $10^{-9}$ contrast in 20% bandwidth at 2λ/D inner working angle.

Five coronagraph options were evaluated for use on the mission: hybrid Lyot, phase-induced amplitude apodization (PIAA), shaped pupil, vector vortex, and the visible nuller. These evaluations resulted in the selection of the hybrid Lyot as the baseline for a 2017 new start, primarily on the basis of its greater technical readiness. The vector vortex and PIAA coronagraphs have the potential for even better science performance, and should continue to be developed as options for a later mission start. All three coronagraphs have already demonstrated performance in the laboratory that is closing in on Exo-C's requirements; they differ primarily in which of three key performance parameters (inner working angle, contrast, and spectral bandwidth) still need to be improved.

The Exo-C study's internal cost estimate is just under $1B, including 30% contingency and the launch vehicle. The independent cost estimates is slightly higher, with the primary difference being additional contingency against design changes. These mission costs are directly comparable to the as-flown cost of Kepler ($700M FY15) plus contingencies. The Exo-C study therefore provides an existence proof that a compelling science mission can be implemented at the probe-scale cost level of ~$1B.

Possible mission enhancements that would increase science performance include the use of larger format detectors and deformable mirrors, a redesign of the pointing system to enable a broader range of general astrophysics, the addition of an auxiliary instrument on the existing optical bench, and operating the mission to its full design lifetime of 5 years. Additional study would be needed to evaluate the costs associated with each of these options.

# 3    State of the Field at the Time of Probe Launch: The Exoplanet Science Landscape in 2024

Planetary systems consist of a range of planet types, from gas giants through sub-Neptunes to solid planets made of rock or ice, plus belts of small bodies that generate debris particles. Ongoing research, upcoming developments in ground-based instrumentation, and the launch of new space missions will continue to advance our knowledge of these exoplanetary system components in the coming decade. Nevertheless, a probe-scale exoplanet direct imaging mission can offer unique capabilities. Below we set the likely context for exoplanet science at the time Exo-C would launch.

## 3.1    Indirect Detections Using Stellar Reflex Motion

Radial velocity (RV) surveys have detected 592 planets as of early 2015 (http://exoplanets.eu). The RV method is sensitive to massive planets or those orbiting close to their stars, with the median orbital period of the detections to date around 1 year. The median semi-amplitude of the host star velocity disturbance is 38 m/sec, larger than the Sun's velocity changes in response to gravitational effect of Jupiter. RV surveys are also limited to stellar types of F8 or later, because earlier stellar types lack a sufficient density of narrow photospheric absorption features with which to undertake the RV measurements. With this sensitivity profile, RV surveys to date have detected most of the Jupiter-mass planets within a few AU of late-type stars, but generally lack sensitivity to Neptune-mass planets outside a few tenths of an AU (Howard and Fulton 2015). Only a dozen planets have measured RV semi-amplitudes below 2 m/sec, with the best claimed detection to date being the 50 cm/sec semi-amplitude for the very bright star alpha Centauri B.

Today's RV measurement precision of 50 cm/sec is expected to improve toward 10 cm/sec with the Very Large Telescope (VLT)/Echelle SPectrograph for Rocky Exoplanet and Stable Spectroscopic Observations (ESPRESSO) and similar instruments on extremely large telescopes (European Extremely Large Telescope (E-ELT), Giant Magellan Telescope (GMT), Thirty Meter Telescope (TMT)). However, stellar RV jitter arising from spots and activity sets a natural noise floor near 2 m/sec (Bastien et al. 2014). Only in the quietest stars—or through careful averaging, filtering, and detrending of the data—will RV detections be achieved for semi-amplitudes below 1 m/sec.

A new dedicated RV program with 50 cm/sec precision and focused on direct imaging targets could, by 2024, extend this sensitivity to planets of Saturn-mass and greater with periods up to 20 years, and to 8 $M_\oplus$ super-Earths with periods of several years. Complementary measurements of stellar astrometric wobble by the European Space Agency (ESA) Gaia all-sky survey will detect and measure orbit inclinations for planets of Jupiter mass or larger and periods <5 years around unsaturated nearby stars (V>6), and could potentially be extended to stars as bright as V=3 with pipeline software improvements (Martin-Fleitas et al. 2014). The orbital elements for the inner giant planets of nearby late-type stars should be well in-hand by 2024.

## 3.2    Transits

Transit observations with the *Kepler* mission (and to a lesser extent, the COnvection ROtation et Transits (*CoRoT*) mission) have revealed the frequency and radius distribution of short-period (P <1 yr) exoplanets by photometrically monitoring selected fields of solar-type stars. The 2017 Transiting Exoplanet Survey Satellite (TESS) mission will identify shorter-period (P ~< several weeks) planets around several hundred thousand bright field stars distributed around the sky. Around M

stars, TESS detections will extend down to 1 $R_\oplus$ in the habitable zone. RV follow-up of TESS detections will reveal their mass distribution and the planetary mass-radius relationship. Spectroscopic measurements made during transit and secondary eclipse by the James Webb Space Telescope (JWST), ELTs, and other facilities will constrain the temperatures and albedos of these planets, and for clear, low-molecular weight atmospheres may detect high-opacity atmospheric species such as Na I, $H_2O$, and $CH_4$. The PLATO mission will launch in 2024 and identify a new sample of transiting planets. By 2024, transit work should have built a strong statistical picture of the bulk properties of inner planetary systems and collected atmospheric spectral information for many of their larger objects.

## 3.3 Exoplanet Imaging Detections

Only a handful of exoplanets have been imaged directly in their near-infrared thermal emission (e.g., Marois et al. 2010; http://exoplanets.eu). This is due to the limited contrast capabilities of current instrumentation (Lawson 2013, Figure 1), especially at small angular separations from a star. A new generation of high-contrast imagers based on extreme adaptive optics systems is now being deployed behind large ground-based telescopes. Dozens of exoplanet imaging detections at $10^{-7}$ contrast and ~0.5″ separation should be achieved by these systems in the near-infrared (Gemini Planet Imager (GPI), VLT Spectro-Polarimetric High-contrast Exoplanet Research (SPHERE), Subaru Coronagraphic Extreme Adaptive Optics (SCExAO)), which would enable detection and spectroscopy of thermal emission from warm (T >~400 K; very young or massive) gas giant planets. An appropriately designed extremely large telescope (ELT) in the 30-m class would be capable of such detections at even smaller inner working angles ~0.12″, but with only modestly better contrast. However, the extreme adaptive optical systems needed for such observations are not currently baselined for ELT first-generation

instruments, and thus are not expected to be on-sky until the late 2020s.

Ground-based, high-contrast imaging is limited by rapid wavefront changes arising from atmospheric turbulence. For a solar twin at 10 pc distance (H mag 3), a deformable mirror sized to create a ~0.5″ radius dark field cannot suppress the residual speckles to levels fainter than $10^{-7}$ of the central star brightness. This limit is defined by the available photons per subaperture in a reduced coherence time (Oppenheimer and Hinkley 2009, Table 2) and is nearly independent of telescope aperture size. To detect fainter objects, speckle averaging and subtraction methods must be employed. It is unclear how well this could be done, as the temporal behavior of residual atmospheric speckles at $10^{-7}$ contrast has never been characterized. Experience at less challenging contrast levels suggests that detections a factor of 10 below the raw contrast floor should be achievable. $10^{-8}$ contrast would enable detections of thermal emission from nine massive giant planets around nearby solar-type stars (Stapelfeldt 2006). It has been suggested that ELTs could detect planets in reflected light as small as 1 $R_\oplus$ at this contrast level, if they are present in the 0.1 AU radius habitable zones of bright nearby M dwarfs (Guyon and Martinache 2013). However, the required stellar properties (V<8 for sufficient guidestar photons, d <22 pc to resolve the habitable zone with an ELT) results in only a few suitable targets.

JWST/Near Infrared Camera (NIRCam) coronagraphy should be capable of detecting companions at contrasts of $10^{-6}$ at separations beyond 1.5 arcsec, capturing objects like our own Jupiter in 4.5 μm thermal emission if they are orbiting the nearest M stars. The uncertain luminosity evolution of young giant planets clouds the picture somewhat (Marley et al. 2007), but it appears that the some of the more massive planets orbiting nearby (d <20 pc), young (age <1 Gyr), low-mass (M <1.0 Msun) stars could be in view by 2024.

## 3.4 Disk Imaging

Imaging of protoplanetary disks is being revolutionized by the Atacama Large Millimeter/submillimeter Array (ALMA), which will be able to resolve dynamical structures driven by protoplanets at angular resolutions approaching 0.01 arcsec. Proto-planetary disks in the nearest star-forming regions (d ~150 pc) are ideal ALMA targets, as their high optical depths give them high surface brightness in the submillimeter continuum. Debris disks are found around older main-sequence stars, with many nearby (d ~25 pc) examples. They are optically thin with a much lower dust content and much fainter submillimeter continuum emission; it will therefore be a challenge even for ALMA to resolve their detailed structure. ALMA will map a limited number of the brightest debris disks ($L_d/L_{star} > 10^{-4}$) at 0.1 arcsec resolution. In addition to their exoplanet imaging capability, new adaptive optics coronagraphs now being deployed on large ground-based telescopes should image bright debris disks in the near-infrared (Perrin et al. 2015), at comparable resolution to and with sensitivity a few times better than ALMA's millimeter wave observations. Similar instruments on ELTs would extend the resolution and inner working angles of such studies to 10 and 30 milliarcsec respectively. With its 0.3 arcsec resolution at 20 μm, JWST will resolve warm dust emission around a sample of nearby A stars. New warm disks identified by the Wide-field Infrared Survey Explorer (WISE) mission will be particularly important targets. A wealth of new data detailing the internal structure of bright circumstellar disks will have emerged by 2024, seeding a new theoretical understanding of disk structure, dynamics, and evolution.

## 3.5 Conclusions

While the advances described above will be remarkable scientific milestones, they fall well short of the goal of obtaining images and spectra of planetary systems like our own, as shown in Figure 3.5-1. The TESS mission will detect inner terrestrial planets transiting nearby cool stars, but their spectroscopic characterization will be restricted to red dwarf stellar hosts and will be challenging even using JWST. High-contrast imaging will detect and characterize warm giant planets, but not cool objects seen in reflected light at $10^{-9}$ contrast, like our own Jupiter and Saturn in their orbits around a solar-type star. Sharp images of dusty debris disks will be obtained, but only those with optical depths several hundred times that of our own asteroid and Kuiper belts. RV and astrometric surveys will have identified the majority of nearby late-type stars hosting giant planets. What is currently missing from the 2024 exoplanetary science toolbox are space observatories that can study photons from cool planets at/beyond 1 AU (ranging from giants down to super Earths) and resolve tenuous dust disks around nearby stars like the Sun.
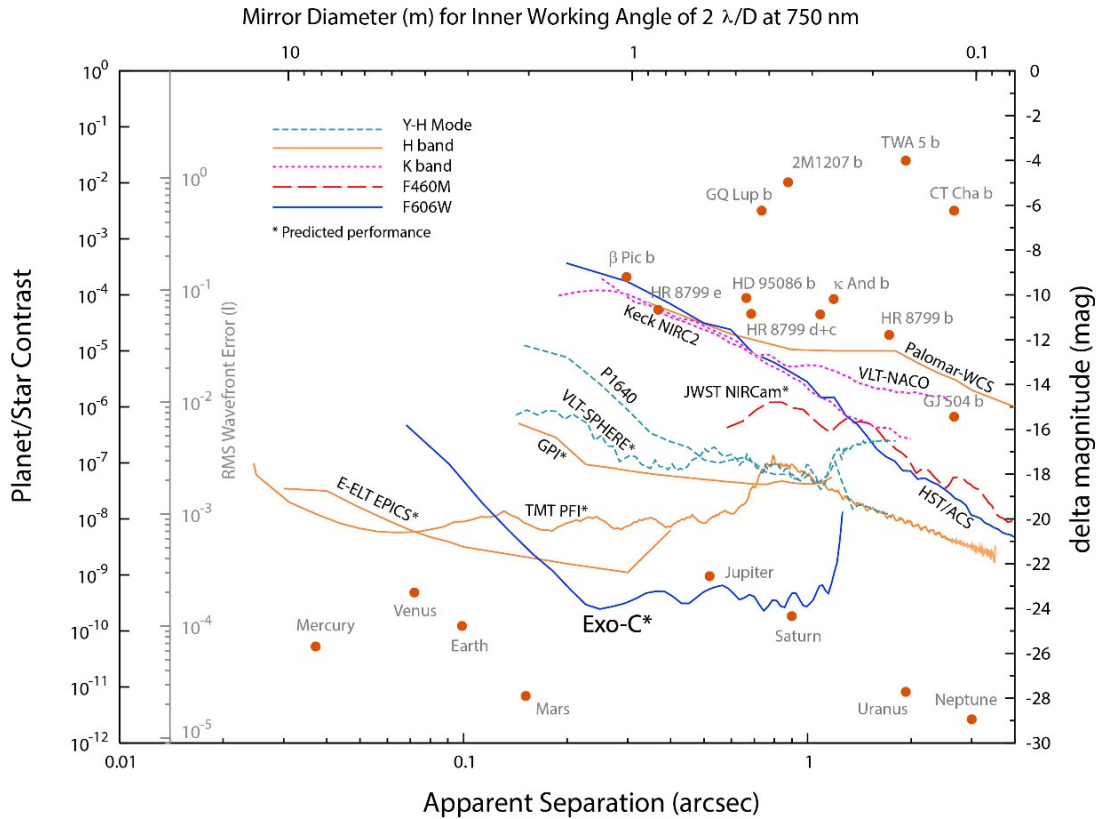
**Figure 3.5-1.** Direct imaging contrast capabilities of current and future instrumentation (Mawet et al. 2012), with the addition of the Exo-C's predicted capability. Solar system planets are shown as seen from 10 pc distance.

For the very nearest stars (d ~<5 pc), analogs to the solar system's planets would appear further to the right in the diagram, making a bright an inner planet such as Venus more easily detected.

# 4 Design Reference Mission

## 4.1 Introduction: High-level Statement of Science Goals

Over the past five decades, NASA has carried out ambitious space observatory projects designed to study the universe at new wavelengths with improved spatial resolution, spectral resolution, and field of view—and with precise timing or photometry. In the 21$^{st}$ century, exoplanet research has emerged as a new focus for astrophysics and offers new space mission opportunities to explore. A new observational domain—imaging at very high contrasts and very small angular separations—must be opened if we are to understand the properties, formation, and evolution of planetary systems around stars like the Sun.

The Exo-C probe mission will be NASA's first space observatory designed from the outset to meet the requirements of high contrast imaging. It brings together a ~1.4-m aperture, active wavefront control, coronagraphs with demonstrated technical readiness, and a highly stable spacecraft environment to enable optical wavelength studies of nearby planetary systems at contrasts exceeding a billion-to-one. Exo-C will directly image and take spectra of planets beyond the reach of other telescopes. The mission and hardware design is patterned on the highly successful Kepler mission to achieve the same goal of delivering groundbreaking exoplanet science at an affordable cost.

In the course of its 3-year mission, Exo-C will carry out four key studies:

Spectroscopy of known exoplanets: Ten nearby stars host 19 radial velocity (RV) planets with apastron distances greater than 0.25″. These are cold objects presenting a contrast of $10^{-9}$ in the optical and near-infrared. Existing ephemerides allow observations to be timed to coincide with their maximum elongations. Exo-C will take spectra of these objects and provide astrometric measurements that will resolve the $\sin(i)$ ambiguity in their masses. The spectra will be sensitive to features of $CH_4$, $H_2O$, Na I, and K I in their atmospheres, thereby constraining their relative abundances, metallicity, and depth of any cloud decks. In addition, Exo-C will obtain optical spectra of hot young planets detected in the near-IR by ground observatories, thus better constraining their atmospheric structure and composition.

*Discovery of new planets in the solar neighborhood:* RV surveys are incomplete for orbital periods >12 years, for mid-F and hotter stars lacking strong metallic lines in their spectra, for stars with high chromospheric activity, and for planets in nearly face-on orbits. Multi-epoch imaging with Exo-C's coronagraph has the potential to discover planets beyond RV limits around as many as 150 nearby stars. There are more than 70 stars within 25 pc that host close-in RV planets and would be prime targets for outer planet searches. Exo-C's contrast capability will permit detections of Jupiter-like planets on orbits out to 9 AU, Neptune-like planets out to 3 AU, 2 $R_\oplus$ mini-Neptunes out to 1.5 AU (where $R_\oplus$=1 Earth radius), and super-Earths at 1 AU. Particularly important survey targets will be the two Sun-like stars of the alpha Centauri binary system, the Sun's nearest neighbor. If exozodi is low and a very stable observatory can be achieved, Earth-sized planets could be detected in the habitable zones of a handful of stars. In addition, spectral characterization of the brightest planet discoveries would be carried out.

*Structure and evolution of circumstellar disks:* Debris disks trace the dust liberated by ongoing collisions in belts of asteroidal and cometary parent bodies. In addition to revealing the location of these belts, debris dust serves as a tracer of the dynamical signature of unseen planets. Exo-C will be capable of resolving rings, gaps, warps, and asymmetries driven by planetary perturbations in these disks. With contrast improved 1000× over the Hubble Space Telescope (HST), Exo-C will be sensitive enough to detect disks as tenuous as our own

Kuiper Belt, enabling comparative studies of dust inventory and properties across stellar ages and spectral types. Several hundred debris disk targets will be surveyed, including nearby stars with far-IR excess and RV planet systems where sculpted dust features might be seen. A smaller survey of young protoplanetary disks will reveal how small dust particles are distributed with respect to the larger particles traced by Atacama Large Millimeter/submillimeter Array (ALMA) imaging.

***Survey of Dust in Habitable Zones:*** Exo-C's inner working angle of 0.16″ at 550 nm is sufficient to spatially resolve the habitable zones of 70 Sun-like stars and another 75 stars with earlier spectral types. A survey of these targets will search for extended surface brightness from exozodiacal dust, to limits within a factor of a few times the dust levels found in our own Solar System. The detected surface brightness will constrain the dust inventory and albedo, thus helping to define the background levels against which future missions will observe Earth-like exoplanets. In the nearest examples, Exo-C images may show asymmetric structures indicative of planetary perturbations to the dust distribution.

## 4.2 Detailed Description of Science Objectives

### 4.2.1 Exoplanet Target Samples

There are more than 70 known planetary systems within 25 pc. The exoplanets in those systems that have widest angular separation are the primary candidates for direct imaging and spectroscopy. Observing these known planets is much more efficient than blindly surveying nearby stars—minimizing integration time and maximizing the science return for the overall mission.

For the systems only known to have short-period planets, additional planets may be present on wider orbits and be detectable through high-contrast imaging. Even for systems not known to have planets, failed planet searches provide useful information in mission planning; the phase space that is ruled out directly constrains the expected yield for each star, enabling further refinement of the target list and improving the mission performance. In addition, as shown below, spectra of the planets detected by RV will be easier to interpret given that their masses will be well-constrained.

#### 4.2.1.1 Radial Velocity Planets

RV surveys have detected many exoplanets around nearby stars; the closest and brightest of these are prime targets for Exo-C imaging. Beyond simply knowing that a planet is present, RV measurements also constrain the orbital separation and relative illumination as a function of time, such that an optimal epoch for observation can be chosen within the mission lifetime. RV measurements by themselves determine the product of the planet mass and the sine of the orbital inclination. Imaging detections of an RV planet provide astrometry which resolves the $\sin(i)$ ambiguity and thus specifies the planet mass, which then aids in subsequent interpretation of its atmospheric spectrum. The RV planets orbit mature, quiet stars for which excellent elemental abundances can be derived. This will allow meaningful comparison of abundances measured in the planetary atmospheres to those of the star.

As seen in Figure 4.2-1 and Table 4.2-1, 19 known RV planets have large enough angular separation and are bright enough for Exo-C to image. With the instrument inner working angle (IWA) increasing with wavelength, a full spectrum from 0.495–1.0 μm can be obtained for about half of these planets.

New exoplanets will continue to be detected by ongoing measurements of their RV signatures. Figure 4.2-2 shows the steady rise in the number of bright exoplanets on wide orbits. By the time Exo-C launches, improved instrumentation and a longer baseline of observations will enable the detection of lower-mass and longer-period planets.
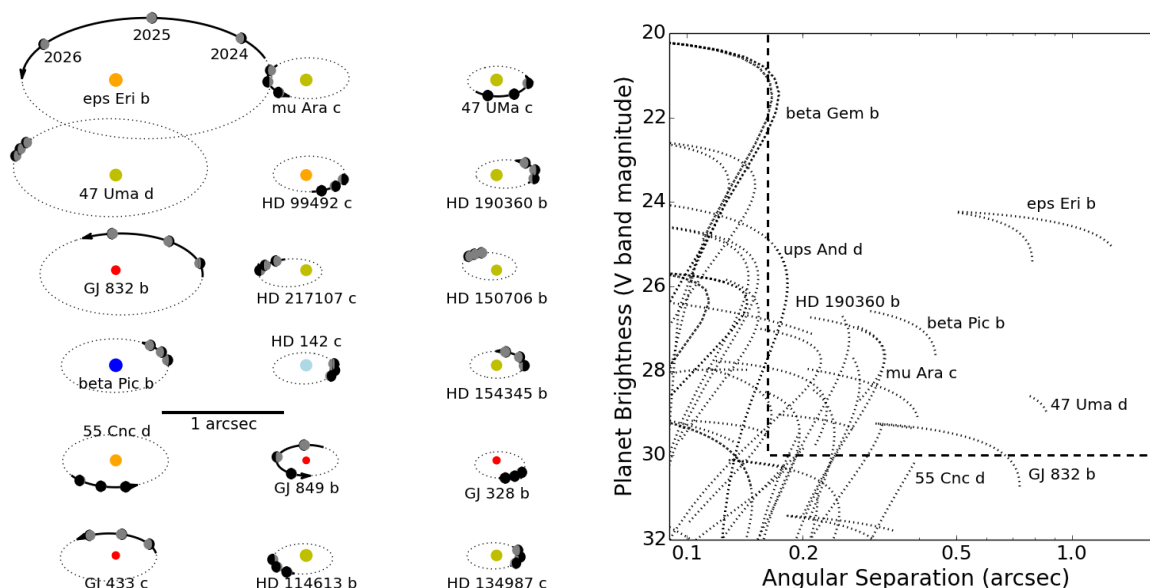
**Figure 4.2-1.** Exo-C will observe several known exoplanets whose orbital radius and orbital phase will be known during each observing epoch. The inclination and the orientation of the orbits remain unknown. Assuming an inclination of 70˚, the illumination of the widest-separation/brightest planets is shown for three epochs from 2024 to 2026 (left panel). The brightness of each planet is shown as a function of orbital separation over the same time period (right panel). Targets must have sufficient angular separation (≥0.16″ at V band) and must be bright enough (V mag < 30) to be detected by Exo-C.

**Table 4.2-1.** Known exoplanets provide primary targets for Exo-C. The properties of the 19 best planets are shown based on their visibility during a 3-year mission starting in 2024, assuming 60° for the unknown inclination of each planet's orbit. Fspec is the fraction of a full 500–1000 nm spectrum that can be obtained outside the coronagraph inner working angle.

| | Star Properties | | | | Planet Properties | | | | Best Viewing (2024–2026) | | | Coverage |
|---|---|---|---|---|---|---|---|---|---|---|---|---|
| Planet Name | Dist. (pc) | Spectral Type | Lstar (LSun) | V* (mag) | Msinl (MJup) | P (yr) | a (AU) | e | Sep (mas) | Contrast (1e-9) | Vp (mag) | Fspec |
| beta Gem b | 10.4 | K0III | 41 | 1.14 | 2.8 | 1.6 | 1.8 | 0.02 | 173 | 10.8 | 21.1 | 0.18 |
| eps Eri b | 3.2 | K2V | 0.3 | 3.73 | 1.1 | 6.8 | 3.4 | 0.25 | 1263 | 6.3 | 24.2 | 1 |
| ups And d | 13.5 | F9V | 3.3 | 4.10 | 4.1 | 3.5 | 2.4 | 0.26 | 182 | 4.5 | 25.0 | 0.24 |
| beta Pic b | 19.4 | A6V | 8.0 | 3.85 | 9.0 | 19.6 | 8.7 | 0.02 | 441 | 0.8 | 26.6 | 1 |
| HD 190360 b | 15.9 | G7IV-V | 1.1 | 5.70 | 1.5 | 8.0 | 4.0 | 0.31 | 327 | 3.9 | 26.7 | 1 |
| 47 UMa c | 14.1 | G1V | 1.5 | 5.05 | 0.5 | 6.5 | 3.5 | 0.09 | 263 | 2.3 | 26.7 | 0.79 |
| HD 39091 b | 18.3 | G0V | 1.4 | 5.65 | 10.1 | 5.9 | 3.3 | 0.64 | 211 | 3.4 | 26.8 | 0.43 |
| mu Ara c | 15.5 | G3IV-V | 1.7 | 5.15 | 1.9 | 11.5 | 5.3 | 0.09 | 324 | 1.9 | 27.0 | 1 |
| 14 Her b | 17.6 | K0V | 0.7 | 6.60 | 5.2 | 4.9 | 2.8 | 0.36 | 222 | 6.5 | 27.1 | 0.51 |
| HD 114613 b | 20.7 | G3V | 4.1 | 4.85 | 0.5 | 10.5 | 5.2 | 0.25 | 280 | 0.7 | 27.7 | 0.91 |
| HD 154345 b | 18.6 | G8V | 0.5 | 6.76 | 1.0 | 9.1 | 4.1 | 0.04 | 230 | 3.4 | 27.9 | 0.57 |
| HD 217107 c | 19.9 | G8IV | 1.1 | 6.16 | 2.6 | 11.7 | 5.2 | 0.51 | 396 | 1.9 | 28.0 | 1 |
| HD 142 c | 25.7 | F7V | 2.7 | 5.70 | 5.3 | 16.4 | 6.7 | 0.21 | 241 | 0.8 | 28.4 | 0.64 |
| HD 134987 c | 26.2 | G6IV-V | 1.4 | 6.45 | 0.8 | 13.7 | 5.8 | 0.12 | 196 | 1.5 | 28.5 | 0.33 |
| 47 Uma d | 14.1 | G1V | 1.5 | 5.05 | 1.6 | 38.3 | 11.6 | 0.16 | 860 | 0.4 | 28.6 | 1 |
| HD 150706 b | 28.2 | G3V | 0.9 | 7.01 | 2.7 | 16.1 | 6.5 | 0.38 | 270 | 1.6 | 29.0 | 0.84 |
| GJ 832 b | 5.0 | M1.5V | 0.03 | 8.66 | 0.6 | 9.4 | 3.4 | 0.12 | 730 | 5.8 | 29.2 | 1 |
| HD 99492 c | 18.0 | K2V | 1.0 | 6.14 | 0.4 | 13.6 | 5.4 | 0.10 | 322 | 0.6 | 29.2 | 1 |
| 55 Cnc d | 12.3 | G8V | 0.6 | 5.93 | 3.5 | 13.4 | 5.4 | 0.02 | 389 | 0.2 | 30.2 | 1 |
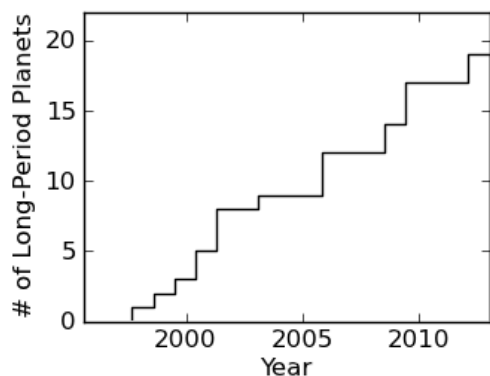
**Figure 4.2-2.** The number of known exoplanets that are good targets for Exo-C imaging continues to increase. The cumulative number of planets is shown for those with angular separation >0.15" and whose host star is brighter than V=7 mag.

While RV detections offer excellent targets for imaging, RV non-detections provide the best upper limits on possible planets. For systems with accurate RV measurements over a ~10-year timeline, Saturn-mass planets at several AU can be ruled out. Many systems cannot be so well constrained however, due to their early spectral type, unusually active chromosphere, or contamination by a stellar companion.

### 4.2.1.2 Transiting Planets

Transit surveys for exoplanets (e.g., Kepler, HAT, and WASP) are highly biased toward short-period orbits and typically concentrate on faint, distant stars. As such, exoplanets detected by their transit signal are too dim and at too small angular separation for direct imaging by Exo-C. While the future Transiting Exoplanet Survey Satellite (TESS) missions will find planets around brighter/closer stars, it will only be sensitive to very short (<1 month) periods.

The cool, distant giant planets visible to Exo-C allow us to answer very different scientific questions than those raised by hot, transiting giant planets whose atmospheres are sculpted by intense irradiation, strong winds, exotic chemical and cloud processes, and atmospheric escape. The giant planets visible to Exo-C will likely be far more similar to Solar System giants to whose spectra they can be directly compared.

### 4.2.1.3 Planets Detected by Astrometry

The ESA Gaia mission (launched Dec. 19, 2013) will provide all-sky measurements of stellar positions capable of detecting exoplanets through their astrometric reflex motion. Estimates of the exoplanet yield, based on initial on-orbit performance by Perryman et al. (2014), have updated the earlier simulation study of Casertano et al. (2008). Exoplanets with periods less than the 3-year nominal mission lifetime, and amplitude larger than 70 μas, will be detectable around a large number of stars. This accuracy is sufficient to detect the wobble induced by a Saturn-mass×sin$(i)$ planet orbiting at 2.5 AU around a solar-mass star at 10 pc. Gaia detections of known RV planets will trace their orbits, measuring both the planet mass and the orbit inclination. To this, Exo-C will add measurement of the atmospheric spectrum and evolution of the illumination phase around the orbit for its accessible targets (Table 4.2-1). Because the Gaia survey does not use an input catalog, the mission has the capability to generate robust statistics for the massive planets of nearby stars with orbital periods less than three years.

The astrometric performance of Gaia for bright stars, however, has not yet been quantified. While most of Exo-C's target stars are brighter than Gaia's nominal limit (V=6 mag; Lindegren et al. 2012), it has been demonstrated that Gaia can observe stars beyond this nominal limit (Martin-Fleitas et al. 2014). Simulations indicate that the single measurement accuracy will likely be slightly poorer at brighter magnitudes, but Gaia should still recover many of the currently-known planets on Exo-C's target list. It should also discover giant planets inaccessible to RV measurements around nearby early-type stars, enhancing the Exo-C target list for spectroscopy.

### 4.2.1.4 Targets from Direct Imaging

New extreme adaptive optics coronagraphs—Gemini Planet Imager (GPI), Very Large Telescope/Spectro-polarimetric High-contrast Exoplanet Research (VLT/SPHERE), Subaru Coronagraphic Extreme Adaptive Optics (SCExAO)—should image dozens of young massive planets in their near-infrared thermal emission. These will be targets for optical spectral characterization with Exo-C. Current examples of such objects include beta Pictoris b and the four planets of the HR 8799 system (Lagrange et al. 2010; Marois et al. 2010).

### 4.2.2 Giant Planet Spectra

Until now, the characterization of individual gas giant exoplanets has focused almost exclusively on the transiting giants. This unusual subset of planets orbits directly under the glare of their primary stars on very short-period orbits. Transit studies from space have measured atmospheric temperatures and identified atmospheric absorbers in a few planets. In the past few years, a few young, self-luminous giant planets have been detected and studied in the near-infrared from large ground-based telescopes. These young objects have warm atmospheres that host exotic cloud decks of silicates and liquid iron drops.

However, giant planets cool as they age. By ages of 2 Gyr, those giants orbiting beyond 2 AU from their primary stars will generally have cooled well below 500 K. By focusing on older stellar systems from space, Exo-C will finally allow us to characterize the atmospheric composition and structure of those more statistically normal and more Solar System-like cool giant planets orbiting far from their primary stars.

The atmospheric envelopes of giant planets are composed predominantly of $H_2$ and He gas enhanced with an uncertain mixture of the other elements. In the atmosphere, among the most abundant and spectroscopically interesting species, carbon will be found as $CH_4$, oxygen as $H_2O$, and nitrogen as $NH_3$. In warmer objects, Na and K gas may also be present. Disequilibrium effects and photochemistry can produce traces of other molecules, notably CO and hydrocarbons such as ethane and acetylene. As with the background $H_2$ and He gas, none of these minor species have strong absorption features in Exo-C's wavelength range, although a pressure-induced absorption feature of $H_2$ may be detected at ~820 nm in some objects. The spectra of Exo-C giants are thus expected to primarily be influenced by $CH_4$, $H_2O$, $NH_3$, and possibly gaseous Na and K, the clouds formed by the condensation of these species, and photochemical hazes.

Spectra of Solar System giants and some model giants are shown in Figure 4.2-3. For such targets, the principal science questions that can be addressed are the relative abundances of these gaseous species, the properties of the cloud layers, the atmospheric temperature, and inferences about planet mass and planetary formation mechanisms.

Figure 4.2-4 illustrates the mass and equilibrium temperature of those RV planets that are most favorable for characterization by a direct imaging mission. Note the large range of masses and temperatures of the target objects. Depending on the atmospheric temperature, ammonia, water, or even methane or alkali clouds will be present in the atmosphere. Clouds are important as they sequester condensable species (e.g., water) and strongly affect the overall spectral shape.

The spectral characterization of extrasolar giant planets will address key science goals for understanding the origin and evolution of planetary systems. In their quick studies done for the NASA Exoplanet Exploration Office, Burrows (2014), Hu (2014), and Marley et al. (2014) demonstrated the diversity of spectra that can be expected from directly imaged giant planets. Exo-C will leverage this remarkable range in plausible planetary spectra to address two key giant planet science objectives.
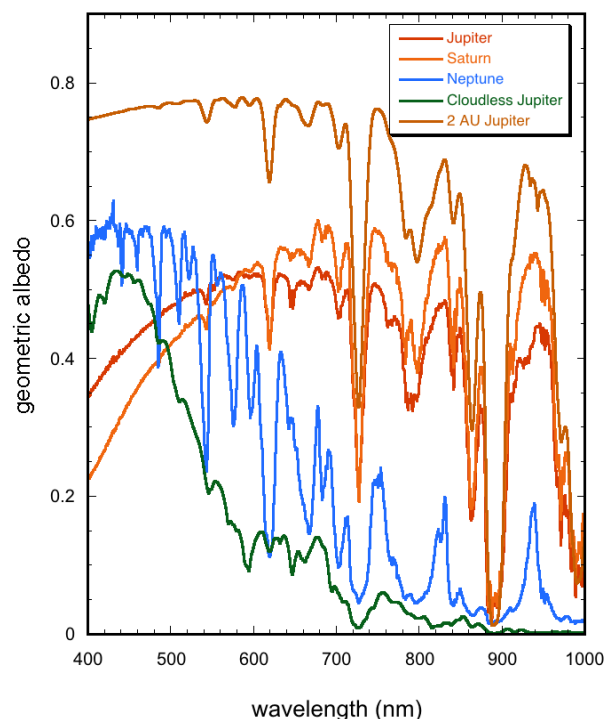
**Figure 4.2-3.** Geometric albedo spectra of real and model giant planets. Shown are Jupiter, Saturn, and Neptune (from Karkoschka 1994) and model spectra for two model giants, both with Jupiter's mass and three-times solar abundance heavy element enhancement (from Cahoy et al. 2010). One model places Jupiter at 2 AU where it will have water clouds, leading (in the absence of photochemical smogs) to a very high albedo. In the second model, clouds are absent, a situation that may arise from a combination of smaller orbital distance and relative youth (such that the internal heat flow is larger than current day Jupiter). Such cloudless planets can be quite dark in scattered light at red wavelengths with a distinctly blue Rayleigh scattering spectral slope.

### How does the composition of gas and ice giant planets vary with planet mass, orbit, and stellar mass and metallicity?

While RV surveys have constrained the architecture of many planetary systems, we do not yet know how the composition of giant planet atmospheres varies with these and other relevant parameters. By probing atmospheric composition for a healthy sample of extrasolar giant planets, Exo-C will ascertain if composition is correlated with mass, orbital radius, stellar type, or other variables and thus provide key new clues for understanding planet formation.
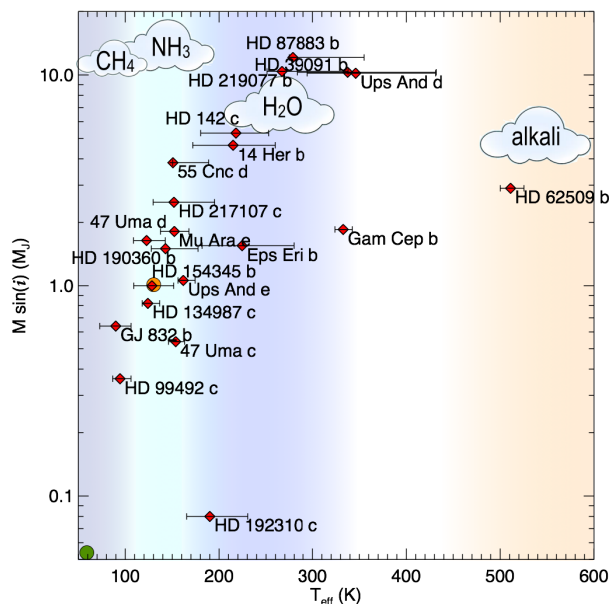


**Figure 4.2-4.** Measured $M \sin(i)$ and estimate equilibrium temperature for known radial velocity planets with favorable angular separations from their primary stars. Equilibrium temperature assumes Jupiter's albedo. Actual atmospheric temperatures will be warmer due to the contribution of internal heat flow, which depends on the age and mass of the planet. Approximate temperature ranges where various cloud decks will appear are indicated by colored bands with species labeled at the top. Some well-known planets are labeled. Jupiter and Neptune are depicted by the orange and green circles. Neptune is in the bottom left corner of the figure.

Solar System gas giants are enhanced in heavy elements over solar composition by factors of three (Jupiter) and 10 (Saturn). The uniform enhancement across many elements (C, N, S) at Jupiter was the greatest discovery of the Galileo entry probe mission and is a valuable piece of information regarding the giant planet formation process (Chabrier et al. 2007; Fortney et al. 2008). The enrichment may represent the accretion of icy planetesimals from the nebula after gas accretion. The roughly 30× solar enrichment in the envelopes of Uranus and Neptune may arise because the nebula did not survive long enough for them to capture large amounts of $H_2$ and He gas. (see D'Angelo et al. 2010) With only four planets, the observed trends (increasing enhancement with decreasing mass, Figure 4.2-5, and increasing orbital radius, for example) are not robust and limit our ability to understand how giant planets form.
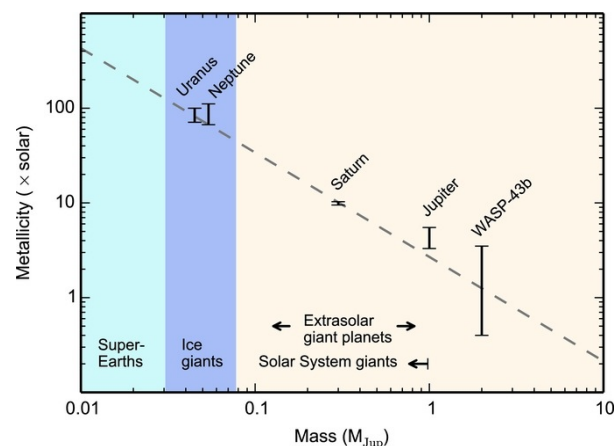
**Figure 4.2-5.** Atmospheric metallicity enhancement as a function of planet mass for solar system giants (inferred from methane) and WASP-43b (as inferred from water by Kreidberg et al. 2014). Dashed line is a power law fit to the data. Exo-C will provide many more data points with abundance retrieval accuracy comparable to that of WASP-43b shown here. Figure from Kreidberg et al.

Statistics from transit, RV, and microlensing surveys suggest that Neptune-mass planets are very common (Sumi et al. 2010, Howard et al. 2010). We have yet to learn whether these objects are mini Jupiters or are enhanced by factors of 30 to 50 over solar composition in heavy elements, like Uranus and Neptune.

The atmospheric elemental abundances that are most amenable to remote measurement are C, O, N, Na, and K. C, O, and N will be present as $CH_4$, $H_2O$, and $NH_3$. Na and K are detectable in warm, cloudless Jupiter-like planets (Cahoy et al. 2010). Methane will likely dominate the visible spectra of directly imaged planets, and in some cases absorption by the pressure-induced opacity of $H_2$, but ammonia and water will be detectable in a few favorable cases. The best visible band for detecting water vapor in an extrasolar giant planet somewhat warmer than Jupiter is 940 nm. Other water absorption bands in the optical spectrum overlap with those of methane. The continuum flux level against which these bands will appear depends upon the height and thickness of atmospheric cloud layers and atmospheric photochemistry. In

contrast, the far-red optical spectra of generally cloudless, hot, young self-luminous Jupiter-like planets will be dominated by the highly pressure-broadened lines of sodium and potassium. These absorption bands of methane, water and alkali metals are the expected signatures of giant planet science targets for Exo-C. Measuring these features will constrain the atmospheric composition and temperature of planets even if the planetary radius and mass are uncertain (Marley et al. 2014).

***How do clouds affect giant planet atmospheres and vary with atmospheric temperature and other planetary parameters?***

Every appreciable atmosphere in the Solar System is cloudy. This is almost certainly true outside of the Solar System as well. Iron, silicate, and various alkali clouds (e.g., $Na_2S$) have been detected in the warm atmospheres of directly imaged young giant planets, and clouds have been seen on at least one transiting planet. Since the giant planets that will be imaged by Exo-C are farther from their primary stars than the transiting planets—and older than the young, directly imaged giant planets—their atmospheres will be substantially cooler than both. Consequently, the giant planet atmospheres observed by Exo-C will likely contain water, ammonia, or possibly methane or alkali clouds (Figure 4.2-4). These clouds will greatly influence the reflected light spectra of these planets and the extraction of gaseous abundances will proceed in parallel with cloud characterization.

Cloud height can be discerned spectroscopically by measuring the relative depths of molecular absorption bands of diverse strengths. Cloud thickness and altitude are indicative of planet temperature. For exoplanets with typical ages of 200 Myr to 10 Gyr and masses of one to five Jupiters, the expected atmospheric effective temperature ranges from below 100 K to about 500 K (Figure 4.2-4). As a Jupiter-like planet cools over this range, water clouds first appear in what is otherwise a relatively cloud-free sky,

and then sink with falling effective temperature. At lower temperatures, ammonia and methane clouds appear (Cahoy et al. 2010). Thus, Exo-C will serve as an exoplanetary weather satellite by constraining cloud properties and atmospheric temperature on the directly imaged planets. The experience gained from interpreting giant planet cloud properties will be invaluable when spectra of directly imaged terrestrial planets eventually become available.

Giant exoplanet characterization will benefit from a long, deep heritage in observing and modeling the reflected solar spectra of Solar System giant planets (e.g., Sato and Hansen 1979). The reflected spectra of Solar System giants (see Figure 4.2-3) are dominated by strong methane absorption bands that punctuate a bright continuum flux set by cloud opacity in the red and by Rayleigh and haze scattering in the blue. Teasing out these effects to discern the atmospheric methane abundance and cloud properties has thus long been a focus for solar system planetary science. For Jupiter, at least, we know that inferences from remote sensing were correct as the Galileo entry probe confirmed the measurement of atmospheric methane by ground-based observers (Niemann et al. 1996). At Jupiter, $NH_3$ and $H_2O$ vapor abundances are challenging or impossible to measure remotely, as these species are condensed out into thick cloud decks. Exoplanets slightly warmer than Jupiter, because of their youth or proximity to their primary stars, will lack these cloud decks, making these gases much more accessible to remote observation.

We expect that planet characterization by Exo-C will follow a two-tiered strategy. All surveyed planets will be imaged in four or five broad filters. This will sample the continuum shape and be sufficient to identify planets with novel characteristics and separate likely gas and ice giants (Figure 4.2-6). A subset of the most interesting and brighter planets will be further characterized by R~70 spectroscopy.

This spectral resolution was chosen as the minimum required to uniquely identify both moderate and strong methane and ammonia bands, along with the water band at 940 nm (see Table 4.2-2). We desire to measure a variety of methane bands of varying strengths since this provides the dynamic range needed to constrain a variety of possible methane mixing ratios. The strongest molecular bands saturate at the higher abundances while the weaker bands, which are subdued at low abundances, become prominent. Multiple examples of this behavior are documented in Sudarsky et al. (2005), Cahoy et al. (2010) and in the quick study reports by Burrows (2014) and Marley et al. (2014). Care must be taken, of course, as in some cases there can be degeneracies between high clouds and high methane abundances (quick study by Hu 2014) although constraining the transition from Rayleigh to particle scattering can resolve many such cases.
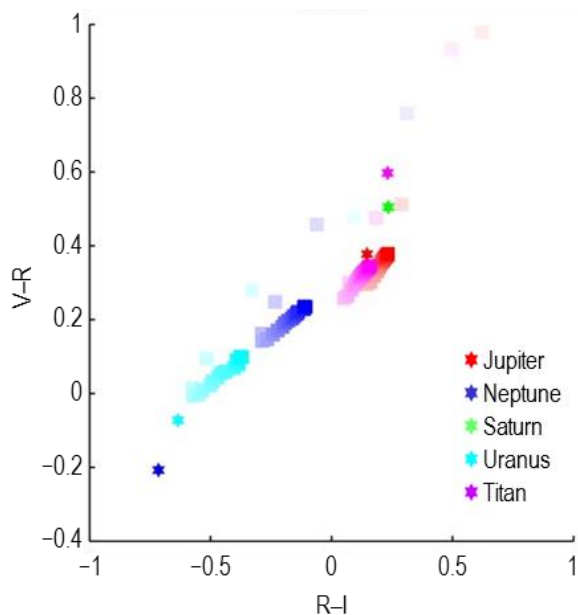


**Figure 4.2-6.** Color-color diagram from Cahoy et al. shows location of methane-rich Solar System objects (legend) and model planets (squares) placed at 2 AU. Red and magenta colors denote Jupiters with 1× and 3× enhancement over solar abundance in heavy elements. Blue and cyan are for 10× and 30× enhanced Neptunes. Intensity of color fades as model phase angle varies from 0° to 180° in 10° increments.

**Table 4.2-2.** Characteristics of diagnostic giant planet absorption bands.

| Species | Band Center (nm) | Width (nm) | R |
|---|---|---|---|
| $NH_3$ | 990 | 23 | 45 |
| $CH_4$ | 990 | 20 | 50 |
| $H_2O$ | 940 | 60 | 15 |
| $NH_3$ | 930 | 20 | 50 |
| $CH_4$ | 890 | 20 | 45 |
| $NH_3$ | 890 | 27 | 35 |
| $CH_4$ | 862 | 12 | 70 |
| $CH_4$ | 840 | 10 | 85 |
| $CH_4$ | 790 | 24 | 30 |
| $CH_4$ | 725 | 10 | 70 |
| $NH_3$ | 650 | 10 | 65 |
| $CH_4$ | 620 | 8 | 80 |

Centers and widths (FWHM) of absorption bands of important absorbers in giant planet atmospheres. R gives spectral resolution (following Des Marais et al. 2002) needed to detect the band if present in an atmosphere (R=center/width, rounded to nearest 5 for clarity).

The spectra of Jupiter and Saturn shortwards of 600 nm are also influenced by absorbing photochemical hazes produced by solar ultraviolet (UV) radiation (Figure 4.2-3). This photochemistry is only partially understood, but plays an important role in the stratospheric energy balance and temperature structure of giant planets. For gas giants on orbits inside of 5 AU, photochemistry and haze production will be important atmospheric processes. Observing the blue-wavelength albedo of a number of giant planets around both solar and non-solar-type stars will substantially increase the number of atmospheres in which photochemical processes can be studied.

### 4.2.3  Small Planet Spectra

#### 4.2.3.1 Scientific Context

The last two decades of exoplanet observations have been dominated by exoplanet discovery and initial physical characterization to determine planetary radius, mass, density, and orbital properties (e.g., Marcy et al. 2005; Lissauer et al. 2011; Howard et al. 2012; Marcy et al. 2014). Close-in giants, being larger and brighter, were the first planets discovered and characterized, but new RV and transit techniques, combined with more powerful instrumentation, are finding and studying progressively smaller planets. Planets of a few Earth masses are now being discovered at distances from their parent star where there is a relatively high probability that they may harbor surface oceans and remotely detectable, global surface biospheres (Borucki et al. 2013; Anglada-Escude et al. 2013; Quintana et al. 2014).

One of the great surprises from this period has been the discovery—primarily by the Kepler mission—of a plethora of planets with sizes and masses between that of Earth and Neptune (Figure 4.2-7, Howard 2013).

These planets have no analog to those in our own Solar System, and prior to their discovery were thought to be relatively rare (Ida and Lin 2004). Observations have found the opposite: super-Earth to sub-Neptune-sized planets are far more common than either ice or gas giant planets in the inner regions of planetary systems, although likely not as common as terrestrial planets (Howard et al. 2012).

Perhaps the most surprising exoplanet discovery to date, however, has been the observational confirmation that planets less massive than 10 $M_\oplus$ are not necessarily solid, terrestrial super-Earth worlds with bulk compositions dominated by iron and silicate (Pollack et al. 1996), but may be low-density water and gas-dominated "mini-Neptunes" (Charbonneau et al. 2009; Lissauer et al. 2011) whose formation, composition, and evolution are not at all understood. Similarly, true super-Earths (rocky planets many times more massive than the Earth) have been confirmed (Leger et al. 2009; Dumusque et al. 2014). Depending on differences in internal structure and composition, they may have very different atmospheres from the terrestrial planets in our Solar System (e.g., Elkins-Tanton and Seager 2008). Their nature and evolution are also not well understood, primarily due to a dearth of observational data. We do not know whether super-Earths and mini-Neptunes are two
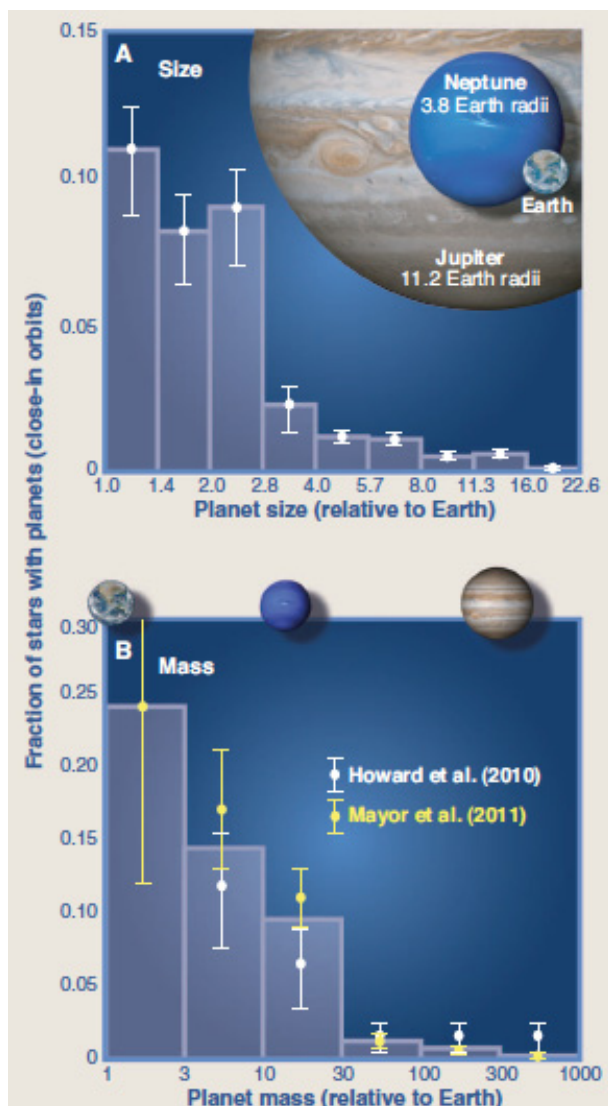
**Figure 4.2-7.** Current observations show the common nature of planets with sizes between Earth and Neptune. Histograms of known planets as a function of planet radius (top), and planet mass (bottom). Potential terrestrial planets smaller than Neptune (17 M$_\oplus$; 3.8 R$_\oplus$) are much more common than larger gas giants (from A. Howard, *Science*, 2013).

distinct planet classes that form via different mechanisms, or if they represent different end products for the same evolutionary sequence (e.g., Luger et al. 2015). The lack of similar planet classes in our Solar System means that Exo-C is ideally suited to guide our understanding of the nature, formation, and evolution of these common objects—and their potential suitability to support life.

While exoplanet detection and physical characterization continues apace—primarily using transit and RV techniques—another era has begun: the compositional characterization of exoplanets through direct imaging and spectroscopy. To date, characterization targets have predominantly been Jovian planets (e.g., Grillmair et al. 2008; Sing et al. 2011), and exo-Neptunes (Fraine et al. 2014), but lower mass planets such as the mini-Neptune GJ1214b are also being characterized through transit spectroscopy (Bean et al. 2011; Kreidberg et al. 2014). Theoretical studies (e.g., Lopez et al. 2013) and observational measurements of density for smaller exoplanets (Rogers et al., 2014) are suggesting a dividing line near R<1.6 R$_\oplus$ between potentially habitable super-Earth objects with a relatively rocky composition and therefore the ability to support a liquid ocean on their surfaces, and likely uninhabitable mini-Neptune-class planets that have a low bulk density and are thought to retain relatively massive volatile envelopes. Empirically testing the nature of objects on either side of this theoretical line will require a spectroscopic census of planets of different sizes to measure the composition of the bulk of their atmospheres and to determine if there is a trend with planetary size. Exo-C will have access to nearly 56 nearby stars in which planets Neptune-sized or smaller are potentially detectable (Figure 4.7-2).

By the start of the next decade, we anticipate having the capability to obtain spectroscopy for planets with radii twice that of the Earth through transit observations with the James Webb Space Telescope (JWST). These transit transmission measurements, while a great step forward, will be fundamentally limited in their ability to characterize planetary atmospheres and surfaces, and will be unlikely to characterize planetary systems like our own. Due to the effects of refraction, transit transmission observations will be limited to probing the uppermost regions of an

atmosphere, especially for planets further from their stars and for planets in the habitable zones of more Sun-like stars (Betremiuex and Kaltenegger 2013; Misra et al. 2014). The limb-grazing observing geometry for transit transmission also means that it is impossible for transit transmission to directly sample planetary surface compositions. Also, for the long atmospheric path lengths sampled by transmission observations, even small amounts of haze and aerosols preclude sampling the atmosphere below the haze layer. For the same amount of haze, direct imaging spectroscopy, like that proposed by Exo-C can still sample a relatively large fraction of the atmosphere. Figure 4.2-8 compares the fractional change in detected light from transit and reflected light observations of the same model planet. The transit spectra is almost perfectly flat (even into the near-infrared, not shown) while for the same planet in reflected light the dynamic range of the spectrum is much greater and absorption features of methane are readily apparent.

JWST will also have very limited ability to study planetary systems like our own. Like Exo-C, JWST will be sensitive down to planets at the very upper end of the theoretical size limits for planetary habitability, but JWST will be better suited to characterize those planets that orbit close to their parent star, and so undergo more transits during the mission lifetime. Consequently, JWST studies of planets in the habitable zone will concentrate on planets orbiting cooler M dwarf stars, where the habitable zone is close to the star. However, the extreme proximity of a potentially habitable planet to its M dwarf parent star can enhance the star's impact on the planetary environment and potentially increase the possibility of false positive biosignatures (Tarter et al. 2007; Barnes et al. 2009; Domagal-Goldman et al., 2014; Luger and Barnes, 2015) Finally, the suite of spectral observations obtainable by JWST for habitable zone planets will likely be extremely small, as spectroscopic data can only be obtained during
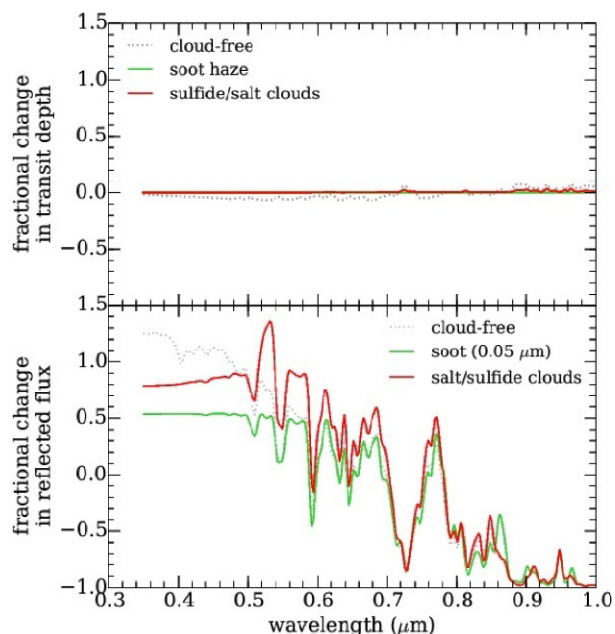


**Figure 4.2-8.** Model spectra of mini-Neptunes with cloud-free, soot aerosols or sulfide/salt clouds seen in transit transmission (top) and direct imaging (bottom). The curves are normalized to show the ratio of the spectrum to the average flux over the wavelength range shown. Direct imaging, with its shorter, more direct path length probes deeper into a planetary atmosphere than the glancing path seen in transit transmission. Direct imaging therefore provides a superior opportunity to probe the bulk of the planetary atmosphere. (Credit: Caroline Morley).

the planetary transit, and multiple transits must be coadded over the lifetime of the mission to achieve adequate S/N for these targets (Deming et al. 2009).

In summary, transit transmission data will provide a limited initial characterization, but will likely be insufficient to adequately address questions related to the fundamental nature of these cooler sub-Neptune/super-Earth objects, including their formation history, whether they represent an evolutionary sequence, and their potential habitability. To advance our ability to classify these objects and understand their nature, evolution, and potential habitability, we require a mission like Exo-C that is designed with the goal of spectroscopy through direct imaging of sub-Neptune planets. This is the only technique that can potentially sample the

entire atmospheric column and the surface properties of these planets, and deliver spectroscopic information from a large enough sample to derive statistically meaningful inferences on their planetary properties and history.

The most challenging and rewarding goals of any such mission will be identifying potentially habitable worlds, and undertaking the first search for life on a planet in a planetary system other than our own. Spectroscopic characterization of planetary environments will be the cornerstone of this search.

### 4.2.3.2 What We Can Learn from the Spectrum

Specific goals for small planet studies for the Exo-C mission include: 1) Searching for time and phase-dependent changes in planet brightness that may be indicative of aerosols or reflectivity from a surface liquid 2) Taking the chemical inventory, including absorbing gases and scattering aerosols, and estimating the bulk atmospheric elemental composition of sub-Neptune/super-Earth planets. 3) Searching for $H_2O$ vapor as a marker of potential habitability for planets imaged in the habitable zone of their parent star, and 4) conducting a preliminary search for biosignature gases for these potentially habitable worlds.

We will obtain photometry of the brightest imaged planets at time-resolved intervals during a single visit and will use these to search for time-dependent changes in planet brightness or color which could be indicative of surface inhomogeneity or cloud activity (e.g. Ford et al. 2001; Cowan et al. 2009). For planets with relatively short orbital periods, we will also attempt to observe the planet at different points in its orbit. This will provide a longer baseline for time-dependent effects, and will also allow us to obtain multiple phase angles, including near quadrature and, for the brighter, closer targets, at phases closer to crescent. These observations could potentially reveal phase-dependent deviations from isotropic scattering that could be indicative of strongly forward-scattering aerosols from a

haze or cloud layer, or due to specularly-reflective "glint" from a liquid surface as has been seen for ethane lakes on Titan (Stephan et al. 2010) and the oceans on Earth (Robinson et al. 2010; 2014). For Earth, phase angles near 130° are sufficient to measure deviations from non-Lambertian behavior due to the presence of water-vapor clouds and ocean glint (Robinson et al. 2014).

In addition to photometry, we will use spectroscopy to search for and quantify trace gas absorption. At the visible wavelengths accessible by Exo-C, for sub-Neptune objects we anticipate that trace gas absorption will be primarily from $H_2O$ and $CH_4$, with the possibility of detecting $NH_3$, $O_3$, and $O_2$. Typical atmospheric bulk gases, those that make up the majority of planetary atmospheres, such as $N_2$ and $CO_2$, do not produce distinct absorption features at visible wavelengths and will not be directly observable. $CO_2$ does have a very weak band at 0.93 μm, which may be visible for massive, $CO_2$-dominated atmospheres with little or no water vapor. However, the presence of even a small amount of water vapor in the planetary atmosphere will produce a 0.94-μm water absorption band that will likely overwhelm and preclude detection of the much weaker $CO_2$. We may also be able to deduce bulk composition from detection of broadening of the trace gases such as water vapor.

Trace gases are more readily observed than bulk atmospheric gases, and detecting and quantifying either $H_2O$ or $CH_4$, or both, will help to constrain the atmosphere's oxidation state and bulk gas composition. Specifically, a spectrum dominated by $CH_4$ and $H_2O$ constrains the atmosphere to be more reducing, and with a higher $H_2$ abundance, than a spectrum that contains no $CH_4$ and is instead dominated by $H_2O$ features and, possibly, $O_3$. The slope of the observed spectrum may also reveal Rayleigh scattering from molecules in the atmosphere (rising toward the blue) or wavelength-dependent slopes produced by photochemical hazes such

as $H_2SO_4$ (grey slope) and hydrocarbons (rising toward the red). A non-blackbody slope can be used to indicate the presence of an atmosphere, and may give clues to the source of the scattering. A spectrally well-resolved Rayleigh slope may be fitted and removed, potentially revealing the presence of $O_3$ Chappuis bands from 0.5–0.7 µm. For cases where the atmosphere is nonexistent or relatively transparent, the surface will be directly sampled. The observed spectrum may then reveal the presence of surface minerals such as iron oxides, which have a strong, broad absorption feature at wavelengths below 0.6 µm, as is seen in the disk-averaged spectrum of Mars (Meadows 2006).

### 4.2.4   Disk Imaging

While exoplanets are the primary targets for this mission, planetary systems can also be imaged indirectly via their debris disks—the remnants left over after planets form. Ongoing destruction of asteroids and comets creates a continual supply of orbiting dust around most Sun-like stars (Bryden et al. 2006), including our own (Figure 4.2-9). In the Solar System, such dust is bright enough to be seen with the naked eye—so called zodiacal light. Far-infrared observations by the Spitzer Space Telescope and the Herschel Space Observatory have identified many neighboring stars with even brighter orbiting debris, orders of magnitude more than in the Solar System (Eiroa et al. 2013). Because they are so bright, optical imaging of debris disks is much easier than detecting their embedded planets.

A key objective for imaging debris disks is to resolve disk structure. High-resolution images taken by HST have revealed a wide variety of disk morphologies (Figure 4.2-10). Some disks are concentrated into narrow, well-defined belts while others are more diffuse. Some are very symmetric while others have pronounced asymmetries—offsets, warps, and clumps. To first order, the location of the debris gives a sense of the overall architecture for each system. Many systems have a two-belt architecture similar to the Solar System's asteroid and Kuiper belts, for example, suggesting intermediate unseen planets. In the case of HR 8799, there are four planets directly seen between the two belts identified by Su et al. 2009. Some disk asymmetries can be used to infer the presence of individual planets. The planet-orbiting beta Pic, for example, was predicted based on the warp it created in the disk (Mouillet et al. 1997), years before the planet itself was eventually observed (Lagrange et al. 2010). Two other systems, Fomalhaut (Kalas et al. 2005) and HD 202628 (Krist et al. 2012), have offset eccentric rings with sharp inner edges, a configuration that will quickly disperse in the absence of a nearby shepherding planet.

Overall, Exo-C images of debris disks will probe the underlying planetary systems both generally, by mapping the system architecture, and specifically, by determining the location of individual planets.
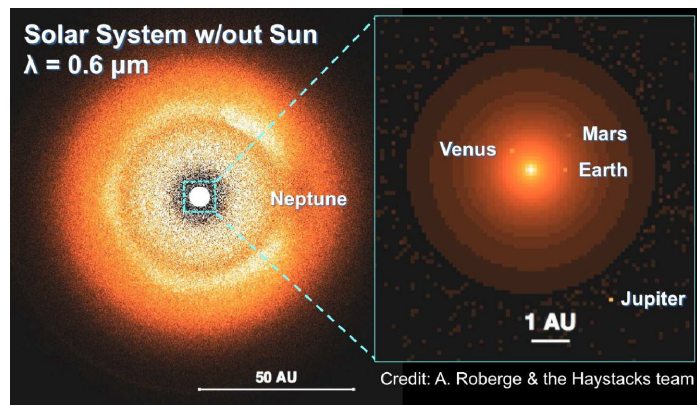


**Figure 4.2-9.** The Solar System's dust is much brighter than its planets. On the scale of the whole Solar System (left panel) or the inner 5 AU (right), the most conspicuous feature is the haze of emission coming from interplanetary dust. (Note that the Sun is not included in the above model, as if it had been perfectly suppressed by a coronagraph.) The partial ring in the outer Solar System's dust is caused by the dynamical influence of Neptune, which itself cannot be seen. The Earth creates a similar structure near its orbit, but with only a 10% enhancement of dust above the background zodiacal light (Kelsall et al. 1998).
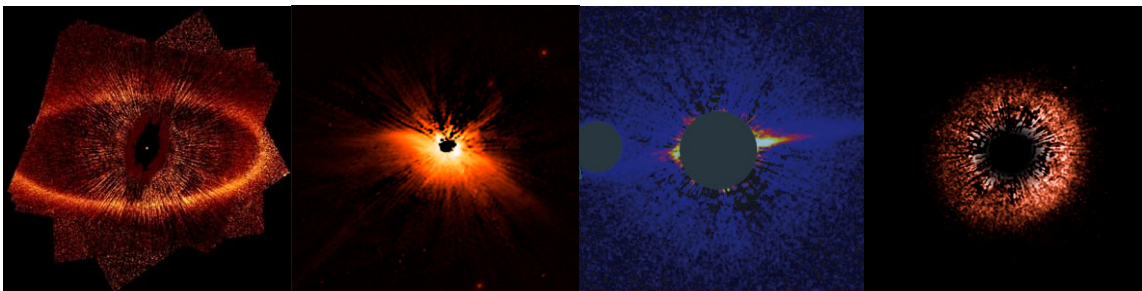
**Figure 4.2-10.** Optical imaging of debris disks by Hubble reveals a variety of disk structures—from smooth belts to eccentric rings, bow shocks, warps, and other asymmetric structure (Fomalhaut, Kalas et al. 2005; HD 61005, Hines et al. 2007; HD 15115, Kalas et al. 2007; HD 107149, Ardila et al. 2004).

### 4.2.4.1 Observation of Known Disks

***Is the Solar System's two-belt architecture normal?***

High-resolution images taken by Exo-C will greatly expand on the ~20 debris disks that have been imaged by Hubble. The rough sizes for over 100 debris disks have now been measured by low-resolution thermal imaging with Herschel (Figure 4.2-11). Whether or not the known orbiting material is spread over a wide disk or concentrated into one or more thin rings remains to be seen. Exo-C observations will not only resolve the known outer disks—typically orbiting at 10s of AU—but also push in toward the inner reaches of each system, potentially identifying new warm asteroidal belts that accompany the cold outer material.

Since the disks already discovered via their thermal emission are relatively large, some of these cold components fall outside of the Exo-C's outer working angle (OWA). Using Exo-C's longest wavelength band for disk observations provides the best match between field-of-view (FOV) and the known disks' angular sizes. For disks that are smaller or have warm components discovered by Exo-C, observations at the shortest wavelength band will provide the best IWA for probing the inner disk. Measurements of disk color provide a constraint on the size of the scattering dust grains.

The primary objective of the disk imaging will be to identify the radial distribution of the orbiting dust. Exo-C will easily distinguish between thin well-defined rings and broad pancake-like morphologies, allowing for identification of multiple-belt systems like our own. As a secondary objective, Exo-C will also measure disk colors. While most disks observed by Hubble have red to neutral colors, AU Mic's disk is blue, indicative of small, submicron grains.
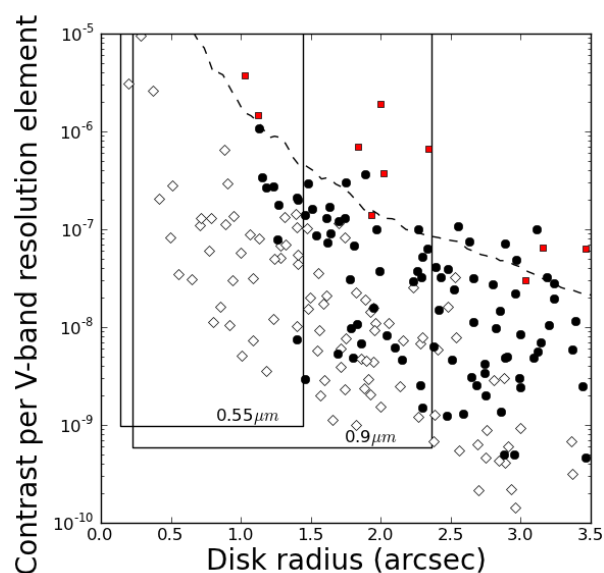


**Figure 4.2-11.** Exo-C will image many known debris disks. For systems observed by Herschel in the far-IR, the estimated contrast per resolution element is shown for systems with a range of disk sizes. Disks that are detected by Hubble are shown as red squares while those marginally resolved by Herschel are black circles. Disk size estimates for unresolved systems are shown as open diamonds. While JWST NIRCam's sensitivity to disks (dashed line) is comparable to Hubble's, the detection space for Exo-C in V and I bands (U-shaped regions) contains many new targets.

### 4.2.4.2 New Discovery Space

**How is dust produced and transported in debris disks?**

Observations by Exo-C will not only expand on the number of imaged disks, but, by pushing to much fainter contrast ratios, will cross an important threshold in disk physics, opening up for the first time an entirely new class of disk images. Brighter disks—all the ones currently imaged—are *collision dominated*; the dust grains we observe are mainly destroyed by collisions with other grains. Disks with optical depths less than $\sim V_{\text{Keplerian}}/c$ are predicted to be *transport dominated*, meaning that grain-grain collisions are rare enough that grains can flow throughout the planetary system under the influence of radiation drag forces until they are sublimated in the star's corona or ejected from the system by an encounter with a planet. This transition between collision dominated and transport dominated is below a contrast level of $\sim 10^{-7}$, so Exo-C will be the first mission capable of confidently detecting a range of transport-dominated disks (see Figure 4.2-10).

The physics of transport-dominated disks is much simpler than that of collision-dominated disks, so it is easier to interpret their morphology in terms of the properties of hidden planets that are perturbing them. Modeling the dust distribution in collision-dominated disks requires an understanding of the details of collisional processing and the distribution of planetesimals, remnants of the complex process of planet formation and migration. However, dust transported away from its source can be modeled with a simple N-body integrator, and the range of possible planet-dust interactions is already understood. Presently, the only known example of a transport-dominated debris disk is the Solar System's, where the dynamics are mostly well understood.

### 4.2.4.3 Indirect Detection of Planets

**What planets exist in the outer reaches of nearby planetary systems?**

Planets orbiting at semi-major axes beyond ~10 AU have orbits too long to permit detection via RV, transit, or astrometric techniques. They are also becoming too low in contrast for direct imaging in scattered light. For mature nearby systems lacking in the strong thermal emission of their youth, the only way to probe the frequency of planets in their outer reaches is to study the structure the planets induce in their surrounding debris disks.

Observations of debris disks commonly identify potential signatures of driving planets such as narrow, eccentric rings (e.g., Fomalhaut, Kalas et al. 2005; HD 202628, Krist et al. 2012) and inclined warps (e.g., beta Pic, Lagrange et al. 2010; AU Mic, Krist et al. 2005). Depending on the optical depth of the dust disk (i.e., whether it is collision dominated versus transport dominated), it can also create patterns by trapping dust grains into mean motion resonances. These resonant structures not only point to the location of the planet, but also constrain its mass and eccentricity.

Furthermore, planets may have detectable amounts of dust orbiting the planet itself, which can build up through inspiraling or captured following a planetesimal collision. The resulting point source has a flux that is inconsistent with planet photosphere models. For example, the object known as Fomalhaut b that orbits within the Fomalhaut debris disk is too bright at optical wavelengths compared to its thermal emission to be explained as a bare exoplanet photosphere. However, the observations are consistent with dust produced by the collisional decay of an irregular satellite swarm around a $\sim 10\,M_\oplus$ planet. Depending on the planet's orbital distance, Exo-C could be capable of detecting Fomalhaut b analogs with a thousand times smaller dust content, allowing an exploration of this newly discovered phenomenon over a wide range of fluxes that have been inaccessible to any previous telescope. Most directly imaged planets so far are associated with debris disks, so understanding the nature of these dust-enshrouded planets is an important step to

interpreting images of exoplanets. Moreover, since these objects may illustrate the process of satellite and ring formation, they may offer clues that will help us understand processes in our own Solar System, like the formation of the outermost satellites such as Callisto and Iapetus.

### 4.2.4.4 Exozodiacal Dust

***How much dust will obscure future images of Earth analogs?***

While many debris disks have been found with cold (~50–100 K) dust orbiting tens of AU from the central star, relatively little is known about the warmer dust (~200–300 K) located in nearby stars' habitable zones. By analogy to the Solar System's zodiacal light, this warm component of debris disks is referred to as exozodiacal dust (or exozodi, for short). Background flux from exozodiacal dust in other systems will likely exceed the signal of an Earth-analog exoplanet in direct images and spectra, even if exozodi levels are no greater than the Solar System level. Therefore, exozodiacal dust complicates direct imaging of exoplanets in two ways: 1) as a source of noise, and 2) as a source of confusion. A discussion of these problems appears in Roberge et al. (2012). The exozodi levels around nearby stars will be as important to the success of efforts to characterize Earth-like exoplanets as the fraction of stars with potentially habitable planets ($\eta_\oplus$).

The most important exozodi characteristic for exoplanet direct imaging at optical wavelengths is the scattered light surface brightness near the target planet, which depends on both the dust abundance and its albedo. A new survey for exozodi around nearby stars using the Large Binocular Telescope Interferometer (LBTI) is slated to begin within the next year (Hinz 2013). The LBTI survey will measure the integrated 10 μm thermal emission from warm dust down to about 10 times the Solar System exozodi level, providing sensitive information on the warm dust content.

However, the LBTI survey will not address two additional aspects of the exozodi problem for a future exo-Earth imager. First is the issue of how to convert the observed 10 μm dust emission flux density to an optical surface brightness: a value for the dust albedo must be adopted. By measuring the scattered light surface brightnesses in the habitable zones of some LBTI target stars, Exo-C can directly measure the dust albedo. The values obtained can then be used to predict scattered light brightnesses for other dust disks observed in the thermal infrared. In the process, valuable information on the composition of the exozodi grains will be obtained, shedding light on the composition of the parent planetesimals and the planet formation processes that created them. Secondly, the LBTI survey data will provide little information on the spatial distribution of the exozodiacal dust. Resolved images in scattered light can reveal greater details of the radial and azimuthal structure of exozodiacal clouds, potentially detecting dust rings or asymmetries driven by planetary perturbations. Exo-C thus provides the added opportunity to detect habitable zone planets indirectly via their gravitational effects.

### 4.2.4.5 Young Disks

***How does the dust in planetary systems evolve?***

The short integration times associated with bright debris disks allow Exo-C to observe many of such disks—a large enough sample to look for statistical trends with stellar age and spectral type. Beyond the core survey of the nearest debris disks, additional disks of different ages will also be included. In particular a select sample of young protoplanetary disks will be observed. The optical scattered-light images of these disks will be complementary to the thermal emission measured by ALMA, allowing for detailed modeling of the disks' constituent particles.

## 4.3 Measurement Requirements

### 4.3.1 Imaging Requirements

#### 4.3.1.1 Starlight Suppression

***Brightness of uncontrolled speckles in coronagraphic dark field:*** As seen by an observer outside of the Solar System, the reflected light brightness of Jupiter at quadrature relative to the Sun is given by $\frac{1}{4} \cdot (\text{albedo}) \cdot (R_J / 5.2 \text{ AU})^2 = 10^{-9}$. In order to detect a Jupiter analog around other stars, or to detect smaller planets in closer orbits, Exo-C must suppress diffracted, scattered, and stray light in a single resolution element down to a direct starlight level of $10^{-9}$. For a V= 4 star, this contrast level also corresponds to the count rate from residual starlight, becoming comparable to the detector dark current background in a single resolution element. A $10^{-9}$ contrast thus serves as a natural break point for background-limited integration times in the majority of our targets.

***Stability of uncontrolled speckles in coronagraphic dark field:*** Exo-C is required to detect planets whose brightnesses are below the residual uncontrolled speckle level specified above. A planet whose contrast is $10^{-9}$ at elongation could appear fainter at another orbital longitude, so achieving detections at more challenging contrast levels is required for robust planet searches. In addition, we aspire to detect planets as small as $1.6 R_\oplus$ (corresponding to the onset of the rocky planet regime), and these will always appear at contrasts below $10^{-9}$. The key to detecting fainter objects is residual speckle pattern stability. Speckle stability at the level of $10^{-10}$ would enable exoplanet detections at contrasts of $\sim 3 \times 10^{-10}$, meeting both of the above objectives. In addition, $10^{-9}$ contrast planets around nearby stars will have reflected light brightnesses in the V=23–29 range, with median V of 27. The median integration time for spectroscopy of these targets with the Exo-C telescope will be 10 days each. Speckle stability will allow these long integrations to take place without interruptions to retune the stellar wavefront. A speckle stability timescale of ~48 hours is a good compromise between operational requirements (the need to break observing sequences for momentum dumps and downlinks) and excessive overheads for frequent wavefront retuning.

***Spillover light from binary stellar companions:*** Exo-C will only be able to resolve a limited number of habitable zones ($T_{eff}$= 300 K) around nearby stars. The best targets will be the two components of the alpha Centauri binary system, the closest Sun-like stars whose habitable zones are located at 0.9″ and 0.6″ separation. At the time of Exo-C's launch, the apparent separation of these two stars will be ~8″ and increasing slowly through the mission to ~10″. Because these two stars are so bright (V = −0.1, 1.3), residual starlight will dominate all other backgrounds against which planets might be detected. We strongly desire that spillover light from the off-axis binary at 8″–10″ separation be at or below the $10^{-9}$ level of residual speckles in the coronagraphic dark field, so as to not drive Exo-C's contrast floor. However, performance modeling (§5.11) shows that the contrast floor of Exo-C's baseline design in the presence of a binary companion of equal brightness at 8 arcsec is $\sim 3 \times 10^{-8}$ due to off-axis diffracted and scattered light. A requirement of $10^{-9}$ could be met by minimizing mirror scatter at this field angle, simultaneously controlling diffraction from both stellar components, baffling to suppress stray light and internal reflections, and new approaches to wavefront control. To highlight technical readiness, however, Exo-C has chosen a capability-driven binary suppression requirement of $3 \times 10^{-8}$ at 8″.

#### 4.3.1.2 Spatial Fields of View

***IWA of coronagraphic dark field:*** Exoplanet orbit sizes and the distances to nearby star targets combine to define the expected angular separation of a planet from its host star. The closer an imager can look to a bright star and still resolve the image of an exoplanet, the

more planets and stellar targets can be examined. The IWA defines the science capability of the Exo-C mission more than any other single parameter. To enable spectroscopy of at least 10 known, nearby exoplanets, an IWA of 0.26″ is required at 900 nm, which is 0.16″ at 550 nm. This corresponds to 2λ/D for a 1.4-m aperture. The uncontrolled speckle contrast and stability requirements stated above should be satisfied at this IWA.

***OWA of coronagraphic dark field:*** The known exoplanet target with the largest angular separation from its host star is Epsilon Eridani b at 1.06″. This object is in a face-on or orbit and is thought to have an orbital eccentricity of 0.3; thus to image it at its maximum elongation, an OWA of at least 1.4″ may be needed. A more stringent requirement comes from circumstellar disk imaging, where the OWA determines whether the full extent of the disk can be imaged or only its inner regions. For the 113 debris disks within 50 pc identified by Spitzer, seventy have an estimated outer radius of 2.8″ or smaller. To enable study of this debris disk sample, we therefore require an OWA of this size or larger at 900 nm. This corresponds to 21 λ/D for a 1.4-m aperture. This OWA will also be sufficient to encompass the outer radii of most of the protoplanetary disks in nearby star-forming regions. Larger OWAs would be highly desirable, as the largest debris disks are also the closest ones that can be studied at the highest linear resolution.

### 4.3.1.3 Astrometry

***Astrometric accuracy:*** Exo-C is required to measure the orbital elements for all planets that it detects. For planets previously detected by RV, the orbit inclination will be the only unknown element. For planets newly discovered by Exo-C, all six orbital elements must be determined; however, the semi-major axis and eccentricity will be of most interest. Exo-C planet searches are most likely to discover new objects a few AU from their host stars. For a fiducial target at 10 pc distance,

this corresponds to an angular separation of ~0.3″. To measure their semi-major axis to 10% accuracy and eccentricities to better than 0.1, the planet centroid must be measured relative to the central star to an accuracy of 30 mas or better. This capability also allows common proper motion of a candidate planet to be established with a second epoch 3 months after the first, for a star at 20 pc distance. To support this astrometric precision, a means must be provided for measuring the stellar position simultaneously with that of the planet over nine orders of magnitude to dynamic range. Furthermore, the planet must be detected with sufficient signal-to-noise (S/N) such that the statistical uncertainty in its centroid position ≈ FWHM/(S/N) [where FWHM is the PSF full-width, half-maximum] is below the 30 mas level.

### 4.3.1.4 Polarimetry

Planetary atmospheres and interplanetary dust particles produce scattered light with significant polarization signatures. To first order the observed polarization amplitude is a function of the scattering angle. When the latter is known, the observed polarization can provide constraints on the particle properties. Measurement of polarization variation with phase angle over a partial orbit would also help constrain the vertical structure of planetary atmospheres.

For the brighter planets and disks, Exo-C should be capable of measuring linear polarizations of ~10%. Additional details on polarimetry science objectives can be found in Schneider (2015).

### 4.3.2 Spectroscopic Requirements

Exo-C is a mission of spectroscopic characterization and exploration, and the spectrometer should be as capable and versatile as possible to measure both expected and unexpected planetary spectral features. Exo-C's spectroscopic requirements are motivated by the scientific need to reliably detect features in the exoplanet spectra, and are

derived from the science requirements described in §4.2.

### 4.3.2.1 Wavelength Range

The wavelength range selected for photometric detection and characterization of planets is 0.45–1.0 μm. This range encompasses many molecular absorption bands of methane, water, ammonia, oxygen and ozone, including several bands of different strengths for methane, water and ammonia, as well as several neutral alkali absorption features.

The intensity of scattered light from an atmosphere at 450 to 600 nm is controlled by a balance between Rayleigh and particle scattering (where the particles often correspond to photochemical hazes in solar system planets), scattering as well as some molecular absorption (e.g., the diversity shown in Figure 4.2-3). By choosing a short wavelength cutoff at 450 nm we can constrain the relative importance of these processes to help better understand the atmosphere and also—by potentially measuring greater dynamic range in reflectivity—place tighter limits on the planetary radius. For airless planets the strongest deviation in phase function from a scattering atmosphere will be found at these shorter wavelengths.

Extending down to 0.45 μm will also allow detection of continuum on the short wavelength side of the ozone Chappuis band from 0.5–0.7 μm for super-Earth planets. Detection of ozone would help constrain the bulk and oxidation state of the atmosphere and indicate the presence of a surface UV shield for life. Large amounts of ozone can be considered a potential biosignature as long as abiotic sources of ozone can be ruled out via knowledge of the star's spectral energy distribution (SED), and the presence of other oxygen bearing gases in the atmosphere.

The long wavelength cutoff is chosen to allow detection of continuum on the red side of the 0.94 μm water band, to allow unambiguous detection and quantification of water for both Jovians and terrestrials. This is the strongest

water band in terrestrial atmospheres, and in fact often the strongest feature in the spectrum. On planets with reducing atmospheres (expected be the case for Jovians, ice giants and mini-Neptunes), this water band is also the cleanest one, as shorter wavelength $H_2O$ bands will overlap with $CH_4$ features

In summary, the 0.45–1.0 μm wavelength range will allow us to discriminate between reducing atmospheres like those seen on the ice giants in our Solar System, and oxygen and water-dominated atmospheres like the Earth's, and make possible the search for biosignature gases.

This wavelength range can be further subdivided for photometric and spectroscopic planetary characterization.

Solar System giant planet spectro-photometry typically relies on images taken in a variety of narrow and wide filter bandpasses centered on methane absorption bands and nearby continuum (Barnet et al. 1992). A comparable set of narrow and broad photometric filters matched to expected giant planet spectral features should be carried. One possible selection of broad filters that would be appropriate for 10% photometry is given in Table 4.3-1.

**Table 4.3-1.** Draft narrow passbands (10% width) for photometric characterization.

| Bandpass (nm) | Comment |
|---|---|
| 450–500 | Rayleigh + weak $CH_4$ |
| 510–570 | Weak $CH_4$ |
| 600–660 | Weak/medium $CH_4$ & $NH_3$ |
| 695–765 | Intermediate $CH_4$ & $H_2O$ |
| 850–940 | Strong $CH_4$ & $H_2O$ |

Spectroscopy behind a wavefront control system limited to 20% wide bandpasses will require four separate spectral bands to cover the 0.45–1.0 μm wavelength range. A full spectrum is then built by combing four shorter spectra that are observed sequentially. The boundaries of each spectral band must be chosen carefully to allow for spectral overlaps to aid stitching of spectra, while avoiding the placement of boundaries in the midst of important diagnostic

bands. Four bandpasses that are acceptable for both giant and terrestrial planet characterization are shown in Table 4.3-2.

**Table 4.3-2.** Draft spectroscopic passbands for coronagraph mask design. The first band is used only with the imaging camera, while the other four are used with the IFS as well. These are the five bands referenced in Tables 5.5-3 and 5.5-4.

| Band Center (nm) | Range |
|------------------|-----------|
| 475 | 450-500 |
| 550 | 495–605 |
| 650 | 585–715 |
| 780 | 700–860 |
| 910 | 820–1000 |

### 4.3.2.2 Spectral Resolving Power

The required spectral resolving power is R~70, which must be achieved for the very brightest targets. We also require sufficient control of detector systematics so that it is feasible to bin down in resolution to increase S/N for our fainter targets. The number of molecular features in exoplanet spectra increases with wavelength, so it is highly desirable that the resolving power scales with wavelength, such that larger resolving powers are obtained at longer wavelengths. At spectral resolving powers below 70, many features of interest are contained in only one resolution element, making robust detection and quantification extremely difficult.

The choice of 70 for the brightest targets is set as the minimum required to detect and characterize methane bands with a variety of strengths, as well as the water band at 0.94 μm for Jovian planets. Figure 4.3-1 depicts the same giant planet spectra shown in Figure 4.2-3 but convolved to R=70. At this spectral resolution the important methane absorption features are still cleanly detectable as well as the continua between absorption bands. At lower spectral resolution the band depths become more difficult to measure against the continuum and the distinction between the various spectra begins to be more difficult to
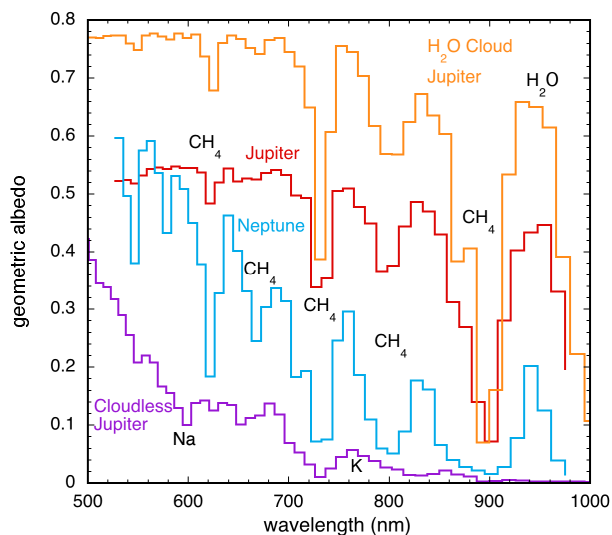


**Figure 4.3-1.** Geometric albedo spectra of real and model planets convolved to R=70 spectral resolution. Shown are Jupiter, Saturn, and Neptune (all from Karkoschka 1999), along with two model planets (from Cahoy et al. 2010), a Jupiter at 2 AU and 0.8 AU, both with three times enhancement in heavy elements. The 2-AU planet is very bright, dominated by water clouds, while the 0.8 AU is relatively dark and cloudless.

discern. Simulated R=70 data for a Jupiter twin at three S/N ratios are shown in Figure 4.3-2.

Additionally, R~70 is optimal for detecting the $O_2$ A-band at 0.76 μm and for identifying continuum between water bands for Earth-like atmospheres. The $O_2$ A-band is a potential biosignature for terrestrial planets, should a super-Earth planet be found in the habitable zone of one of the stars in the alpha Centauri system.

The simulated spectrum for a realistic (with clouds) Earth-like planet with resolving power of R= 20, 50, and 70 is shown in Figure 4.3-3. Similar spectra for simulated super-Earth spectra at R=20 and R=50 are shown in Figure 4.3-4. R=70 is also the pivotal resolution above which very little is gained in S/N benefits for the targeted absorption features, and below which S/N for these features starts to degrade significantly (see Figure 4.3-5).

Obtaining spectra at this resolution on all planets detected by Exo-C will not be possible, but having this capability to characterize the brightest and best-placed planets will be crucial for characterizing the range of solar neighborhood planets, and in particular for searching for signs of life on the closest exoplanets to the Earth.
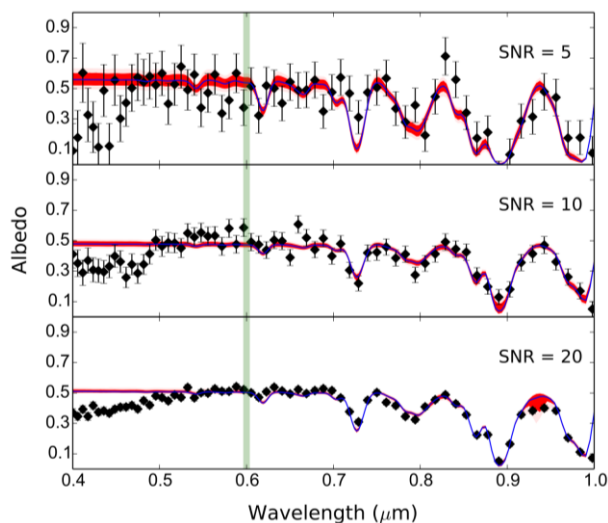


**Figure 4.3-2.** Results from MCMC retrieval of Jupiter cloud properties and methane abundance by Marley and collaborators (2014). Shown are three simulated spectra of an observation of Jupiter taken at R=70 at three S/N ratios. Retrieved variables were gravity, methane mixing ratio, and scattering properties of two cloud layers. Range of retrieved models are shown by blue and red lines. Jupiter is darker than the models in the UV because of the effects of photochemical hazes.
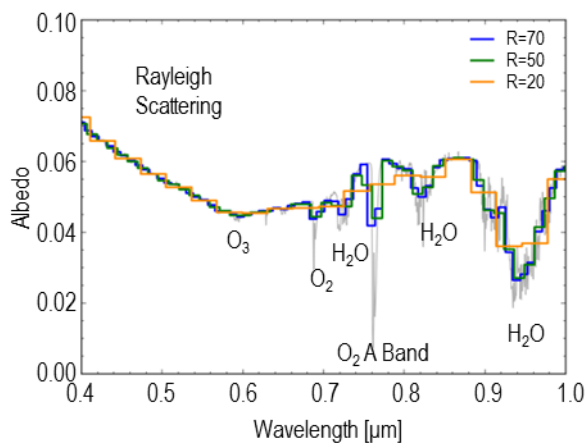


**Figure 4.3-3.** A realistic Earth spectrum (grey) degraded to spectral resolutions of R=20, 50, and 70. The oxygen A-band is seen at 0.76 μm, and the strongest water vapor band in this spectral wavelength range is seen at 0.94 μm.

### 4.3.2.3 Signal to Noise Requirements

We then must consider the SNR required to meaningfully characterize these planets. A bare minimum requirement for giants is to be able to distinguish gas giants with Jupiter-like methane abundance from gas giants with 10×
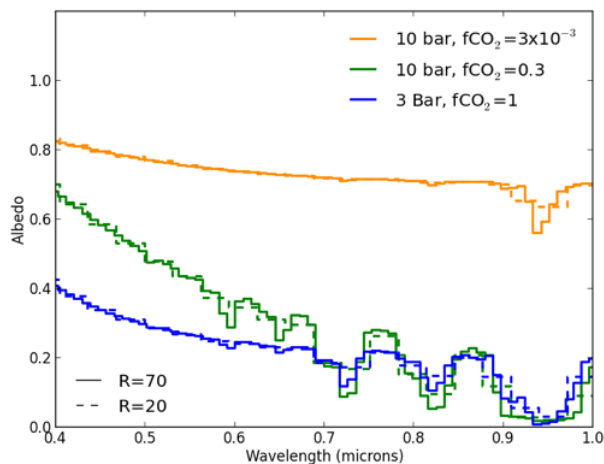


**Figure 4.3-4.** Simulated spectra of super-Earth atmospheres with different total pressures and amounts of $CO_2$ and water vapor. Note the change in Rayleigh scattering slope between 0.4–0.6 microns for different total pressures and $CO_2$ fractions.
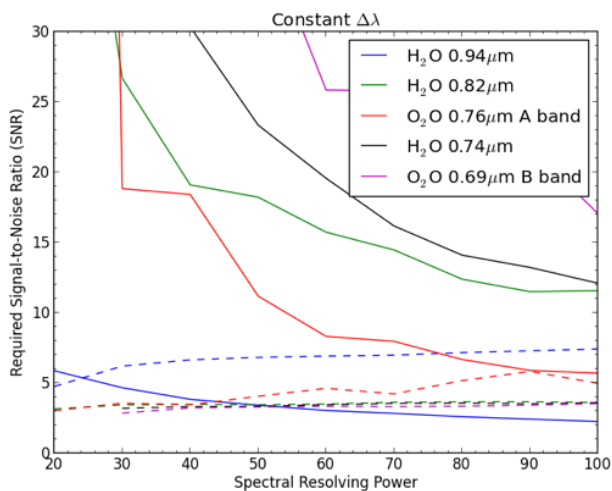


**Figure 4.3-5.** Spectral S/N required as a function of spectral resolving power for water and molecular oxygen in the albedo spectrum of an Earth-like atmosphere. The solid lines are for detection of a feature, and is specifically detection of a deviation from the surrounding continuum with a 3σ confidence level at the wavelength position of the absorption feature. The dashed lines are for measuring the bottom of the absorption band to 3σ, which is required to assist in the quantification of a molecular constituent. For broad, shallow bands, it may be that quantifying the bottom of the band, which will be at a relatively high albedo/flux level, will require less S/N than discriminating it from the surrounding continuum.

greater methane. We find that at R~25 the best bands for distinguishing these two classes of planets are those at 530 and 660 nm. In Jupiter- and Saturn-like planets, these bands are weak, while in Uranus- and Neptune-like they are quite strong. The 660-nm band depth is about 50% of the continuum flux level. To distinguish the presence of this band to 3σ thus requires that the continuum flux level be measured from 600–700 nm at S/N~6. Note, however, that since Uranus's radius is about 1/3 that of Jupiter's it reflects only 11% of the light. Thus the capability to obtain S/N~6 spectra of an ice giant is a much stricter requirement than S/N~6 for a gas giant. To explore whether methane abundance and cloud properties could be extracted from realistic exoplanet spectra, Marley et al. (2014) evaluated whether or not atmospheric abundances of key absorbers and cloud properties could be retrieved from moderate S/N exoplanet reflectivity spectra at R~70. To do so they combined a forward model albedo code with a Markov Chain Monte Carlo retrieval code. As the study was focused on the WFIRST coronagraph it only considered spectral retrievals for noisy λ> 600 nm spectra. Examples of a noisy observation of Jupiter at S/N of 5, 10, and 20 as well as the best fitting model spectra are shown in Figure 4.3-2.

The principal finding of the retrieval study was that the greatest source of uncertainty in constraining atmospheric methane abundance was the uncertain gravity of the planet. If the gravity is completely unconstrained then a very wide range of atmospheric mixing ratios can produce essentially degenerate spectra. Realistically however there will in fact be gravity constraints, particularly for the directly imaged RV planets. Astrometry by Exo-C in conjunction with radial velocity data will likely constrain planetary masses to within 20% (see §4.3.1.3). The mass-radius relationship for giant planets then provides a radius, and thus gravity estimate. Since radius inflation has not been observed for cool Kepler

giants (Miller and Fortney 2011), the radius estimate should be robust. The dynamic range in planetary reflectivity provides a second, independent constraint on the radius (albedos may not be greater than one nor less than zero, if observed spectra are not flat then allowable radii are constrained).

The retrieval study demonstrated that at least for a Jupiter-twin with a gravity constrained within a factor of two of the true value, at S/N=10 the correct atmospheric methane abundance could be retrieved. Even with no gravity constraints the study found that methane abundances could be reliably retrieved to within at least a factor of 10 to 20 of the true value. In addition in a study of real and model planets the cloud single scattering albedo, which provides information on cloud composition, was often tightly constrained to the true value. This was all demonstrated employing only the WFIRST spectral range. The greater spectral capability of Exo-C, particularly in the blue, would likely provide tighter constraints. The study also found that some atmospheric parameters could be obtained even with S/N=5 data, although constraints improved with increasing S/N.

Our requirement is to be able to measure the degree of methane enhancement in a gas giant within 50%. This means measuring the depths of several methane absorption features relative to the continuum and is similar to the problem of distinguishing the reflection spectrum of Saturn from that of Jupiter. For R~70 this requires S/N~10 to uniquely characterize multiple methane bands and the associated continuum.

Detecting and measuring the water band at 940 nm will only be possible for bright gas giant planets with thin water clouds (to provide continuum-scattered flux). For a Jupiter-like planet at 2 AU, detecting a 20% deep band at 3σ requires S/N~20.

Considering the S/N required to characterize terrestrial planets, in Figure 4.3-5, we show a plot of SNR required as a function

of spectral resolving power for $O_2$ and $H_2O$ features in an Earth-like planetary atmosphere. For the realistic Earth case sampled with constant-width wavelength bins that give R=70 at 630 nm, we see that we would need a S/N of ~3 to detect the $H_2O$ 0.94 um band at the 3-σ level, and a S/N of ~7 to detect the bottom of this band to 3σ. To obtain the continuum on the longward side of the water band, we would need a S/N of 6 for a 3σ result and a S/N of 10 for a 5σ result. To obtain another, weaker, water band as a confirmation of water detection, would require S/N close to 15 (this S/N would rise to 19 for R=50). To detect the $O_2$ A band, we would need a S/N close to 8, which would rise to 11 at R~50). For a 10-bar atmosphere on a $CO_2$ and water-dominated world, we would need a S/N of ~8 to discriminate the 0.94 μm band from the adjacent methane band to help distinguish between a reducing and oxidizing atmosphere.

In summary, a S/N of ~10 is very desirable for terrestrial planet spectra across the 0.9–1.0 μm region. This would provide 5σ confidence for the detection of the bottom of the water band and the continuum on either side of it. This S/N obtained from 0.7–0.9 μm would also allow us to potentially obtain the $O_2$ A-band at 0.76 μm, which is a potential biosignature.

### 4.3.2.4 Simulated Spectra

In Figure 4.3-6 we show simulated spectra with 1σ-error bars, and calculated average exposure times for a single wavelength bandpass (one fourth of the 0.49–1.0 μm spectrum) for representative targets to be observed with Exo-C. These simulations are run using anticipated instrument throughput and a realistic noise model that includes noise sources from residual stellar speckles, the planet itself, and zodiacal light in both our Solar System (zodi) and the planetary system that contains the target planet (exozodi). The exposure times required to achieve a S/N of 10 at 550 nm are given in the caption. Figure 4.3-7 shows simulated spectra for
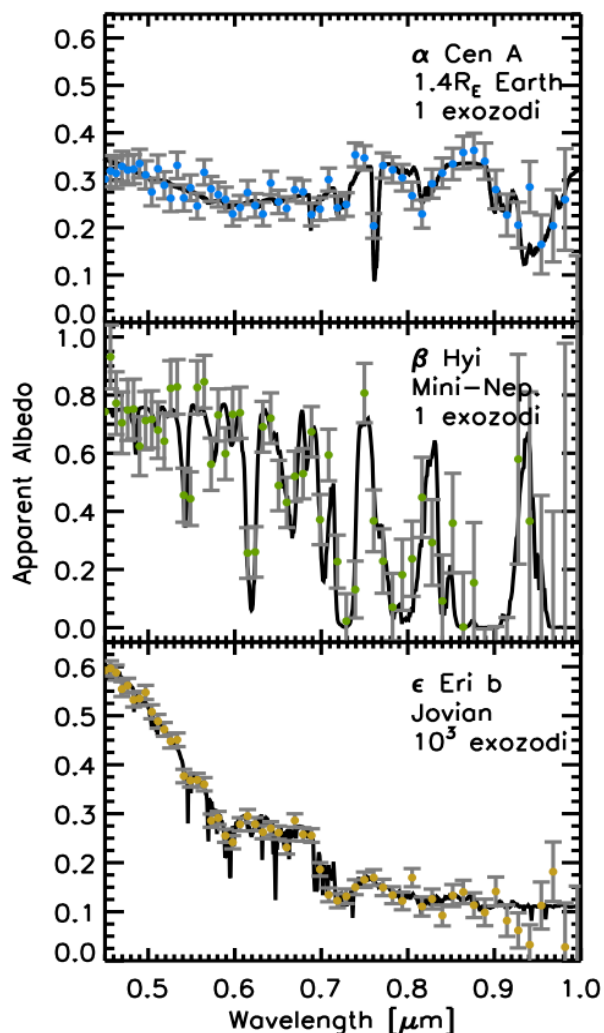


**Figure 4.3-6.** Simulated Exo-C spectra of the known RV planet around epsilon Eridani (bottom panel) and two hypothetical planets around the nearby stars α Cen A and β Hyi. The integration times (per bandpass) assumed for each planet are 660, 620, and 150 hours, respectively. Note how the S/N degrades beyond 0.8 μm due to the declining quantum efficiency of the detector.

planets orbiting the bright star Altair at 5 pc with 1 exozodi.

### 4.3.2.3 Mission Lifetime

The Exo-C mission should be of sufficient duration to carry out the following science programs: 1) spectral characterization of at least 10 known, nearby planets; 2) meaningful searches of at least 100 nearby stars for planets beyond the limits of previous detection surveys; and 3) imaging surveys of several hundred circumstellar disks. The second
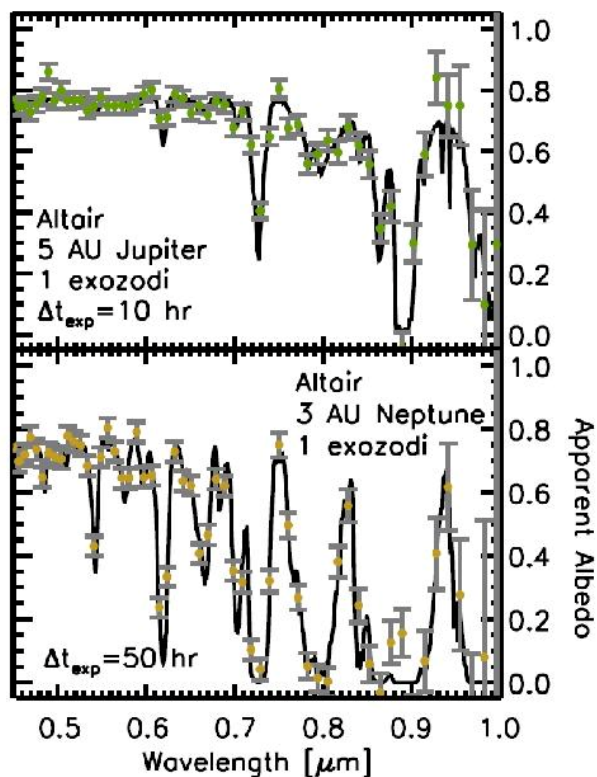
**Figure 4.3-7** Simulated Exo-C spectra of hypothetical planets around the bright star Altair at 5 pc.

program includes imaging searches for objects with the orbital period of Jupiter at multiple epochs. To maximize the completeness of a search for objects with 12-year orbital periods, images at two epochs separated by almost 3 years is required; this will allow a planet that happened to be at stellar conjunction at the first observation epoch to move through 90° of orbital longitude to elongation at the second epoch and be detected. A minimum mission lifetime of 3 years is therefore required.

## 4.4 Derived Instrument Requirements

### 4.4.1 Overview

The instrument requirements presented in this section encapsulate the wide range of exoplanet and disk objectives for this mission. These top-level instrument requirements are derived from the science requirements described in §4.2 and their detailed measurement requirements described in §4.4.

### 4.4.2 Telescope Aperture

The inner working angle requirement and spectral bandpass conspire to set a minimum telescope diameter. The inner working angle is required to be at least 0.26″ at 900 nm. Coronagraph demonstrations with unobscured apertures have achieved high contrast at 2 λ/D, but smaller angular separations are expected to be far more challenging, as those separations impose stringent pointing and wavefront stability requirements. For this IWA choice, the diameter of the telescope must then be at least 1.4 m, as represented in Figure 4.4-1.
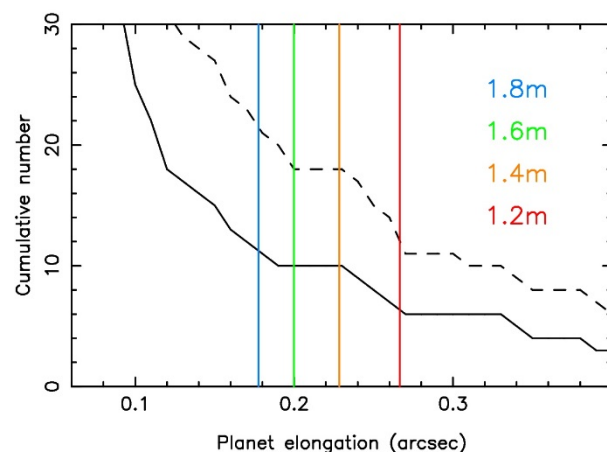


**Figure 4.4-1.** Cumulative number of RV planets known in late 2014 that can be accessed outside the telescope inner working angle, as a function of aperture size. The solid line shows planets brighter than V=29, and the dashed line all planets.

### 4.4.3 Coronagraphy

The coronagraph must be used to provide point source sensitivity of $10^{-9}$ contrast at an angular separation of 2 λ/D (0.16″ at 550 nm). There are several coronagraph architectures that can meet this requirement, all of which were considered in this study. The high-contrast coronagraphs include the hybrid Lyot, phase-induced amplitude apodization (PIAA), visible nulling coronagraph, and the vector vortex. There is a full description of each coronagraph design and simulated performance in Appendix B. The hybrid Lyot, PIAA, and vector vortex all meet the baseline mission requirements. A detailed analysis was conducted in order to trade the coronagraph performance (e.g., inner

working angle, contrast, and throughput) against the science metrics and technology readiness, as described in Appendix B of the non-redacted version of this report (§B.1.1.5).

### 4.4.4 Wavefront Control

A wavefront control system must be used in order to correct wavefront aberrations that degrade contrast in the optical system. The deformable mirrors must be able to provide high contrast from the IWA (2 λ/D) to the OWA (~20 λ/D) as described in §4.3.1.2. In order to control these spatial frequencies, the deformable mirror must have at least 48 actuators across the telescope pupil. The high contrast regions must be corrected on both sides of the image plane, and therefore, two deformable mirrors must be employed. The operational plan for wavefront control is described in §4.5.2.

The 30 mas (or better) relative astrometric precision required for orbital motion characterization corresponds to half a pixel in either the imaging camera or the integral field spectrograph. Fiducial markers will be generated in the science camera FOV by applying specific spatial frequencies on the deformable mirror, as demonstrated by ground-based telescopes. Centroiding on these DM-generated PSFs will be used to locate the center of the star behind the coronagraph to high accuracy, which will be used to bootstrap to determine the relative astrometric position, and the projected separation of the exoplanet from the target star. The positions of the star and the exoplanet need to be measured to roughly half of a pixel (or spaxel in the IFS).

### 4.4.5 Stray Light

The science requirements to achieve high contrast on binary stars places requirements on stray light control. For example, the binary alpha Centauri will have a separation between ~8 and 12 arcsec during the lifetime of Exo-C (Figure 4.4-2). Coronagraphic masks have been designed to reduce the stray light. However, the telescope optics can generate aberrations that are not controlled by occulting masks. This will place requirements on the high-frequency errors on the optics upstream from the coronagraph. For light that passes through the coronagraph, baffling and wavefront control schemes will be used to further suppress the starlight.

### 4.4.6 Imaging

The spatial sampling at the image plane of the science camera must be at least Nyquist sampled at the diffraction limit for the shortest wavelength in regular use (i.e., 550 nm). The spatial sampling adopted in this study is 41 mas, which is two pixels per λ/D for a 1.4-m diameter primary mirror. This critical sampling results in the fewest number of detector pixels that are required for the mission. The science camera detector will also be integrated into the wavefront control architecture, where it will serve as a focal plane wavefront sensor used to estimate aberrations.

The science requires that the field sample the entire dark hole at the longest wavelength (i.e., 1000 nm). At the longest wavelength, λ/D is 147 mas, and therefore the imager should cover at least a 6.5×6.5 arcsecond field of view. Combined with the 41 mas spaxel (i.e., spatial pixel) scale required for Nyquist sampling at 550 nm, this means we need at least 158×158 spatial samples to cover the entire diameter of the dark hole. However, the combination of telescope diameter, stellar distances, and reflected light from the exoplanets makes it most probable to discover planets near the inner working angle (see Figure 4.4-1). The largest exoplanet projected separation expected from the RV sample is 1.1″ (epsilon Eridani b), which therefore sets the minimum spectroscopic field of view. This corresponds to a field of view with at least 54×54 spatial samples for the exoplanet science. The implemented design provides a slightly larger field of view with 71×71 spaxels.
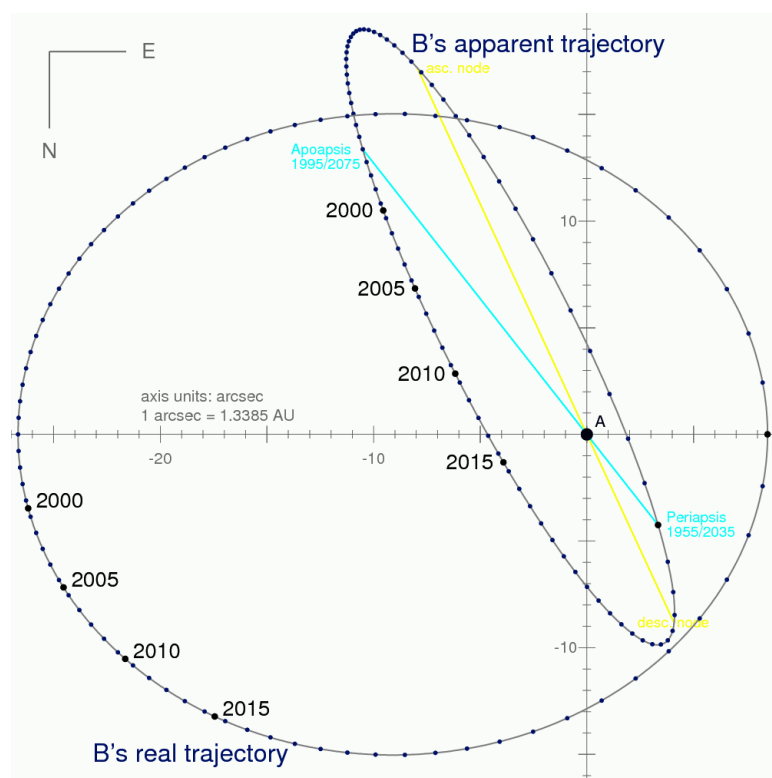
**Figure 4.4-2.** The orbital separation of the alpha Centauri binary system sets the requirement for stray light suppression between 8 and 10 arcseconds.

### 4.4.7   Spectroscopy

The full spectral coverage of the science camera should cover at least 450–1000 nm. While the spectrum covers a 75% spectral bandwidth, this full spectral coverage is not required to be taken instantaneously. The instantaneous spectral bandpass should be no less than 20%. This requirement is necessary to measure broad spectral features and adjacent continuum spectra within the same dataset. Furthermore, this bandpass will enable multiple adjacent spectra to be overlapped together for subsequent merging. The full spectral coverage combined with the instantaneous spectral coverage means that, at minimum, four separate instantaneous bandpasses would be required for the spectrograph.

The instantaneous spectral coverage could be limited by the broadband contrast achievable with the selected coronagraph technique. Coronagraphs experience optical chromatic effects that degrade contrast spectrally when

expanding to larger bandpasses. To date, the broadband laboratory demonstrations have been limited to 20%.

The spectral resolution shall be greater than R~70 ($\lambda/\Delta\lambda$) across the entire spectral bandpass, thus each spectral channel would need to have width W=1/R=1.4%. For example, at the critically sampled wavelength each spectral resolution element on the detector should be no more than 7.85 nm (550 nm/70). The detector must critically sample each spectral resolution element, which places a requirement of 3.92 nm/pixel on the spectrograph detector.

The spectrophotometric precision of the instrument should be 0.06 mag (5%) with respect to the central star. This level of spectrophotometric precision ensures that high S/N spectroscopy (S/N~20) is not limited by the spectrophotometric precision. The spectrograph must be able to maintain an intrascene contrast of $10^4$.

### 4.4.8   Detectors

The baseline detector must cover the entire spectral bandpass from 450–1000 nm. The quantum efficiency must be high across the entire bandpass in order to meet the sensitivity requirement defined in §4.4.2.3, but the exact requirement is dependent on the coronagraph choice. A deep depletion Charge Coupled Device (CCD) detector would meet these requirements, but is more susceptible to space radiation effects than a standard CCD. The specific detector performance requirements for read and dark noise are dependent on the system throughput and the length of the science integration times. In addition to reaching saturation, detector integration times may be limited by cosmic ray impacts. The AFTA design team is investigating the

radiation environment in geosynchronous orbit to determine the cosmic ray exposure time limit to impose on their mission, and Exo-C would utilize the results of their study. A conventional CCD with an analog register has high heritage and could in principle meet the science requirements for the imaging camera if long integration times are acceptable. If instead the maximum integration times are limited to an hour or less, Electron-Multiplying CCDs (EMCCDs) would be needed to meet more challenging read and dark noise requirements.

### 4.4.9    Baseline Instrument Concept

Exo-C has baselined a lenslet-based integral field spectrograph to meet the requirements specified in §4.3.2. As calculated in the spectral resolution section, the spectral sampling on the detector should be 3.92 nm/pixel at λ=550 nm and 7.14 nm/pixel at the longest wavelengths, following the R~70 ($\lambda/\Delta\lambda$) across the entire spectral bandpasss. This corresponds to spectral channels that have bandwidths of 1.4% (B=1/R). In order to cover the full ~80% bandpass (B=$\Delta\lambda/\lambda$= 550 nm/700 nm=80%), it would be necessary to have four separate 20% spectral channels to cover this bandpass. In each of the four spectral bandpasses, it is necessary to have 14 independent spectral channels. Each spectral channel will need two pixels, which requires at least 28 pixels per spectrum on the detector. The design also requires at least four boundary pixels on the end of the spectrum to obviate crosstalk between the adjacent spectrum on the detector resulting in a minimum spectral length of 32 pixels. With a vertical spacing of 5 pix to mitigate spectral crosstalk, each spectrum therefore occupies at minimum 160 sq pix. A 1024×1024 detector can then fit no more than 6553 spectra in total, or a square field of view with 81×81 spaxels. The actual assembly of spectra on the detector do not follow this exact pattern and a design that achieves 71×71 spaxels has been implemented. In this configuration the lenslet should be rotated by an angle of 18.4° such that each second spectrum will align on the same row of the detector. Model spectra that

could be obtained for a hypothetical terrestrial planet, an ice giant, and a known gas giant planet were shown in Figure 4.3-6.

In addition to the IFS, Exo-C will have an imaging camera for target acquisition and circumstellar disk science. The star trackers have an angular acquisition range of better than 30″. The imager field of view must be at least 1′ to ensure the target is visible when repointing the telescope to acquire new targets. This requires a separate detector for the imaging camera. The imager should also Nyquist sample the telescope diffraction limit at 550 nm (i.e., 0.041″/pixel). The imager will use a 1024×1024 detector to sample this field, and if possible, the same detector and electronics will be used for both the IFS and imager detectors.

## 4.5    Mission Science Operations

Exposure times are calculated for each target in each observing band according to the prescription described in §4.7. Note that the known RV planet host stars are on average two magnitudes fainter than the target stars for new planet searches. As a result, Exo-C is likely to obtain its highest quality spectra in the sample of new planets discovered by the mission itself.

### 4.5.1    Observation Strategy

**Table 4.5-1.** Exo-C observing program includes known targets (both planets and disks) and surveys for new discoveries. The number of target stars is listed here for each of Exo-C's science programs, along with the median brightness of the stars in each sample.

| Target Category | #Stars | Median V |
|---|---|---|
| Known RV planet spectroscopy | 11 | 5.7 |
| Search for super-Earths in HZ | 15 | 3.7 |
| Search for Neptune-size planets | 41 | 3.7 |
| Search for Saturn-size planets | 62 | 4.1 |
| Search for Jupiter-size planets | 51 | 3.7 |
| Survey of HZ dust in A-K stars | 150 | 3.7 |
| Protoplanetary disks | 43 | 11.4 |
| Debris disk search in RV planet systems | 55* | 5.3 |
| Debris disks detected in far-IR surveys | 160** | 6.5 |

*Totaling all subsamples, 100 targets have known RV planets.
**Totaling all subsamples, there are 191 nearby debris disk targets.

### 4.5.1.1 Planet Detection

The primary goal of the Exo-C mission is to detect and characterize planets around nearby stars. While known RV planets will be the primary targets, a large fraction of the observatory lifetime will meanwhile be spent searching for new planets. The V band will be the primary reconnaissance filter for the acquisition of RV planets and for the new-planet survey. The V band is a compromise between the need to access the smallest inner working angle while also having high expected planet fluxes. The latter is the case due to the absence of strong atmospheric absorbers seen at longer wavelengths, and the smaller stellar illuminating fluxes at shorter wavelengths.

Searches for new planets need to take place over multiple epochs in order to obtain good photometric and obscurational completeness. Targets are chosen to be stars where two to six visits can produce good completeness for the orbital periods of interest (1–20 years). The number of visits required to search each target depends on how close the projected separation of the planet being searched is relative to the coronagraph inner working angle. In general, the number of visits NV required to approach 100% obscurational completeness can be written as:

$$NV = \frac{90^\circ}{\mathrm{acos}\left(IWA \times \frac{d}{a}\right)}$$

with temporal separation P/(2×NV), where a is the planet semi-major axis in AU, d is the distance in pc to the target star, and P is the orbital period. Thus, two visits separated by 1/4 orbital period are needed for a/d=1.4×IWA, three visits separated by 1/6 orbital period for a/d=1.15×IWA, and six visits separated by 1/12 orbital period for a/d=1.04×IWA. Because the number of revisits needed to achieve high search completeness becomes large when a/d is close to the IWA, such searches will only be conducted for those targets where the highest value planets—

Neptunes, mini-Neptunes, super-Earths, and Earths—are detectable.

Gas giants such as Jupiter and Saturn are large enough to be detectable out to ~20 year orbits. The search targets for planets in this size range will be limited to those with a/d ≥1.4×IWA. One V band search observation should be scheduled as early as possible in the mission followed by another during the last 6 months of the prime mission. Ice giants such as Uranus and Neptune are discoverable on 1–8 year orbits and will be sought in systems where a 1-year orbit would have a/d ~1.15×IWA—thus requiring three visits. Mini-Neptunes and super-Earths are accessible in the smallest number of stars and will be sought using six search epochs in systems where a 1-year orbit has a/d down to 1.04×IWA. With optimal scheduling of new visits with respect to prior ones, and the targets selected as described above, a search completeness approaching 100% could be achieved for the orbital semi-major axis of interest. However, optimal visit scheduling will be constrained by Exo-C's field of regard, restricted to boresight angles of 50–130° from the Sun. Targets on the ecliptic will only be accessible for half the year. For habitable zone planet searches (orbital periods close to 1 year), scheduling constraints will limit the search completeness to about 50%.

To achieve high photometric search completeness, the target S/N of the observation will be adjusted as a function of how close the target a/d is to the IWA. Our fiducial planet brightness is for quadrature illumination. Consider now the case of nearly edge-on orbits. When a/d≥ 1.4×IWA, the observation will be obscurationally complete ±45° about elongation. For this search observation to be photometrically complete as well, a S/N of 10 is needed on the quadrature brightness so that a planet placed 45° degrees of orbital longitude in the foreground can still be detected at S/N of 3. When a/d~ 1.15×IWA, the planet is visible ±30° about elongation. It would appear faintest

30º of longitude in the foreground, in which case S/N of 7 will be needed on the quadrature brightness to detect it in the foreground at S/N of 3. Finally for a/d ~1.04×IWA, the planet is detectable ±15º of longitude and S/N of 5 on the quadrature brightness would suffice to detect a planet 15º of longitude in the foreground at S/N of 3. In all cases, the foreground (crescent) illumination phase is the worst-case and most planets falling within the unobscured range of orbital longitudes will appear much brighter.

Lastly, our observational strategy includes tactics to help distinguish true planetary signals from residual speckles or background objects. Spectral discrimination is provided when observations are made with the IFS. Photometric observations with the science camera will make use of observations at two spacecraft roll angles separated by 30°. Because of its smaller bandwidth and the effects of detector dark current, the integration times required for measuring residual speckles with the IFS are at least five times greater than those using the science camera for broadband photometry. It is thus more efficient to conduct planet searches using the imaging camera at two spacecraft roll angles. A spacecraft roll runs the risk of the speckle field being perturbed by thermal changes to the telescope and instrument, but structural/thermal/optical models of the Exo-C design (see §5.10) show that a 30º roll will only perturb the speckle field at the $10^{-11}$ contrast level at the IWA, well below the coronagraph contrast floor. We thus baseline broadband imaging at two roll angles as Exo-C's primary planet detection strategy for stars with V>3. On brighter stars V<3 the IFS can be used for initial searches without a large integration time penalty.

### 4.5.1.2 Planet Characterization

**Multi-band imaging:** For the RV planet targets, if the initial V band image shows a candidate detection with roughly the expected brightness and angular separation, the next step will be to take images in the other four photometric bands. For new planet candidates that are found, spectral follow-up would ideally wait until the candidate is confirmed by a second detection at a later epoch to establish common proper motion. However, if the candidate is presented very close to the IWA then it will be too risky to wait for a second epoch, and imaging in the other 4 photometric bands will be scheduled within a month.

**Spectroscopy:** RV planet spectroscopy is the highest priority observation type for the Exo-C mission. Spectroscopy observations in the four IFS bands will follow observations in the photometric V/R/I/z filters whose measurements of planet brightness will allow the spectroscopic integration times to be refined. For their first epoch, radial velocity planet targets will be observed at the most optimal epoch near maximum elongation and, if possible, not at the predicted nodal sky plane crossing (where the orbit inclination is degenerate with the projected separation). While as many RV planet observations as possible will be done in the first year, it will be necessary to wait for some of the targets to reach their optimal orbital position during the three year prime mission lifetime.

**Orbit determination:** Each planet will be observed for multiple observing epochs in order to trace its orbit and determine its illumination phase at the time of each observation. The V band will be used on the imaging camera because the planets are likely brightest in this band and because the small telescope PSF should enhance the astrometric precision. Deep V band images to S/N~20 will be used, leading to an astrometric accuracy of 18 mas assuming good mapping of focal plane systematics.

For planets with measured RV signals, imaging astrometry is needed to determine the unknown orbital inclination and thereby measure the planet's mass. Based on Monte Carlo simulations using the known ephemeris information for each planet, we find that three epochs is generally sufficient to measure the

inclination with enough accuracy to determine planet mass within 10% (depending on the quality of the RV signal). For newly discovered planets, a single image cannot translate projected separation into true orbital semi-major axis, nor can it determine what fraction of the planet is illuminated. Multiple observations relieve this ambiguity, allowing for measurement of the planet's semi-major axis and illumination phase. Imaging detections at three or more epochs will be sought for each newly discovered planet. In all cases, orbit is necessary in order to put each planet spectra into the context of its incident stellar radiation flux.

### 4.5.1.3 Disk Imaging

As described in §4.2.4, observations of circumstellar disks will compare the architecture of exoplanetary systems against the Solar System's planets and asteroid belts, will identify unseen planets via their induced disk structure, and will explore a new regime of debris disk physics. These disk systems are less challenging targets than planets, with much higher contrast ratios. Single visits with relatively short integration times are sufficient. As such, extending the science program to include both planet and disk targets results in an overall sample with hundreds of targets covering the entire sky, allowing for efficient scheduling with small angle changes between observations.

We consider several disk samples as targets. Among known disks we include both young protoplanetary disks and nearby debris disks identified by Spitzer, Herschel, and WISE via their far-IR thermal emission. Exo-C surveys for new disks will concentrate on two samples of particular interest: 1) stars where Exo-C can probe the habitable zone and 2) stars already known to host an RV exoplanet. (See Table 4.5-1 for the number of disks in each sample and their median brightness.)

Our observing strategy for imaging each of these disk samples is straightforward. Searches for habitable zone dust will be done in the V filter in order to achieve the smallest inner

working angle. In the protoplanetary disk systems and targets where detection of exo-Kuiper dust is being sought, only a single visit will be made using the I-band filter on the imaging camera. Using this longer wavelength band provides a larger outer working angle for detection of extended dust, while maintaining high quantum efficiency and throughput. Integration times for known disks are calculated based on models anchored in the known far-IR properties of each disk and an assumed grain albedo of 10%. The total time required for each survey is listed in Table 4.5-2.

### 4.5.2 Observing Efficiency

#### 4.5.2.1 Instrument Optimization

All of Exo-C's science goals are predicated on its ability to image with high contrast. Periodic sensing and correcting of the telescope wavefront is required to maintain a relatively clean dark hole for imaging. As described in §5, the coronagraphic instrument contains two deformable mirrors (DM) that are used for this wavefront correction. A series of probe patterns is placed onto the DMs and its effect on the residual speckles observed. Because the speckles are so faint ($10^{-9}$ of the central star), detecting the speckles during this wavefront sensing and correction procedure amounts to a significant portion of the observing overhead. This is particularly true the first time a dark hole is created; for each waveband, ~20 hours will be required to determine the initial DM settings. Subsequent maintenance of the DM settings will not require as many iterations before converging on a clean solution, but nevertheless can take hours for all but the brightest stars. For this reason, our strategy for optimizing high contrast is to concentrate on bright (V< 3 mag) stars for adjusting the DMs during the course of the mission. In some cases our target star will meet this requirement, but more typically a ~15° slew to a neighboring calibrator target will be required. Based on structural-thermal-optical analysis, the changes to the telescope and instrument during such pointing maneuvers are expected to produce

contrast changes well below our stability requirement. See §5.6 and §5.10 for a more detailed discussion of thermal changes.

The robustness of this approach will be validated in orbit. During the observatory's initial checkout phase, the deformable mirror settings needed to achieve two-sided and one-sided dark holes in all five photometric wavelength bands will be derived from observations of a bright star in the continuous viewing zone. Thermal settling times will be measured for slews from a fiducial star to a second star at different solar incidence angles. Settling times will also be measured for observations of the same star at different spacecraft roll angles. The observed settling times will be a refinement/confirmation of modeled values derived before launch, and will be incorporated into the schedule for routine science operations. Once dark hole solutions are established for each spectral band, their repeatability will be assessed by cycling through the five wavelength bands and measuring the speckle floor. A bright star on the galactic plane (such as Deneb) will be a valuable fiducial for assessing the detection of adjacent targets at a range of delta magnitudes and separations.

### 4.5.2.2 Additional Overheads

In addition to the wavefront sensing and control required for the high-performance coronagraph, Exo-C's overall observing efficiency is further limited by common overheads—telescope slews and subsequent settling, telecommunications, desaturation of the reaction wheels, etc. Thermal stability following each slew is particularly important, probably requiring ~1 hour settling time after each maneuver (but see §5.6 and §5.10). For further detail on mission operations and scheduling, see §6.

### 4.5.3    Survey Time Allocations

Science observations are governed by science objectives and fall into three categories: 1) Spectroscopy of Known Exoplanets, 2) Planet Discovery Surveys, and 3) Disk Imaging Surveys. Planets discovered by the survey also become candidates for spectroscopy. We have estimated the duration required to conduct mission operations in support of these science objectives. The detailed discussion, along with duration justifications, are described in §4.7. The summary time budget is shown in Table 4.5-2. In the *Visits* columns, we estimate the number of targets and number of revisits per target in each category. *Total Observation Time* is calculated by multiplying the *number of targets*, *number of visits*, and the median *integration time per visit*. *Observation efficiency* considers the spacecraft management; retargeting and thermal stabilization of the observatory following each new pointing; and instrument optimization, i.e., tuning the deformable mirrors to obtain the required contrast. Nominal spacecraft management consists of weekly telecom passes and momentum management events. Multiple observations will occur during a week (see §6), therefore in Table 4.5-2 we assign a portion of weekly spacecraft management time to each observation, roughly proportional to its duration.

**Table 4.5-2.** Our science plan allocates time between planet detection, planet characterization, and disk imaging. Allocations within the 3-year lifetime are given here, along with estimates for the efficiency of each mode of observation.

| | Visits | | Science Observation Times | | | |
| Science Type | # of Visits<br>N_target | Average # of Visits<br>N_visit | Average Integration Time/Visit<br>t_I (hrs) | Total Observation Time per Science Type<br>T_Obs=N_Target*N_visit*t_I (days) | Total Mission Time<br>T_M (days) | Observation Efficiency<br>T_Obs/T_M |
|---|---|---|---|---|---|---|
| **Planet characterizations** | | | | | | |
| Exoplanet spectra (known and mission-discovered planets) | 20 | 1 | 250 | 208 | 215 | 97% |
| Exoplanet astrometry & multicolor photometry (known and mission-discovered planets) | 35 | 3 | 30 | 131 | 166 | 79% |
| **Planet discovery surveys** | | | | | | |
| Survey nearby stars for Super-Earths within the habitable zone | 15 | 6 | 25 | 94 | 113 | 83% |
| Search for giant planets around nearby stars | 135 | 2.3 | 20 | 259 | 323 | 80% |
| **Disk imaging surveys** | | | | | | |
| Survey for HZ dust in A-K stars | 150 | 1 | 8 | 50 | 69 | 73% |
| Detection survey in RV planet systems | 60 | 1 | 12 | 30 | 36 | 83% |
| Known debris disks from Spitzer, Herschel, and WISE | 150 | 1 | 12 | 75 | 91 | 83% |
| Nearby protoplanetary disks | 40 | 1 | 12 | 20 | 24 | 83% |
| **Total on-orbit ops time** | | | | 867 | 1037 | |
| Initial on-orbit checkout (days) | | | | | 60 | |
| Total (days) | | | | | 1097 | 79% |
| **Total (years)** | | | | | **3.0** | |

## 4.6    Data Processing and Analysis

Several speckle subtraction techniques have been demonstrated to suppress speckle noise in post processing by a factor of 10 or more. These include various kinds of difference imaging: spectral (SDI, Lafreniere et al 2004), angular (ADI, Marois et al 2006) also known as roll subtraction, polarization (PDI, Murakami et al 2006), and coherence (CDI). In addition, low order dynamic error (such as vibration and decentering) can be measured by the LOWFS and subtracted out in software if it is too fast to be corrected directly. All these techniques are applicable and useful for different Exo-C science goals. ADI appears to be the best option for imaging data given our current understanding of Exo-C's telescope/instrument stability, while SDI will be used to remove residual speckles from IFS data. The degree to which post-processing can be used to detect objects below the raw contrast floor depends on the instrument wavefront stability; depending on the latter, the post-processing requirements range from a factor of 3–100.

A key mission requirement is that a preliminary assessment of planet search data be made within two weeks of it being downlinked. This turn-around will enable a new planet candidate that is discovered in one two-week mission schedule block to be prioritized for follow up observations in the following month. This capability will be particularly important for scheduling spectroscopy observations of short-period planets such as those in the habitable zone.

## 4.7    Mission Science Yield

Based on our mission lifetime science observations budget, we expect to observe spectra of 20 known and mission-discovered exoplanets, survey 15 nearby stars for super-Earths, and search 135 nearby stellar systems for the presence of giant planets. We also expect to image ~200 circumstellar disks in the subcategories shown in Table 4.5-2.

Integration times for the initial planet search observations are calculated using a detailed performance model for the coronagraph instrument and science detector, estimates of sky backgrounds, and assumed exoplanet properties such as planet radius, albedo and orbital illumination phase. The calculation uses contrast curves, mask profiles, system throughputs, and point-spread functions developed by the Exo-C Design Team. See Table 4.7-1 for the assumed performance parameters.

We make the conservative assumption that our survey of 135+15=150 nearby stars discovers new exoplanets in only 10% of the targets. If spectra can be obtained for half of these 15, then the total number of exoplanetary spectra returned by the mission is around 20. Multicolor photometry can be obtained for 20 currently known exoplanets plus all 15 of the new discoveries. It should be noted that that some works (Traub et al. 2015) project a much higher planet frequency of 30-40%, so Exo-C's planet search could be substantially more fruitful than assumed here.

### 4.7.1    Known RV planets

For RV planets, the planet is assumed to have

Jupiter radius and albedo (V-band albedo of 0.50; Cahoy et al. 2010). Each planet is assumed to appear at quadrature illumination phase, or 1/3 its full-phase brightness. The epoch of elongation is known from the RV orbital ephemeris and thus observations can be optimized to occur then; the apparent angular separation is then assumed to be just the orbital semi-major axis divided by the host star distance in pc. Orbital eccentricity may increase or reduce the projected separation at elongation. The stellar magnitude and colors are used in the calculation, while the planetary albedo is treated as wavelength-independent.

Figure 4.7-1 shows example imaging results that would be obtained for a known RV planet system—data needed to track the planetary
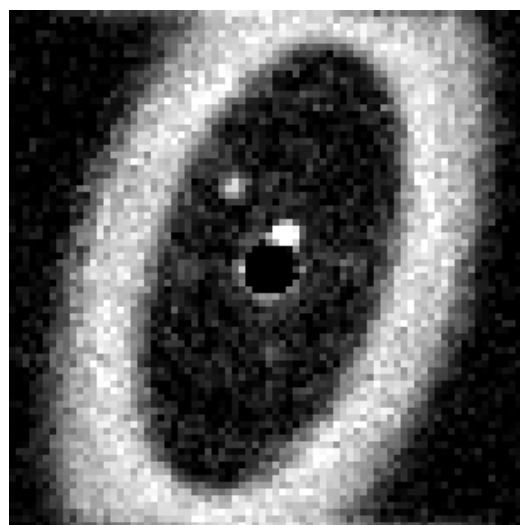


**Figure 4.7-1.** Simulated Exo-C image of the 47 UMa system for V band and 2 days integration. The occulted star is at center. Planet c is seen near the inner working angle at top right, while planet d is visible to top left. A hypothetical debris disk extends around them and out of the field of view.

**Table 4.7-1.** Count rates (in detected photons/sec) and required integration times to take V band RV planet spectra at S/N 10.

| Planet | V | Planet Count Rate | Zodi Count Rate | Exozodi Count Rate | Speckle Count Rate | Dark Count Rate | Integration Time (hrs) |
|---|---|---|---|---|---|---|---|
| eps Eri b | 3.73 | 7.8e-03 | 2.4e-03 | 4.0e-04 | 4.9e-04 | 2.7e-02 | 4 |
| beta Pic b | 3.86 | 1.5e-03 | 2.4e-03 | 6.3e-05 | 1.1e-03 | 2.7e-02 | 96 |
| mu Ara e | 5.15 | 1.3e-03 | 2.4e-03 | 1.7e-04 | 4.0e-04 | 2.7e-02 | 130 |
| 47 UMa c | 5.04 | 2.2e-03 | 2.4e-03 | 3.5e-04 | 3.8e-04 | 2.7e-02 | 46 |
| HD 190360 b | 5.71 | 1.1e-03 | 2.4e-03 | 3.0e-04 | 2.2e-04 | 2.7e-02 | 190 |
| ups And d | 4.10 | 5.4e-03 | 2.4e-03 | 7.0e-04 | 5.9e-03 | 2.7e-02 | 9 |
| HD 39091 b | 5.67 | 7.6e-04 | 2.4e-03 | 4.2e-04 | 1.4e-03 | 2.7e-02 | 360 |
| HD 62509 b | 1.14 | 6.2e-02 | 2.4e-03 | 1.6e-03 | 1.4e-01 | 2.7e-02 | 0.4 |

orbits. Table 4.7-1 details the spectroscopy observations that would be obtained.

### 4.7.2 Planet Searches

For planet searches, we consider the detectability for a fixed range of possible planet radii—Jupiter (11 $R_\oplus$), Saturn (9.5 $R_\oplus$), Neptune (4 $R_\oplus$), super-Earth (2 $R_\oplus$), and Earth. Each planet is assumed to be half-illuminated, and the expected brightness is then derived from the given planet radius and best available albedo analogy within the Solar System. For super-Earths we assume a spherical albedo of 0.5. Any planets possessing a bright ring system would be brighter than is assumed here. The target S/N of the observations varies as described in §4.5.1.1.

The results for a search program capped at 6600 hours of integration time are shown in Figure 4.7-2. The distribution of accessible targets is bounded at smallest orbital radii by the coronagraph inner working angle, and at largest orbital radii by the assumed wavefront stability floor of $10^{-10}$ contrast against which $3\sigma$ detections are required. The latter may be conservative, as Exo-C structural/thermal/
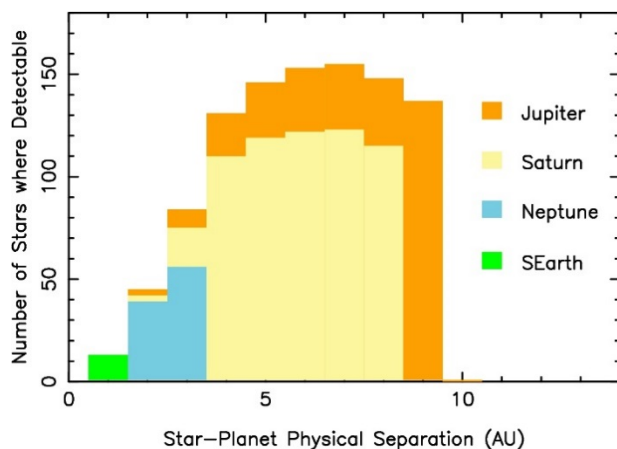


**Figure 4.7-2.** Exoplanet search space for Exo-C in V band with the Hybrid Lyot coronagraph. As the largest archtypical planet, Jupiters appear brightest and are thus most easily detected. At 7 AU separation they can be found around more than 150 nearby stars. Smaller planets must be located closer to the star to be detected, thus Neptune-size planets at 3 AU can be seen in 56 systems. Exposure times are individually calculated for each star (including revisits as described in §4.5.1.1 and are capped at 5 days integration.

optical models suggest an order of magnitude better stability may be obtained (§5.10). Within these bounds, the overall number of detectable planets (7 AU Jupiters around 150 nearby stars, 7 AU Saturns around 120 stars, 3 AU Neptunes around 55 stars, and 1 AU super-Earths around 15 stars) is a function of the time allocated to the survey and the coronagraph throughput.

Example imaging discoveries of new planets are shown in Figures 4.7-3 and 4.7-4. Altair is an A7 star unsuitable for precision radial velocity measurements, so there are no current bounds on its possible planetary system. Gaia may detect planets in this system if it can cope with a first magnitude star.

Earth analogs in the habitable zone are of high scientific interest and represent a stretch goal for Exo-C. For the mission inner working angle of 0.16″ and a contrast cutoff of $5\times10^{-11}$ (consistent with the wavefront stability described in §5.10) they would be detectable around at least the five stars listed in Table 4.7-2. Six optimally-spaced visits would be made to each target to maximize search completeness. The two components of the alpha Centauri system are the most favorable cases because of their proximity and brightness. Figure 4.7-4 shows what an exo-Earth detection around alpha Cen A might look like. Spectroscopy could be done yielding the results shown in Figure 4.3-6.

**Table 4.7-2.** Detectability of Earth-sized planets in the Habitable Zones (HZs) of nearby stars. For the two components of the alpha Centauri system, scattered light from the companion at 8″ has been in included as a noise source. Eta Cas is 12″ binary and will be easier to observe. Exozodiacal light at the minimal 1 zodi level is assumed. Tau Ceti and epsilon Eridani are both observed to have far-IR excess which may mean high levels of dust in their habitable zones; this is not taken into account for the integration times given here.

| Star | V Mag | HZ inner Radius (AU) | Elon-gation (arcsec) | Contrast | Integ Time (hrs) |
|------|-------|----------------------|----------------------|----------|------------------|
| alpha Cen A | 0.1 | 1.2 | 0.93 | 9×10⁻¹¹ | 51 |
| alpha Cen B | 1.2 | 0.8 | 0.60 | 2×10⁻¹⁰ | 99 |
| tau Ceti | 3.6 | 0.7 | 0.20 | 3×10⁻¹⁰ | 99 |
| epsilon Eri | 3.7 | 0.6 | 0.18 | 4×10⁻¹⁰ | 80 |
| eta Cas A | 3.6 | 1.2 | 0.21 | 9×10⁻¹⁰ | 109 |

**Figure 4.7-3.** Simulated observation of the nearby bright star Altair, assuming 12 hours integration in each of V, R, and I bands. Jupiter and Saturn analogs are seen at left and right, along with a 1 zodi dust disk between 2–4 AU.
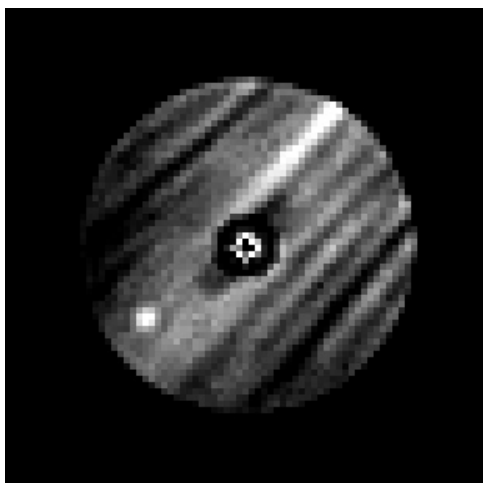


**Figure 4.7-4:** Simulated 5-day V band exposure of an Earth analog in the habitable zone of $\alpha$ Cen A (star occulted at center). Residual scattered light from $\alpha$ Cen B (out of the field, 8" away to top right) is the primary noise source, filling in the coronagraphic dark hole around $\alpha$ Cen A. The result is shown after reference star subtraction to 3% accuracy.

### 4.7.3 Contingency Observing Time

The allocation of mission time to various science program areas is shown in Table 4.5-2. The total science integration time of 867 days is the sum of multiple independent observing programs. As shown in Appendix D, some stars appear in two or more of the individual program target lists for observations in the same mode. If these redundant observations

are removed by retaining the longer of the planned integrations, approximately 100 days of mission time are freed up. This savings is not shown in Table 4.5-2; instead, this it is held as contingency observing time to allow for uncertainties in the mission performance estimates. This ~10% contingency time, if still available at launch, could support observations of additional targets, more observing time on the current listed targets, or a modest General Observer program.

### 4.8 Science Return vs. Adopted Performance Assumptions

The most important instrument parameters that affect science performance are shown in Table 4.8-1. The throughput includes 98% reflectivity at all optical surfaces, dual polarization operation, 60% in-band transmission at the photometric filter, 80% detector quantum efficiency at V band, and 42% pupil throughput for the Hybrid Lyot Coronagraph. Individual 2000 sec readouts are stacked to produce the total required exposure time. Read noise and dark current are calculated for the

**Table 4.8-1.** Performance assumptions.

| Value | Parameter |
|---|---|
| 16%, 12% | Imager, IFS throughput |
| 1, 0.1 e$^-$/read | Imager, IFS detector read noise |
| 0.0005 e$^-$/sec | Detector dark current |
| 0.041" | Imager pixel, IFS lenslet spatial sampling (0.5 $\lambda$/D at 550 nm) |
| 0.16" | Inner working angle (IWA) (2 $\lambda$/D at 550 nm) |
| 0.2, 0.014 | Bandwidth $\Delta\lambda/\lambda$ per channel for detection with imager, IFS |
| 1e-10 | Speckle contrast floor added in quadrature to coronagraph contrast curve |
| (1.5 $\lambda$/D)$^2$, 0.52 | Photometry aperture and ensquared energy for Lyot coronagraph |
| 9, 54 | Number of detector pixels sampling the photometry aperture for the imager and IFS spectral bandwidths |
| 50–130º | Allowable boresight angle wrt Sun |
| 22.7 mag/arcsec$^2$ | Local zodiacal light brightness |
| 22.0 mag/arcsec$^2$ | Brightness of one exozodi at HZ |

number of pixels used to sample the photometry apertures. The coronagraph contrast curve shown in Figure 4.8-1 was used for the case of 0.8 mas of pointing jitter on the occulting spot.
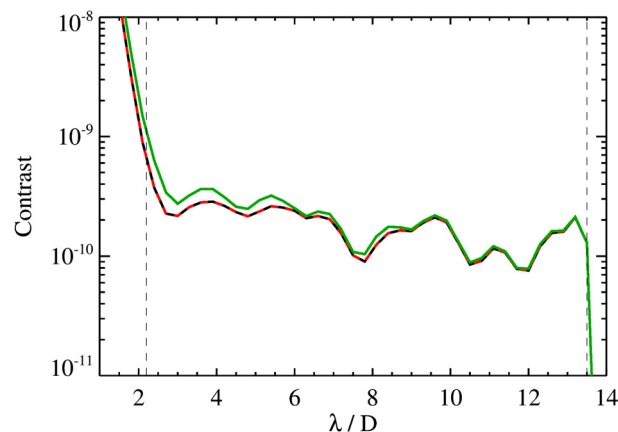


**Figure 4.8-1** Image contrast achieved by Exo-C using a Hybrid Lyot Coronagraph, including the effects of pointing jitter. The black and red lines show the indistinguishable effects of 0 and 0.4 mas of jitter, while the green line is for Exo-C adopted performance requirement of 0.8 mas.

### 4.8.1 Exoplanet Spectra

Exoplanet spectra are the highest-priority science dataset to be obtained by Exo-C. Thus it is appropriate to consider how variation in the Table 4.8-2 parameters affect the number of known RV planets whose spectra can be obtained by the mission. The table below shows these effects, under the assumption that all observations must be obtained in a 6600-hour block of integration time.

The tabulated results show that Exo-C's spectroscopy science return would be most improved if one of the alternate coronagraph types could be matured to technical readiness. The return is only weakly dependent on exozodi (as the targets are giant planets) or the contrast floor of the dark hole speckle background (whose shot noise contribution is, for the most part, eclipsed by the detector dark

**Table 4.8-2.** Number of known RV planets for which Exo-C can obtain spectra within one year of mission time, as a function of varying the parameters given in Table 4.8-1.

| | |
|---|---|
| Baseline HLC | 7 |
| Exozodi 10 | 7 |
| Exozodi 100 | 6 |
| Dark current 0.00025 e/sec | 8 |
| Dark current 0.001 e/sec | 5 |
| Read noise 1 e/read | 6 |
| Read noise 3 e/read | 4 |
| Speckle background 1e-9 | 7 |
| Speckle background 1e-8 | 6 |
| 1.3 m telescope aperture | 5 |
| 1.5 m telescope aperture | 8 |
| PIAA coronagraph | 12 |
| Vector vortex coronagraph | 10 |
| Vector vortex and IWA 1.7 λ/D | 12 |
| Vector vortex and IWA 2.2 λ/D | 8 |

counts and foreground zodiacal light). Achieving the specified 0.0005 e/sec detector dark rate is crucial for assuring Exo-C's spectroscopic science return.

### 4.8.2 Exoplanet Searches

Here we also assume a 6600-hour observing program to search nearby bright stars for new exoplanets, with the number of revisits set to the values given in §4.5.1.1. Figures 4.8-2 and 4.8-3 show the planet search space for our two alternate coronagraph architectures using the baseline performance assumptions. Both the vector vortex and the Exo-C PIAA designs offer a 10% better inner working angle. Relative to the hybrid Lyot, the vector vortex design offers 1.4× better throughput and the PIAA design 2.8× better. These allow a larger number of stars to be surveyed as shown. The HLC is baselined for a 2017 Exo-C project start due to its better demonstrated technical readiness. These results, and those for spectroscopy in the previous subsection, show what could be gained if the Exo-C PIAA or the vector vortex were matured in time for a later project start.
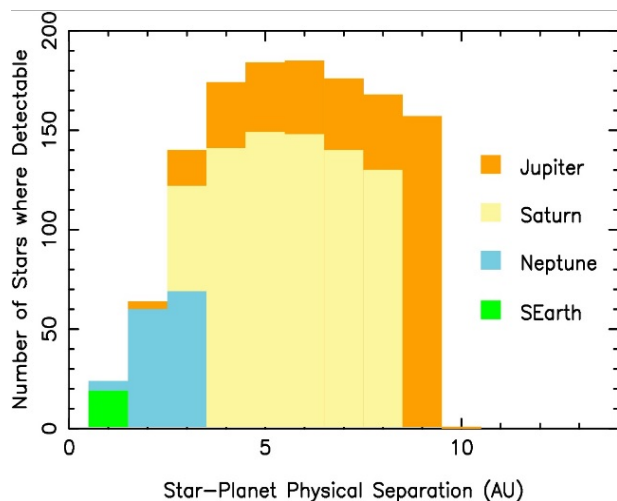
**Figure 4-8.2.** As for Figure 4.7-2, but now for the case of the Vector Vortex coronagraph.
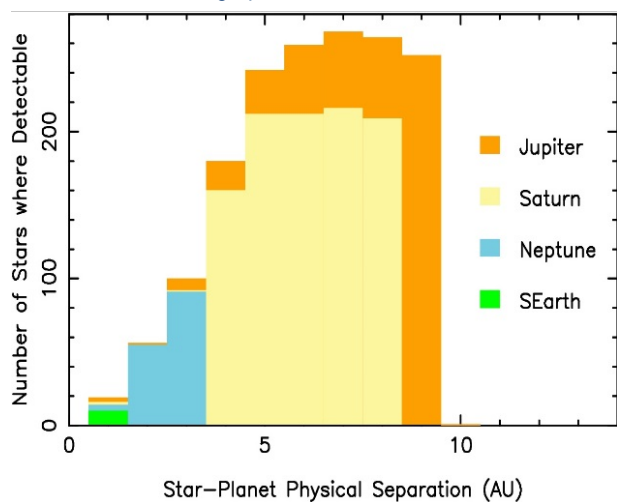


**Figure 4-8.3.** As for Figure 4.7-2, but now for the case of the Exo-C PIAA design.

### 4.8.3    Science versus Mission Duration

The Exo-C mission is designed for a nominal three year lifetime with sufficient consumables and telecom to enable an extension of two more years. An extended mission would enable the following enhancements to the Exo-C science return:

- Spectroscopy on planets discovered late in the mission
- More spectroscopy integration time on all detected planets to increase S/N
- More epochs of astrometry to improve orbit determination for imaged planets

- More epochs of photometry to measure phase variations in reflected light and polarization around planetary orbits, to provide additional constraints on atmospheric clouds and hazes
- Search a larger number of stars for new planets
- Expand the disk imaging sample
- General astrophysics with the Exo-C prime instruments
- Science with an Auxiliary Instrument

Conversely, if the mission lifetime was curtailed by a technical fault or by availability of funds, spectroscopy of all RV planets accessible to Exo-C would be retained. Disk imaging and imaging searches for new exoplanets would be curtailed by dropping the fainter targets.

### 4.9    Science Requirements Flow-Down

The Exo-C Science Objectives and desired Science Capabilities are captured along with the STDT Program Requirements and Program Constraints in the Science Traceability Matrix (Table 4.9-1). An organized Science Traceability Matrix documents the high-level goals that drive the trades considered by the study team, and is developed into Key Mission Requirements.

The STDT Charter is the primary source of the Program Requirements and Constraints (STDT Charter v7, June 2013). In general, the Program Requirements are consistent with the Science Objectives and Capabilities desired by the Exo-C STDT as discussed in §4.2 and §4.4. The Program Constraints that include TRL restrictions were relevant in making design trade decisions and defining the capabilities in the mission and instrument level requirements.

In addition to the tables, it is helpful to visualize the flow from Science Objectives and Capabilities to Key Mission Requirements. This flow is captured in the diagram in Foldout 4-1.

### 4.9.1 Science Requirements to Mission Requirements

The Exo-C STDT considered both the Science Objectives and desired Capabilities along with the Program Requirements and Constraints to develop the top-level mission requirements, and these are documented in the Key Mission Requirements Matrix in Table 4.9-2. These Key Mission Requirements are consistent with the top-level instrument requirements from §4.5 and include wavelength range, spectral resolution, astrometric precision, inner and outer working angle, post-processed contrast, mission lifetime, target star magnitude, duration of observations, and the Exo-C self-imposed requirement on suppression of binary partners of target stars.

The Key Mission Requirements were used not only to guide the baseline Exo-C spacecraft and observatory design, but also as the framework for the observatory performance simulations that helped the STDT assess the science return of the mission.

For clarity, the Key Mission Requirements table does not include in detail some of the requirements flow to spacecraft systems and subsystems, such as orbit selection, power system configuration, or communications data rate. While these additional mission and spacecraft design elements are of course important, they are fairly straightforward to implement and were not the "key" drivers of science performance, cost, and schedule. The rationale for all of the detailed mission and baseline spacecraft system and subsystem decisions are discussed further in §5.

### 4.9.2 Flight System Requirements

Observatory requirements flow from the Key Mission Requirements and affect both the Exo-C payload and spacecraft systems and subsystems. For example, the pointing systems requirements flow from the mission contrast, astrometric precision, inner working angle, and clear aperture diameter requirements to telescope jitter and then to spacecraft vibration isolation. Requirements that are important but had less of an impact on design decisions are captured in more detail in the baseline design in §5. For example, the communications system requirements are described in the baseline design but not captured in detail in the Key Missions Requirements table and flowchart.

### 4.9.3 Payload Requirements

For Exo-C, the payload consists of the pointing system, telescope assembly, the coronagraph (and its detector), the IFS (and its detector), and the LOWFS. The science objectives lead to the mission requirements and then payload requirements. The matrix and flow diagram also do not capture in detail how some of the constraints, such as those on TRL, drive the coronagraph architecture trade (see §5.1.1.6). Notably, the science objectives and program constraints (largely cost) lead to the current telescope aperture choice of 1.4 m, where its cost is related both to its mass, structural rigidity, and its optical quality.

### 4.9.4 Spacecraft Requirements

Spacecraft constraints capture how spacecraft hardware limitations interact with science observations and are linked to Observatory requirements. For example, one of the important constraints on science observations is how long the spacecraft can maintain pointing at a desired target before needing to perform a maneuver to desaturate its reaction wheels. For the spacecraft, the top two driving requirements are jitter and pointing. The jitter requirement has resulted in a two-layer isolation system, and the pointing requirement has resulted in the multi-layer control architecture (see §5.7.2).

### 4.9.5 Subsystem Requirements

The discussion of instrument requirements were presented in §4, motivated by the science objectives, and the spacecraft subsystem requirements and baseline decisions are next discussed in §5.

**Table 4.9-1.** Exo-C science traceability matrix.

| Science ID | Science Objectives | Science ID | Science Capabilities | Program ID | Program Requirements | Constraint ID | Program Constraints |
|---|---|---|---|---|---|---|---|
| S-1 | Exo-C shall characterize known exoplanets around nearby stars.[1] | S-1.1 | Exo-C shall be able to determine atmospheric composition. | P-1 | Exo-C shall be able to image a "Jupiter-twin" at quadrature in a Solar System twin at a distance of 10 pc.[1] (S-1, S-2). | C-1 | Exo-C mission cost capped at $1B in FY15, including launch vehicle, launch operations, and technology development costs (for technologies whose development is not currently funded).[1] |
| | | S-1.2 | Exo-C shall be able to determine exoplanet orbital parameters. | | | C-2 | Exo-C shall use an internal coronagraph to accomplish mission.[1] |
| S-2 | Exo-C shall survey nearby stellar systems for exoplanets.[1] | S-2.1 | Exo-C shall be able to discover Super-Earths within the Habitable Zone. | | | C-3 | Exo-C shall use technologies that are >TRL 5 by the start of Phase B.[1] |
| | | S-2.2 | Exo-C shall be able to discover exoplanets with R >2 $R_\oplus$. | P-2 | Exo-C shall be able to characterize a "Jupiter-twin" at quadrature in a Solar System twin at a distance of 10 pc by R>70 spectroscopy across 0.5 to 1.0 µm. [1] (S-1, S-2) | C-4 | Exo-C shall use technologies that are >TRL 6 by the start of Phase C.[1] |
| | | S-2.3 | Exo-C shall be capable of discovering exoplanets around Alpha Centauri.[2] | | | | |
| S-3 | Exo-C shall image dust disks in planetary systems.[2] | S-3.1 | Exo-C shall be able to assess dust content near the Habitable Zone. | | | C-5 | Exo-C shall meet mission reliability class B standards as specified in NPR 8705.4.[1] |
| | | S-3.2 | Exo-C shall be able to characterize dust properties. | | | | |
| | | S-3.3 | Exo-C shall be able to resolve dust disk spatial structure. | | | C-6 | Exo-C shall exceed the expected ground capability at end of mission as judged by CAA.[1] |

[1] STDT Charter v7, June 2013
[2] Exo-C self-imposed objective

**Table 4.9-2.** Exo-C key mission requirements.

**Mission**

| Mission ID | Mission Requirements [units] (parent) | Req. | Cap. |
|---|---|---|---|
| M-1 | Wavelength Range λ [μm] (S-1.1) | 0.45–1.0 | 0.45–1.0 |
| M-2 | Spectral Resolution [λ/Δλ] (S-1.1) | >70 | 200 |
| M-3 | Astrometric Precision [milliarcsec] (S-1.2) | <30 | 20 |
| M-4 | Inner Working Angle at 550 nm [arcsec] (S-2.1) | <0.16 | 0.16 |
| M-5 | Post-Processed Contrast [-] (S-2.1) | 1E-10 | 5E-11 |
| M-6 | Outer Working Angle at 550 nm [arcsec] (S-2.3) | 1.37 | 1.58 |
| M-7 | Suppress binary star sep. by 8–10 arcsec [-] (S-2.3) | 5E-09 | 0.00000003 |
| M-8 | 3 year mission lifetime [years] (C-1, S-1, S-2) | 3 | 3 |
| M-9 | Target star magnitude [Vmag] (P-1) | 7 | 7 |
| M-10 | Target obs. allocated time (S-1, S-2, S-3) | Varies | Meets req. |

**Observatory**

| Observatory ID | Observatory Requirement [units] (parent) | Req. | Cap. |
|---|---|---|---|
| O-1 | Clear Aperture Diameter [m] (M-4) | 1.3 | 1.4 |
| O-2 | Raw Speckle Contrast [-] (M-5) | 0.000000001 | 0.000000005 |
| O-3 | Observe binary stars separated by [arcsec] (M-7) | 8–10 | 7–12 |
| Spacecraft ID | Spacecraft Constraint [units] (parent) | | |
| SC-1 | Longest observation due to RWA desat [min] (hw) | 60 | 60 |
| SC-2 | RWA Jitter with Dual RWA Vibration Iso. [mas] (hw) | 450 | 300 |
| Payload ID | Payload Requirement [units] (parent) | | |
| PL-1 | Coronagraph Pointing Stability (post FGS FSM) [mas] (M-3, M-4, O-1) | 0.8 | 0.36 |
| PL-2 | Wavefront Stability [nm/hrs] (M-5) | 1 | 0.3 |
| PL-3 | Coro./IFS detector perf., incl. # pixels (O-1, O-2) | 1k×1k | 1k×1k |

**Subsystem**

| Subsystem ID | Payload Subsystem Requirements | Req. | Cap. |
|---|---|---|---|
| TL-1 | Telescope thermal drift [mK/hr] (PL-2) | 30 | 10 |
| TL-2 | Telescope diameter [m] (O-1) | 1.3 | 1.4 |
| TL-3 | Telescope pointing stability [mas] (PL-1) | 16 | 4 |
| TL-4 | Telescope jitter after isolation [mas] (TL-3) | 5 | 3.4 |
| TL-5 | Binary star scattered light [-] (M-7) | 3E-08 | 3E-08 |
| CO-1 | Mask IWA [λ/D] (O-1) | 2.2 | 2 |
| CO-2 | N actuators in DM [-] (M-6) | 48×48 | 48×48 |
| CO-3 | Coronagraph Arch. Contrast [-] (O-2) | `E-09 | 1E-09 |
| IFS-1 | Min. Spectral Resolution [λ/Δλ] (M-2) | 70 | 70 |
| IFS-2 | Wavelength Range λ [μm] (M-1) | 0.49–1.0 | 0.49–1.0 |
| LOWFS-1 | LOWFS stability [nm] (M-4, O-2) | 25 | 15 |
| LOWFS-2 | LOWFS Bandwidth [Hz] (LOWFS-1) | 0.001 | 0.0025 |

[1] STDT Charter v7, June 2013
[2] Exo-C self-imposed objective

## 4.10 Beyond Imaging of Exoplanetary Systems: Exo-C Extended Science

Exo-C coronagraphic imaging and spectro-scopy capabilities can be readily employed for studies of bright general astrophysics targets. These could include imaging the structure of circumstellar shells around post-main sequence stars or the host galaxies of quasars and active galactic nuclei. An assessment of general astrophysics enabled by the AFTA coronagraph has been compiled for the COPAG by Ebbetts et al. 2015 (http://cor.gsfc.nasa.gov/sags/sag6.php); most of its suggested observations could be pursued with Exo-C as well.

Exo-C could potentially be used to image small targets without use of the coronagraph. This includes solar system objects as large as Jupiter, targets of opportunity such as comets and novae, and resolving source confusion for TESS-detected transits or microlensing events. The IFS could be used to image emission jets from young stellar objects or Ly $\alpha$ structures redshifted into the optical at z~5. However, the current Exo-C pointing architecture depends on the presence of a V<13 star in the coronagraph. A redesign of the pointing system would be needed to support these suggested investigations.

### Possibilities for an Auxiliary Instrument

The Exo-C instrument bench (§5.3) and launch vehicle mass margins are sufficiently large that an auxiliary science instrument can be contemplated. Given the constraints it would exist as a module within the existing instrument bench and not as a stand-alone instrument. An auxiliary instrument is not part of the Exo-C baseline mission or included in current cost estimates. Nevertheless, it is interesting to consider what might be added to the mission for relatively little additional cost.

A compact, optical/near-IR instrument with the capability to contribute to exoplanet science would be an ideal complement to the primary coronagraph mission. Two possible science goals would be the measurement of transit timing variations with precision photometry and transit spectroscopy with an optical/NIR spectrograph. Either type of observation would be conducted in dedicated pointings to targets of interest and not conducted in parallel with coronagraphic imaging.

Transit Timing Variations, or TTVs, allow constraints to be placed on the masses of transiting planets as their orbits are perturbed by other planets, including ones which are not transiting. Transit spectroscopy probes the atmospheric composition and cloud properties of transiting planets. Since observations would be of known transiting systems, the small field of view afforded by Exo-C would be appropriate to either instrument.

A dedicated photometer could follow up hundreds of multiple planet systems discovered by Kepler and TESS to precisely measure transit variations over very long temporal baselines. TTVs have been measured precisely for the shorter period multi-planet systems, but a photometer could follow up systems of high scientific value.

While JWST is expected to provide outstanding transit spectroscopy for a limited set of exoplanets, realistic limits on available time will preclude large surveys. Mission studies of dedicated transit spectroscopy telescopes, such as the FINESSE Explorer Mission (Deroo et al. 2012), have demonstrated the value of large transit spectroscopy surveys. The exceptional stability of the Exo-C telescope and the large size compared to FINESSE would allow for exquisite spectrophotometric precision at high spectral resolution. The FINESSE Explorer proposed to operate over a wavelength range of 0.7–5.0 µm, while an Exo-C auxiliary instrument would be limited to wavelengths shortward of the thermal background from a warm telescope: 0.4–1.0 µm if a CCD was used, or 0.7–1.7 µm with a HgCdTe detector. Absorption features of multiple interesting atoms and molecules could be probed for

dozens to hundreds of transiting planets, with a near-IR capability being particularly valuable.

ESA's PLATO mission is scheduled for launch in 2024. At that time the JWST mission may have concluded, leaving the photometric and spectral follow-up of PLATO transiting planets solely to Exo-C equipped with a dedicated transit instrument.

## 4.11  Exo-C Preparatory Science

There are a number of precursor activities that would enable a greater science return from Exo-C or any exoplanet direct imaging mission. Some of these will happen organically within the research community and others will require specific new NASA support. In priority order, they are:

1. *Further modeling of planetary atmospheres* in the setting of specific Exo-C planetary targets, meaning for the specific stellar hosts listed in the target list (Appendix D) and at the range of orbital semi-major axis shown in Figure 4.7-2. This is especially needed for super-Earths and mini-Neptunes, which remain largely unexplored.

2. *Further spectral retrieval studies* beyond Marley et al. (2014), to better understand how accurately exoplanetary atmospheric abundances and cloud properties can be ascertained given various combinations of spectral coverage, resolution, and signal to noise ratio. While Exo-C requirements stated in §4.3.2 are well-grounded, a more exhaustive survey of the parameter space of stellar types and instrument characteristics might allow some of the requirements to be relaxed.

3. *Modeling of debris disk dust structures driven by planetary perturbations*, including the effects of collisions between parent bodies and grains and the effects of radiative dust transport, to better calibrate the ability to infer

planet properties from observed disk structures.

4. *Obtain dedicated radial velocity precursor observations* for all exoplanet imaging targets where precision RV observations are viable. A long time baseline is especially important for identifying planets beyond 1 AU. Maximum effort should be made on the quietest stars in the sample once they have been identified by a quick survey for RV stability. The Exo-C STDT strongly endorses the recommendations in section 6 of the November 2014 Radial Velocity Completeness Study by Howard and Fulton.

5. *Build the astrophysical datasets on the specific nearby stars* whose planets would be accessible to Exo-C direct imaging. The needed data include:
   - *Stellar metallicity determinations.* This data is already available for stellar type ranging from late F through K. However, 2/3 of the stellar hosts most suitable for direct imaging have earlier spectral types (Howard and Fulton 2015) and generally lack modern metallicity values. Metallicity is directly correlated with planet occurrence frequency and the host star value will be an interesting comparison to metallicities derived from exoplanet spectra.
   - *Age dating.* Known ages should be compiled from the literature and observing programs initiated to get missing ages. This could include dedicated new asteroseismology work. The system age affects the level of internal heat in giant planets and thus their atmospheric properties.
   - *Stellar radii and orientations.* The angular size of the star affects the brightness of the instrumental halo

background at the coronagraph inner working angle, and thus is a calibration issue for measurements of exozodiacal light. For fast-rotating stars, measurements of rotational flattening would constrain the orientation of the stellar rotation axis. This information would allow observational tests of the perpendicularity of planetary orbits and debris belts to the stellar rotation axis, as well as suggest preferred sky regions around the star for the deepest planet searches. Near-IR stellar interferometry could provide these measurements.

6. *Fully exploit the Gaia and TESS mission datasets* on exoplanet direct imaging targets. This means understanding the properties of the detected planets, astrometric or transit timing trends that are present, and limits these mission datasets provide on unseen planets. Any constraints these datasets provide on the host star properties should also be assessed.

7. *Quantitative modeling of mid- and far-infrared excess emission*, or limits to IR excess, provided by the Spitzer, Herschel, WISE, and LBTI data on exoplanet direct imaging targets. This modeling would aim to constrain the range of dust belt densities, locations, and dust properties that might plausibly be seen in scattered light by direct imaging.

8. *Compile estimates of background source confusion* that might be seen around each exoplanet imaging target. While the extragalactic background is expected to be largely uniform, the galactic stellar background will vary widely. This might be done by dedicated new observations and/or the use of galactic star-count models to the needed depth.

**Science**

**Key Requirement [units]**

| Req. | Cap. | % Margin |
|---|---|---|

Characterize known exoplanets around nearby stars

Survey nearby stellar systems for exoplanets

Image dusk disks in planetary systems

Determine the atmospheric composition | Determine planet's orbital inclination | Discover Super-Earths within the Habitable Zone | Discover R > 2R$_\oplus$ planets | Discover planets around Alpha Centauri | Assess dust content near the Habitable Zone | Characterize dust properties | Resolve spatial structure — **All**

**Mission**

**Wavelength Range (λ) [μm]**

| 0.45–1.0 | 0.45–1.0 | N/A |
|---|---|---|

**Inner Working Angle (IWA) at 0.9 μm [arcsec]**

| 0.25 | 0.24 | 4% |
|---|---|---|

**Post-processed Contrast [---]**

| 1e-10 | 0.5e-10 | 50% |
|---|---|---|

**Outer Working Angle (OWA) at 0.8 μm [arcsec]**

| 2.0 | 2.3 | 17% |
|---|---|---|

**Suppression of a Binary Star Separated by 8–10 arcsec**

| 3e-8 | 3e-8 | 0% |
|---|---|---|

**Mission lifetime of 3 years (Sec. 4.3.3)**

**Observation allocation times (see Sec. 4.5)**

**Min. Spectral Resolution [λ/Δλ]**

| 70 | 200 | 185% |
|---|---|---|

**Astrometric Precision [milliarcsec]**

| 30 | 20 | 33% |
|---|---|---|

**Target magnitude:** All requirements must be met with stars up to 7th Vmag

**Observatory**

**Clear Aperture Size [m]**

| 1.3 | 1.4 | 7% |
|---|---|---|

**Raw Speckle Contrast [---]**

| 1e-9 | 0.5e-9 | 50% |
|---|---|---|

**Observe Binary Stars with a Separation Range of [arcsec]**

| 8–10 | 7-12 | N/A |
|---|---|---|

**Payload**

**Coronagraph (past FSM) Pointing Stability [milliarcsec]**

| 0.8 | 0.36 | 55% |
|---|---|---|

**Wavefront Stability [nm/hrs]**

| 1 | 0.3 | 70% |
|---|---|---|

**Spacecraft**

**Longest Observation Length [min]**

| 60 | 60 | 0% |
|---|---|---|

**Pointing System**

**Pointing Bandwidth [Hz]**

| 50 | 100 | 100% |
|---|---|---|

**Telescope**

**Telescope Thermal Drift [mK/hr]**

| 30 | 10 | 200% |
|---|---|---|

**Telescope Diameter [m]**

| 1.3 | 1.4 | 15% |
|---|---|---|

**Telescope Pointing Stability [milliarcsec]**

| 16 | 4 | 75% |
|---|---|---|

**Telescope Jitter (after isolation Sec 5.7) [milliarcsec]**

| 5 | 3.4 | 33% |
|---|---|---|

**Binary Star Scattered Light**

| 3e-8 | 3e-8 | 0% |
|---|---|---|

**Coronagraph**

**Mask IWA [λ/D]**

| 2.2 | 2.0 | 12% |
|---|---|---|

**No. of Actuators in DM**

| 48 × 48 | 48 × 48 | N/A |
|---|---|---|

**Coronagraph Arch. Contrast [---]**

| 0.7e-9 | 0.3e-9 | 57% |
|---|---|---|

**Integral Field Spectrograph (IFS)**

Detector Performance (5.5.4.1)

**No. of Pixels**

| 1K x 1K | 1K × 1K | NA |
|---|---|---|

**Min. Spectral Resolution [λ/Δλ]**

| 70 | 200 | 185% |
|---|---|---|

**Wavelength Range (λ) [μm]**

| 0.495–1.0 | 0.495–1.0 | N/A |
|---|---|---|

**Imager**

Detector Performance (5.5.4.1)

**No. of Pixels**

| 1K x 1K | 1K × 1K | NA |
|---|---|---|

**LOWFS**

**LOWFS Stability [pm]**

| 25 | 15 | 40% |
|---|---|---|

**LOWFS Bandwidth [Hz]**

| 0.001 | 0.0025 | 150% |
|---|---|---|

Time between desats

RWA

Dual RWA vibration isolation system (Sec. 5.7)

**RWA Jitter [milliarcsec]**

| 450 | 300 | 33% |
|---|---|---|

**Foldout 4-1.** Overview of EXO-C key requirements flow-down.

# 5    Baseline Configuration and Implementation for Detailed Study

Starting from the science requirements in §4, the design team performed many trade studies, culminating in the baseline configuration presented in this section. A summary of the trade results [1] is shown in Table 5.1-1. §8 identifies a technology plan that advances the baseline configuration to flight readiness. Some technology areas are currently under development by the WFIRST-AFTA project, while some are specific to Exo-C. Each trade would be revisited at the start of Phase A, depending on the results of the technology plan, and the start date of Exo-C. Many of the design trades have resulted in a similar architecture to that of the Kepler mission, giving Exo-C a proof-of-existence model for this report. Kepler, with a 1.4-m primary mirror telescope, dedicated to exoplanet science, and a total mission cost around $750M FY15—well below the Probe study $1B requirement—makes an excellent starting point for the Exo-C design.

**Table 5.1-1.** High-level baseline configuration trade studies.

| Summary of Trade Studies Performed | Outcome |
|---|---|
| Telescope: obscured vs. non-obscured | Non-obscured |
| Telescope: design | Cassegrain |
| Primary mirror: Low CTE glass vs. SiC | Low CTE glass |
| Orbit: L2 vs. Earth trailing | Earth-trailing |
| Aperture size | 1.4 meter |
| HGA: fixed vs. articulating | Fixed |
| Isolators: between RWA and S/C and between S/C and payload | Two passive layers |
| Deformable mirror actuator count | 48×48 |
| Instrument location: lateral vs. behind PM | Lateral |
| Solar shielding: Outer barrel vs. MLI-tent vs. flat sunshade | Flat sunshade |
| Coronagraph Architecture | Hybrid Lyot |
| Science Detectors | 1K×1K EMCCD |
| LOWFS architecture | Zernike phase sensor |
| Mission Lifetime | 3 years |

---

[1] See Appendix B of the non-redacted version of this report for the details of the trade studies.

§5 begins with a design overview, §5.1, followed by a description of each subsystem, in §5.2 through §5.9. Detailed Structural Optical Thermal Performance (STOP) modeling was performed on the baseline design, and is documented in §5.10. The results were then passed on to the science team to evaluate science performance, which is documented in §4. Another analysis, documented in §5.11, investigates Exo-C's ability to detect exoplanets in a binary star system. §5 ends with an overview of the spacecraft design, §5.12, and an analysis of slew times, §5.13.

## 5.1    Baseline Configuration Overview

Aside from the payload, Exo-C is very similar to Kepler in design. They each have fixed solar panels, a fixed high gain antenna, and a payload recessed into the spacecraft bus (see Foldout 5-1 E and G). The Exo-C spacecraft bus needs to add a two-stage passive vibration isolation system to the original Kepler architecture, and a reconfiguration of the solar panels. The passive isolators are flight proven technology. Other planned changes to the bus are more reliable reaction wheels and some structural panel resizing.

Although the payload is significantly different, the telescope is of comparable size and complexity to Kepler, each having a 1.4-m primary mirror. Exo-C has an unobscured Cassegrain architecture, whereas Kepler has an obscured Schmidt with a transmissive Schmidt Corrector in the 0.95-m aperture.

The coronagraph instrument is positioned along the optical barrel in order to minimize angles-of-incidence on the optics, which reduces polarization errors. It also reduces the need for fold mirrors compared to the usual location of instruments behind the primary mirror. The coronagraph instrument has two science detectors: an imager and an integral field spectrograph. The overview of the configuration can be seen in Foldout 5-1 D.

## 5.2    Mechanical Configuration

Exo-C consists of the instrument payload attached to the spacecraft bus via an isolation hexapod assembly, as seen in Figure 5.2-1. The payload comprises the barrel assembly, primary and secondary mirror assemblies, primary support structure (PSS), instrument bench with instruments and optics, lid, and the star trackers.

The barrel bolts to the top of the PSS through six invar fittings that are bonded to the bottom of the barrel. Both the cylindrical portion of the barrel assembly, the barrel structure, and the scarfed baffle structure (see Figure 5.2-1) are made from composite panels with carbon fiber facesheets. The barrel structure panels use graphite-based composite honeycomb core, while the scarfed structure uses aluminum honeycomb core. Along the height of the barrel are evenly spaced ribs that bond to the barrel's interior facesheet via clips. All ribs and clips are made of graphite-based composite. The lid attaches to the top of the scarfed structure at four points. Three points contain release actuators and one point

contains a hinge. The two actuators on the side of the lid provide additional structural support during launch. Once on-orbit, the two side actuators are released first. When the remaining actuator is released, the lid rotates about its hinge, detaches from the structure, and drifts away from the telescope.

The PSS is a 2.0-m wide, 0.19-m deep composite structure comprised of graphite-based composite facesheets and internal rib structure. It also contains bonded, metallic fittings at attachment points to its various interfaces, including the primary mirror bipods (six fittings), the barrel assembly (six fittings), the isolation hexapod assembly (six fittings), and the star trackers.

The primary mirror assembly mounts to the top of the PSS (see Figure 5.2-1). The assembly comprises the 1.4-m aperture primary mirror and a primary mirror wedge. The light-weighted mirror is made from low coefficient of thermal expansion (CTE) glass and attaches to the composite wedge via three flexured bipods. With an overall depth of 0.14 m, it has an areal density



**Figure 5.2-1.** Isometric and sectioned side view of the baseline mechanical configuration with labeled major mechanical components.

**A**

## Integral Field Spectrograph (IFS)

LENSLETS  LENSLET FOCUS  DISPERSED LENSLET IMAGES  EXTRACTED DATA CUBE

The IFS uses 4 bands to produce an R=70 spectra from 495 to 1000 nm over the central 2.3 by 2.3 arcseconds using 71 by 71 lenslets.

**B**

The Science Imager has a 41 milli-arcsecond/pixel plate scale to image the dark hole region around the target star.

## Imaging Detector

**Optical layout of Coronagraph**

**Mechanical layout of Coronagraph Instrument**

**D**

**G**

## Exo-C inside launch vehicle

The Exo-C solar panels are configured such that the barrel assembly receives the same solar thermal power at +15 and -15 degrees roll w.r.t. the Sun. This results in a better than 1e-10 contrast stability for differential image speckle subtraction.

**C**

## Master Equipment List

| Mass | |
| --- | --- |
| **Telescope Assembly** | |
| Optical Telescope Assembly | 160 kg |
| Barrel Assembly | 149 kg |
| Avionics Assembly | 9 kg |
| Telescope Harness Assembly | 10 kg |
| Telescope Mass (CBE) | 328 kg |
| Telescope Contingency | 98 kg |
| Telescope Mass (PBE) | 426 kg |
| **Coronagraph Instrument** | |
| Optics and Mounts | 2 kg |
| Focal Plane / Detetor Assembly | 0.4 kg |
| Electronics | 24 kg |
| Mechanical | 46 kg |
| Thermal Control | 24 kg |
| Instrument Mass (CBE) | 96 kg |
| Instrument Contingency | 29 kg |
| Instrument Mass (PBE) | 125 kg |
| **Spacecraft** | |
| Attitude Determination and Control | 66 kg |
| Command and Data Handling | 70 kg |
| Power | 32 kg |
| Propulsion | 11 kg |
| Structure and Mechanisms | 403 kg |
| Telecommunication | 37 kg |
| Thermal | 26 kg |
| Spacecraft Dry Mass (CBE) | 645 kg |
| **Observatory** | |
| Payload (Telescope and Coronagraph) | 424 kg |
| Observatory Dry Mass (CBE) | 1069 kg |
| Spacecraft Contingency | 108 kg |
| Payload Contingency | 127 kg |
| Additional Systems Contingency | 225 kg |
| Observatory Dry Mass (PBE) | 1529 kg |
| Propellant | 20 kg |
| **Total Launch Mass and Power** | **1549 kg** |

| Power | |
| --- | --- |
| **Telescope Assembly** | |
| Optical Telescope Assembly | 157 W |
| Barrel Assembly | 231 W |
| Avionics Assembly | 16 W |
| Telescope Power (CBE) | 403 W |
| Telescope Contingency | 121 W |
| Telescope Power (PBE) | 524 W |
| **Coronagraph Instrument** | |
| Focal Plane / Detetor Assembly | 9 W |
| Electronics | 96 W |
| Mechanical | 26 W |
| Thermal Control | 30 W |
| Instrument Power (CBE) | 161 W |
| Instrument Contingency | 48 W |
| Instrument Power (PBE) | 209 W |
| **Spacecraft** | |
| Attitude Determination and Control | 155 W |
| Command and Data Handling | 167 W |
| Power | 9 W |
| Propulsion | 21 W |
| Telecommunication | 58 W |
| Thermal | 75 W |
| Spacecraft Power (CBE) | 485 W |
| **Observatory** | |
| Payload (Telescope and Coronagraph) | 564 W |
| Observatory Power (CBE) | 1049 W |
| Spacecraft Contingency | 145 W |
| Payload Contingency | 169 W |
| **Total Observatory Power (PBE)** | **1363 W** |

Exo-C has over 50% mass margin w.r.t to medium class launch vehicles lift capabilities to an Earth trailing orbit.

Exo-C has over 30% power margin w.r.t. worst case observing scenario of 40 degrees pitch and 15 degrees roll away from the Sun vector.

**E**

## Spacecraft Bus

Instrument

Isolator Strut Assembly

Isolators

S/C and Payload Electronics Boxes

Spacecraft Bus

Exo-C uses a Kepler-like space-craft buss, only needing to re-arrange the solar panels and adding an extra vibration isolation layer to the payload.

**F**

**Temperature maps of the 1.4 m primary mirror and barrel assembly.**

Temperature (K): 293, 284, 274, 265, 255, 246, 236, 227, 217, 208, 198, 189, 179, 170, 160, 151

Exo-C achieves its extraordinary pico-meter wavefront stability with a benign Earth-trailing orbit and careful thermal-mechanical design. Temperature drifts of the primary mirror and optical barrel are kept at the milli-Kelvin level even through a 40° pitch or a 30° roll.

**Foldout 5-1.** Overview of the Exo-C baseline configuration.

of approximately 49 kg/m$^2$. The secondary mirror assembly is attached to the top of the barrel. The assembly comprises the secondary mirror, made from low CTE glass, and the secondary support structure. The titanium support structure attaches to the mirror via three flexured bipods and attaches to the barrel via three bipods with rigid body actuators (RBAs).

The instrument bench is mounted to the side of the barrel via three bipods, made of graphite-based composite tubes with flexured end fittings. The optics and instruments are enclosed within the instrument bench, which is comprised of composite panels with carbon fiber facesheets and aluminum honeycomb core. The Fine Guidance Sensor (FGS)/Low-Order Wavefront Sensor (LOWFS) and the Integral Field Spectrograph (IFS) are each installed onto separate sub-benches that are subsequently installed and aligned to the rest of the instrument bench. Access holes in the top bench panel, with removable closeout panels, enable installation and adjustment of the bench components. A computer-aided design (CAD) model of the bench is shown in Figure 5.2-2. The optics layout will be discussed in more detail in §5.5.

The Instrument Enclosure, a composite/aluminum honeycomb panel micro-meteoroid shield, mounts to the flat side of the barrel, encompassing both the Secondary Mirror and the Instrument Bench (see Figure 5.2-2). The bench supports two dual-stage radiators, one for the FGS/LOWFS and one for the IFS. Each radiator comprises a conductive path to the detector assembly, a first stage with a total surface area of 0.141 m$^2$, and a second stage with a total surface area of 90 cm$^2$ for the FGS/LOWFS and 180 cm$^2$ for the IFS/Imaging Detector. Two star trackers, oriented 90° apart, along with the star tracker electronics, attach to the outer surface of the PSS directly below the instrument bench. Having the star trackers attached to the PSS, rather than in the spacecraft, improves the pointing stability of

the line-of-sight of the telescope, which in turn reduces beam walk and hence improves performance of the coronagraph.

The first mode of the payload, assuming locked-out isolators and a fixed base at the spacecraft interface, can be seen in Figure 5.2-3. The stiffness of the payload can be further increased by future optimization of the isolator strut layups. Future analysis incorporating a higher fidelity spacecraft bus will be required.

Launch load, vibro-acoustic, and buckling analyses were performed. Positive margins of safety were calculated using a factor of safety of 2.0. Further details can be found in Appendix C of the non-redacted version of this report.
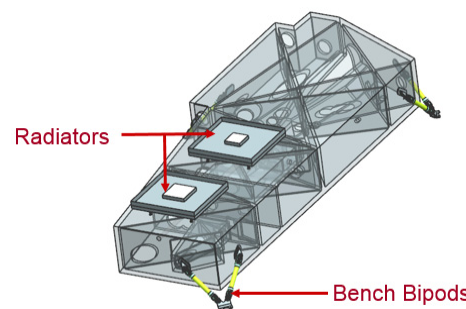


**Figure 5.2-2.** The instrument bench supports the optics and science instruments, as well as the instrument radiators.
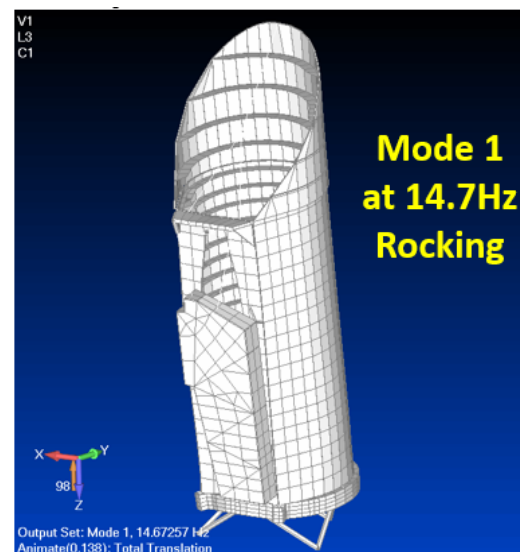


**Figure 5.2-3.** The first mode off the Exo-C barrel assembly is a rocking mode at 14.7 Hz. With an estimated S/C bus stiffness, the launch requirement of a first mode >10 Hz is met.

## 5.3    Payload Optical Configuration

The optical portion of the payload (Figure 5.3-1) comprises the telescope and instrument assembly. The instrument assembly has two main subsections: the wavefront control optics and the coronagraph. Within these two subsections, there are subassemblies that support their indicated function. The control subsection contains a fine-guidance sensor (FGS) and a low-order wavefront sensor (LOWFS) used for pointing and wavefront error correction, respectively. The final focal planes are the imager and the integral field spectrograph (IFS).

The physical configuration of the payload is shown in Figure 5.3-2 and Figure 5.5-1. The
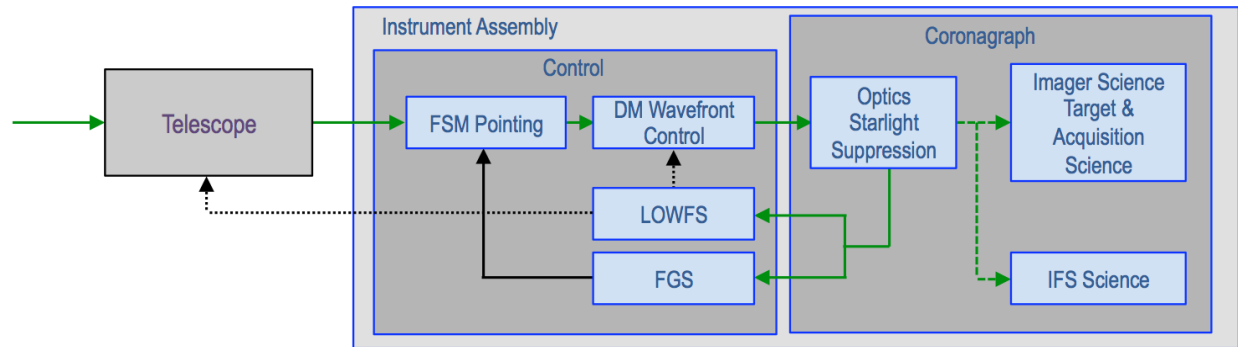


**Figure 5.3-1.** Optical system block diagram. Green arrows show the path of the light through the system, black arrows are control connections; solid black is a real-time update process during observations, while dashed black is a slow update between observations on an as-needed basis.
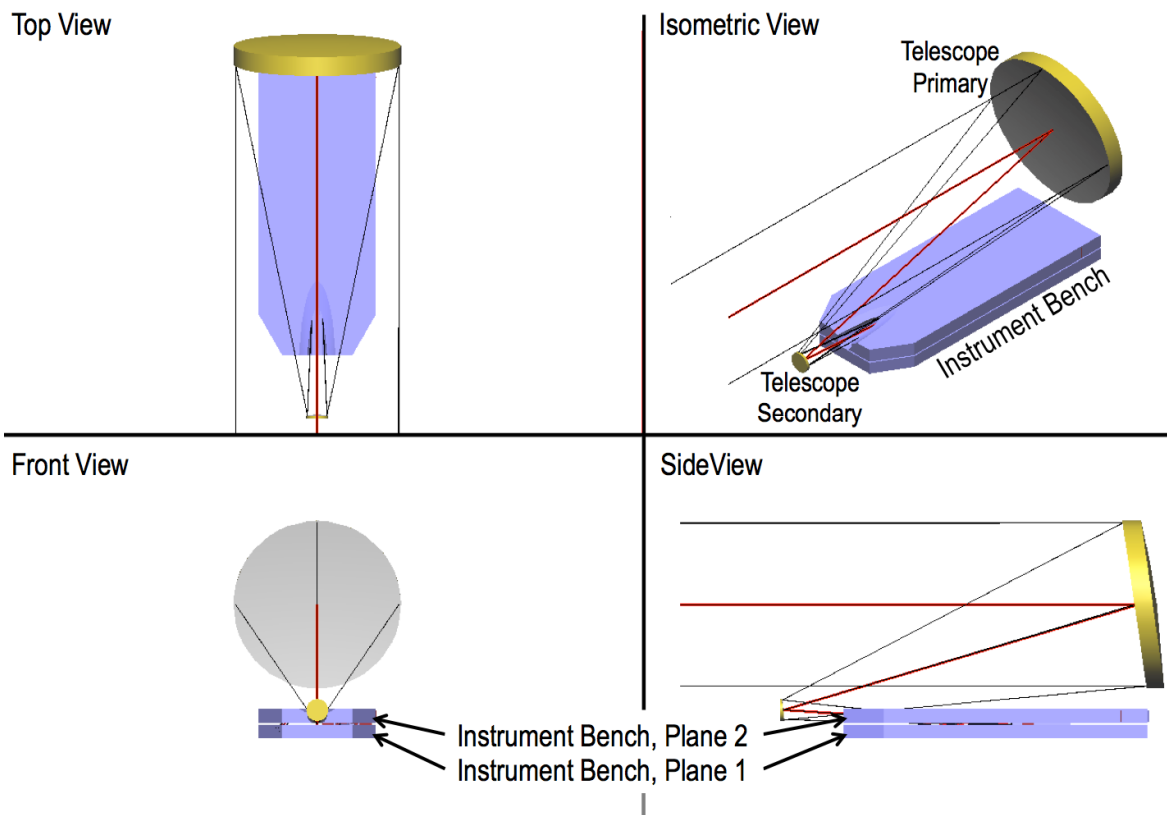


**Figure 5.3-2.** Payload configuration of optics. The Instrument Bench planes are illustrated as distinct blocks to highlight the optical configuration; however, the mechanical implementation is a single integrated assembly.

instrument bench is located laterally with respect to the telescope axis, in two planes parallel to the telescope axis and offset to one side. The volume available in this configuration for the packaging of the instrument assembly allows for the use of a minimum number of fold mirrors, and provides for low angles-of-incidence (AOI) on all sensitive surfaces to provide the least impact to instrument performance (i.e., higher throughput, minimal polarization effect). This configuration also provides an accessible volume of approximately 600×525×100 mm that may be used to host an auxiliary instrument; the optical configuration is readily adapted to direct light into the auxiliary volume from several points along the light path (e.g., directly from the telescope, or following the wavefront control optics, or from the coronagraph focal plane), depending on the specifics of the auxiliary science identified.

## 5.4    Telescope

The first two telescope mirrors (M1 and M2) are in an unobscured Cassegrain configuration, with a 1.4-m diameter entrance pupil located at the primary. A field baffle for rejecting out-of-field light is located where a real image of the sky is formed by the two mirrors, followed by a third mirror (M3) that recollimates the light and creates a 48-mm diameter real image of
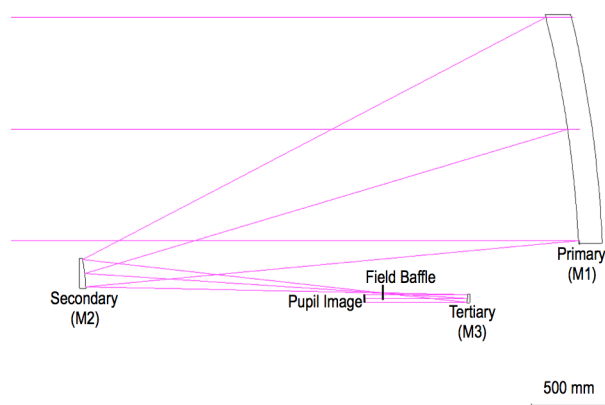


**Figure 5.4-1.** Telescope configuration. Mirrors M1 and M2 are in a Cassegrain form with an unobscured aperture. The optical path following M3 is folded out-of-plane to create a pupil image offset from the field baffle location.

the pupil.

The telescope properties are:
- Entrance pupil diameter=1400 mm
  - Primary focal ratio=f/2.5
  - Focal ratio to field baffle = f/11
- Magnification (M)=29.17
- Field-of-view (FOV)= ±0.7 arcmin

## 5.5    Instrument

### 5.5.1    Coronagraph

There are multiple coronagraph technologies that provide varying degrees of contrast, inner working angle, and throughput. This study selected the Hybrid-Lyot Coronagraph (HLC) as it offers the best-demonstrated contrast and bandwidth performance in testbed experiments to date, i.e., it is closest to our needed technical readiness in 2017. While Phase-Induced Amplitude Apodization (PIAA) and Vector Vortex coronagraphs have better theoretical performance, their demonstrated lab performance lags what the HLC has achieved; they remain under consideration for a 2020 launch. The following describes the elements, functions, and rationale for the coronagraph's optical system; refer to Figure 5.5-1.

Light from the telescope M1 and M2 mirrors enters from the left, focuses at the field baffle, and is recollimated by the telescope M3 to form a pupil image. This is followed by the instrument elements, distributed into two parallel planes to fit into a compact package:

1. Fine-steering mirror (FSM) located at the pupil image*
2. Pupil reimaging mirror pair M4, M5
3. Deformable fold mirror 1 (DM1) located at the reimaged pupil
4. Deformable fold mirror 2 (DM2) located 1 meter away from DM1*
5. Focusing mirror M6, which creates an f/30 image at
6. Hybrid-Lyot Coronagraph mask, which also splits off a portion of the light to*
7. FGS/LOWFS
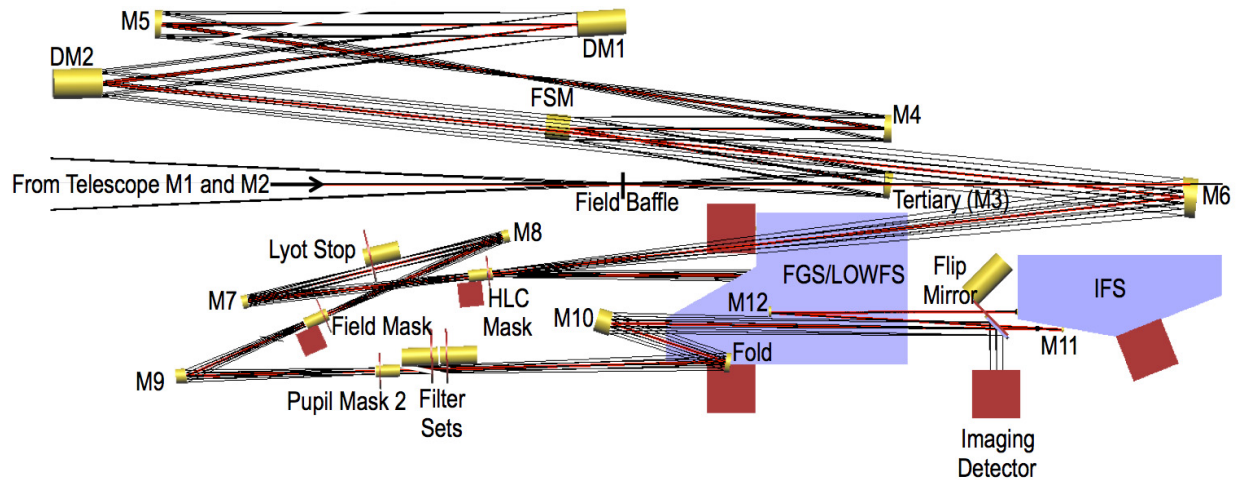
**Figure 5.5-1.** Instrument bench optical layout. The elements are distributed into two planes to provide a compact package, so there are no interferences between elements and light paths even where apparently conflicting in the figure.

8. Collimating mirror M7, which forms a pupil image for
9. Lyot stop*
10. Focusing mirror M8 which creates an intermediate focus at
11. Field Mask, followed by
12. Recollimating mirror M9, which creates a reimaged pupil for
13. Pupil mask position 2, followed by
14. Filter sets*, then through a fold and
15. Focusing mirror M10, creating an f/68.8 image through
16. Flip mirror, which selects the incoming beam for
17. Imaging detector (flip mirror in) or
18. Integral Field spectrograph (IFS) (flip mirror out) via relay mirrors M11 and M12.

(*) Discussion of selected elements follows.

All mirrors within the instrument are either flat (FSM, DMs, fold, flip mirror) or off-axis concave paraboloids. See Appendix C.2 of the non-redacted version of this report for a list of instrument mirror parameters.

The full system optical prescription performance on-axis is 0.0001 waves rms (@ wavelength=550 nm). At 2 arcsec off-axis performance is $<\lambda/50$ waves rms, i.e., Strehl is >0.98 within the outer working angle of the coronagraph (*units comparison: typical field measure is expressed in multiples of $\lambda/D$ = 550 nm/1400 mm = 0.39 µrad = 0.081 arcsec, so 2 arcsec = 24.7 $\lambda/D$*).

### 5.5.1.1 Fine Steering Mirror

The FSM is located at the pupil image formed by the telescope. This mirror is used to stabilize the optical system line-of-sight for two purposes. First, it keeps the target star image centered on the coronagraph mask as the spacecraft attitude wanders within the limits of its control capability. Second, it minimizes the beam walk influences on wavefront error (*beamwalk: as the line-of-sight changes, the specific portion of an optical surface that light path covers varies slightly. This "walk" exposes the beam to slight changes in the surface imperfections, which subtly changes the wavefront error in the beam*). The nominal range of FSM motion to cancel the spacecraft pointing residual motion is:

- ±(s/c pointing stability)*(telescope magnification at FSM)/2
- ±(3*16 mas)* (29.17)/2=±700 milli-arcsec (3.4 µrad),

Note that the maximum stroke of the FSM is sized to be large enough to handle spacecraft pointing biases in addition to the stability. The stroke is also kept small enough to achieve a negligible angular resolution compared to

other pointing error sources. The FSM control loop achieves a control gain crossover frequency of 86 Hz. The FSM function is implemented as a 2 degree-of-freedom (DOF) stage carrying a plano fold mirror.

### 5.5.1.2   Deformable Fold Mirrors

DM1 is used to provide wavefront control in a plane conjugate to the primary mirror (pupil). One meter farther along the optical path is DM2; this distance is a compromise between the ideal 4m separation derived from Talbot length considerations and instrument packaging constraints. Simulations show that this separation between the two DM units is sufficient to provide a capability in wavefront control in both amplitude and phase domains, correcting minute wavefront errors due to fabrication and alignment inaccuracies in the system and facilitating the ability to achieve the deep $(10^{-9})$ contrast ratios for this instrument. The DM surface shape is driven by an array of actuators, 48×48 at 1 mm pitch, yielding 1800 actuators over the 48 mm beam diameter.

### 5.5.1.3   Coronagraph Mask

The collimated beam reflecting off DM2 is then brought to a focus by M6 at a focal ratio of f/30. The focused star image has a point spread function (PSF) core Airy disc diameter of 40 microns (@550 nm wavelength). The hybrid-Lyot mask element is placed at this focal plane. Since the star image size varies by wavelength due to diffraction spreading, a single mask functions best (optimum blocking with minimum inner working angle) over a limited bandwidth. Hence, multiple masks are needed to provide the best occulting efficiency (contrast) over the full wavelength range. Five overlapping bands are adequate to cover the entire science wavelength range (Table 5.5-1).

These masks are carried by a wheel mechanism, with the appropriate mask rotated into position depending on the science waveband selected for observation.

**Table 5.5-1.** Coronagraph bands. The first band is optimized for the smallest inner working angle, while the rest are optimized for the integral field spectrometer.

| Band # | Wavelength Start (nm) | Wavelength End (nm) | Bandwidth (%) |
|--------|-----------------------|---------------------|---------------|
| 1 | 450 | 500 | 10.5 |
| 2 | 495 | 605 | 20.0 |
| 3 | 585 | 715 | 20.0 |
| 4 | 700 | 860 | 19.6 |
| 5 | 820 | 1000 | 19.8 |

The hybrid-Lyot coronagraph uses a partially opaque spot to block the majority of the target star light; in our implementation, the mask is slightly tilted and the spot is made reflective. This reflected light is collected by the FGS/LOWFS, the elements of which are discussed later in this section. Assuming an eight-slot wheel implementation (guided by bench packaging considerations), this leaves three remaining slots in the wheel that can be used for instrument checkout and diagnostic functions, as well as non-coronagraphic observations. One will be "Open" (a broadband anti-reflection coated substrate the same optical thickness as the masks) that transmits virtually 100% of the light when operations are desired that do not require FGS/LOWFS feedback; another will be a broadband beamsplitter of similar construction when FGS/LOWFS operations are needed along with the non-coronagaphic. The final slot would hold a mirror that would direct 100% of the light to the FGS/LOWFS and would support a simple direct imaging mode of operation (see Table 5.5-2.)

**Table 5.5-2.** Coronagraph Mask wheel population. The three slots identified as "non-coronagraphic" function support instrument checkout and diagnostics.

| Slot | Mask | Function |
|------|------|----------|
| 1 | Band 1 | Band 1 HLC |
| 2 | Band 2 | Band 2 HLC |
| 3 | Band 3 | Band 3 HLC |
| 4 | Band 4 | Band 4 HLC |
| 5 | Band 5 | Band 5 HLC |
| 6 | Open | Non-coronagraphic, no FGS/LOWFS |
| 7 | Beamsplitter | Non-coronagraphic, w/ FGS/LOWFS |
| 8 | Mirror | Non-coronagraphic, FGS/LOWFS only |

#### 5.5.1.4   Lyot Stop

Like the mask, a single Lyot stop provides the best performance (best contrast at best transmission) over a limited wavelength range; like the mask, several Lyot stops are carried on a wheel mechanism, with the appropriate stop selected for the current observation. Keeping one slot open for non-coronagraphic functions leaves three remaining slots which will carry special diamond-shaped stops. The purpose of these apertures is to shape the pupil function so that the diffracted light from a binary companion star is directed away from the dark hole surrounding the target star. Due to the area impact implicit in the diamond shape the throughput difference between wavebands is minimal, so a single aperture is sufficient for the entire science wavelength range. However, the orientation of the diamond axis needs to be roughly aligned to the target-binary vector; three apertures clocked at 30 degrees from one to the other covers all cases such that the maximum difference in clocking angle would never be more than ±15 degrees (see Table 5.5-3).

Another field image is formed following the Lyot stop that allows the rejection of light beyond the OWA, thus keeping extraneous light from reaching the detectors and degrading performance. The OWA varies by wavelength, so a wheel is again used to carry band-specific masks. With an eight-slot wheel

**Table 5.5-3.** Lyot Stop and Field Mask wheel populations. "Diamond" stops shape the diffraction patterns for binary system observations, sized to yield acceptable performance across the full science waveband. See Table 4.3-2 for band definitions.

| Slot | Lyot Stop | Field Mask |
|------|-----------|------------|
| 1 | Band 1 and 2 Stop | Band 1and 2 OWA |
| 2 | Band 3 Stop | Band 3 OWA |
| 3 | Band 4 Stop | Band 4 OWA |
| 4 | Band 5 Stop | Band 5 OWA |
| 5 | 0° Diamond Stop | TBD |
| 6 | 30° Diamond Stop | TBD |
| 7 | 60° Diamond Stop | TBD |
| 8 | Open | Open |

implementation, several slots are available beyond those needed for the base functionality for this wheel as shown in Table 5.5-3.

Re-collimating the light following this image results in another pupil image, which may be used as a secondary Lyot stop or other optical function (see column "Pupil Mask 2" in Table 5.5-4).

**Table 5.5-4.** Filter wheel populations. Spectral functions are hosted in separate wheels from mask or polarizer functions to allow the most flexibility in observations. See Tables 4.3-1 and 4.3-2 for band definitions.

| Slot | Set 1 | Set 2 | Pupil Mask 2 |
|------|-------|-------|--------------|
| 1 | Band 2 wide | Band 1 narrow | Band 1&2 mask |
| 2 | Band 3 wide | Band 2 narrow | Band 3 mask |
| 3 | Band 4 wide | Band 3 narrow | Band 4 mask |
| 4 | Band 5 wide | Band 4 narrow | Band 5 mask |
| 5 | Blocker | Band 5 narrow | 0° Polarizer |
| 6 | $CH_4$ Continuum (835nm, 6% BW) | Pupil Imaging Lens | 45° Polarizer |
| 7 | Strong $CH_4$ (885nm, 6% BW) | $H_2O$ (940nm, 6% BW) | 90° Polarizer |
| 8 | Open | Open | Open |

#### 5.5.1.5   Filter Sets

Three wheels carry multiple filters and other elements to support the various wavebands of interest for observation. Packaging considerations permit eight slots per wheel, which gives a total of 16 slots between the two wheels "Filter Set 1" and "Filter Set 2" (labeled jointly as "Filter Sets" in Figure 5.5-1). The wheel labeled "Pupil Mask 2," primarily available for pupil-specific masks, is also utilized for filter functions. This is necessary even if open slots remained in the two dedicated filter wheels; it is important that like functions be grouped in the same wheel, and orthogonal functions be in different wheels for optimum instrument capability. One open slot is held in each wheel for times when there is no need for the use of any filter in that particular wheel.

Additional functions hosted in the wheels are a lens that creates an image of the pupil at the detector ("pupil-imaging lens"), an

opaque disk to act as a "blocker" to collect darks or for spacecraft safing, and polarizers in various orientations to permit polarimetric data collection. A proposed population of slots is provided in Table 5.5-4, where "wide" is the full 20% bandwidth and "narrow" is a 1–10% region where the reduced bandwidth potentially enables even better contrast to be achieved. Options to support more filters (larger wheels to support 10 slots instead of eight, or adding a Set 3 wheel) can be considered in subsequent work; for example, it would be valuable to add Orange Continuum/Weak $CH_4$ (650 nm, 5% BW) and Moderate Strength $CH_4$ (793 nm, 3% BW) filters to provide a fallback capability to perform additional planetary spectral characterizations if a fault should develop in the IFS.

### 5.5.2 Fine-Guidance Sensor

The FGS is part of the FGS/LOWFS module. It consists of five elements, fed by light reflecting off the coronagraph mask: an OAP collimating mirror, a beamsplitter used in transmission (while the reflection goes to share light with the LOWFS path), an OAP focusing mirror, a fine alignment mirror (mechanism),

and a detector, as illustrated in Figure 5.5-2.

Once the spacecraft has been slewed to a target star and stabilized, an acquisition process results in the star being centered on the coronagraph occulting mask, and the star light reflecting off the mask. This light is reimaged by the two FGS OAP mirrors onto the fine guidance detector; the centroid of the star image is monitored, and any motion creates an error signal that feeds back to the FSM to correct. Running in such a manner (similar to how quad cells are often used) makes the system insensitive to detector non-uniformities, optics distortion, and aberrations. However, centroiding accuracy is not perfect, still being affected by star magnitude, integration time, and the image location with respect to the pixel edges.

The image size on the FGS detector is 2/3 that on the mask, i.e., approximately 27 microns Airy diameter. Thus, for a detector with 13-micron pixels, 84% of the starlight falls in a 2-pixel diameter. Under these conditions, studies performed for this mission indicate that the necessary pointing control is achieved only when the star centroid is within 15% of a pixel corner. To ensure that happens, at hand-off from initial acquisition the fine
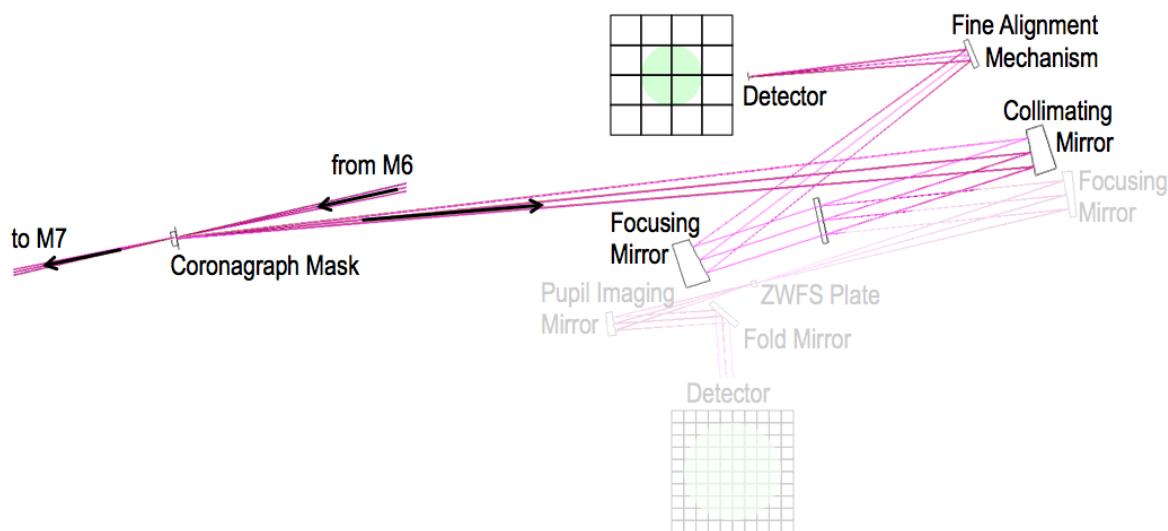


**Figure 5.5-2.** FGS portion of FGS/LOWFS module. The Fine Alignment Mechanism updates once at the beginning of the acquisition to center the star image at the intersection of four pixels; thereafter, any deviation of the image from this location is a pointing error that feeds back to the FSM for correction.
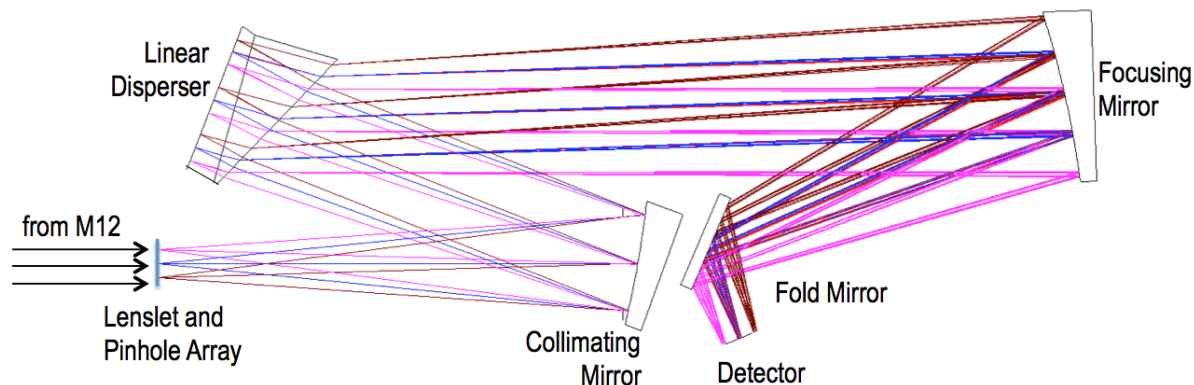
**Figure 5.5-3.** IFS module optical path. The 71×71 lenslet/pinhole arrays separate the field such that the subsequent collimator, disperser, and focuser produce a non-overlapping spectrum for every lenslet, using 4 bands to produce R=70 spectra from 495 to 1000 nm.

alignment mirror (FAM) will be adjusted to shift the image as needed to satisfy the 15% condition. The FAM is then placed in a stable "hold" state for the rest of the observation, and any image motion is corrected per above.

### 5.5.3   IFS

The IFS functions to provide spectrographic information simultaneously for every diffraction-limited resolution element within its field-of-view, including the astrophysical scene and the residual optical speckles. Following Figure 5.5-1, the image formed by M10 is relayed and magnified by mirrors M11 and M12, and then passed into the IFS module.

Figure 5.5-3 follows the optical path within the IFS module. The coronagraph field of view is sampled by a f/5 lenslet/pinhole array at a spatial pitch of 186 microns. The pinholes are located at the focus of the lenslets in an integrated assembly; the pinholes serve to field-limit as well as truncate the PSF wings in order to reduce cross-talk between adjacent lenslets. Combined with the M11/M12 relay magnification, this results in a scene sampling of two samples per PSF core (@ 500-nm wavelength). The axis of the lenslet/pinhole array is rotated compared to that of the other components, which allows for efficient sampling of the field and mapping to the detector while preventing overlapping of

spectra from adjacent samples (Foldout 5-1B and McElwain et al. 2013).

Light passed through the pinholes is collimated and enters a doublet disperser used in double pass. This disperser form creates nearly linear dispersion across the full instrument waveband, while providing the ability to control both the dispersion amount and direction. The focusing mirror has the same focal length as the collimating mirror, so the net magnification within the IFS module is 1×. By optimization of the disperser properties, taking into account detector pixel count and pitch, each pinhole of the array is imaged onto the detector with a 28-pixel long spectrum in each 20% waveband, giving double-sampled R=70 across all wavelengths. The design of the IFS collimator and focuser was constrained by the desire for maximum throughput (minimum number of surfaces) and minimum size. In doing so, the optical performance was not driven to the best possible condition. Future work should explore the trade between throughput and volume vs. optical performance (e.g., by the introduction of multi-element reflective or refractive forms in place of the OAPs shown here).

### 5.5.4   Detectors

The Exo-C instrument's science subsystems are the imager and the IFS. Each of these instruments requires its own detector. In

addition, the LOWFS and FGS employ array detectors. The requirements on these detectors are significantly varied, and in this section we discuss the status of each.

### 5.5.4.1 Requirements for the Detectors

The primary functional requirements of the detectors are summarized in Table 5.5-6.

**Table 5.5-6.** This table lists the main detector requirements for each of the four detectors.

| Requirements | Imaging | IFS | LOWFS | FGS |
|---|---|---|---|---|
| Minimal Format | 1K×1K | 1K×1K | 64×64 | 64×64 |
| Sensitive Range | 0.45–1.0 µm | 0.495–1.0 µm | 0.45–0.80 µm | 0.45–0.80 µm |
| Special Modes | 256×256 central readout | 2×2 binning support | | 50 fps readout, window track (8x8 pixels at 1000 Hz) |
| Special Features | Minimal blooming | | | |

The performance requirements of these detectors are functions of the signal-to-noise ratio (SNR) and the time available to achieve the required SNR. Besides the scene characteristics, SNR is most sensitive to the detector characteristics of quantum efficiency (QE), read noise, and dark current. Since Exo-C targets will be very dim (typically $10^{-9}$ of the host star in brightness), photon rates are exceedingly low (order 0.01 e/s or less), and it is very likely that ordinary charge coupled devices (CCDs) will have a read noise that is too high to accommodate the science needs of Exo-C. As such, electron multiplication CCDs (EMCCDs) are baselined for both Exo-C science detectors (the imager and IFS).

EMCCDs are similar to regular CCDs, except that they employ an extended multiplication register (also referred to as a gain register) with a high-voltage phase (typically around 40 V) where electrons undergo an avalanche multiplication process as they move across the stages. The probability for getting an extra electron at each stage is low (typically <2%), but the cumulative effect can be quite high. For example, a gain register with 600 stages and a single-stage

multiplication probability of 1.5% can have a gain of $(1+1.5\%)^{600}\sim=7500$. Lower voltages produce lower gain.

A drawback of EMCCDs is that the electron multiplication process is stochastic in nature, introducing its own noise. This is referred to as "excess noise factor" (ENF) in the literature, and asymptotically approaches sqrt(2) for large enough gains (>10 or so).

Detailed performance calculations (§4.7) show that an EMCCD is essential in order to keep spectroscopy integration times to reasonable values. Broader band observations with the imaging camera can tolerate higher read noise, so while it is desirable, it is not essential that the imaging camera also employ an EMCCD detector (see Table 5.5-7 for detector performance requirements).

**Table 5.5-7.** Detector performance requirements.

| Requirements | Imaging | IFS | LOWFS | FGS |
|---|---|---|---|---|
| Baseline Detector | EMCCD | EMCCD | CCD | CCD |
| QE at red | >80% | >80% | >50% | >50% |
| Read Noise | ≤1 e- | ≤0.1 e- | ≤3 e- | ≤3 e- |
| Dark Current | <0.001 e-/pix/s | <0.0005 e-/pix/s | <0.01 e-/pix/s | <0.01 e-/pix/s |
| Frame Rate | 1/300 fps | 1/10 fps (ph. ctg.) | 1/30 fps | 1000 fps |

Since the LOWFS and the FGS will be using the starlight, the requirements are very different, and other choices are more appropriate. Here CCDs can be viable, as well as scientific complementary metal–oxide–semiconductor (CMOS) sensors, among others.

These numbers and baselines are, of course, preliminary at this stage. EMCCD detectors are currently the leading choice for the WFIRST-AFTA coronagraph's imaging cameras (the imager and the IFS). Future WFIRST-AFTA detector modeling and trade studies over detector architectures will help inform our decision as to the best detectors for Exo-C.

### 5.5.5    LOWFS

#### Executive Summary

The dominant source of wavefront drift is expected to be body-pointing errors, which the pointing control architecture is designed to remove with a fast-steering mirror (FSM) in closed loop with the FGS. Low-rate higher order wavefront drift due to changing thermal loads has the potential to degrade the dark field speckle over long periods. The Low-Order Wavefront Sensor (LOWFS) is used to track these changes in WFE and guide the update of the secondary mirror position and the deformable mirror settings in between observations to maintain contrast levels of $10^{-9}$.

#### 5.5.5.1    LOWFS Introduction

The $10^{-9}$ contrast dark field produced by the coronagraph is initialized by focusing the telescope light onto the coronagraph mask via secondary positioning, and driving deformable mirrors to minimize the speckle on the imaging camera. After initialization, light from the central star will be suppressed to $10^{-9}$ contrast within the dark field and it will be held stable to $10^{-10}$ contrast for the duration of the exposure. The dominant wavefront error (WFE) sensitivities, in order of decreasing significance are focus, astigmatism, and coma. High-order Zernike modes can, however, mimic planets and are difficult to subtract in post processing. Ultimately, long-term wavefront drift needs to be controlled at the picometer level. The predicted performance of the LOWFS is presented in detail in §5.10.4. An integration time of ~60 sec is predicted to be sufficient to sense contrast drift of $10^{-10}$ on a sixth-magnitude star.

To image faint planets it is expected that single exposures will be limited by rad hit noise sources to about an hour. When longer integration times are needed, the dark field can be reinitialized between exposures and multiple exposures can be stacked to increase the signal-to-noise ratio. During the exposure (whether using the imaging camera in the discovery phase of the mission or using the IFS during the characterization phase of the mission) the speckle drift must be maintained at the $10^{-10}$ level without reference to the imaging camera readout. This stability is achieved by the thermal control design; however, over long periods there may be unacceptable drift not predicted by the models. The LOWFS can protect the integrity of the science collection in several ways. It can be used real time to trigger retuning of the dark hole in instances of excessive drift. It can be used as a post processing tool to de-rate data that does not meet the drift requirement. In addition, it can be used in closed loop with the secondary mirror or the deformable mirrors to maintain the dark field at the imaging camera and IFS.

#### 5.5.5.2    WFS Architecture

The imaging camera and the IFS are not well suited for wavefront drift measurements because the suppression of the target star means very few photons are available on these cameras. For HLC (and other) coronagraphs employing a focal-plane mask, it is most effective to pick up light from the target star at an image plane upstream of the focal-plane mask where photons are plentiful. In this design, that plane is the front surface of the coronagraph mask; a reflective occulting spot which redirects the light that otherwise would have simply been reflected to a beam dump. This simultaneously preserves maximum throughput in the science path, and maximizes light to the LOWFS. Since this approach is optimum for both the FGS and the LOWFS due to their functional similarity, the two were packaged into a common module. While line-of-sight error is sensed by the LOWFS, the line-of-sight drift is better handled by the dedicated FGS in a high bandwidth loop with an FSM in order to suppress not only the thermal drift of the optics but also body pointing errors and jitter. This division of function allows us to optimize the LOWFS for slowly varying WFE terms. Figure 5.5-5 is a
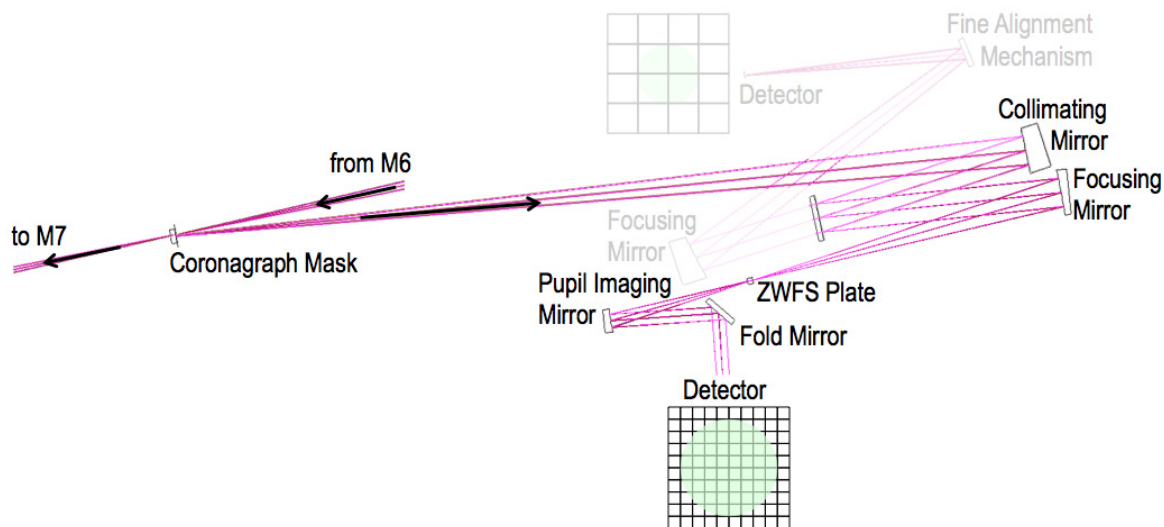
**Figure 5.5-5.** LOWFS portion of the FGS/LOWFS Module. The ZWFS plate (one of four band-specific units selected by a wheel mechanism) puts a phase shift into the core of the starlight PSF, setting up interference between the core and the wings of the PSF. Detecting the interference at a pupil image provides detailed information about the wavefront aberrations.

layout of a LOWFS and its relation to the FGS and the coronagraph mask.

To sense WFE beyond the tip tilt and focus terms, it is necessary to sample the wings of the central star's PSF. In the implementation of the Zernike Wavefront Sensor (ZWFS) in the LOWFS shown in Figure 5.5-5, the ZWFS maps the WFE of all optics upstream of the coronagraph mask. Since the role of the LOWFS is simply maintenance, a reference image is stored just after the dark hole is generated and deviations from the reference image are interpreted as wavefront drift. In this way, the LOWFS is insensitive to calibration errors.

### 5.5.5.3    WFE Drift Requirements

The WFE drift requirements are derived from the residual speckle stability requirement of $10^{-10}$ contrast drift over 48 hours. Modeling of the Exo-C configuration converted the contrast stability requirements into WFE drift requirements broken down into Zernike components and weighted by the impact each Zernike term has on planet detection. Studies showed that the allowable WFE is a few pm rms with low-order Zernike terms dominating the WFE drift budget. Models of the Exo-C design indicate that the benign earth trailing orbit in combination with careful mechanical and thermal design reduce the WFE drift rate to manageable levels.

### 5.5.5.4    LOWFS Conclusion

Wavefront drift has the potential to degrade the dark field over long periods. Wavefront sensing of light from the target star provides update information for the secondary and the deformable mirrors, which can mitigate the detrimental effects of the thermal drift. Further, the LOWFS data tracking the time-varying evolution of the wavefront can be utilized in post-processing to enhance the science data analysis. The hardware architecture is compatible with implementing a real-time control loop between the LOWFS and the actuators on the secondary and DMs. Testbed activities supporting coronagraph technologies include a study of the practicality of such an approach; if the results are favorable, the concept can be readily implemented in this design.

### 5.5.6    Field Layout

The science imager has a 0.7×0.7 arcmin field-of-view (FOV) which gives a high probability that the target star will be acquired after spacecraft pointing maneuvers (for a maximum 30-arcsec uncertainty between star tracker and

instrument lines-of-sight). While the FGS has a comparable field-of-regard, its acquisition is achieved by scanning its much narrower FOV via a mechanism; with the instrument FOV supporting initial acquisition, a more efficient timeline is supported.

The portion of the FOV required for science operations is significantly smaller than the total instrument capability; the nominal outer working angle (OWA) within which sufficient starlight suppression occurs is 3.2 arcsec (radial), equivalent to ~8 percent of the instrument FOV.

Figure 5.5-6 illustrates how the imaging detector maps to the FOV, and how the central zone is sampled by the 1 K×1 K detector. It is significant to note that the PSF core (one Airy disc diameter) covers an area of 5×5 pixels, which provides for subpixel centroiding of targets, supporting the ability to determine orbital parameters.

## 5.6    Thermal

### 5.6.1    Telescope

The purpose of the payload thermal control system is to maintain temperatures within limits to enable science performance and hardware safety. To meet science objectives, the thermal

control system needs to drive thermo-elastic distortions down to acceptable levels within acceptable time periods. This is accomplished by minimizing the effect of thermal disturbances, both environmental and bus-based, while also applying active temperature control through a cold-bias/heater system.

The heliocentric, Earth-trailing orbit baselined for Exo-C is associated with extremely small planetary-based thermal loads, and the thermal design focuses on minimizing disturbances from varying incident solar loads. As shown in Figure 5.6-1, this is accomplished with a flat solar panel design that serves as a solar radiation shield for the optical barrel assembly (OBA). The solar panel assembly is mounted directly to the spacecraft bus, isolating it mechanically and thermally from the telescope and instrument. To minimize radiative heat transfer between the solar panel and OBA, the backside of the solar panel is covered with multi-layer insulation (MLI).

The OBA serves as the secondary mirror metering structure. It is actively temperature controlled to maintain its dimensional stability and to provide a more constant temperature environment for the primary and secondary mirror surfaces, when subjected to varying
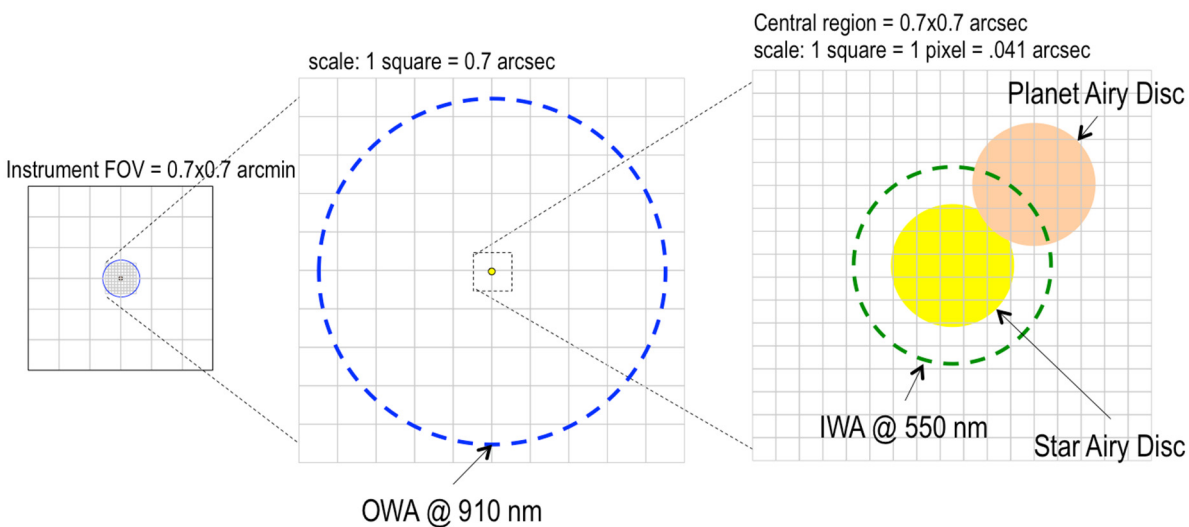


**Figure 5.5-6.** Instrument field-of-view mapping to the detector. The OWA is illustrated at a wavelength of 910 nm, while the IWA and Airy disks are illustrated at a wavelength of 550 nm. Note that the Airy disc diameter of a point source spans 5 pixels in the shortest wavelength band.

solar incidence angles. Atop the OBA is a scarfed solar shield to allow pointing to as close as 45º of the Sun. The OBA and scarf are covered with MLI to minimize the impact of varying solar loads and also to keep temperatures low when exposed to direct sunlight.

The primary and secondary mirror temperatures are controlled through active radiative heating to reduce wavefront drift errors and to achieve settling times of a few hours. All heater controllers, including those on the OBA, are single-input/single-output with proportional-integral-differential (PID) compensation at a bandwidth of 0.2 Hz. The set-point temperature for each control zone is summarized in Table 5.6-1. The instrument bench will run at room temperature. Heat dissipated from the bench electronics is transported to a pair of radiators via

**Table 5.6-1.** Telescope heater power analysis. The required heater power depends strongly on the set-point temperatures.

| Telescope Heater Locations | # of Heaters | Set point (K) | Peak Power (W) |
|---|---|---|---|
| Primary Support Structure | 3 | 200 | 118 |
| Lower Barrel | 18 | 190 | 63 |
| Upper Barrel | 11 | 170 | 56 |
| Barrel Scarf | 8 | 150 | 111 |
| Primary Mirror | 6 | 240 | 33 |
| Primary Mirror Bipods | 6 | 240 | 5 |
| Secondary Mirror | 2 | 240 | 1 |
| Total | 60 | - | 387 |
| Total with 30% cont. | | | 503 |

constant conductance heat pipes. The detectors are sufficiently close to the radiators such that a solid-state link is used to transport waste heat.

Figures 5.6-3 through 5.6-5 illustrate the active thermal control zones of the telescope.

The heater power required for the telescope was calculated by first determining the observing scenario that minimizes solar loading, which occurs at a pitch of 45º and a roll of 15º away from normal to the Sun. Then, a science observation was simulated for 24 hours, and the power draw for the telescope was calculated to be 387 W. The power required of each control zone is tabulated in Table 5.6-1. This analysis only considers the telescope heater power, and does not consider power to the spacecraft or instrument. Telescope heater power depends strongly on the set-point temperatures. The telescope heater power only varies ~15 W between the cases of minimum and maximum solar loading, due to the solar shield and MLI blankets.

The thermal temporal response of the telescope to a 30º pitch maneuver is shown in Figure 5.6-2. The telescope reaches thermal equilibrium quickly, in a little over 1 hour, enabling science observations to resume promptly after communication downlinks and slews between science targets.

One important lesson learned from Kepler is that spacecraft thermal disturbances can degrade telescope performance. To minimize



**Figure 5.6-1.** The Exo-C observatory thermal model. The model includes the spacecraft bus, telescope (including the vibration isolation system), an instrument bench, and a flat solar panel that also serves as a sun-shield. The spacecraft and instrument bench are modeled as constant temperature boundary conditions, and the stability of the telescope was simulated over varying sun angles.

**Figure 5.6-2.** Thermal settling time of representative points on the solar array and telescope optical barrel in response to a 30° pitch maneuver. The solar panel temperature decreases approximately 7 Kelvin with the change in solar load, while the active thermally controlled optical barrel decreases less than 1 milliKelvin. The primary mirror, not plotted above, also decreases less than 1 milliKelvin.



**Figure 5.6-3.** Twenty nine thermal control zones are baselined for the optical barrel assembly and eight for the scarfed Sun shield. The optical barrel assembly is thermally isolated from the primary support structure.
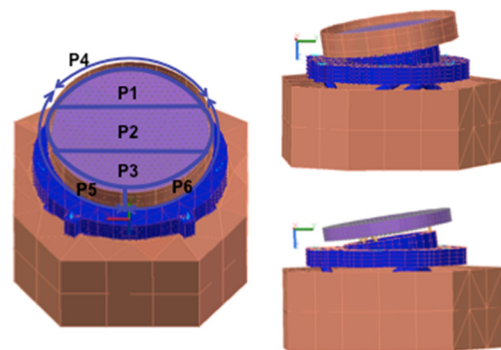


**Figure 5.6-4.** The primary mirror is precision controlled to maintain milli-Kelvin stability when subjected to changing solar incidence angles. The six control zones enable settling times less than a few hours. Note that all heaters are mounted to a heater shroud that is radiatively coupled to the back and outer diameter of the low CTE primary mirror. The figure at the lower right shows the primary mirror with the heater shroud removed.

the impact of spacecraft disturbances on the Exo-C telescope performance, heaters are placed at strategic locations between the spacecraft and telescope. A heater is placed on each isolator strut (6), where each isolator pair connects to the primary support structure (PSS) (3), and at each fixture between the PSS and optical barrel (6). A spacecraft bus disturbance of 1 degree with a 4 hour period (square wave) was simulated and shown to have negligible impact on telescope performance. All telescope performance modeling is presented in §5.10.

## 5.7 Pointing Control

### 5.7.1 Introduction

A small inner working angle (IWA) on a coronagraph is only useful if the image of the star can be centered on the coronagraph mask

**Figure 5.6-5.** The secondary mirror is controlled through radiative heating from a cylindrical shroud with one zone on the back surface of the low CTE glass, and one zone along the circumference.

to within a few percent of the IWA and maintained there over the entire exposure. While the pointing accuracy and stability is challenging for the Exo-C coronagraph, the techniques for achieving the required accuracy and stability have flight heritage. Simulations show that achieving the pointing requirements is feasible with this proven architecture. Pointing performance for additional astrophysics measurements is also briefly analyzed.

### 5.7.2    Pointing Architecture and Heritage

A review of the state-of-the-art in pointing technology for relevant space observatories, Spitzer (Bayard et al. 2004), Kepler (Koch et al. 2004), and Hubble (Sharkey et al. 1992), and recent coronagraph studies, WFIRST-AFTA (Spergel et al. 2013), and the Extrasolar Planetary Imaging Coronagraph, EPIC, (Champin et al., 2009), was performed, leading to a flight-proven pointing architecture that builds upon previous experience. It employs a two-stage pointing architecture with telescope pointing achieved by the spacecraft attitude control system (ACS) while precision pointing and jitter rejection is achieved with a fast-steering mirror (FSM) in the payload.

The key features of this architecture are:

- **Fine guidance sensor (FGS).** The FGS, located in a telescope focal plane, provides high-rate pointing

measurements with respect to the science target star.

- **Fast-steering mirror (FSM).** A high-bandwidth FSM compensates for residual spacecraft pointing errors and keeps the science target star centered on the coronagraph.

- **Earth-trailing orbit.** As demonstrated by Spitzer and Kepler, an Earth-trailing orbit provides a stable environment, where the only exogenous disturbance is the solar flux. This orbit selection mitigates pointing disturbances associated with eclipse-induced thermomechanical snap, gravity gradient, magnetic field, and aerodynamic drag associated with an Earth orbit.

- **Observatory structural design.** The spacecraft structural design is as rigid as possible to eliminate control-structure interactions (CSI) between the control loop and the vibration modes of the structure. It does not have any deployable or articulated structures. For example, the telescope cover is ejected upon reaching orbit. A preliminary rendering of the Exo-C observatory is shown in Foldout 5-1.

- **Passive isolation.** Passive isolators at the reaction wheels and at the payload-to-spacecraft interface mitigate the effect of high-frequency reaction wheel disturbances.

- **Enhanced spacecraft ACS.** The spacecraft ACS is enhanced with a fine guidance signal from the instrument that provides precise pointing information derived from the coronagraphic instrument.

Figure 5.7-1 shows the pointing control system diagram for this architecture. The diagram depicts the two-stage pointing architecture of the spacecraft ACS and the payload pointing system.
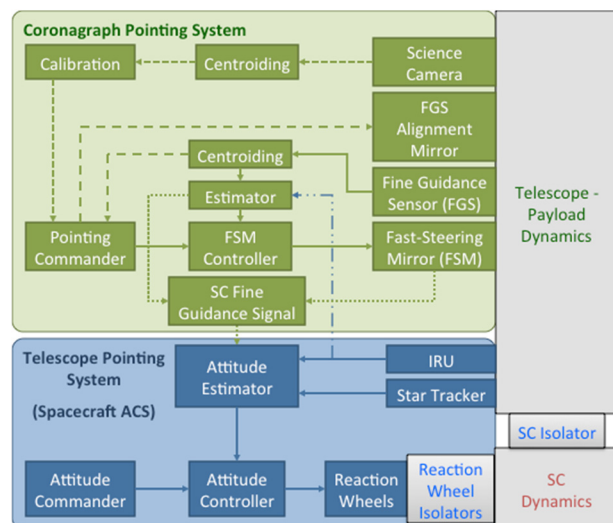
**Figure 5.7-1.** Control system diagram showing the two-stage payload pointing system and spacecraft attitude control system. Individual reaction wheel isolators and the spacecraft isolator mitigate the effect of internal spacecraft disturbances on the payload pointing.

The spacecraft ACS (shown in blue in Figure 5.7-1) is a three-axis attitude stabilization system. Star trackers and an inertial reference unit (IRU) are mounted on the payload side to sense the payload attitude. As was done in Hubble and Kepler, the FGS from the payload is combined with these measurements to greatly improve the attitude estimate. An attitude controller then computes the torque required to regulate the spacecraft to the desired attitude. These torques are then allocated to the reaction wheels. These reaction wheels are mounted on passive isolation to reduce high-frequency disturbances generated by the spinning wheels. A second isolator between the spacecraft and payload further isolates the reaction wheels from the payload. The passive isolators have isolation frequencies in the range of 0.5−5 Hz to provide the desired isolation. The isolators have launch locks as indicated in §5.11. The ACS also includes a propulsion system that is used for momentum desaturation (not shown in the block diagram).

The coronagraph pointing system is shown in green in Figure 5.7-1. The control loop consists of the FGS, centroiding, estimator, FSM controller, and FSM. The FGS outputs a small, windowed image of the target star that is then centroided. This centroid can optionally be combined with IRU measurements in an estimator. A controller then computes the FSM angles to null the payload pointing error.

This pointing control loop relies on the performance of the FGS to output window images (8×8 pixel) of the target star at a fast rate (1000 Hz). To achieve this performance, an FGS alignment mirror is used to align the center of the target guide star to within 15% of the crosshairs of four pixels as proposed in the ACCESS study (Trauger et al. 2009). Note that this FGS alignment mirror only affects the FGS pointing. This allows the target star to be appropriately positioned on the FGS without affecting the pointing of other instruments.

To ensure the FSM control results in the target star being centered on the coronagraph, the science camera is also used to infrequently calibrate the payload pointing. The "punctured disk" from the science camera is centroided, which provides a measurement of the offset of the target star with respect to the coronagraph. This offset is used by the pointing commander to correct the FSM control set point.

The proposed pointing architecture leverages flight-proven technology and lessons learned from seven previous missions notably Kepler, Spitzer, and Hubble. Table 5.7-1 summarizes this heritage.

### 5.7.3   Pointing Requirements

Coronagraphic missions call for high-precision pointing to mitigate contrast degradation due to errors in centering the coronagraphic instrument on the target star and errors due to beamwalk on the optics ahead of the FSM.

The proposed pointing requirements per axis, shown in Table 5.7-2, come from a detailed analysis of the degradation of science measurements in the presence of jitter. The pointing error budget allocations are derived from analysis of pointing performance from Kepler, Spitzer, and Hubble, and from bounding models of the isolators and FSM pointing loop.

**Table 5.7-1.** Flight heritage of the Exo-C pointing control system. IRIS (De Pontieu et al. 2014), PICTURE (Mendillo et al. 2012), Kepler (Koch et al. 2004), Spitzer (Bayard et al. 2004), Chandra (Weisskopf et al. 2003), Hubble (Sharkey et al. 1992), and TRACE (Handy et al. 1998).

| Key Features of the Pointing System | Exo-C | IRIS SmEx (2013) | PICTURE Sounding Rocket (2011) | Kepler Discovery (2009) | Spitzer (2003) | Chandra (1999) | Hubble (1990) | TRACE SmEx (1990) |
|---|---|---|---|---|---|---|---|---|
| Fine-guidance sensor (FGS) | X | X | X | X | X | X | X | X |
| High-bandwidth fast-steering mirror (FSM) | X | X | X | | | | | X |
| Enhanced attitude control system (ACS) using FGS | X | X | | X | | X | X | X |
| Passive isolation | X | | | | | X | X | |
| Low-disturbance Earth-trailing orbit | X | | | X | X | | | |
| High-stiffness observatory (no deployables/articulations) | X | | | X | X | | | |

In this context, pointing accuracy is defined as the expected value of the mean pointing error within the 1000-second window. Pointing stability is defined as the expected value of the pointing error variance within the 1000-second window.

The telescope pointing error stability requirement (Table 5.7-2) has a power spectral density (PSD) bound associated with it (Figure 5.7-2). This PSD bound is very similar to Kepler's flight performance with a steeper rolloff achieved by the use of reaction wheel and spacecraft isolators. Note that the area under the

PSD corresponds to the 16-milliarcsec RMS requirement for tip/tilt telescope stability.

Error budgets for the pointing stability requirements are shown in Figures 5.7-3 and 5.7-4. These error budgets allocate 75% and 55% to margin against the requirements. Then, they flow allocations to pointing knowledge and control errors. These allocations are further suballocated to the key elements (sensors, actuators, isolators, and algorithms) of the pointing system.

**Table 5.7-2.** Accuracy and stability requirements (RMS per axis) for the telescope and coronagraph pointing to meet the science objectives of Exo-C.

| Pointing Requirements | |
|---|---|
| Telescope Pointing (Angle in the sky, RMS per axis) | |
| Accuracy | 2 milliarcsec (Line-of-sight tip/tilt) |
| | 10 arcsec (Line-of-sight roll) |
| Stability (1000s) | 16 milliarcsec (Line-of-sight tip/tilt) |
| | 10 arcsec (Line-of-sight roll) |
| Coronagraph Pointing (Angle in the sky, RMS per axis): | |
| Accuracy | 0.2 milliarcsec (Line-of-sight tip/tilt) |
| Stability (1000s) | 0.8 milliarcsec (Line-of-sight tip/tilt) |

### 5.7.4  Pointing Simulation and Results

A time-domain simulation was developed to generate a current best estimate (CBE) of the achievable pointing stability. This can then be compared against the error budget and requirements. Figure 5.7-5 shows a block diagram of this simulation. Note that this simulation focuses on the inner payload
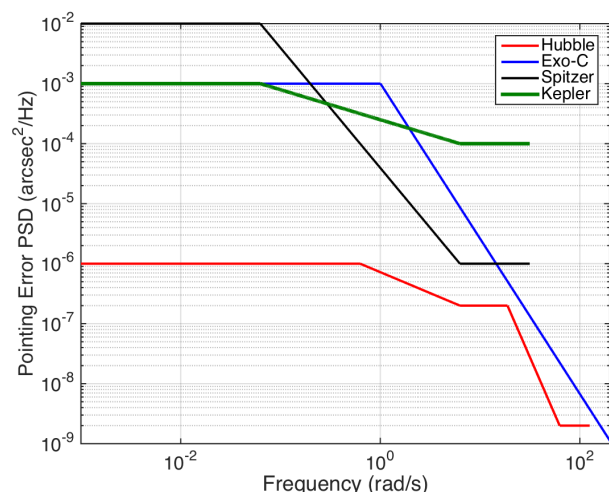


**Figure 5.7-2.** Comparison of the telescope line-of-sight (tip/tilt) PSD bound of Exo-C versus Kepler, Spitzer, and Hubble. The required performance of Exo-C is very similar to that of Kepler at low frequencies. At high frequencies, it exceeds Kepler by using dual vibration isolators (which Kepler does not have).
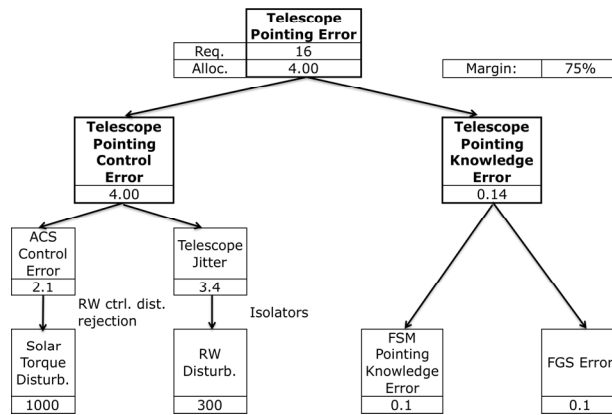
**Figure 5.7-3.** Telescope pointing stability error budget (per axis). Allocations show a margin of 75% versus the requirement.
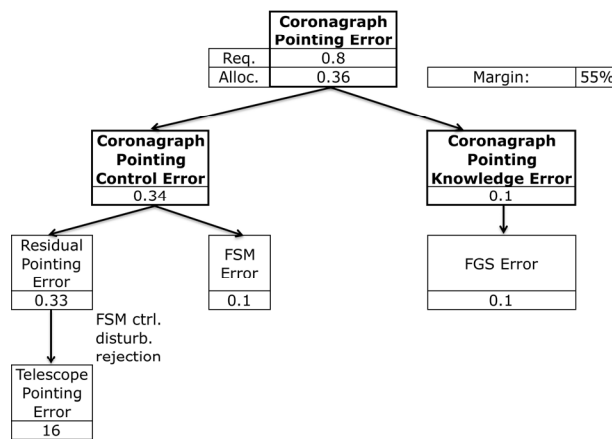


**Figure 5.7-4.** Coronagraph pointing stability error budget (per axis). Allocations show a margin of 55% versus the requirement.



**Figure 5.7-5.** Pointing simulation block diagram showing the four main models (telescope pointing, FGS + centroiding, FSM, and FSM controller) and the three main noise sources (telescope pointing, FGS noise, and FSM noise).

pointing through the optical sensitivity matrices. This flexible-body motion is combined with the rigid-body motion to create pointing errors with a PSD that approximates the telescope pointing PSD bound shown in Figure 5.7-2.

A combined FGS and centroiding model generates noisy target star centroid measurements at the desired rate. For a target star magnitude of 7.5, the FGS operates in window track mode at 1000 Hz. A centroid noise of 0.1 mas RMS can be achieved when the target star is centered to within 15% of the crosshairs of four pixels with the fine alignment mirror as shown in the ACCESS study (Trauger et al. 2009).

The FSM is modeled as a lightly damped system with a resonance appropriate for the expected mirror mass. The reaction torque produced by the FSM acceleration is used to excite the flexible-body model to determine the effect the FSM movements have on the coronagraph pointing. Broadband FSM noise is also injected into the system. The FSM controller is simply a proportional-integral (PI) controller. A time delay model captures the expected transport and software processing time delays.

A linear system analysis was used to tune the PI controller gains and evaluate the stability margins of the closed-loop system. A gain margin (GM) of 6.3 dB and phase margin (PM) of 71.6° was achieved with the

pointing control loop. The outer spacecraft attitude control loop and residual telescope pointing errors are modeled as representative exogenous disturbances acting on the payload pointing control system. A brief description of the four main models in this block diagram will be provided.

The telescope-pointing model simulates the pointing of the telescope through the use of a shaping filter that generates angular accelerations. These accelerations are used to excite the flexible body dynamics model of the spacecraft, generated by a finite-element model, and determine the resulting telescope

selected gains, which meet JPL design principles (GM >6 dB, PM >30°). With the controller running at 1000 Hz, the gain crossover frequency is 86 Hz.

The nonlinear, time-domain simulation was then used to predict the coronagraph pointing performance. Figure 5.7-6 shows, for the tip axis, the telescope pointing PSD, coronagraph pointing PSD, and the contributions to the coronagraph pointing PSD. It also shows the cumulative mean-square value (MSV), which exhibits large increases at frequencies with a large contribution to overall pointing error. Overall pointing performance was predicted to be 0.27 mas and 0.24 mas RMS in the tip and tilt axes, respectively. This meets the requirement of 0.8 mas with approximately 70% margin. It should also be noted that FSM-induced disturbance torques are small and do not excite the structural flexible-body dynamics. From this analysis, it was concluded that momentum compensation is not needed on the FSM at this time.
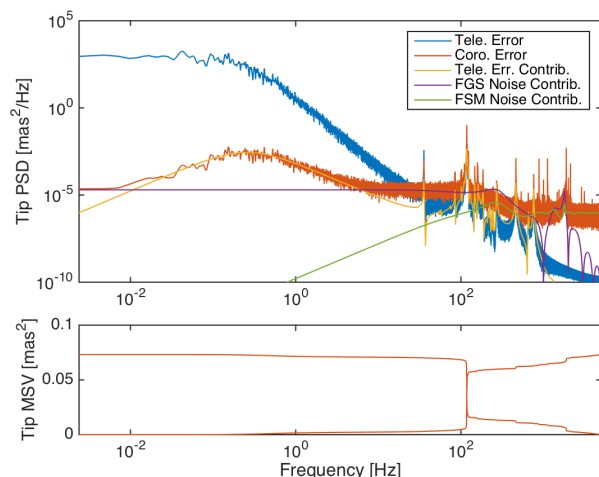


**Figure 5.7-6.** Pointing error PSD and MSV plots for the nominal target star magnitude. The CBE meets the requirement with 70% margin.

### 5.7.5    *Pointing without Bright Star Reference*

To perform more general astrophysics measurements, the payload may need to point in a direction without a bright star as a reference. This section will analyze two scenarios. The first is pointing at dimmer

science target stars and the second is pointing without a reference star.

For dimmer science target stars, the simulation was modified to assess the pointing performance. The performance is expected to degrade since there are fewer photons for the FGS. This has two potential, negative effects: it can increase the noise on the centroid measurements and the integration time may need to be increased thereby reducing the rate of the FGS. The first four columns of Table 5.7-3 show the FGS parameters selected for this study.

**Table 5.7-3.** Predicted pointing performance for various star magnitudes. The first row shows the nominal star magnitude case and the subsequent rows show the dimmer star magnitudes.

| Case | Targ. Star Mag. | FGS Samp. Rate | FGS RMS Noise | CBE RMS Tip Pnt. Stab. | CBE RMS Tilt Pnt. Stab. |
|---|---|---|---|---|---|
| 1 | 7.5 | 1000 Hz | 0.1 mas | 0.27 mas | 0.24 mas |
| 2 | 10 | 100 Hz | 0.1 mas | 0.52 mas | 0.51 mas |
| 3 | 12.5 | 100 Hz | 1 mas | 0.82 mas | 0.81 mas |
| 4 | 15 | 10 Hz | 1 mas | 4.3 mas | 4.3 mas |

Note that for every 2.5 star magnitudes, the flux decreases by a factor of 10. Therefore, to keep the same number of photons per image, the FGS sampling rate must be decreased by a factor of 10. If the sampling rate is decreased, the controller gains must also be decreased to maintain stability as well as gain and phase margins. This causes a subsequent order of magnitude reduction in controller bandwidth, allowing more telescope pointing errors to pass through the payload pointing control loop.

Table 5.7-3 summarizes the pointing assessment for dim star observations. The first row shows the pointing performance for the nominal target star magnitude. The subsequent rows show the performance for dimmer stars for different cases of FGS sampling rate and centroid noise. As expected the performance degrades for dimmer stars. Note that there is a large decrease in performance for 15th magnitude stars. This is due to the large reduction in controller bandwidth letting

significant amounts of low-frequency telescope pointing errors (shown in Figure 5.7-6) through.

Without any target star, the performance degrades even further. The entire payload pointing control loop cannot be used since the FGS does not have a star to image. The spacecraft, therefore, must rely on the ACS loop alone. This loop is no longer augmented with the FGS and must only use the star trackers and IRU. With these changes, it is expected that the pointing performance will be on the order of 100 mas RMS.

If higher performance is required, there are a few options to improve the pointing performance. One option is to use more expensive star trackers and IRU to improve the ACS estimation. Other options include using the FGS to guide off of nearby objects or extended objects (e.g., Jupiter). Further work is required to determine the pointing performance for these additional science cases.

## 5.8    Electrical Configuration

The Exo-C payload electronics are distributed into three separate electronics boxes: the Payload Processing Electronics (PPE), telescope Thermal Control Electronics (TCE) and Instrument Control Electronics (ICE). The PPE is the brains of the instrument, providing the processing power and commands to control the instrument thermal and mechanical drivers, as well as bringing in and processing data taken from the sensors. The TCE and ICE house the thermal and mechanical sensors and drivers. These units take in commands from the PPE via a 1553 interface and perform the necessary functions required to control the instrument and telescope.

The PPE contains one backplane and seven different circuit boards. The Processor board provides the interface to the spacecraft electronics and performs all the processing needs of the instrument, including any compression, analysis and sequencing for the instrument. Interface boards and memory are

included in the PPE. The PPE provides the necessary interfaces and data for the other electronics boxes.

The TCE and ICE contain the necessary drivers to control the telescope and the instrument respectively. The TCE contains a number of thermal control electronic boards for each thermal zone of the telescope. This allows for customizable control of the thermal environment throughout the telescope.

The ICE provides the thermal control of the instrument starting from the secondary onward as well as the mechanical driver boards that control the instrument's filter wheels. The separation of the instrument and telescope functions enables a modular approach to developing, integrating, and testing the instrument and telescope.

## 5.9    Interfaces

The Exo-C telescope and instrument are designed to be as isolated from the spacecraft as possible. The only interfaces to the telescope lie within the mechanical isolators that mount the telescope to the spacecraft and the 1553 communications and the electrical interface providing the instrument with power, commanding and transmitting processed data. The entire payload has been designed to be thermally isolated from the spacecraft bus.

### 5.9.1    Isolators

The mechanical isolators consist of six isolators that mount to the base of the telescope attaching to the spacecraft bus. These isolators are responsible for dampening out any vibration induced by the spacecraft during science observations.

### 5.9.2    Electrical

An electrical interface will go across the isolator, between the instrument and spacecraft. It will carry power and command information to the instrument and return processed data for down-link back to the spacecraft.

### 5.9.3 Thermal

To minimize the impact of spacecraft thermal disturbances on the telescope, active thermal control is implemented on each mechanical isolator, and also at the base of the telescope where each isolator is attached.

## 5.10 Payload Structural Thermal Optical Performance Modeling

### 5.10.1 Overview

This section highlights the results of integrated Structural, Thermal, and Optical Performance (STOP) modeling of the Exo-C Instrument Payload. Figure 5.10-1 illustrates the component models and their relationships to the STOP model.

As shown in Figure 5.10-2, detailed finite element models (FEMs) were developed to analyze structural deformations of the optical barrel (OB), the PSS, the primary mirror (PM), and the primary mirror bipods (PMB). The effects of spacecraft thermal disturbances, pitch and roll, quasi-static WFE are computed as a function of time. The WFE is broken down into Zernike aberrations and finally into changes in the field contrast. The aberrations modeled here include effects from thermal-mechanical deformations of the structure and figure deformations of the PM, as well as structural dynamics due to spacecraft bus disturbances. The pointing and control models are covered in §5.7.

### 5.10.2 Coronagraph Dynamic Performance

Figure 5.10-3 shows the contrast of the Exo-C baseline Hybrid Lyot Coronagraph. The telescope optics and coronagraph are modeled in PROPER. The reaction wheel disturbances were simulated in the structural model to predict the rigid body displacements of the PM, SM and optic bench. The analysis includes wavefront jitter due to rigid body displacements of the front end optics as well as tip/tilt errors outside the control authority of the FSM. There is only modest degradation of
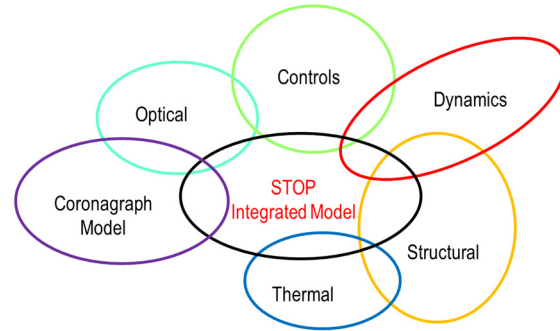


**Figure 5.10-1.** STOP modeling integrates results from six modeling tools to produce the performance predictions. For example, MACOS produces optical sensitivities for rigid body displacement of the optics which are then combined with structural displacements to produce wavefront error due to environmental disturbances. The wavefront error is then combined with sensitivities produced by the coronagraph model (PROPER) to predict the impact on the contrast of the imaged planetary system.
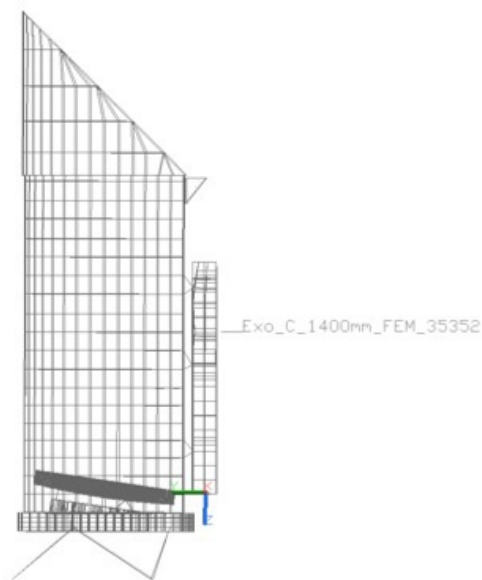


**Figure 5.10-2.** The performance is assessed with finite-element models which capture thermally induced deformations as well as the dynamic response to disturbances originating in the SC and from the FSM.

the contrast at the IWA from twice the current best estimate of the reaction wheel disturbance.

### 5.10.3 Thermal Drift

The system quasi-static performance is analyzed for the two maneuvers that most affect the science return: pitch relative to the orbital plane and roll around the boresight.
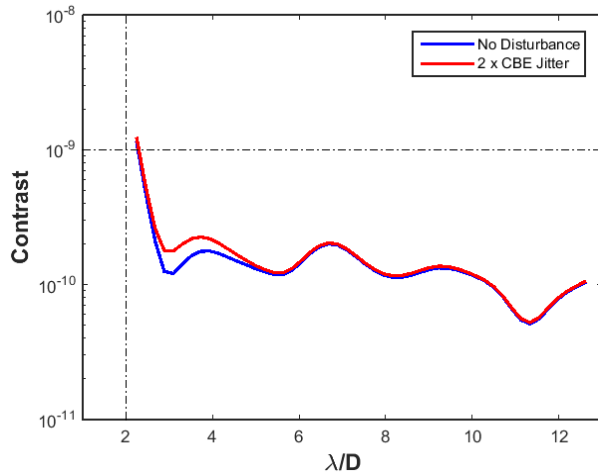
**Figure 5.10-3.** The blue line is the contrast as a function of field angle for the baseline HLC, neglecting drift and dynamic disturbances. The red line shows the modest degradation of the contrast at twice the current best estimate for the reaction wheel disturbance. The jitter results are based on the dynamic response to disturbances at the base of the isolator struts. The input is modeled as white noise passed through a shaping filter simulating the reaction wheel disturbance. The jitter is broken into two components: line of sight residual jitter (not corrected by the FSM) and higher order Zernike terms beyond tip/tilt.

The pitch maneuver is executed when changing targets. Exo-C is designed to operate over β angles from 50° to 130°. The resulting solar load can vary by as much as 3 kW for an extreme pitch maneuver. The challenge is to maintain the dark-hole solution after a pitch maneuver and to minimize the duration of the thermal transient in order to maximize observational efficiency. A 30° pitch maneuver was simulated where the sun is initially along the normal to the plane of the sunshade (θ=0°, β=90°) and the spacecraft is pitched away from the sun. The maneuver is completed in ½ hour (30 time steps in the thermal model). Because we employ a flat sunshade, the magnitude of the distortions are, to first order, proportional to the change in solar flux incident on the sunshade. Any other maneuver can be evaluated by scaling it by the ratio of the change in the solar flux to the change in the solar flux of this representative 30° pitch:

$$Z_n^m{}_{(\Delta\theta)} = \frac{\Delta Q_{(\Delta\theta)}}{\Delta Q_{(30°)}} Z_n^m{}_{(30°)} \quad \text{(Eq.5.10.1)}$$

where $Z_n^m$ are the Zernike coefficients and $\Delta Q$ is the change in heat flux due to a change in the solar incident angle, $\Delta\theta$. Because the sunshade is flat, this result holds for both pitch and roll maneuvers. The residual low-order Zernike terms (after the LOS tip/tilt is removed by the FSM) for the 30° pitch maneuver are plotted in Figure 5.10-4. The resulting contrast drift is presented in Figure 5.10-5. The model indicates that once the $10^{-9}$ contrast is achieved, it is robust to even large maneuvers and slewing from one target to another should not require retuning the dark hole. This highly stable performance makes it possible to tune the dark hole on a bright calibration star and slew to a much dimmer target for the science collect, saving many hours of integration time needed to dig a dark hole on a dim star.

When a dark hole is generated by the coronagraph, a residual static speckle field is inevitably produced. The speckles result from interference of coherent light from the central star. At the limits of detectability, a speckle is indistinguishable from a planet with a single exposure. The baseline technique to overcome the speckle limitation is to take advantage of the static nature of the speckle field by rolling the observatory 30° and taking a second exposure. The speckles in the second exposure remain static on the focal plane while a planet is displaced azimuthally by 30°. Simple subtraction of the two images reveals a planet that was otherwise hidden in the speckles. The magnitude of the roll is chosen to prevent overlap of the planet's PSF at the inner working angle of the coronagraph. Key to the success of this technique is thermal stability of the observatory in order to ensure that the changing solar load does not alter the speckle field.

The flat sunshade is designed specifically to minimize drift of the background speckles due to the roll maneuver. The exposure pairs are taken with the observatory rotating between +15° and −15° of the sun. In this way, the solar flux incident on the flat sunshade is
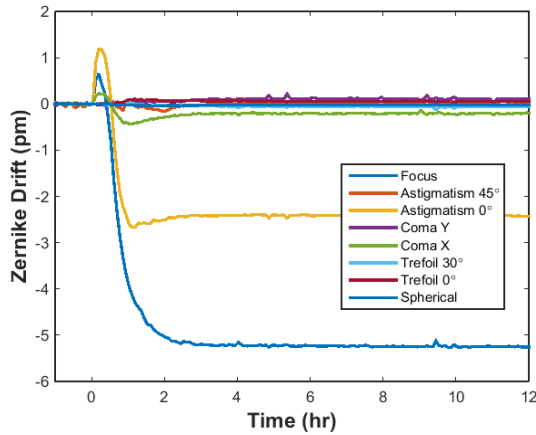
**Figure 5.10-4.** The Zernike decomposition of the WFE due to a pitch maneuver. At time = 0, a 30° pitch maneuver was simulated and the resulting drift in the dominant Zernike terms over 12 hours was calculated. The relatively large focus and astigmatism terms are due to displacement of the SM.
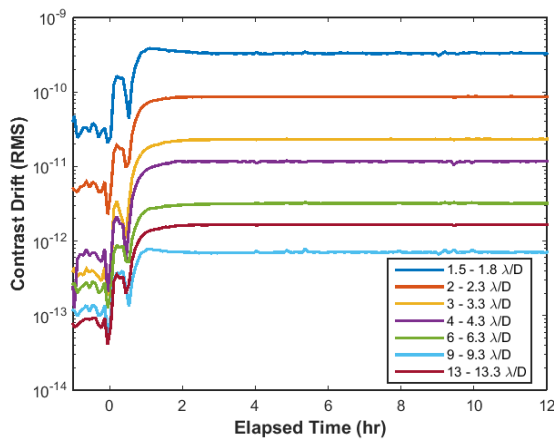


**Figure 5.10-5.** RMS HLC contrast drift at six different radial zones. At time = 0, a 30° pitch maneuver was simulated and the resulting drift in the contrast over the next 12 hours was calculated. Even at the 2 λ/D IWA, the drift never exceeds 2×10$^{-10}$ so immediately upon completing the pitch maneuver, Exo-C is ready to begin taking science data on the next target.

the same before and after the roll, minimizing the thermal disturbance on the instrument. The solar load is maximum at the midpoint of the roll. By executing a fast 15-minute roll (15 steps in the thermal model time sequence), the transients are minimized. The resulting contrast drift is held well below the requirement of $10^{-10}$ even at the $2\lambda/D$ inner working angle. Utilizing this technique, the observatory becomes an ultra-stable

instrument for planet detection (see Figures 5.10-6 and 5.10-7).

In the quiescent state, the solar load varies very slowly as the spacecraft orbits the Sun. From the analysis of the pitch maneuver, we
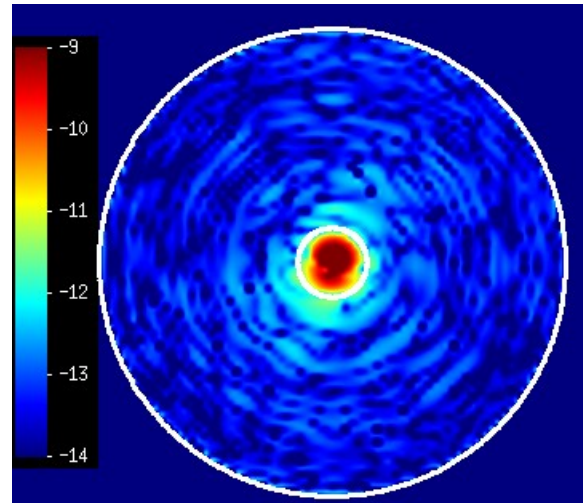


**Figure 5.10-6**. HLC contrast drift due to a -15° to +15° roll. PROPER is used to model the drift due to thermal deformations of the structure and deformations of the PM figure. The white circles demark the field angles 2 λ/D and 14 λ/D. The color bar indicates the log of the contrast drift. The residual speckle is dominated by figure errors outside the spatial bandwidth of the deformable mirrors.
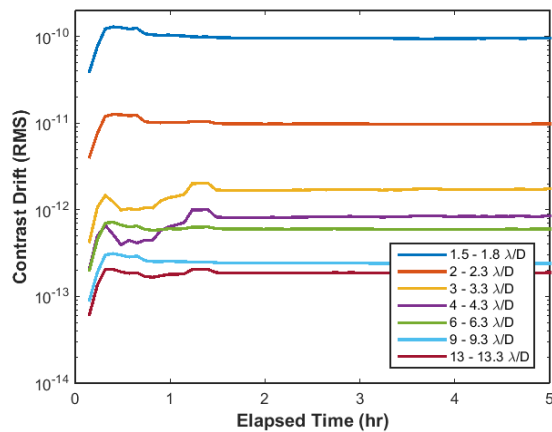


**Figure 5.10-7**. RMS HLC contrast drift at 7 different radial zones. At time = 0, a 30° roll maneuver was simulated and the resulting drift in the contrast over the next 5 hours was calculated. Even at the 2λ/D IWA, the contrast drift never exceeds 10$^{-11}$ and the speckle field remains so stable that there is no need to wait for the thermal transient to die down before imaging. This ultra-stable roll maneuver greatly enhances the ability to detect faint planets and reduces the likelihood of false detections.

know that the contrast drift is acceptable as long as the sunshade angle to the sun changes by less than 30°. The angle to the sun changes at about 1° per day due to the orbital motion so data collection can continue for a month before the dark hole needs re-tuning. For data collects lasting less than a week, the dominant thermal disturbance is variation in power dissipation of electronics in the spacecraft bus. The changing heat load to the telescope was modeled as a periodic 1°C change in the temperature of the entire spacecraft bus. The interfaces between the spacecraft bus have local heater control and thermal radiation barriers which thermally isolate the instrument from the spacecraft bus. The analysis includes rigid body motions of all optics up to the coronagraph mask. The resulting picometer wavefront error has no significant impact on the contrast drift, see Figure 5.10-8.
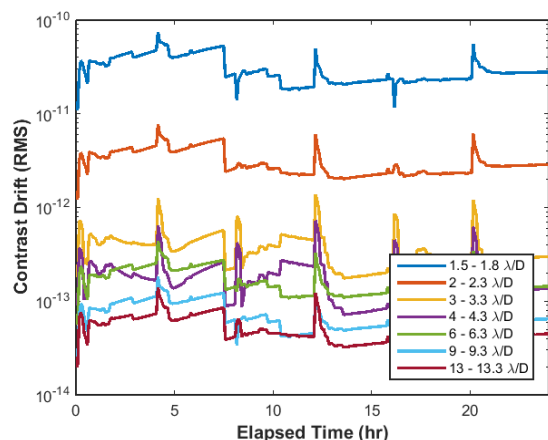


**Figure 5.10-8.** The spacecraft bus thermal disturbance was modeled as a 1°C amplitude square wave with a period of 8 hours. The telescope is well isolated from the spacecraft bus so the contrast drift is kept below $10^{-11}$ at the $2\lambda/D$ IWA, an order of magnitude below the requirement.

### 5.10.4  LOWFS Performance

Different coronagraph architectures have different sensitivities to the Zernike modes of the WFE, but all three coronagraphs studied for this report meet the $10^{-10}$ contrast drift requirement even without the LOWFS. Still the LOWFS can be useful in post processing to model residual wavefront drift. To verify that the LOWFS has enough bandwidth to sense picometer level wavefront drift, the LOWFS was modeled for the baseline configuration centered on a 6th magnitude star. Losses from reflections, the CCD quantum efficiency, read noise and shot noise were included in the model. As seen in Figure 5.10-9, an integration time of ~60 seconds is sufficient to sense contrast drift of $10^{-10}$, indicating that the LOWFS can easily keep up with the wavefront drift.
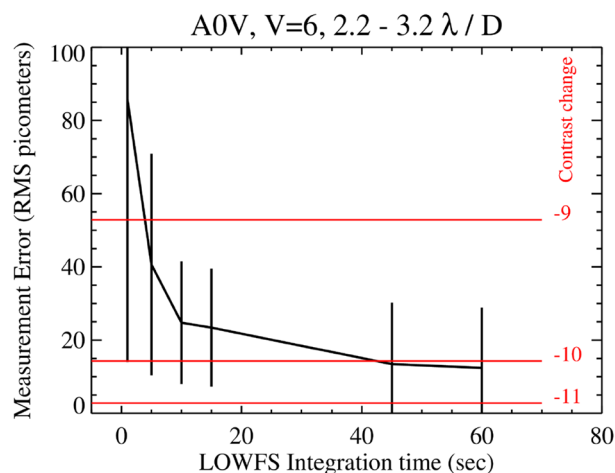


**Figure 5.10-9.** LOWFS accuracy vs. integration time assuming a 6th magnitude central star. Error bars represent 1-σ scatter in measurements for 20 different noise realizations. The input disturbance was 1 nm RMS, two orders of magnitude larger than the expected thermal drift. The model includes Z4–Z11 (tip/tilt excluded).

### 5.11  Binary Star Performance Modeling

Binary star systems pose a unique challenge for coronagraphic imaging because off-axis light from a nearby stellar companion leaks onto the detector, degrading the image contrast. This section quantifies the amount of diffracted light and scattered light that reaches the detector from an off-axis binary companion at 8 arcsec (the separation of alpha Centauri A and B in the mid-2020s). Results show that diffracted light from a stellar companion at 8 arcsec will reduce the achievable contrast to ~1e-9 while scattered light will further reduce the achievable contrast to ~3e-8.

Three possible countermeasures were considered in this study, 1) improving the surface finish on telescope optics, 2) adding a diamond mask to block out binary diffracted
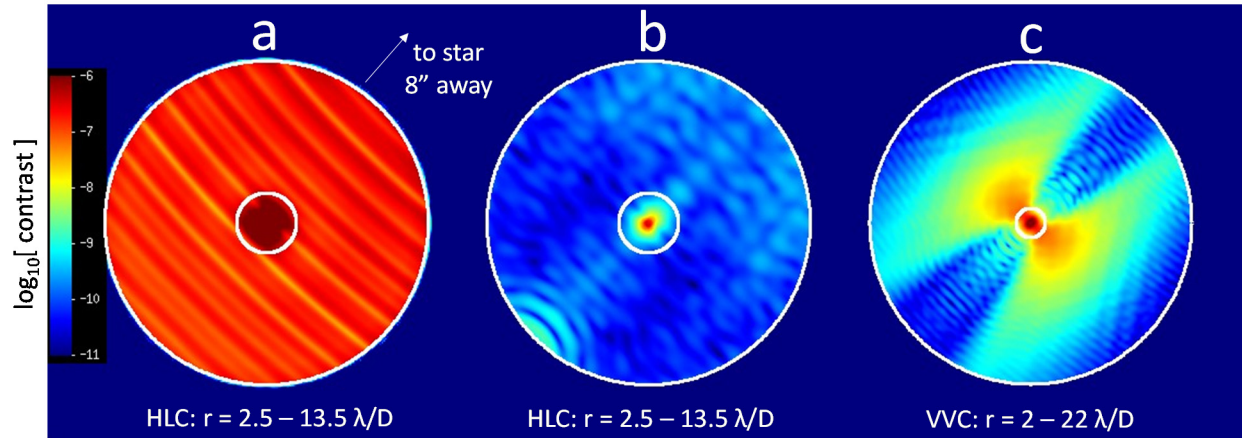
**Figure 5.11-1.** Maps of the dark hole region around the science target showing the diffracted light (no aberrations) from an equal-brightness star located 8 arcsec away, expressed in terms of contrast over a 495–605 nm bandpass. No light from the science target is included. If the companion star is brighter than the science target, then the values shown would increase proportionally. (a) HLC coronagraph without a field stop on the focal plane mask. (b) HLC with a 50 λ/D radius field stop on the FPM. (c) VVC with the same size field stop on its FPM.

light, and 3) a novel wavefront control algorithm, called Super-Nyquist Multi-Star Wavefront Control (Thomas et al. 2015)[2], that rejects the binary starlight in addition to the target starlight. To ensure technical readiness in 2017, Exo-C has adopted a capability-driven contrast requirement of $3 \times 10^{-8}$ for binary star systems, which corresponds to the current baseline design without any countermeasures for binary starlight suppression.

### 5.11.1  Simulating Binary Starlight

The contributions to the background around the science target from diffracted and scattered light from a star 8 arcsec away were computed using the same PROPER numerical modeling codes that were used to evaluate the performance of each coronagraph.

***Diffracted light:*** The simulation of just the diffraction component was straightforward as it was dependent on the specific design parameters of the coronagraph and involved propagating through an unaberrated system. The only free parameter was the radius of a

field stop placed on the focal plane mask of the HLC and VVC to block light from the core of the companion star's PSF, preventing it from passing through the remainder of the system (the PIAA coronagraph already had a field stop on the occulter).

Figure 5.11-1 indicates the diffraction-only contributions in the HLC and VVC to the dark hole background around the science target from an equal-brightness star 8 arcsec away, expressed in terms of contrast. As Figure 5.11-1a shows, without a field stop the light from the core of the companion star's PSF could diffract within the system and fill the dark hole around the science target with light of contrast $>10^{-7}$. If a field stop was placed on the focal plane mask, this could be reduced significantly, down to $10^{-9}$ contrast levels or less (Figure 5.11-1b). A field stop radius of 50 λ/D was used (a smaller field stop would degrade coronagraph performance unless the coronagraph was explicitly designed for a smaller stop, and a larger one would allow more light through). A field stop on the VVC also reduced the light from the companion star, though in a less uniform manner (Figure 5.11-1c).

PIAA presented a more complex diffraction pattern because the remapping optics greatly distorted the PSFs of off-axis

---

[2] Thomas, S., Belikov, R., Bendek, E., "Techniques for High Contrast Imaging in Multi-Star Systems I: Super-Nyquist Wavefront Control," submitted to *ApJ* (2015). (http://arxiv.org/abs/1501.01583).

sources (Figure 5.11-2) as viewed in the plane of the field mask, which was prior to the inverse remapping optics that restore the PSF shape. The PIAA field mask already included a $35\,\lambda/D$ radius field stop to mask diffraction from the binary pre-apodizer. The highly comatic PSF of the companion star was truncated by the field stop, and a significant fraction of the light made it through the inverse remapping optics and to the final image plane. This filled the dark hole with $10^{-6}$–$10^{-7}$ contrast light between the science and companion star, while the far side was about $10^{-8}$ (Figure 5.11-3).

*Scattered light:* More difficult to estimate was the contribution from scattered light from the optical surface errors, most importantly the mid-spatial-frequency (MSF) polishing errors. As these were hypothesized fabrication defects rather than design specifications like aperture mask diameters, they required some educated assumptions of what the potential properties of the optics might be. One could simply specify that the polishing errors that contribute to scattered light at the field angles of interest ($\sim 100\,\lambda/D$) be below the level to create a problem, but that would be unrealistic. The control of the relevant MSF errors during fabrication involves a trade between cost, time, and increased low-spatial-frequency errors. Reviews of existing optics, such as the primary of the Hubble Space Telescope and modern ground-based telescopes such as Gemini, Magellan, and VLT, show that the spatial frequency distribution of MSF error power (i.e., the power spectral density or PSD) follows an approximate $f^{-2.5}$ power law, where f is the spatial frequency (e.g., cycles per diameter). This behavior tends to hold even for smaller optics, such as collimators. Synthetic optical error maps with similar spatial frequency distributions were generated for the Exo-C models, with the amplitudes scaled to match the error levels expected for similar optics using current fabrication techniques (e.g., the primary had an 8 nm RMS wavefront
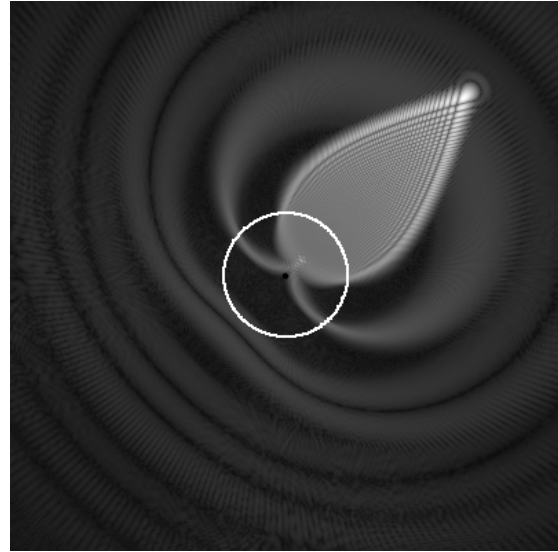


**Figure 5.11-2.** The field at the location of the PIAA focal plane mask with a star located 8 arcsec off-axis to the upper right. The distortion of the star is due to the wavefront remapping by the PIAA optics. The focal plane occulter is located at the center of this field (the occulted star is not shown). The circle indicates the diameter of the field stop.
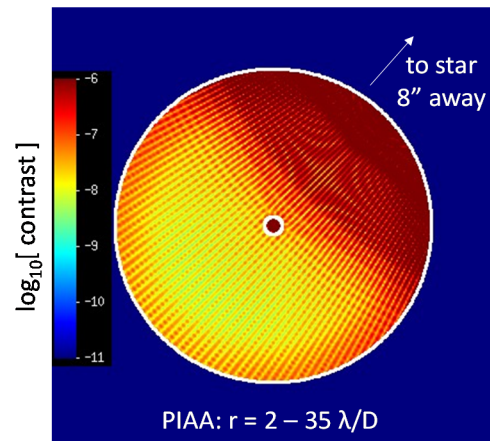


**Figure 5.11-3.** Same as Figure 5.11-1b except showing the light from diffraction from the 8 arcsec offset star in PIAA, with the default PIAA field stop included.

error compared to HST's 18 nm RMS, the secondary was 4 nm RMS, other off-axis optics were 2.5 nm RMS, and flats were 1.5 nm RMS). The primary and, to a lesser degree, the secondary errors dominate. The effect of the scattered light from the companion was derived by propagating wavefronts from an off-axis source through the telescope+coronagraph models with these aberrated surfaces.

Figure 5.11-4 shows the addition of scattered light from the 8 arcsec-distant companion in the dark hole around the science target for the HLC and VVC (PIAA would be similar, except it had a higher diffracted light component; all scatter results included the previously described field stops). The scatter created a $>10^{-8}$ contrast background in the dark hole region.
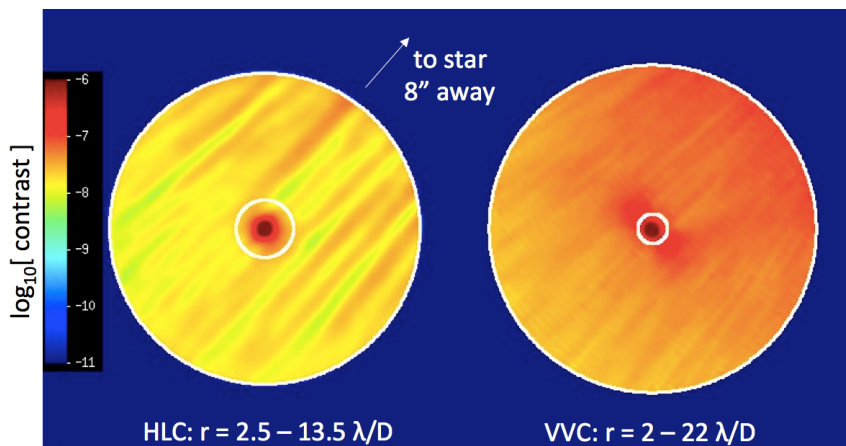


**Figure 5.11-4.** Same as Figures 5.11-1b and 5.11-1c (field stops included) but with scattered light from the optical surface errors included.

### 5.11.2 Binary Starlight Mitigation Approaches

***Improved surface finish of optics:*** Since the intensity of the scattered light is proportional to the square of the wavefront error, reducing the scatter to a $10^{-9}$ contrast level would require optics with MSF errors at least 3–10× lower than assumed. The synthetic Exo-C primary mirror MSF error was already 10× better than HST's (which was not polished with any significant MSF constraints). The technological readiness of polishing methods required to reach another order of magnitude reduction in MSF error on an optic of this size is unknown. The errors have been suppressed to significantly lower levels on smaller optics (D≈20 cm) developed for extreme ultraviolet lithography.

***Diamond Lyot stop:*** A diamond shaped Lyot stop modifies the diffraction pattern to place most of the light into a cross shape that avoids the region of interest around the target star. The proposed optical layout and resulting diffraction pattern are depicted in Figure 5.11-5. The diamond mask needs to be clocked to align to the binary; accomplished by a small
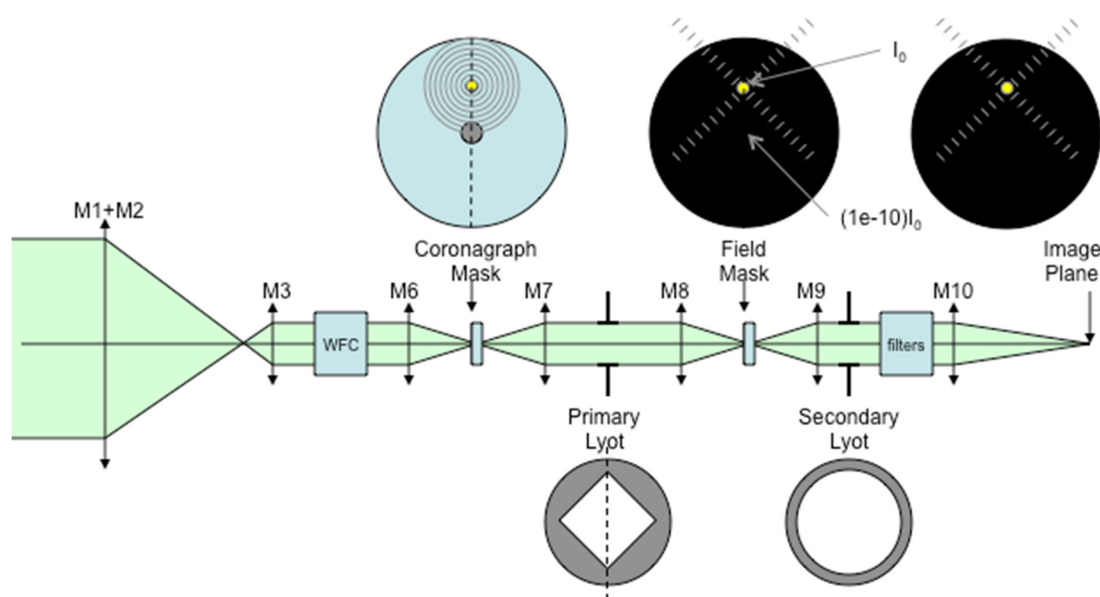


**Figure 5.11-5.** A diamond shaped Lyot mask modifies the diffraction pattern to place most of the diffracted binary starlight outside of the region of interest. The diamond mask suppresses diffracted binary starlight to ~1e-10, however, it does not help to suppress scattered binary starlight.

selection of diamond masks at various orientations, a mask clocking mechanism, or by spacecraft roll. The baseline design includes three diamond masks clocked at 30 degrees from each other, which requires at most a ±15-degree spacecraft roll to align the mask with the binary star vector. The diamond mask does not affect target star suppression, but does reduce throughput by approximately 25%. The diamond mask suppresses the diffracted binary starlight to a contrast of $\sim 10^{-10}$, but does help to suppress scattered starlight.

***Super-Nyquist Multi-Star Wavefront Control:*** A new wavefront control method has recently been proposed called Super-Nyquist Multi-Star Wavefront control (SNMSWC). SNMSWC can control and remove speckles from more than one star simultaneously, and do so even when the stars are separated by a distance greater than the Nyquist control region of the DM. Furthermore, SNMSWC can remove the diffraction from the off-axis star. No new hardware is in principle necessary (as long as the DM has a sufficiently strong print-through pattern), as SNMSWC relies purely on computing DM shapes in a different way.

SNMSWC consists of two components which are also useful by themselves: Super-Nyquist Wavefront Control and Multi-Star Wavefront Control. Super-Nyquist Wavefront Control (SNWC) enables control of speckles in single-star systems beyond the conventional (Nyquist) limit of the DM. Multi-Star Wavefront Control (MSWC) enables the suppression of diffracted starlight in two-star systems when both stars (or their replicas) are within the control range of the deformable mirror. MSWC relies on the idea that independent DM modes can be used on each star. The dark zone size in this case is reduced by a factor of 2. Proof-of-principle simulations have been performed of both, and a funded effort is under way to demonstrate the techniques in the lab.

In Figure 5.11-6 shows the successful combination of the above two steps, enabling the removal of starlight in a region of interest in binary star systems even when the separation of the two stars is beyond the normal range of the deformable mirror. Figure 5.11-6 shows results in polychromatic light and with a standard apodized Lyot coronagraph. The separation between the two stars is 29 $\lambda$/D and the potential planet is at 4 $\lambda$/D from the on-axis star.
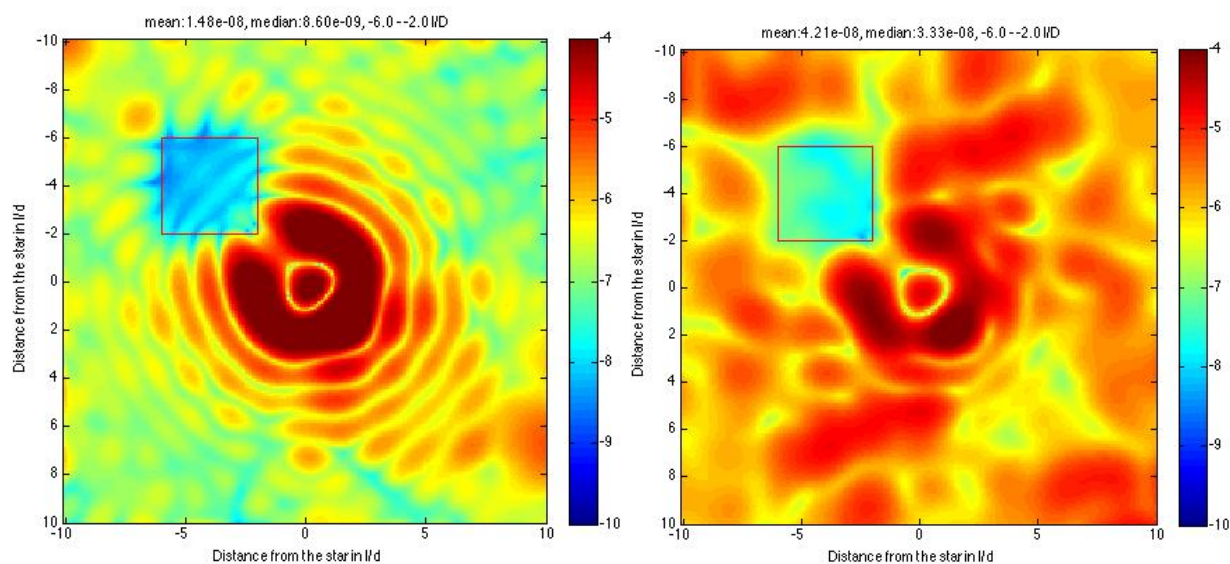


**Figure 5.11-6.** Demonstration of SNMSWC for a 10% band configuration centered around 550 nm, without aberrations (left) and with 10 nm rms of aberrations (right). This simulates a hypothetical binary star system with a separation of 29 λ/d. The contrast achieved without aberrations is 8.6x10^{-9} and with aberrations 3.3×10^{-8}.

(This does not correspond to Alpha Centauri with Exo-C, but does demonstrate the general principle.) We are simulating a 10% band around 550 nm and the amount of residual aberrations added is 10 nm rms.

## 5.12 Spacecraft

### System Overview

The Exo-C spacecraft is designed to use significant Kepler heritage to meet the science requirements defined for the mission. With few exceptions, including structure, high-gain antenna (HGA), optics, and very reliable components, the spacecraft is designed to be fully redundant with all subsystems necessary to deliver the payload to orbit and support it through primary operations. The spacecraft utilizes a low-profile hexagonal box structure at the base of the coronagraph to minimize the total Flight Segment height and satisfy the fairing envelope constraints defined by intermediate class launch vehicles. The spacecraft meets all fairing volume constraints, as can be seen in Foldout 5-1G.

The spacecraft utilizes a three-axis stabilized architecture, maintaining a fixed solar array pointed toward the Sun. This type of architecture minimizes jitter disturbances and shades the coronagraph telescope, helping to maintain payload thermal equilibrium. A body fixed Ka-band high-gain antenna (HGA) is used for high-rate data transmission with body-mounted X-band low-gain antennas (LGAs) for low-rate data transmission and commanding.

### 5.12.1 Structure

The spacecraft structure's primary requirement is to support the observatory loads during launch and to provide a stable surface to mount the various sensors, avionics, communication and propulsion hardware. To meet these requirements, the bus structure consists of seven shear panels, a top deck, middle deck and bottom deck, reaction control system (RCS) deck, and the launch vehicle adapter ring. The shear panels, decks, and solar array substrates consist of sandwiched aluminum face-sheets on aluminum honeycomb core and machined aluminum clips that are bonded around the edges. These components are all bolted together using integral aluminum clips, fittings and brackets. The seven shear panels provide structure to accommodate mounting of the spacecraft electronics, battery, reaction wheels, inertial reference units (IRUs), radio frequency (RF) equipment, and LGAs. The upper deck serves to provide a rigid closeout for the shear panels, and provides the mounting surface for the solar array panels. The bottom deck serves as a rigid lower closeout for the shear panels and provides the load path from the shear panels to the launch vehicle adapter ring. The bottom deck also supports the thrusters, associated propellant lines, and launch vehicle umbilical connectors. The RCS deck is attached to the inside of the launch vehicle adapter ring, and provides a mounting surface for the RCS tank, pressure transducer, latch valves, distribution plate, and propellant lines.

The payload attaches to the spacecraft bus via an isolation hexapod assembly between the bottom of the Primary Support Structure (PSS) and the mid-deck of the bus, as shown in the cut-away view of Figure 5.12-1. The hexapod comprises six struts with composite tubes and
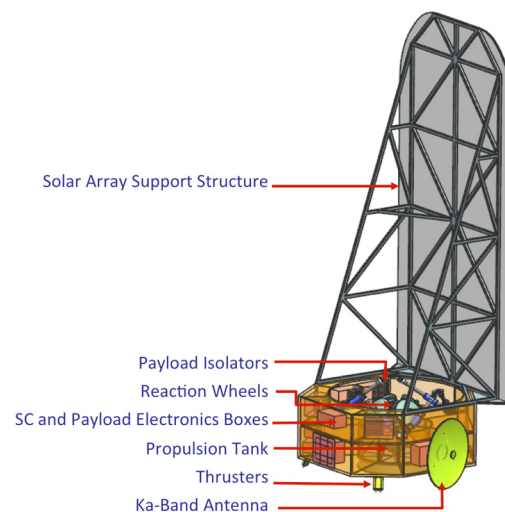


**Figure 5.12-1.** Exo-C bus and solar array structure.

flexured, titanium end fittings. In series with each strut is a passive isolator, with a launch lock, to isolate the payload from bus disturbances.

### 5.12.2  Propulsion

The Earth-trailing orbit selected for the Exo-C mission requires no significant maneuver to achieve or maintain orbit. As a result, the only driving propulsion requirement is to provide the observatory with attitude control functionality including: 1) Nulling residual tip-off and spin rates of the flight segment (FS) after separation from the launch vehicle (LV), 2) RWA desaturation, and 3) Attitude control in emergency mode.

To meet these requirements, Exo-C employs a blow-down mono-propellant reaction control system (RCS), shown in Figure 5.12-2. The hydrazine ($N_2H_4$) propellant is stored in a readily available, flight-qualified 13″ diameter diaphragm titanium tank. The diaphragm is used to separate the propellant from the pressurant in the tank, which is sized to hold approximately 20 kg of propellant. The propulsion system also includes two fill-drain service valves, system filter, pressure transducer, two latch

valves, lines, fuel, pressurant (gaseous nitrogen (GN2)) and the eight thrusters separated into two redundant thruster branches. The two thruster branches, each containing four thrusters, are mounted on the +Y and −Y axes of the spacecraft bus and isolated by latch valves. The eight thrusters produce about 1 Newton of thrust each and are capable of providing the roughly 4500 N-s of RCS impulse required for reaction wheel desaturation and the 485 N-s required to null out tip-off rates and residual spin after separation from the LV.

### 5.12.3  Attitude Control

The attitude determination and control system (ADCS) is required to meet the following determination and control functions: 1) stabilize attitude after launch vehicle separation, 2) point the telescope to the science attitude, 3) hold science pointing by using a fine-guidance signal provided by the instrument, 4) point solar array to Sun and point HGA to Earth when required, 5) protect coronagraph from imaging Sun, 6) perform roll maneuvers when commanded, and 7) provide attitude control during safe and emergency modes. Fine pointing and control is discussed in more detail in §5.7.

The ADCS subsystem consists of a combination of attitude determination sensors and active control systems. For attitude determination, fourteen Coarse Sun Sensors (CSS) are mounted on the flight structure allowing for coarse pointing by locating the Sun at all times. Two star trackers on the PSS provide the spacecraft with inertial attitude data, while redundant IRUs provide angular rates.

Spacecraft control is provided by a reaction wheel assembly (RWA) consisting of four wheels mounted on non-orthogonal axes. They are active redundant, meaning that all four are normally used, and share the momentum load while remaining single fault tolerant to a wheel failure. Reaction wheels will provide coarse pointing during science observations, solar
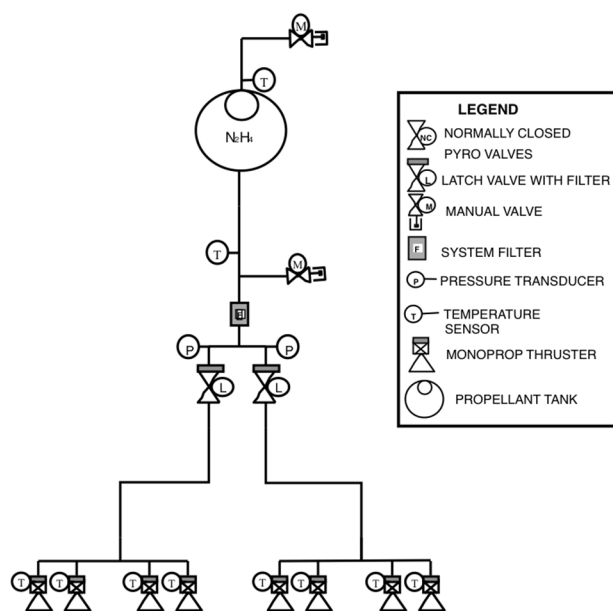


**Figure 5.12-2.** Exo-C propulsion block diagram.

array and communication pointing, and slew maneuvering during nearly the entire mission except during the initial tipoff from the LV. In addition to the RWA, the ADCS commands the RCS thrusters for attitude control when the reaction wheels are unavailable (such as during launch and early operations and Emergency mode). The RCS thrusters will also be used to desaturate the reaction wheels' solar-pressure-accumulated angular momentum.

### 5.12.4  Electrical Power

The Electrical Power Distribution System (EPDS) is responsible for providing the spacecraft and instrument with sufficient power throughout the lifetime of the mission. The required power by subsystem is shown in the Exo-C Power Equipment List (PEL) in Foldout 5.1-C. EPDS will be required to: 1) provide at least 1363 W of power (PBE) throughout the course of the mission, 2) provide a consistent, stable voltage throughout the mission, and 3) manage and distribute the power to the required subsystems and instrumentation. The EPDS meets these requirements via two methods, solar array and battery, for power distribution and management (see Figure 5.12-3)

The EPDS architecture uses a direct energy transfer system that operates by switching on the solar array strings as required to supply power, while regulating the supply voltage within the normal operating range of 24–35 VDC. Strings are arranged into blocking diode-protected subsegments further arranged into segments, resulting in extensive string loss tolerance.

Exo-C uses a fixed solar array of triple-junction photo-voltaic cells (efficiency = ~27.5%), with a surface area of 6m$^2$, to provide power to the spacecraft and payload. This array is designed to meet the power requirements of at least 1363 W with one string failure, which includes the 30% contingency. The solar panels can meet this requirement for a worst-case solar panel orientation of 40° pitch and 15° roll away from the Sun vector. The 6 m$^2$ surface area is expected to generate at least 1400 W at end of mission, assuming this worst-case orientation, as seen in Figure 5.12-4.

A 20 A-hr (15 A-hr end of mission energy storage) Li-Ion battery provides
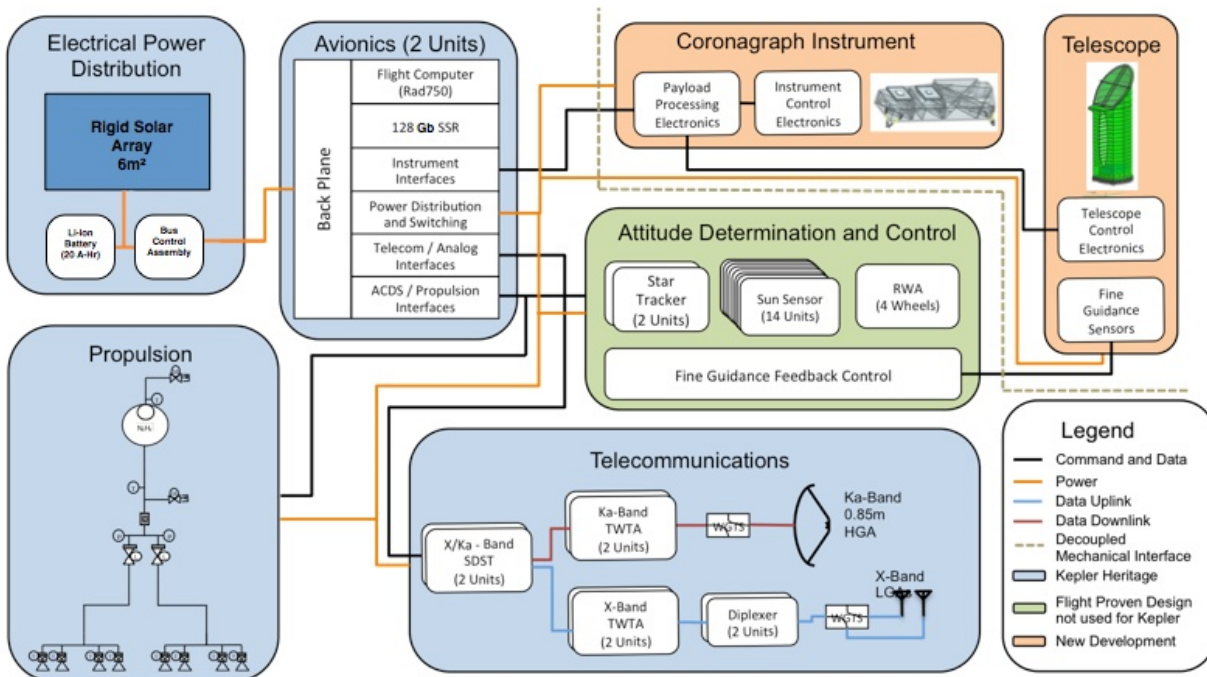


**Figure 5.12-3.** Exo-C draws significant heritage from the Kepler flight system.

launch load support, voltage stability during the mission, and energy reserve if needed for contingency operations.

The bus control assembly (BCA) electronics provides the distribution current-monitor shunts, and fault-isolation fuses capability for the mission. The single point ground is formed by connecting power bus returns to battery returns, solar array returns, and structure.

### 5.12.5　Avionics

The avionics subsystem is required to: 1) command and control the flight system, 2) store and playback engineering and science data, 3) encode all telemetry for downlink, and 4) time-tag the science data. The Exo-C control box (ECB) utilizes a similar architecture to that used for the Kepler mission. At the heart of the system is the RAD750 flight computer, which processes the spacecraft commands and science data for downlink. Command and telemetry, solid-state recorder, attitude determination, and instrument interface boards are located within the ECB and provide the necessary interfaces and drivers for spacecraft operations. A 128 Gigabit SSR provides the necessary data storage for science data prior to downlink.
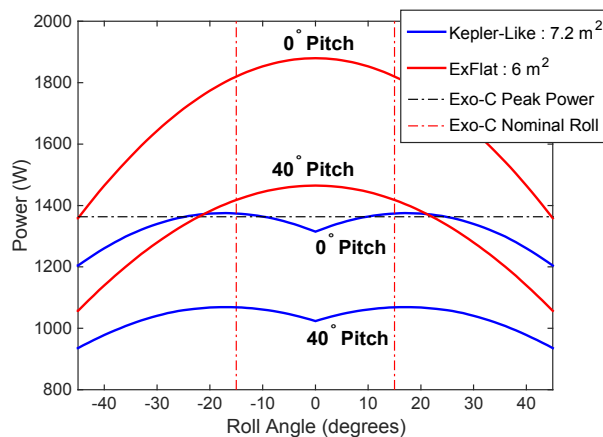


**Figure 5.12-4.** The Exo-C solar array will generate >1400W at end of mission for a worst-case orientation of 40° pitch and 15° roll away from the Sun vector, which exceeds the Exo-C peak power requirement including 30% contingency of 1363 W depicted by the black dotted line.

### 5.12.6　Communications

The telecom subsystem will be required to: 1) receive commands from the science operations team, 2) transmit engineering and navigation data back to Earth, and 3) provide a 4Mbps data rate communication link at the end of the 3 year life using a 34-m Deep Space Network (DSN) station for science data. The telecom subsystem meets these three requirements through a combination of communication frequencies, radios, and antennas.

Exo-C's communication strategy employs a similar architecture to that used by Kepler. Consisting of a Ka-band high-gain antenna, (HGA), two transmit/receive X-band only LGA pairs, two small deep space transponder radios (SDSTs) capable of operating in the X and Ka-bands, two 35 W Ka-band and two 25 W X-band traveling wave tube amplifiers (TWTAs), the subsystem is fully capable of meeting the data requirements of the mission. A telecom subsystem block diagram is shown in Figure 5.12-3.

The two communication frequencies are used for varying operation modes. X-band is used for uplink while both X-band and Ka-band are used for downlink. Engineering data can be downlinked via X-band or Ka-band, however the higher data rate Ka-band system will be used to meet the science data requirements of the mission. The uplink and downlink data rates are listed in Table 5.12-2 (Note: DSN uplink rates are capped at 200 Mbps).

**Table 5.12-2.** Exo-C's Telecom Subsystem has been designed to meet the required downlink and uplink performance at maximum distances from the Earth.

| Time Past Launch | Ka-Band Rate, Down (bpd) | X-Band Data Rate, Down (BPS) | X-Band Data Rate, Up (bps, no limit) |
|---|---|---|---|
| 1 year | 6.0E+10 | 3.0E+06 | 2.0E+08 |
| 2 years | 2.5E+07 | 1.5E+03 | 1.0E+05 |
| 3 years | 4.0E+06 | 2.0E+02 | 1.5E+04 |
| 4 years | 1.5E+06 | 8.0E+01 | 5.0E+03 |
| 5 years | 7.5E+05 | 4.0E+01 | 2.5E+03 |

### 5.12.7 Thermal

The thermal control subsystem (TCS) is responsible for: 1) maintaining spacecraft component temperatures within operational limits, and 2) providing temperature sensors for sensing of spacecraft critical temperatures.

All thermal control of the telescope and instrument is provided by the instrument, in order to minimize mechanical and electrical interfaces to the spacecraft. The instrument thermal design can be found in §5.6.

Heat generated inside spacecraft electrical boxes serves to maintain them at flight-allowable temperatures, while the spacecraft bus serves as a radiator of excess heat. Redundant heaters and heater controllers are used to maintain survival temperatures in the event of a failure. Heaters are usually controlled automatically; Flight Software (FSW) compares thermistor data with temperature limits to maintain temperatures by powering the heaters on and off. If necessary, heater setpoint tables can be changed by flight team command.

## 5.13 Slew Time Analysis

Exo-C should nominally perform a 30-degree roll in 15 minutes and a 30-degree pitch in 30 minutes. A control authority analysis was performed to verify that the spacecraft could complete the required slews in these given amounts of time.

For this analysis, the spacecraft performs a trapezoidal spin-up/coast/spin-down profile with typical acceleration and rate limits of $0.02$ mrad/s$^2$ and 3 mrad/s, respectively. The roll and pitch inertias are conservatively assumed to be 760 and 2400 kgm$^2$, respectively. Based on these numbers, the total slew time is 5.4 minutes for both the roll and pitch axes. This meets the requirement and leaves approximately 10–25 minutes for the spacecraft to settle, including any transients such as damping out flexible modes excited during the slew.

To accelerate and coast at the specified levels requires the reaction wheels to provide a torque of 48 mNm and a momentum of 7.2 Nms for the largest inertia axis (pitch axis), which is well within the capability of the reaction wheels.

# 6 Mission Operations and Data Analysis

## 6.1 Mission Operations

Exo-C operations fall into the following categories: spacecraft management, target acquisition, instrument optimization and management, and science observations. The Exo-C baseline design, described in §5, along with the science objectives described in §4, allows us to derive durations and repeat rates for these activities, along with the data volume. Operations flow and mission time estimates are based on these durations. Durations and repeat times are summarized in Table 6.1-1.

Based on our preliminary analysis, we show Exo-C can accommodate all of the mission operations and science observations. More detail is given in following subsections.

### 6.1.1 Spacecraft Management

These activities include communications with the spacecraft, orbit and attitude management, and general housekeeping. Since Exo-C is in an Earth-trailing orbit no time needs to be spent on orbit management or maintenance maneuvers. Due to the high number of available targets, Exo-C's observing schedule will be constructed in such a way that Earth and Moon avoidance maneuvers will not be necessary, as their positions in relation to the spacecraft will always be known.

Communications with the spacecraft are conducted via two low-gain X-band antennas and a body-fixed Kepler-like Ka-band high-gain antenna. Key characteristics and resulting telecom pass times are shown in Table 6.1-1.

The reaction wheels have been chosen to allow greater than 100 hours of uninterrupted observing times between momentum management events to accommodate spectroscopy observations.

At this point, no specific time has been allocated for anomaly investigations. The assumption is that the routine occurrences are reflected in average duration estimates in the operations database, while more extreme cases should be handled as risks.

### 6.1.2 Target Acquisition

The target acquisition time is dominated by how long it will take the instrument to come to its required thermal stability after the Sun angle has been changed. This will depend greatly on the magnitude of the maneuver and the thermal control system design. Modeling to date indicates very small wavefront disturbances will take place after a slew or roll about the boresight, perhaps avoiding the need to hold operations for thermal settling. To be conservative the operations plan includes a two hour settling time after a slew before resuming observations. Details of the payload's thermal performance are covered in §5.6 and §5.10.

### 6.1.3 Instrument Optimization and Maintenance

The coronagraph uses four images to tune the deformable mirrors (DM) to obtain the required contrast. The integration time to obtain the images depends on the apparent magnitude of the star and will vary from target to target. Based on the current target list we have calculated the average time needed to reach $10^{-9}$ contrast to be 6 hours on the brightest stars. Once that is done, a 1 hour fine-tuning of the dark hole will be performed before each science observation. The observing sequence will be such that the brightest stars are interspaced with the other science observations such that Exo-C always maintains an adequate dark hole.

### 6.1.4 Science Observations

Science observations are governed by science objectives and fall into three main categories: Spectroscopy of Known Exoplanets, Planet Discovery Surveys, and Disk Imaging Surveys. The durations of each observation will depend on the target characteristics and instrument design. Detailed simulations based on the target list, given in Appendix-D, were performed to evaluate the required durations and given in §4.5.

**Table 6.1-1.** Mission operations time estimates. These are the overhead times needed for various spacecraft and non-science activities. The science observation time is listed in Table 4.5-2.

| Activity | Duration (hrs) | Repeat Period (hrs) | Description |
|---|---|---|---|
| **Spacecraft Management** | | | |
| **Communications** | | | |
| C4 Low data rate spacecraft command and telemetry | 0 | | Two LGAs on each face. X-band, 16 kB/sec. No power limitation, but maneuvers may be required. Need to investigate further. For now assume this does not take time away. |
| C3 High data rate scientific data downlink maneuver | 1 | 336 | The current estimate for downlink science is 15 Gbits every 2 weeks. The body-fixed Kepler-like 0.85-m antenna would support 4 Mbits/sec transmissions at the end of the 3-year primary science mission. In this configuration, there would be one science downlink per two week, lasting approximately 1 hour. This is an acceptable configuration. |
| C2 Set up a link for telecon pass | 1 | 336 | A half hour at the frontend and a half hour at backend is required slew and point the body fixed antenna to Earth, and set up the telecon. |
| C1 Maneuver spacecraft into place | 1 | 336 | Requires 0.5 hr at the front end and 0.5 hr at the back end. The 0.5 hr on back end may not be necessary, as it may be part of subsequent retargeting. |
| **Orbit Management** | | | |
| Orbit correction maneuver | N/A | N/A | Not needed for Earth-trailing orbit. |
| MM Momentum management | 0.5 | 120 | The baselined reaction wheel assemblies, similar to the ones used by SMAP, would allow the spacecraft to maintain pointing without desaturation maneuvers for up to 120 hours. This accommodates the up to 100 hr spectroscopy observation. |
| Earth/Moon avoidance maneuvers | N/A | N/A | Should be able to pick targets such that these maneuvers are not necessary. |
| **Housekeeping** | | | |
| Anomaly investigation | | | For now, assume this is included in other estimates as overhead. |
| **Retargeting** | | | |
| RT Retargeting maneuver | 0.2 | | Typical slew maneuver time. |
| TA Settling time; thermal stab A | 2 | | For spectroscopy and imaging of planets. |
| TB Settling time; thermal stab B | 1 | | For disk imaging. |
| **Instrument Optimization and Maintenance** | | | |
| DM1 Instrument optimization (DM speckle) | 6 | | For the brightest targets, all those that are brighter than 2.5th mag, Exo-C will dig the dark hole. |
| DM2 Instrument optimization (DM speckle) | 1 | | Before each observations, the dark hole will be fine-tuned before taking science data. |

## 6.1.5   Operations Flow

Based on the durations in Operations Database, shown in Table 6.1-1, a candidate operations flow is shown in Table 6.1-2. A two-week duration is shown to accommodate a 100-hour spectroscopy observation, which needs to be fitted in between momentum management events. Our current estimates of the 120 hours between momentum management events are based on fairly conservative assumptions and should not be viewed as restrictive. Observation times longer than 100 hours should easily be accommodated from the momentum management perspective. This sample observation plan shows we can accommodate all the needed operations within a two-week sequence. The entire mission lifetime would be comprised of 78 such observing sequences stitched together and optimized to maximize the science return. The two-week down-link cadence allows for preliminary data analysis and uploading of the next sequence such that follow up observations can be made in less than one month after a new exoplanet discovery.

**Table 6.1-2.** A two-week subset of operations flow.

| Hrs | Day N+0 | Hrs | Day N+1 | Hrs | Day N+2 | Hrs | Day N+3 | Hrs | Day N+4 | Hrs | Day N+5 | Hrs | Day N+6 |
|---|---|---|---|---|---|---|---|---|---|---|---|---|---|
| 1 | T0001 Retargeting (RT) and Thermal Stabilization (TA) | 25 | | 49 | | 73 | T0004 Instrument Optimization (DM) | 97 | T0005 RT and Thermal Stab (TB) | 121 | | 145 | |
| 2 | | 26 | | 50 | | 74 | | 98 | | 122 | | 146 | |
| 3 | T0001 Instrument Optimization (DMA) | 27 | | 51 | | 75 | | 99 | T0005 Instrument Optimization (DMB) | 123 | | 147 | |
| 4 | | 28 | | 52 | | 76 | | 100 | | 124 | T0007 Instrument Optimization (DMA) | 148 | |
| 5 | | 29 | T0002 RT and Thermal Stab (TB) | 53 | | 77 | | 101 | | 125 | | 149 | T0008 RT and Thermal Stab (TB) |
| 6 | | 30 | | 54 | | 78 | | 102 | | 126 | | 150 | |
| 7 | | 31 | T0002 Instrument Optimization (DMB) | 55 | | 79 | | 103 | | 127 | | 151 | T0008 Instrument Optimization (DMB) |
| 8 | | 32 | | 56 | | 80 | | 104 | T0005 Disk Imaging (I_DI) | 128 | T0007 I_PD | 152 | |
| 9 | | 33 | | 57 | | 81 | | 105 | | 129 | | 153 | |
| 10 | | 34 | | 58 | T0003 Planet Discovery Observation (I_PD) | 82 | | 106 | | 130 | | 154 | |
| 11 | | 35 | | 59 | | 83 | | 107 | | 131 | | 155 | |
| 12 | | 36 | T0002 Disk Imaging (I_DI) | 60 | | 84 | | 108 | T0006 RT and Thermal Stab (TB) | 132 | | 156 | T0008 Disk Imaging (I_DI) |
| 13 | | 37 | | 61 | | 85 | | 109 | | 133 | | 157 | |
| 14 | | 38 | | 62 | | 86 | T0004 I_PD | 110 | T0006 Instrument Optimization (DMB) | 134 | | 158 | |
| 15 | | 39 | | 63 | | 87 | | 111 | | 135 | | 159 | |
| 16 | T0001 Planet Discovery Observation (I_PD) | 40 | T0003 Retargeting (RT) and Thermal Stabilization (TA) | 64 | | 88 | | 112 | | 136 | T0007 Planet Discovery Observation (I_PD) | 160 | |
| 17 | | 41 | | 65 | | 89 | | 113 | | 137 | | 161 | |
| 18 | | 42 | T0003 I_PD | 66 | | 90 | | 114 | | 138 | | 162 | |
| 19 | | 43 | | 67 | | 91 | | 115 | | 139 | | 163 | |
| 20 | | 44 | T0003 Instrument Optimization (DM) | 68 | T0004 Retargeting (RT) and Thermal Stabilization (TA) | 92 | | 116 | T0006 Disk Imaging (I_DI) | 140 | | 164 | Unassigned |
| 21 | | 45 | | 69 | | 93 | | 117 | | 141 | | 165 | |
| 22 | | 46 | | 70 | | 94 | | 118 | | 142 | | 166 | |
| 23 | | 47 | | 71 | T0004 I_PD | 95 | | 119 | MM – Momentum Comp | 143 | | 167 | |
| 24 | | 48 | T0003 I_PD | 72 | | 96 | | 120 | T0007 RT and TA | 144 | | 168 | |

**Table 6.1-2.** A two-week subset of operations flow (continued).

| Hrs | Day N+7 | Hrs | Day N+8 | Hrs | Day N+9 | Hrs | Day N+10 | Hrs | Day N+11 | Hrs | Day N+12 | Hrs | Day N+13 |
|---|---|---|---|---|---|---|---|---|---|---|---|---|---|
| 169 | T0009 Retargeting (RT) and Thermal Stabilization (TA) | 193 | | 217 | | 241 | | 265 | | 289 | | 313 | |
| 170 | | 194 | | 218 | | 242 | | 266 | | 290 | | 314 | |
| 171 | T0009 Instrument Optimization (DMA) | 195 | | 219 | Unassigned | 243 | | 267 | | 291 | | 315 | |
| 172 | | 196 | | 220 | Unassigned | 244 | | 268 | | 292 | | 316 | |
| 173 | | 197 | T0010 RT and Thermal Stab (TB) | 221 | MM – Momentum Comp | 245 | | 269 | | 293 | | 317 | |
| 174 | | 198 | T0010 Instrument Optimization (DMB) | 222 | T0012 Retargeting (RT) and Thermal Stabilization (TA) | 246 | | 270 | | 294 | | 318 | |
| 175 | | 199 | | 223 | | 247 | | 271 | | 295 | | 319 | |
| 176 | | 200 | | 224 | | 248 | | 272 | | 296 | | 320 | |
| 177 | T0009 Planet Discovery Observation (I_PD) | 201 | | 225 | T0012 Instrument Optimization (DMA) | 249 | | 273 | | 297 | | 321 | T0012 Spectroscopy Observation (I_SP) |
| 178 | | 202 | T0010 Disk Imaging (I_DI) | 226 | | 250 | | 274 | | 298 | | 322 | |
| 179 | | 203 | | 227 | | 251 | | 275 | | 299 | | 323 | |
| 180 | | 204 | | 228 | | 252 | T0012 Spectroscopy Observation (I_SP) | 276 | T0012 Spectroscopy Observation (I_SP) | 300 | T0012 Spectroscopy Observation (I_SP) | 324 | |
| 181 | | 205 | | 229 | | 253 | | 277 | | 301 | | 325 | |
| 182 | | 206 | | 230 | T0012 Spectroscopy Observation (I_SP) | 254 | | 278 | | 302 | | 326 | |
| 183 | | 207 | | 231 | | 255 | | 279 | | 303 | | 327 | |
| 184 | | 208 | T0011 RT and Thermal Stab (TB) | 232 | | 256 | | 280 | | 304 | | 328 | |
| 185 | | 209 | | 233 | | 257 | | 281 | | 305 | | 329 | |
| 186 | | 210 | T0011 Instrument Optimization (DMB) | 234 | | 258 | | 282 | | 306 | | 330 | |
| 187 | | 211 | | 235 | | 259 | | 283 | | 307 | | 331 | Setup Telecom (C1,C2) |
| 188 | | 212 | | 236 | | 260 | | 284 | | 308 | | 332 | |
| 189 | | 213 | | 237 | | 261 | | 285 | | 309 | | 333 | C3 Science Download |
| 190 | | 214 | T0011 Disk Imaging (I_DI) | 238 | | 262 | | 286 | | 310 | | 334 | |
| 191 | | 215 | | 239 | | 263 | | 287 | | 311 | | 335 | |
| 192 | | 216 | | 240 | | 264 | | 288 | | 312 | | 336 | End Telecom (C1, C2) |

## 6.2    Data Volume

Based on the number of science observations from Table 4.5-2, we calculated the science data volume (Table 6.2-1). The effective average integration time are assumed to be 15 min for the spectrograph and 5 min for the science imager. These are not taken as a single integration time on the detector, but may be co-added in the instrument electronics. The data volume per image is also listed, and these

are used to calculate the volume per science category. The total science data volume is ~860 Gbits. We have assumed similar overheads as the WISE mission and added 50% margin. The total volume to be downlinked, after a factor of 2 compression, is ~1150 Gbits. The downlink cadence is two weeks. Hence, each downlink will contain ~15 GBits of data and will take just over 1 hour at the end of the 3-year primary mission time.

**Table 6.2-1.** Data volume estimates for the individual science observation programs defined in §4.

| Science Type | Visits | | Data Volume | | |
| --- | --- | --- | --- | --- | --- |
| | Number of Targets | Average Number of Visits | Averaged Effective Readout Time | Science Image Data Size | Total Data Volume for Science category |
| | N_target | N_visit | (min) | (kbits) | (Gbits) |
| **Planet characterizations** | | | | | |
| Spectroscopy of Known and new Exoplanets (from RV and Exo-C surveys) | 20 | 1 | 15 | 8192 | 164 |
| Astrometry and multi-color photometry of known and new Exoplanets (from RV and Exo-C surveys) | 35 | 3 | 5 | 4096 | 155 |
| **Planet discovery surveys** | | | | | |
| Survey nearby stars for super-Earths within the habitable zone | 15 | 6 | 15 | 4096 | 37 |
| Search for giant planets around nearby stars | 135 | 2.3 | 5 | 4096 | 305 |
| **Disk imaging surveys** | | | | | |
| Survey for HZ dust in A-K stars | 150 | 1 | 15 | 4096 | 20 |
| Detection survey in RV planet systems | 60 | 1 | 5 | 8192 | 71 |
| Known debris disks from Spitzer, Herschel, and WISE | 150 | 1 | 15 | 8192 | 59 |
| Nearby protoplanetary disks | 40 | 1 | 5 | 8192 | 47 |
| Total science data (GBits) | | | | | 857 |
| 30% for LOWFS, pointing, etc. | | | | | 257 |
| 20% for spacecraft overhead (based on WISE) | | | | | 429 |
| 50% margin (on science and telemetry) | | | | | 772 |
| Compression factor | | | | | 2 |
| Total data to be downlinked (GBits) | | | | | 1157 |
| Number of downlinks (bi-weekly for 3 years) | | | | | 78 |
| Data to be downlinked per down-link (Gbits) | | | | | 15 |
| Total effective data rate (kbits/sec) | | | | | 25 |
| Downlink length of time needed with HGA (after 3 years) (min) | | | | | 62 |
| On-board memory needed, assuming two missed passes (Gbits) | | | | | 45 |
| On-board storage (Gbits) (based on Kepler) | | | | | 128 |
| Reserve | | | | | 65% |

## 6.3    Science Data Analysis

The Exo-C science data will go through a science-processing pipeline, similar to that of Kepler. This process will produce Level–4 data products. The data will then be distributed and archived.

### 6.3.1    Science-processing Pipeline

The science-processing pipeline will take the raw instrument data and telemetry and produce data products. The preliminary data products are required to be available within one week of down-linking. This is needed such that the science team can adjust the next science observation sequence in the case of a discovery.

### 6.3.2    Data Distribution and Archiving

A data distribution center will receive the raw science data and will be responsible for generating and archiving all of the Exo-C science data. The center will produce the high-level science data products, in the form of images and spectra, to the science team.

## 6.4    Ground Subsystem

The Exo-C Mission Ground Segment (GS) is responsible for the execution of Exo-C to ensure the accomplishment of the Level 1 Requirements/Mission Success Criteria. The GS is the final destination of the mission data products. It consists of the people, policies, procedures, facilities, hardware, and software required to successfully complete Exo-C.

As the project prepares for launch and begins the transition from a development organization to an operations organization, more and more emphasis is placed on the development of team procedures and interfaces and validation of the project's capabilities through ground segment integration tests, mission scenario tests, and ultimately operational readiness tests.

Figure 6.1-1 shows the project organization during operations, where the project no longer includes a mission design element and the mission operations system is divided into
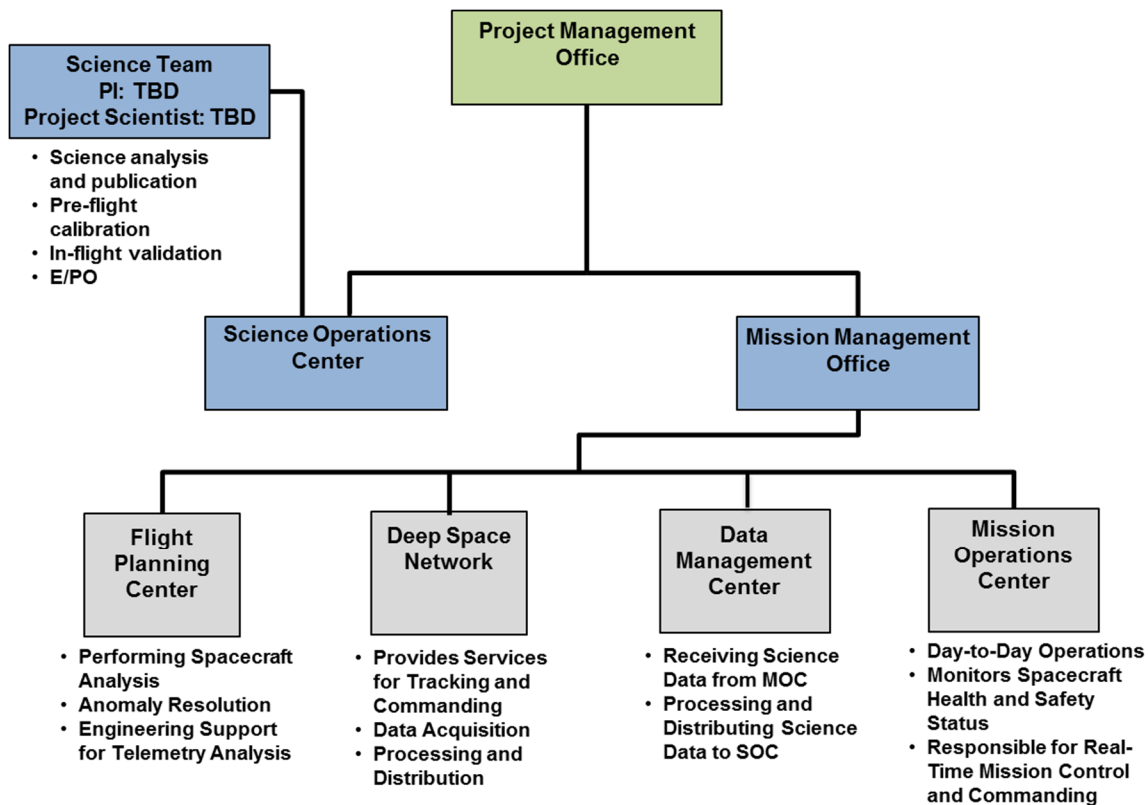


**Figure 6.1-1.** Exo-C utilizes a simple straightforward distribution of management during Phase E operations.

separate function-based elements.

The Mission Director heads the Mission Management Office (MMO) and reports to the Project Manager. The Project Management Office is administratively responsible to NASA Headquarters to assure that financial, schedule, and staffing resources are properly applied. The MMO will also manage the Flight Planning Center and the Science Operations Center elements as well as performing project system engineering during flight.

The Science Operations Center (SOC) runs the science processing pipeline, manages the database of science targets, provides target data to the MOC when configuration changes are required, analyzes data from each contact to determine if there are any issues and is responsible for monitoring the payload. Planning of science activities is the responsibility of the Science Office (SO).

The Flight Planning Center (FPC) is responsible for performing spacecraft analysis and flight system anomaly resolution. In addition, the FPC is responsible for overseeing activity planning and command product generation. The FPC also includes the engineering support to manage the flight system including analyzing telemetry, trending subsystem performance and generating any activity requests required to maintain the flight system. The FPC maintains and operates the system test bed (STB), which is used to validate all new command products before they are sent to the FS.

The Mission Operations Center (MOC) will perform the following functions: day-to-day science operations, health and safety monitoring, data recorder playback for science data downlinks, archival of engineering data for performance trending, and activity planning with oversight from the FPC.

The Data Management Center (DMC) is responsible during operations for receiving science data from the Mission Operations Center and routing processed (decompressed, partially calibrated) science data to the Science Operations Center as well as archiving of science data.

The DSN provides services for tracking and commanding of the spacecraft, data acquisition from the spacecraft, processing and distribution. The Project Scheduling Service (PSS) will interact with the Exo-C project to schedule, allocate, and prioritize DSN resources.

The Mission Operations Center (MOC) will perform the day-to-day operations of the Flight Segment to acquire science and spacecraft data as well as monitor health and safety status. The MOC is responsible for the real-time mission control functions. The MOC also commands data recorder playbacks to downlink science data, accounts for (and replays if required) science data, and archives engineering data for performance trending. The MOC is primarily responsible for the activity planning function, with oversight from the FPC.

The Data Management Center (DMC) is responsible during operations for receiving science data from the Mission Operations Center and routing processed (decompressed, partially calibrated) science data to the Science Operations Center as well as archiving of science data.

The DSN provides services for tracking and commanding of the spacecraft, data acquisition from the spacecraft, processing and distribution. The Project Scheduling Service (PSS) will interact with the Exo-C project to schedule, allocate, and prioritize DSN resources.

# 7　Mission Cost Estimation

## 7.1　Cost

As part of the Exo-C concept development, Aerospace Corporation produced two diagnostic Cost Appraisal and Technical evaluations (CATEs). The first placed the 1.5 m design described in the Exo-C Interim Report at $1.2B. This resulted in a series of design changes that drove Exo-C even closer in construct to the $735M Kepler mission. The primary mirror is now the same diameter as Kepler's (1.4 m); also like Kepler, the telescope mounting point has been lowered part way into the spacecraft bus. The inner- and outer- barrels were replaced with a single barrel and a more optimal solar panel configuration that also serves as a thermal shield. These changes lowered the final CATE cost estimate to a value not far from the Exo-C internal cost estimate.

The CATE process endeavors to produce a low risk cost estimate and includes a 70% probability cost estimate (an estimate assessed to have a 70% chance of overestimating and a 30% chance of underestimating the actual costs) plus additional cost assessments for technical and programmatic risks. This was used as the cost evaluation method in the ASTRO 2010 Decadal Survey. As such, it represents a very conservative estimate; missions of the Exo-C scale may be achievable for less than the CATE estimate (as in the case of Kepler).

The Exo-C internally generated cost estimate of $948M total project cost is also a very conservative estimate (see Appendix A for the breakdown of the Exo-C estimate by WBS element). The spacecraft cost is based on Kepler's as-flown cost with upward adjustments for the few, small design differences. The payload estimate is based on the single-variable telescope model (Stahl, 2013) and the NASA Instrument Cost Model (NICM), both constructed from many as-flown

telescope and instrument costs and both in regular use within the aerospace cost estimation community. In addition, Exo-C added the Kepler actual payload management and payload systems engineering costs to these model estimate. The total Exo-C payload cost (without reserves) exceeds the Kepler as-flown payload costs by over $65M (30%)—again both payloads use the same size (1.4 m) telescope primary. Kepler as-flown costs were used for pre-launch science, ground system, mission operations development and Phase E operations as well. Incorporating even more conservativism, Exo-C adds 30% reserve to an estimate that already exceeds the Kepler full mission cost.

Figure 7-1 illustrates just how conservative the Exo-C estimate is. Cost data was collected from all past NASA missions with a single telescope in the visible, UV or IR, launched since 1990. Hubble was not included since it was human rated, serviceable, Class "A", and had a much longer design life and larger aperture than the other telescopes and the Exo-C design trade space. This data was augmented with data from commercial ground imaging telescope missions launched in this same timeframe; the commercial data was taken from a presentation of a NASA-commissioned study titled *NASA Productivity Study* (Coonce 2008). When development costs are plotted against aperture, a clear trend emerges. With the single exception of Spitzer the other 11 telescope missions roughly follow a linear relation of about $44M ($FY15) of mission development cost for every 10cm of aperture. Extending this trend out to 1.4m gives a mean development cost of $610M. By building on the Kepler actual costs then adding 30% reserves, the Exo-C estimate is $150M above this mean trend of actual telescope missions and $210M above Kepler's actual development cost. From least squares statistics, the Exo-C development estimate corresponds to a cost exceeding 93% of similarly sized telescope missions based on this historically derived model.
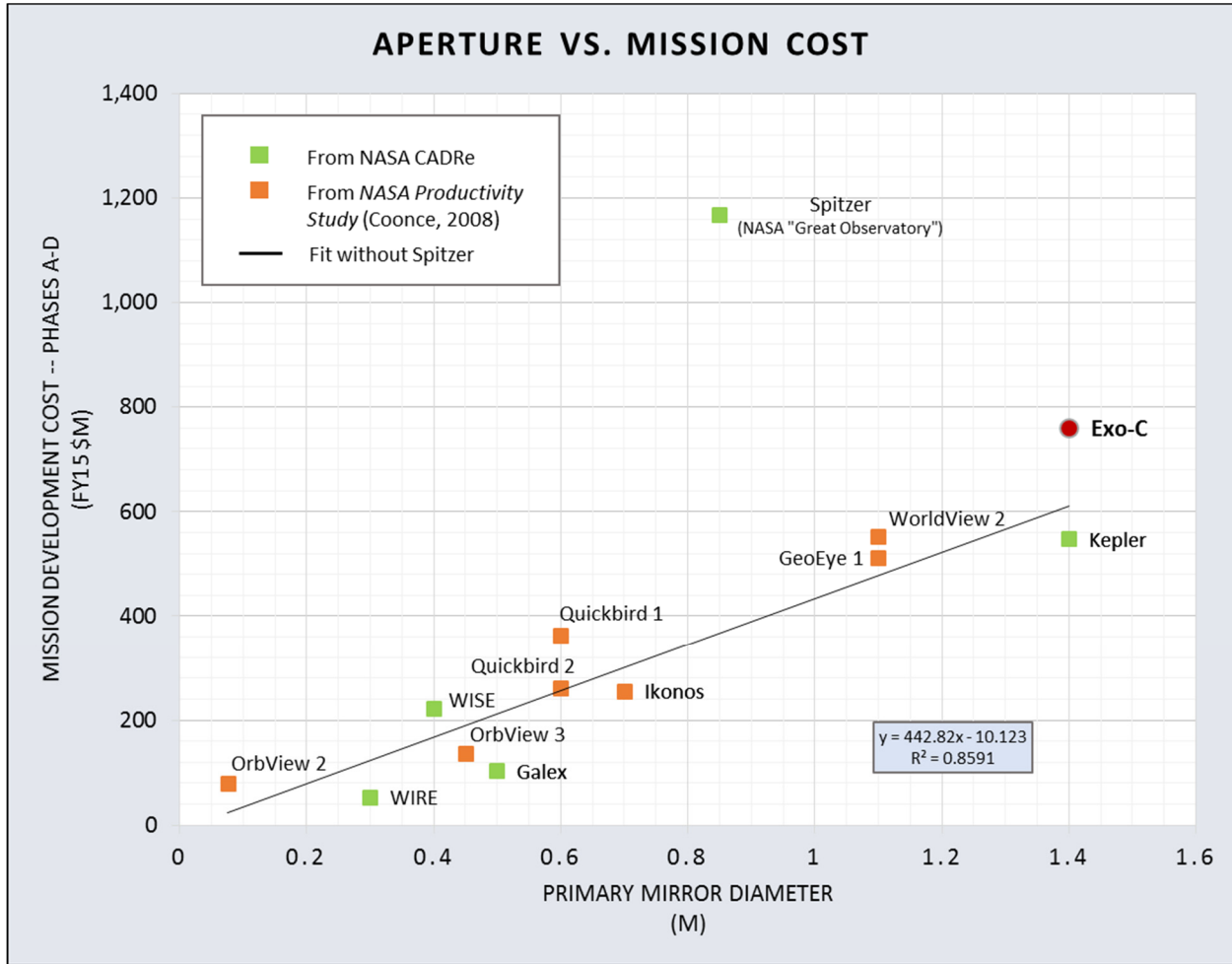
**Figure 7-1.** Mission development cost as a function of telescope primary mirror diameter for space telescopes smaller than 1.5 m. Exo-C exceeds the fitted curve of actual costs for its aperture. This is due to the conservative approach of adding 30% cost reserves in addition to the mass, power and schedule reserves.

Spitzer departs from the trend for a number of reasons. Its operating temperature (<5.5 K) requires the use of exotic materials (e.g., liquid helium coolant, beryllium optics) and greatly complicates the system design and the integration and test process. The mission suffered a number of delays related to the Challenger disaster and budget-driven redesigns that eventually made it one of the longest development efforts in NASA history. But the most significant departure is that Spitzer is a *directed* mission (one of NASA's four "Great Observatories") while the other NASA missions are *competed*. As a directed mission, Spitzer needed to address multiple science objectives and carry multiple remote sensing instruments in support of a wide research community. More objectives bring more requirements, adding complexity and cost to the overall mission. Competed missions are led by a single Principal Investigator usually looking to address a focused set of goals important to a much narrower group of researchers. Not surprisingly, most of the competed missions carry a single sensing instrument behind the telescope.

This common element in the competed missions—a single mission purpose—is shared by the commercial remote imaging missions. In addition, many aspects of the competed and commercial telescope mission architectures are similar. To keep missions cost low to enable

selection in a cost constrained competition, almost every winning NASA mission—from SMEX to New Frontiers—has relied heavily on commercial vendor participation. Buses, telescopes and ground systems are largely commercial for both telescope mission data groups. This being so, the apparently similar cost/aperture behavior is understandable and the merging of the two groups is reasonable. The early Exo-C CATEs received to date show a significant reduction in cost in comparison to CATEs for similarly sized telescope/coronagraph concepts evaluated during the last Decadal Survey. This is, in part, due to advancement in technology since the 2010 Survey, but the majority of the reduction comes from a ground-up design-for-cost approach adopted at the beginning of the Exo-C concept study. By making cost a top design priority, Exo-C has shown that a coronagraph mission with meaningful exoplanet science is achievable within a probe-class budget.

## 7.2    Schedule

Exo-C developed a concept schedule based on a Phase A start at the beginning of FY17, project Preliminary Design Review (PDR) in FY19 and a launch no later than December 31, 2024. Technologies requiring development must be at Technology Readiness Level (TRL) 5 by the start of FY17 and TRL 6 at the start of FY19.

The Exo-C schedule is shown in Foldout 7-1. This schedule was developed largely from the Kepler as-built schedule, including all technical delays and programmatically-driven funding delays. The overall schedule is 140 months long and includes 12 months of pre-Phase A development, 92 months of spacecraft and payload development (Phase A through launch), and 36 months of operations. Pre-Phase A technology development work is not included in the $1B cost cap and is discussed in §8. In keeping with the study charter, Phase A begins at the start of FY17. Formulation (Phases A and B) runs for 43 months and includes requirements definition,

system and subsystem design, and the start of procurements for long-lead items. It also encompasses the work needed to complete the technology development of the low-order wavefront sensor (LOWFS) and the coronagraph by the start of FY19. The flight system implementation (Phases C and D) takes 50 months and includes the fabrication, integration and test of the flight system. Implementation ends with the launch and initial on-orbit checkout of the flight system in July 2024. The critical path is highlighted in the schedule and runs through the detector procurement, coronagraph development, telescope and payload integration and test, flight system integration and test, and launch. Durations for the telescope, spacecraft bus, payload and flight system integration and test, and ground system development are all based on the actual time required to develop Kepler. The schedule for the coronagraph development was based on expert judgment for JPL instrument systems engineers with experience in developing complex optical observation systems. The schedule shows an overall margin of 6 months, which is in keeping with JPL margin practices for a schedule of this duration.

The Phase A through Phase D duration for Exo-C is 93 months, compared to 91 months for Kepler. At 91 months, Kepler had the longest Phase A–D schedule of any NASA Discovery or New Frontiers mission launched to date. The New Frontiers-class planetary missions are around the $1B cost cap placed on these studies so they represent comparable scope to the Exo-C mission concept. Of the dedicated telescopes launched by NASA since 2000, Wide-field Infrared Survey Explorer (WISE) and Galaxy Evolution Explorer (Galex) have respective developments times of only 87 and 72 months.

Upon review of the Exo-C schedule for the two diagnostic CATEs, the CATE team found no issues with the schedule and did not assign a schedule threat to either estimate.

It should be noted that both the Exo-C cost and schedule estimate show unusual conservatism when compared to actual completed mission costs and schedules (cost above 93% of similarly sized telescope missions based on earlier data fit, schedule above all Discovery and New Frontiers actual development schedules to date). Were a probe-class competition to be happen, proposed coronagraph missions similar to Exo-C could produce lower estimates based on more causal input such as vendor quotes and grass root estimates. To a point, lower concept estimates would still be seen as credible by independent reviews strongly connected to historic data.

## 7.3   Optional Descopes

While the current design meets the objectives of this study, there are a number of descopes that still remain before reaching the science floor. The two most apparent are a reduction in the size of the telescope to 1.3 m, and the elimination of the LOWFS. Initial evaluation shows that the reduction in the primary mirror diameter will reduce the number of targets that can be evaluated (and accordingly the science yield) over the currently planned mission life, but Exo-C will still produce an acceptable science return (see §4.4 and §4.8 for discussion on the aperture/science trade). From Figure 7-1, this 10-cm reduction would typically reduce the project's development costs by ~$46M. Thermal analysis performed during this study raises the question of the need for a LOWFS as part of this design. With the change to a flat panel thermal shield and the already benign thermal environment, analysis indicates that contrast stability during roll maneuvers meets performance requirements (see §5.6 for a discussion of the thermal design of the telescope). If subsequent analyses and tests confirm this initial finding, the LOWFS might be dropped from future designs. This would result in a cost savings of $5–6M.
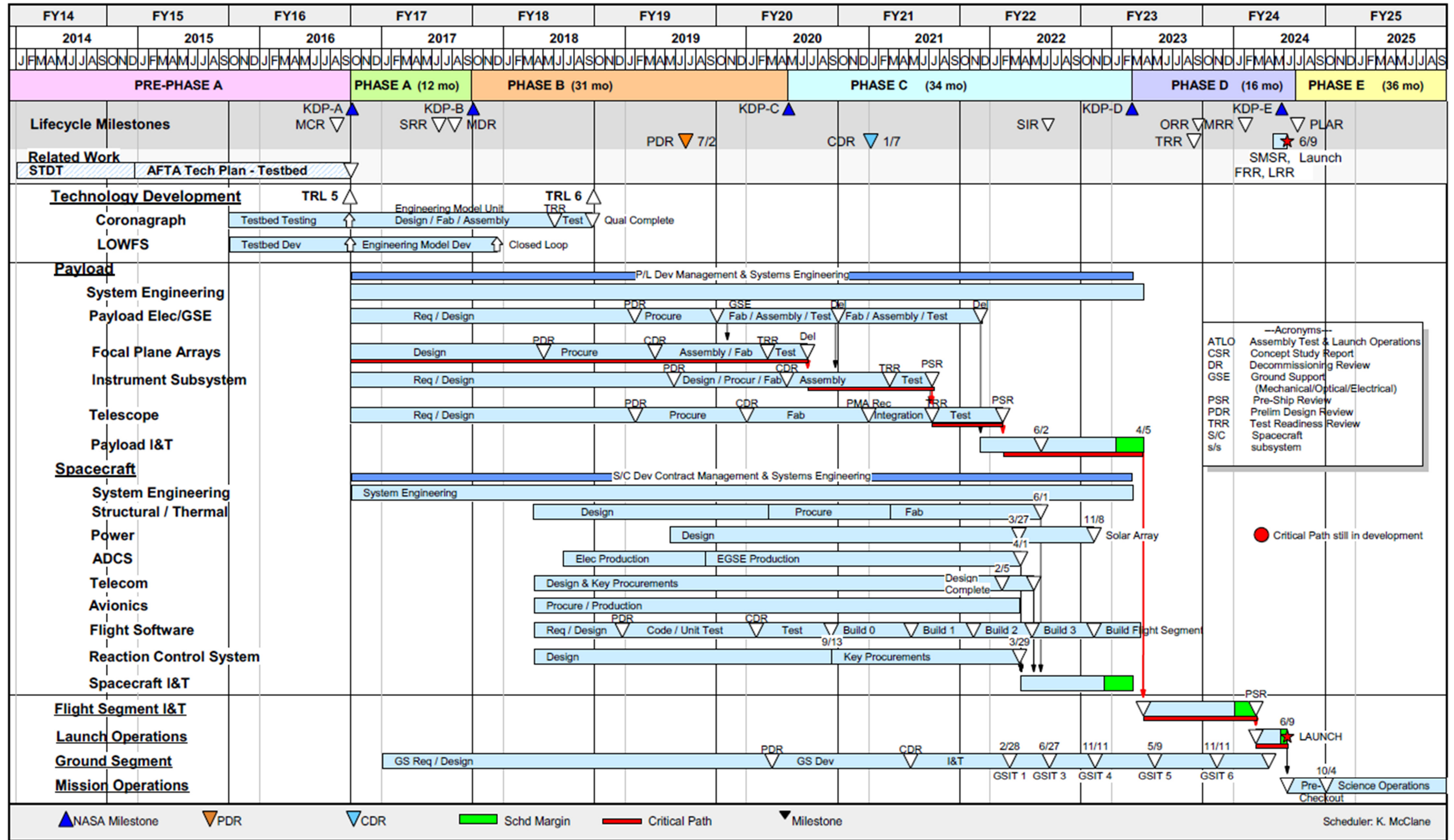
**Foldout 7-1.** Exo-C top level schedule.

# 8 Technology Needs Assessment

## 8.1 Exo-C Baseline Configuration and Future Trades

This section details the key technologies required for Exo-C, including a coronagraph, imaging detectors, wavefront correction with active optics, a spectrograph, and the need for flight qualification, supporting system models for prediction and validation, operational approaches, and analysis methods. Several of the technology needs for Exo-C were captured in Lawson et al. (2014).

The Exo-C architecture can support different "front end" coronagraph (occulter or apodizer) designs with minor modifications and still use the same "back end" key technologies (e.g., detectors, wavefront correction, and spectrograph).

Different coronagraph technologies may be baselined depending on the Exo-C program start date. In this report we have assumed a 2017 program start date. However, selection of the baseline coronagraph should be reassessed for a later program start date (such as 2020).

## 8.2 Technology Heritage

The Exo-C coronagraph instrument is a visible-wavelength optical system that is designed to take extremely high contrast images. The Exo-C coronagraph instrument makes use of several NASA-sponsored engineering design studies and technology investments over the past decade. These studies have brought many of the critical technologies needed for these components to an advanced state of readiness. NASA's Astrophysics Strategic Mission Concept Studies (ASMCS) program, which was completed in 2009, sponsored four relevant coronagraph mission studies: Actively-Corrected Coronagraphs for Exoplanetary System Studies (ACCESS) (Trauger et al. 2010), Pupil mapping Exoplanet Coronagraphic Observer (PECO) (Guyon et al. 2010), Extrasolar Planetary Imaging Coronagraph (EPIC) (Clampin et al. 2010), and Dilute Aperture Visible Nulling

Coronagraphic Imager (DAViNCI) (Shao et al. 2008). These studies developed the mission design and technology requirements for five types of coronagraph architectures: the hybrid Lyot, vector vortex, shaped pupil, pupil mapping phase-induced amplitude apodization (PIAA), and the visible nuller (VNC) coronagraphs. Over the past five years, NASA's Strategic Astrophysics Technology (SAT) Technology Development for Exoplanet Missions (TDEM) program has brought each of these coronagraph technologies to vacuum testbeds at JPL in order to test and improve their contrast performance. NASA plans to continue demonstrations of high contrast coronagraph technologies in a simulated space environment over the next few years. In addition, the Small Business Innovation Research (SBIR), Astronomy and Physics Research and Analysis (APRA) programs and institutional investments have made important contributions to technology readiness, including JPL's work with precision high-actuator count deformable mirrors now baselined for the Exo-C mission. As a result, Exo-C's critical technologies are well-positioned to advance to flight readiness.

## 8.3 Critical Technologies for Exo-C

In this chapter we discuss the current state of the technologies needed for high-contrast space coronagraphy. Key items include:

*Coronagraph.* The high-contrast coronagraph suppresses the starlight from the parent star such that the reflected or thermal light from the exoplanet can be detected. Coronagraph architectures considered by Exo-C include optical elements such as masks, apodizers, occulting spots, and Lyot stops. In earlier trades (see Appendix B), shaped pupil masks and nulling coronagraphs were also considered.

*Detectors.* Low read-noise detectors with high sensitivity across the band of interest are useful for both the imaging detector and spectrograph, such as an electron multiplying CCD (EMCCD). Ideally, the detector would

have enough pixels to sense the wavefront across the entire dark hole region created by the coronagraph (for the current Exo-C design, this requires a 2K×2K detector).

*Wavefront correction (WFC).* Active optical elements and algorithms are needed to perform both *low-order* (fast, high bandwidth) and *high-order* (slow, low bandwidth) wavefront correction to maintain raw contrasts better than $1\times10^{-9}$. Low-order correction helps to manage the effects of telescope jitter and pointing as well as thermal drift. High order correction manages more slowly varying and higher spatial frequency speckles and noise in the image to create a high-contrast "dark hole" search space for exoplanets.

- *High-order* *wavefront correction is performed by a key technology element, the high-actuator count deformable mirror (DM). The DM suppresses high spatial frequency speckles and creates and maintains the high contrast "dark hole" in the images.*

  ▪ The more actuators on the DM, the higher the order of spatial frequencies that can be corrected, corresponding to larger angular separations in the image plane. DMs with higher actuator counts will help to increase the angular extent of the dark hole, which is Nyquist-limited to N λ/2D, where N is the actuator count mapped across diameter D of the primary mirror.

  ▪ For example, the dark hole extends to an angular radius of 1.9 arcsec for λ=550 nm, N=48, D=1.4 m. To achieve the desired contrast of $1\times10^{-10}$, the DM should be able to control its surface on the order of λ/10,000 (Lawson 2013).

  ▪ The coronagraph detector is used as a focal plane wavefront sensor for high order correction.

- *Low-order* *wavefront correction is performed to improve contrast and reduce the amount of fast, large-amplitude correction needed from the DM. Low-order*

*wavefront correction is split into two instruments. The FGS monitors the rapid line of sight (tip/tilt) variations due to telescope jitter while the LOWFS monitors the slow thermal drift. The FGS and the LOWFS use starlight rejected by the coronagraph. The FGS/LOWFS compensate for these low order errors with active optical elements. For line of sight errors, the FGS is in closed loop with the FSM to keep the starlight centered on the coronagraph mask. The LOWFS monitors aberrations beyond line of sight. It requires three components. A passive optical element that maps wavefront distortions to a detectable intensity measurement, a fast detector with which to make the intensity measurement, and at least one active optical element that is informed by an analysis of the wavefront measurement and corrects the low order distortions. The passive optical element is located at or before the coronagraph occulting mask, active optical element(s), and fast detector.*

  ▪ Two LOWFS systems initially considered for Exo-C were the Zernike Wavefront Sensor (ZWFS) (N'Diaye et al. 2013) and the Coronagraphic Low Order Wavefront Sensor (CLOWFS) (Guyon et al. 2009).

  ▪ ZWFS has been baselined as discussed in §5.

- *WFC flight electronics. Development of flight-like electronics and full environmental system testing with post-test performance validation for deformable mirrors. The flight-like electronics should include miniaturization of the mirror drivers, with the goal of using efficient Application Specific Integrated Circuits (ASICs).*

- *Two-DM system-level demonstrations. While most lab experiments and demonstrations currently use only one DM, the flight system will use two DMs, and test setups should be upgraded and configured*

*to test hardware and software early on (Lawson 2013).*

- **Combined FSM and DM.** *It would be efficient and reduce the number of optical surfaces in the system to use a DM that is mounted on an FSM base. This is because both the FSM and DM are ideally placed in the exit pupil of the telescope. Separating the FSM and DM functions means creating one additional pupil plane, which would add two off-axis parabolas as well as one more mirror surface, plus the additional volume and alignment sensitivity of these elements. The extra optics increase the size, weight, and complexity of the overall system. In addition, these are all upstream of the coronagraph in the highly corrected optical beam, which is another important factor to consider when minimizing the number of optical elements and critical alignments.*

  - One approach to combining the FSM and DM is a tilt platform for high spatial frequency deformable mirrors, which combines the functions of a deformable mirror and tilt mirror into a single package. The tilt stage is designed using PMN solid state actuators which are driven by the same driver electronics as the DM. The actuators require low power and generate an order of magnitude greater force than typical voice-coil driven systems. Such a configuration can achieve angstrom level displacement accuracy with its tip/tilt system, unlike other mechanical actuator devices. These units have been developed but not yet demonstrated or qualified for flight. This effort would improve efficiency and reduce complexity.

**Integral field spectrograph.** A spectrograph is used for characterization of exoplanet atmospheres. The spectrograph will disperse the light from the exoplanet using an integral field spectrograph (IFS) with resolution R=70. The spectrograph consists of passive optical elements such as an array of microlenses and a dispersing element. It also requires a low pixel-to-pixel crosstalk and a moderate format detector with low read noise.

**Instrument system engineering models.** Such models are typically included as part of program development to assess design trades, for example, the valuable models used to develop the baseline design in §5. In addition, the program would benefit from additional investment to develop even higher fidelity dynamic and thermal models of the telescope and spacecraft bus and validate these with laboratory tests early in the program in order to confirm optical stability and the associated wavefront errors. Related activities include:

- *Laboratory demonstrations and performance model validation.*
- *Environmental testing and flight qualification of a star, planet, and optical telescope simulator with the telescope-specific pupil obscuration.*
- *Development and validation of post-processing algorithms.*

**Test facilities and trained staff.** The JPL High Contrast Imaging Testbed HCIT) is the workhorse behind many of the high contrast milestones (with preliminary results reported at other facilities). However, the HCIT is oversubscribed with new experiments sometimes waiting years to gain access. We recommend that the HCIT take the steps necessary to consistently support two user communities: 1) flight mission development testing, integration, and validation, and 2) new investigator-led research efforts pursuing not-yet-baselined approaches. Too often the latter is sacrificed in favor of the former. If necessary, the ExEP should construct new facilities to assure that both these communities are supported.

## 8.4   Technology Needs

While the Exo-C technologies are all based on laboratory-tested techniques, some areas have been identified where further development is needed to raise the technology from

technology readiness level (TRL) 4 to TRL 5. We note that some of these technology development needs are shared with the AFTA coronagraph program (JPL Document D-81964), specifically, the demonstration of coronagraph contrast milestones and the spectrograph detector and readout capabilities. There may be additional overlap in some of the AFTA risk reduction efforts such as mask mechanisms. There are some differences in that the Exo-C telescope aperture is smaller, the pupil is unobscured, and the Exo-C observatory stability is excellent. This results in Exo-C prioritization of coronagraph technologies that maximize throughput (HLC, PIAA, VVC). Exo-C does not require management of a complex and obscured pupil, tasks at which other coronagraph candidates initially considered have an advantage, such as the Shaped Pupil and VNC. Still, the Exo-C technology development program expects to significantly benefit from technology plans already in place for the AFTA program.

In this section, we first present the "common" key technologies that are applicable to the Exo-C architecture and that are not specific to the choice of which coronagraph (occulter or apodizer and associated optics) is selected. We next present the three leading coronagraph candidates that were extensively considered, the Hybrid Lyot Coronagraph, the Phase Induced Amplitude Apodization Coronagraph (PIAA), and the Vector Vortex Coronagraph (VVC).

Exo-C baselined the Hybrid Lyot Coronagraph (HLC) for a 2017 program start because it has achieved broader bandwidth and deeper contrast in demonstrations to date. Exo-C also considered the PIAA and the Vector Vortex coronagraphs for their small inner working angle capabilities, and these should be revisited in the case of a 2020 or later program start. The Shaped Pupil and VNC coronagraphs may also be reassessed for a 2020 or later program start, especially if a larger aperture is considered, as aperture size changes the IWA.

## 8.4.1 Detectors

Exo-C uses imaging detectors in both the filter imaging camera and the imaging spectrograph. These have different intended functions. The imaging detector has wider wavelength-band channels and is intended for planet searches and very coarse R=5 characterization. Ideally the detector should have enough pixels to sense the wavefront across the entire dark hole region created by the coronagraph. The IFS can be used as a wavefront sensor, although technology development work remains to be done on how to best use data from the fourteen narrowband channels available in a 20% bandpass to refine and accelerate the process of setting the DM. The spectrograph disperses light across its pixels, and is intended for R=70 spectral characterization of exoplanet light. The IFS thus needs low read-noise detectors that are extremely sensitive across the band of interest, such as an electron multiplying CCD (EMCCD). The coronagraph imaging camera can use either a CDD or EMCCD. It may be programmatically more efficient to use the same detector for both the coronagraph and the IFS. The coronagraph imaging camera also would benefit in reduced integration time from using a EMCCD, but Exo-C mission requirements and the desired search numbers can be achieved without using an EMCCD for the coronagraph imaging detector; EMCCD technology is currently only required to meet mission requirements for the IFS detector.

The two separate detectors also each contribute in different ways to speckle discrimination. It is also important that any detector technology development consider this intended use. The coronagraph detector can be used for spatial discrimination taking images at two different roll angles. The IFS can do spectral discrimination of speckles.

As baselined, the best approach appears to be using the coronagraph imaging detector for

search and initial characterization, as it takes about 5–10 times longer to achieve a signal-to-noise ratio of 5 in a 10% band on the IFS detector vs. using the coronagraph detector with its 20% band. (Note the 5–10 range given is due to the dependence on the assumptions made regarding read noise and dark current for each detector).

### 8.4.2 Wavefront Correction

#### 8.4.2.1 Deformable Mirrors for Wavefront Control

Precision high actuator-count deformable mirrors are needed for optical wavefront control to meet mission contrast requirements. High-order surface figure control (i.e., 24 spatial cycles across the pupil with a 48×48 actuator DM) is used along with the coronagraphic apodizers, masks, and stops to achieve the high contrast dark field coronagraphic images.

Two deformable mirrors would be used in a flight experiment configuration. Only very recently have ground validation experiments taken place using two DMs.

There have been several previous as well as ongoing investments in development of commercial DM technology that will achieve Exo-C's mission requirements. These investments include environmental testing of commercial DM products (Lawson 2013). The baseline DM for Exo-C that is paired with the Hybrid Lyot Coronagraph is manufactured with a continuous fused silica mirror facesheet controlled by a 48×48 array of electrostrictive actuators. This technology has been used in coronagraph validation testing over the past decade in the vacuum testbed (HCIT) environment at JPL (see Figure 8-3 and (Trauger 2007)). High contrast results in HCIT have been achieved with such a 32×32 DM. High-contrast results have also been achieved in the NASA ARC testbed and at Lockheed Martin using a vacuum-compatible 32×32 MEMS DM.

Recent three-axis vibration tests have been completed with flight-configured DMs. Further thermal and radiation testing in the next two years will bring the DM technology to TRL 6.

#### 8.4.2.2 Wavefront Sensing and Control Algorithms

Wavefront sensing algorithms have been developed and demonstrated for high actuator count deformable mirrors in an Exo-C-like configuration, using the coronagraph imager as the sensor. These algorithms improve contrast iteratively by introducing diversity in the images with the two DMs. The wavefront errors are estimated and controlled with updates to the DM settings and produce high-contrast exoplanet discovery fields. Algorithms such as speckle nulling, electric field conjugation (EFC), and stroke minimization have all been demonstrated on the HCIT. Speckle nulling is a slower algorithm than EFC, but is less sensitive to model errors and is often used as a limiting factor diagnostic tool.

These demonstrations used "static" optical systems in earlier SAT/TDEM programs and now need to be extended to "dynamic" systems that include the predicted effects of telescope pointing jitter and thermal drift in the Exo-C observatory systems. Current high-fidelity dynamic and thermal models for the Exo-C observatory systems will guide future broadband algorithm developments.

#### 8.4.2.3 Modeling, Characterization of Sensitivity, and Error Budgets

Coronagraph modeling has made significant advances as a result of several NASA-funded modeling studies (Krist 2013). Available modeling tools include approaches such as high accuracy diffraction, geometric remapping with wave propagation corrections, and end-to-end system models.

Testbed models are ideally run in parallel with laboratory tests to validate our understanding of test data. Any discrepancy is investigated to identify its source. Once

identified, the source is either eliminated or incorporated into the models and calibrated. These calibrated models are then used to predict performance, test the importance of suspected limiting factors, help develop wavefront control algorithms and tune optical layouts, and develop realistic error budgets for tolerable levels of wavefront error and misalignment.

A major modeling effort is also being carried out by the AFTA program to characterize expected thermal and mechanical environmental instabilities on orbit, and replicate similar disturbances in the lab. These results are being used in the coming years to estimate the corresponding magnitudes and temporal characteristics of low order error and component misalignments. While the AFTA model development efforts will benefit Exo-C by advancing the state of the art, it is important to develop models that are specific to the telescope and optical configuration of each mission. There are substantial differences between the implementations of AFTA and Exo-C, and funding should support models that include high fidelity representation of the specific mission configuration.

### 8.4.2.4    Low Order Wavefront Sensor

The low-order wavefront sensor (LOWFS) is a useful capability for wavefront maintenance during the science measurements. The original idea is to image light reflected by the focal plane mask and use the analyzed image to measure low-order modes (c.f. (Guyon et al. 2009)). Exo-C's baseline implementation is to not update during science observing, but rather in between observations if needed. The low-order modes corrected will depend on the configuration of the LOWFS, the FGS, and the DM. Corrections are computed and sent to either the deformable mirrors or the secondary mirror.

The Zernike Wavefront Sensor (ZWFS) is a low-complexity approach to WFS, as shown in Figure 8-1 (N'Diaye et al. 2013). A phase mask in the form of a small circular depression in a glass plate is placed at the focal plane where the star image is formed, introducing a phase change for the complex amplitude of the central part of the star image going through the mask. This leads to interference between the electric fields going through and outside the phase disk in the relayed pupil plane, producing an intensity pattern that is related to the wavefront aberrations. The exact intensity encoding of wavefront errors depends on the size and depth of the mask, and quasi-linearity is achieved with an appropriate choice of these parameters.

The fundamental operation of the sensor is to introduce a phase shift in the core of a point-spread function ($1–2$ $\lambda/D$) at the focal plane conjugate to and/or coincident with the coronagraph focal plane. In the subsequent pupil plane, phase variations in the input pupil are imaged as intensity variations. This method is simple yet sensitive.

The FGS and LOWFS configurations for Exo-C are shown in Figures 5.5-2 and 5.5-5 respectively, with LOWFS predicted performance in Figure 5.10-9. The ZWFS has been chosen for its simplicity, excellent mechanical stability and theoretically ideal performance. AFTA-C will demonstrate this LOWFS architecture in the HCIT to verify it has the necessary subnanometer resolution and stability in a flight-like environment.

The current TRL of the ZWFS is estimated to be 3 based on work performed in N'Diaye et al. 2013, namely, experimental laboratory studies to validate the analytical predictions of the Zernike phase-contrast optical element. At JPL, a static Zernike phase-plate has been fabricated, but its performance has not yet been assessed at the same level as the N'Diaye group.

To mature this technology for Exo-C, it would be useful to assess possible improvements in throughput by integrating the phase-contrast optical element with the coronagraph focal-plane-mask optical element. Supporting detailed analyses to quantify the
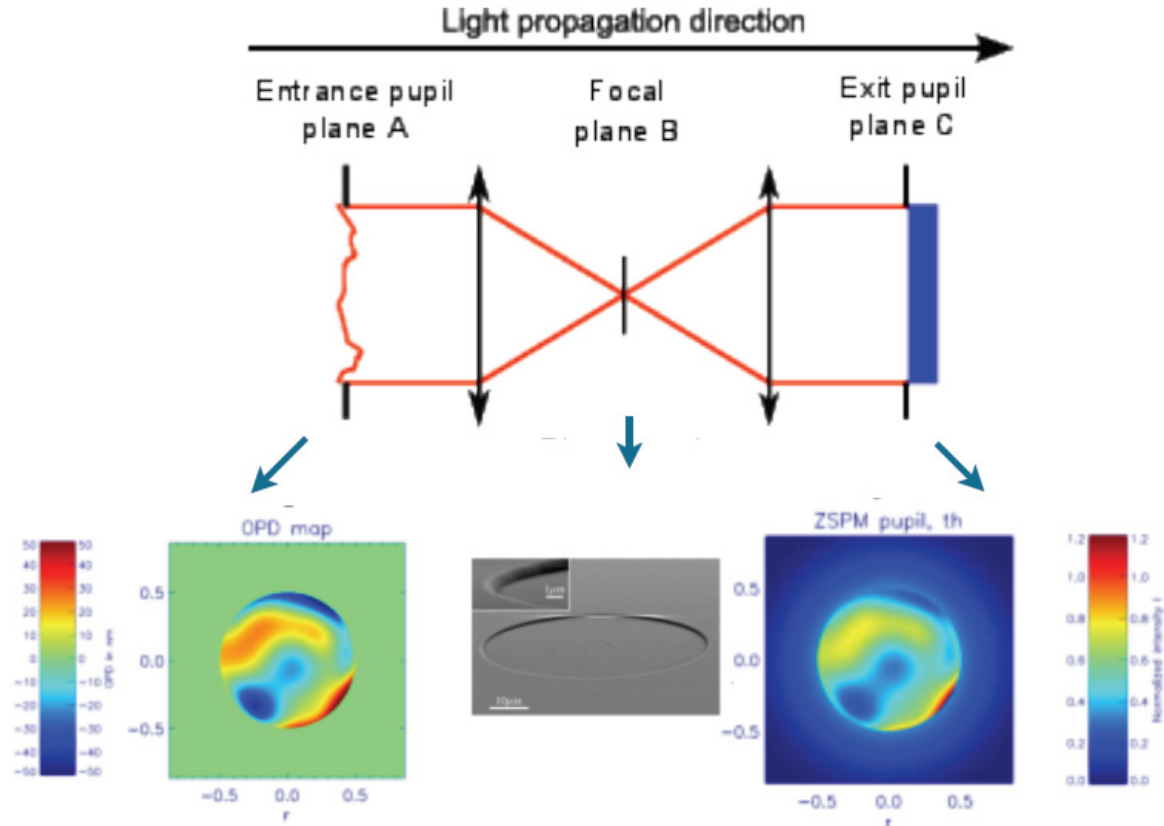
**Figure 8-1.** Zernike phase plate wavefront sensor configuration (N'Diaye et al. 2013). See Figures 5.5-2 and 5.5-5 for the Exo-C FGS and LOWFS schematic, and Figure 5.10-9 for the LOWFS predicted performance.

sensitivity of this approach, based upon realistic assumptions about the optical system and the wavefront sensing detector and pupil sampling, would be valuable. These analyses should then be validated by laboratory demonstration.

*LOWFS technology development process:*

1. Refine requirements for the LOWFS.
2. Establish baseline assumptions of system parameters.
3. Conduct analysis to determine architecture and interactions of coronagraph and low-order sensor.
4. Perform analysis of LOWFS to determine fundamental operation.
5. Specify and fabricate brassboard LOWFS/coronagraph focal plane mask.
6. Demonstrate brassboard LOWFS and coronagraph in open-loop operation consistent with error budget.

7. Demonstrate brassboard closed-loop control with LOWFS as sensor in representative disturbances and within a representative control scheme.

### 8.4.3 Integral Field Spectrograph

Spectroscopic characterization of exoplanet atmospheres is one of the primary science goals of the EXO-C mission and the integral field spectrograph (IFS) has been chosen as the most promising technology for efficient capture of the spectra. The IFS is a proven technology utilized widely on large ground-based telescopes, but the IFS has yet to be demonstrated in a flight environment.

The Exo-C mission's science requirements specify its imaging and spectroscopic capabilities. In addition to imaging and spectroscopy, the instrument must be able to maintain high contrast between each of the spectra. The instrument

will be used for 1) spectral characterization of the science targets (e.g., exoplanets and circumstellar disks), 2) starlight suppression in post processing, and 3) focal plane wavefront sensing. IFSs deployed on ground-based observatories are now capable of taking thousands of spectra simultaneously. By the end of the decade, the James Webb Space Telescope will fly two IFSs: the Near InfraRed Spectrograph (NIRSpec) and the Mid InfraRed Instrument (MIRI).

Lenslet-based IFSs are very similar to conventional slit-based spectroscopy. The slit is replaced by a lenslet array that is used to separate the spatial locations in a focal plane. Each lenslet compresses the light incident upon it into a spot one focal length behind the lenslet array, and the entire array creates a grid of spots in the lenslet focal plane. These spots are passed into a conventional set of spectrograph optics that include collimation, dispersion, and focusing onto the IFS detector. The general concept of a lenslet-based IFS is shown in Figure 8-8. The first lenslet-based IFS was a visible-light instrument at the Canada France Hawaii Telescope (Bacon et al. 1995), and later it was proven to also be viable in the infrared with the OH-Suppressing InfraRed Imaging Spectrograph (OSIRIS) IFS at Keck (Larkin et al. 2006). Now, all of the next-generation, ground-based, high-contrast imaging systems include lenslet-based IFSs as their science cameras (e.g., Apache Point Observatory/GIII, Palomar/P1640, Gemini Planet Imager (GPI), Very Large Telescope (VLT)/Spectro-polarimetric High-contrast Exoplanet Research (SPHERE), Subaru/Coronagraphic High Angular Resolution Imaging Spectrograph (CHARIS)). The selection of lenslet-based IFSs for all ground-based high contrast instruments was based on a complementary set of science and instrument requirements that are also imposed on Exo-C. The science from lenslet-based IFSs on ground observatories support placing this instrument at TRL 4.

Although no IFSs have flown in space to-date, the only nontraditional optic in a lenslet-based IFS is the lenslet array itself. Lenslet arrays have been used to conduct science at low contrast on ground-based telescopes for the past 18 years. However, lenslet arrays have never been demonstrated to meet the spectral crosstalk requirements (e.g., preserving intrascene contrasts of $10^3$ for giant planet studies, $10^4$ for terrestrial planets) for a space-based, high-contrast imaging IFS. Recent designs suppress the starlight to preserve the $10^4$ contrast, but this technology has not been demonstrated in a laboratory. Therefore, high-contrast lenslet arrays are at TRL 3. High-contrast lenslet arrays must be matured as soon as possible.

***IFS milestones:***
1. Develop a verified error budget.
2. Develop calibration and operational procedures for a high-contrast IFS.
3. In a testbed demonstration, characterize the performance limits of the high-contrast IFSs.
4. Demonstrate high-contrast (e.g., $10^{-9}$) at small angular separations (e.g., $3\,\lambda/D$) over a large spectral bandpass (e.g., 20% bandpass).
5. Compare the IFS model predictions with experimental data to validate the model.

NASA has funded the development of a prototype IFS to demonstrate the needed performance (McElwain et al. 2014). After 1.5 years of development it will be delivered to the HCIT in late 2015. During 2016 it will be integrated with the HCIT at JPL and its performance demonstrated. It will then become a facility instrument to support multiple users and coronagraph performance demonstrations at the HCIT.

### 8.4.4 Post-Processing of Raw High-contrast Data

Science mission studies assume that post-processing of raw image data will be employed

to suppress background speckle noise. These algorithms leverage the known imaging characteristics of the observatory, and can be developed and demonstrated on the testbed once the observatory dynamic and thermal models have been perfected. Several mature speckle subtraction and PSF-fitting techniques exist to suppress speckle noise in post processing by a factor of 10 or more (Marois et al. 2010) and are critical in order to reach the ultimate limits of the instrument. These include difference imaging: spectral (SDI), angular (ADI), polarization (PDI), coherence (CDI); as well as LOCI (locally optimized combination of images), and PCA (principal component analysis). In addition, low order dynamic errors (such as vibration and decentering) can be measured by the LOWFS and later subtracted in software if they are too fast to be corrected directly. Some of these techniques have been demonstrated in space with HST coronagraphy (Krist 2006).

As an example, Figure 8-2 shows a test demonstrating the extraction of synthetic planet signals below raw contrast in lab data using CDI and matched filtering. CDI in particular is a technique that can be very useful in space but has not seen much use on the ground because it requires static speckles.

Such speckles can be calibrated and subtracted even when the DM cannot remove them (e.g., amplitude errors in the 360° field of view). These techniques require no special hardware beyond what exists already for raw contrast demonstrations. Further development of these techniques is needed to assess and realize their benefit.

### 8.4.5 Coronagraph

Exo-C baselines the Hybrid Lyot Coronagraph (HLC). Exo-C also considered the PIAA and the Vector Vortex coronagraphs. HLC was selected for the baseline, and the HLC team will continue development to improve its inner working angle (IWA). The state of the art demonstrated in lab with the HLC is a contrast of $2\times10^{-10}$ with a 2% and $2\times10^{-9}$ with a 20% bandwidth at 3–15 $\lambda/D$ with linear 4th order band-limited Lyot hybrid masks (Lawson et al. 2014).

PIAA and VVC remain contenders and their teams will continue development to improve broadband contrast. The Exo-C mission can be configured to support any of these three coronagraphs. The Exo-C team advises reassessing the priority of the coronagraph candidates if the mission starts later than 2017.
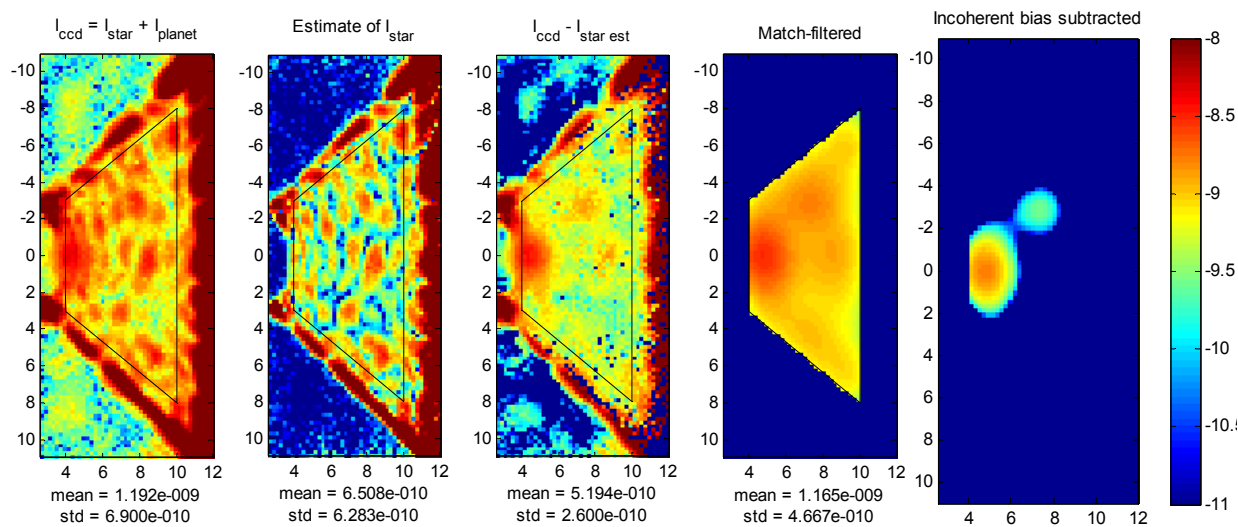


**Figure 8-2.** Extraction demonstration of synthetic planet signals below raw contrast in post-processing (at HCIT). Panel 1: raw contrast image; 2: EFC estimate of coherent speckles; 3: Coherence Difference Imaging (CDI) approach to removing coherent speckle; 4: matched filtering; 5: incoherent bias subtraction (zodi, exozodi, and stray instrument light) (Belikov et al. 2007a).

Five different candidate coronagraph types have completed TDEM development and performance demonstrations in JPL's HCIT as part of the SAT/TDEM program. Three of these (including two Exo-C candidates, the hybrid Lyot, and PIAA, as well as the shaped pupil coronagraph) will advance to TRL 5 under the Exoplanet Exploration Program (ExEP) in the coming two years as part of the WFIRST-AFTA coronagraph technology development (Poberezhskiy JPL Document). The WFIRST-AFTA telescope architecture is substantially different than Exo-C's (WFIRST-AFTA is on-axis with spiders), which leads to a different prioritization of candidate coronagraph types.

### 8.4.5.1 Baseline Design, Hybrid Lyot Coronagraph

HLC has a small focal plane mask with carefully optimized layers of nickel and dielectric which create a profile of intensity and phase transmission that stops the bulk of the starlight and sends the rest of the light toward a so-called Lyot stop in the pupil plane, as shown in Figure 8-3 and Figure 8-4. The Lyot stop blocks the remaining starlight but passes the light from the planet. The hybrid Lyot masks that have been developed to date are image-plane masks that appear as a fringe pattern of metal deposited on glass, with an additional (thus hybrid) layer of dielectric to compensate for residual phase errors.

### 8.4.5.2 Alternate Coronagraph: PIAA

This section describes the PIAA coronagraph option for Exo-C. The PIAA coronagraph uses pairs of aspheric mirrors to reshape the pupil plane intensity distribution, resulting in a Gaussian-like (prolate spheroidal) distribution which eliminates diffraction sidelobes. In a flight configuration, there would be two DMs located before the input PIAA optics and a second (inverse) set of PIAA optics after the focal-plane mask prior to the science camera.

Most of the work on PIAA has been carried out at NASA JPL's HCIT and the

Ames Coronagraph Experiment (ACE) testbed at NASA Ames Research Center (ARC) and a vacuum chamber at Lockheed Martin ATC, as

(a)



(b)



(c)
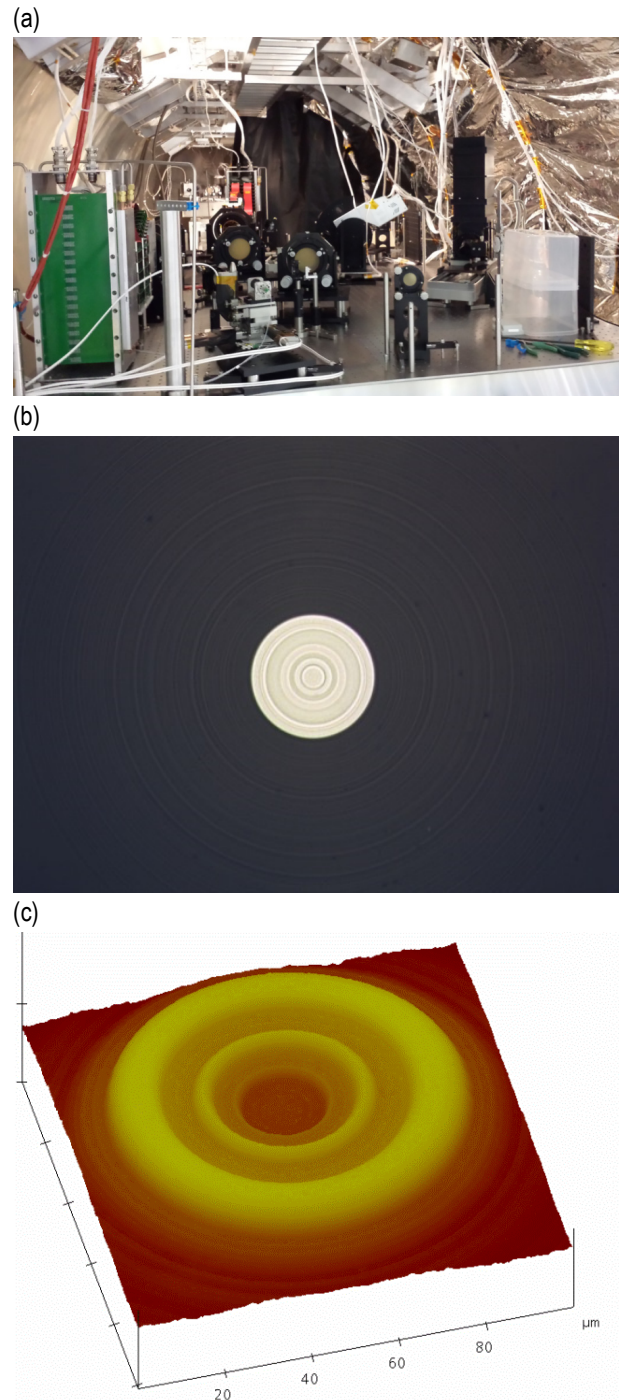


**Figure 8-3.** (a) Hybrid Lyot coronagraph testbed moving into a vacuum tank at JPL HCIT for commissioning and starlight suppression experiments; circular hybrid Lyot coronagraph mask imaged under (b) optical, and (c) atomic force microscope (Poberezhskiy 2014).
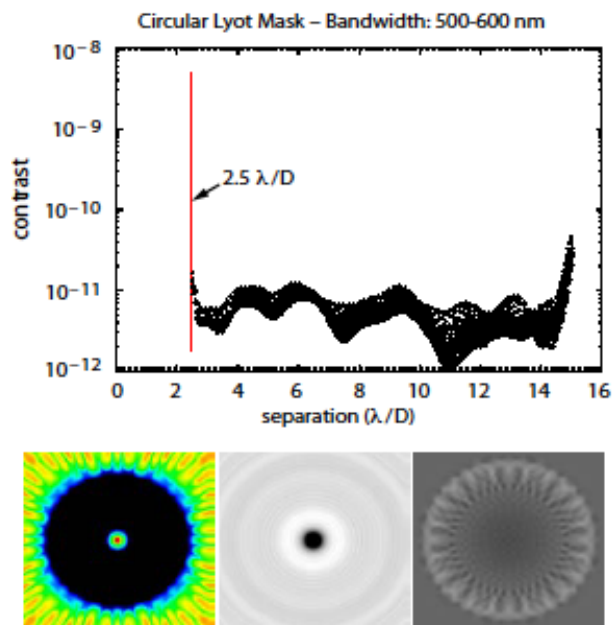
**Figure 8-4.** Ideal performance of circular HLC mask with raw contrast of $5.3e^{-12}$ from 2.5 to 15 $\lambda$/D and 48×48 actuator DM. Simulations are still being refined that show predicted performance with jitter at ~$5e^{-10}$ (Trauger 2012).

part of the technology development under the TDEM program, the Explorer program, and internally funded work.

The 2009 and 2010 TDEM effort with PIAA demonstrated mean raw contrasts of $1.0\times10^{-8}$ with a 10% bandwidth in a field of $10\ (\lambda/D)^2$ extending from 2.2–4.6 $\lambda$/D. Raw contrasts of $1.3\times10^{-10}$ were demonstrated in monochromatic light.

All of the PIAA components have been tested in a vacuum environment in lab, but not under flight-like conditions and are therefore at TRL 5. A simplified version has met Exo-C inner working angle (IWA) and raw contrast requirements in vacuum with monochromatic light (Guyon et al. 2014a), while broader band demonstrations have also been made at less favorable contrast (Guyon et al. 2014b).

A system functionally similar to the Exo-C layout has also been tested at Lockheed Martin ATC as part of the EXCEDE technology development (Belikov et al. 2013). However, the existing demonstrations have not been tested under realistic thermal and vibrational

environments expected on orbit. Planned technology development efforts for WFIRST-AFTA will demonstrate PIAA technologies to TRL 6 by 2018, and there are useful similarities between the Exo-C and WFIRST-AFTA missions even if there are differences in exact configuration and expected disturbances.

Several PIAA optics have been successfully manufactured and tested, including sets of Axsys-made PIAA lenses and three sets of PIAA mirrors: a "first generation" dual set made by Axsys and a "second generation" set made by Tinsley (Figure 8-5). These were tested at NASA ARC and Lockheed Martin ATC (for the EXCEDE project), achieving inner working angles of 1.2 $\lambda$/D with $1.8e^{-7}$ contrast between 1.2 and 2.0 $\lambda$/D in monochromatic light (surpassing required EXCEDE performance); as well as at JPL, achieving contrasts of $5\times10^{-10}$ at a less aggressive IWA of 1.8 $\lambda$/D in monochromatic
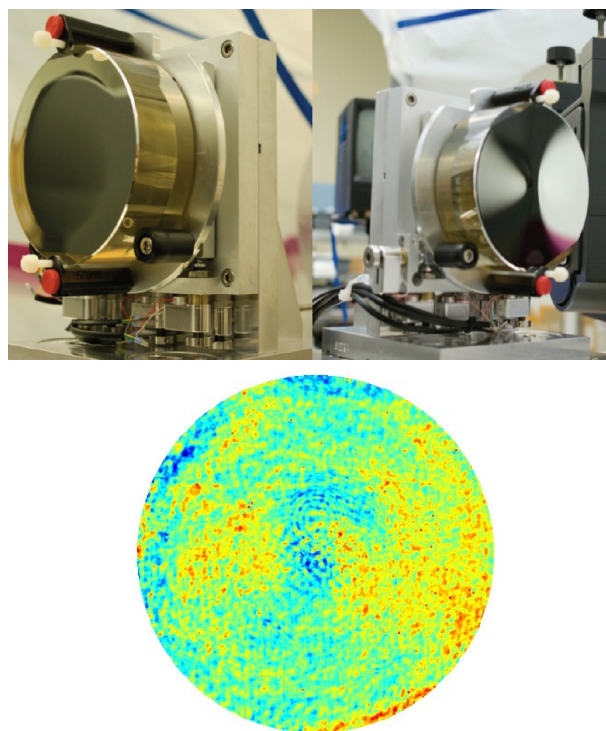


**Figure 8-5.** PIAA mirrors manufactured by Tinsley (top) and a surface error map of the second mirror (bottom) showing a surface error of 3.8 nm rms (Image source: http://exep.jpl.nasa.gov/files/exep/10_Belikov_2013_ExoPAG_v3.pdf).

light (Belikov et al. 2013).

The Exo-C PIAA design uses a preapodizer, a hard-edged focal plane mask with 2 λ/D inner working angle, and beam shaping optics with curvature only half that of pre-2014 designs. It is less challenging than previous PIAA designs both in terms of the mirror manufacturing and the telescope pointing/stability requirements. Prior laboratory experience gives confidence that it should achieve better performance than previous PIAA designs. An implementation of the Exo-C PIAA design in the HCIT is needed to verify this expectation.

### 8.4.5.3  *Alternate Coronagraph: Vector Vortex*

The vector vortex coronagraph (VVC) applies a spiral phase wrap to the stellar Airy pattern by means of a focal plane phase mask. Recent TDEM work in the HCIT has already demonstrated monochromatic light suppression below $10^{-9}$ for the VVC. Specifically, an average suppression of $5\times10^{-10}$ has been obtained in monochromatic light for VVC dark holes covering both 2–7 λ/D and 3–8 λ/D in the HCIT. Figure 8-6 shows radially-averaged contrast data from two such dark-hole runs, where the suppression is seen to be below $10^{-9}$ everywhere but in the innermost 2–3 λ/D bin, where it is a factor of 2 higher.

VVC tests with light covering a broader band were also carried out in the HCIT, using a supercontinuum laser source. A dark half-hole over the region of 1.5–9.5 λ/D for the central 2% band of light is shown in Figure 8-7. Over the full 10% band, this same dark hole region shows an average suppression of $9\times10^{-9}$. Thus, the VVC has already demonstrated quite deep contrasts inside the default inner working angle of the probe mission under consideration, which is at 2 λ/D.

Vortex mask performance must account for the effects of 1) central defect in which the vortex structure loses its proper orientation, 2) ghost reflections from the interfaces within the vortex's layered structure, and 3) bandwidth.

*1. VVC central defect.* Near the center of the vortex, the liquid crystal polymer (LCP) layer tends to lose the desired orientation pattern, as a result of small misalignments of the rotation axes in the manufacturing processes, although at small enough scales, the elasticity of the polymers will contribute to this degradation. A central defect allows starlight at the center of the Airy pattern to leak through the center of the mask without being affected properly by the vortex, and so the size of the
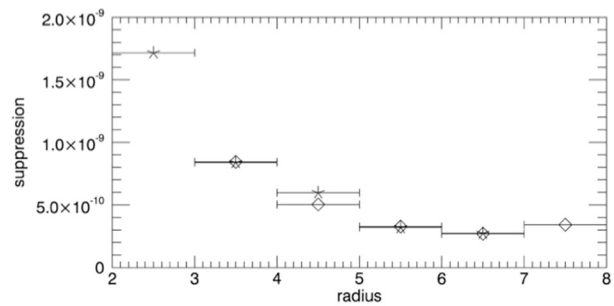


**Figure 8-6.** Radial contrasts for two VVC monochromatic nulling runs that targeted dark holes covering 3–8 λ/D (diamonds) and 2–7 λ/D (asterisks). Each point gives the average suppression over radial bins 1 λ/D wide (Serabyn et al. 2013).
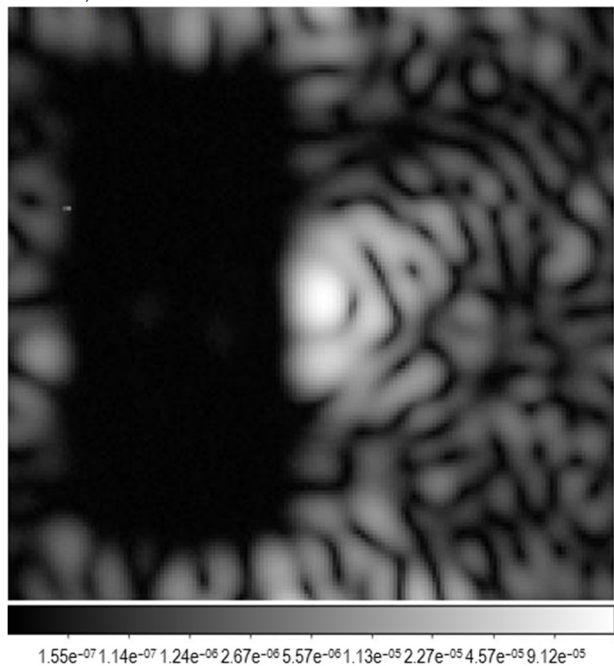


**Figure 8-7.** Dark hole covering 1.5–9.5 λ/D obtained for one of the VVC broadband nulling runs, for the central 2% band of the overall 10% band, for which suppression was $9\times10^{-9}$ over the full band (Serabyn et al. 2013).

defect must be minimized. For example, for $10^{-10}$ contrast, the simplest (charge 2) vortex with an uncovered central defect must be <200 nm in size, while a central defect that is covered with a small opaque spot can be a few microns in size, an order of magnitude larger.

*2. VVC ghost reflections.* Reflections from the various mask interfaces (internal and surface) are seen as "incoherent" light by the detector, and must be minimized. The refractive indices of all of the internal layers must thus be matched by using a multilayer model of the masks' layered structure, together with an anti-reflection coating. However, birefringent layers have two refractive indices, as a result of which, neither of them can be matched perfectly. As the opaque spot covering the disorientation region also allows for an extra reflection, minimization of the central defect also plays a role. Nevertheless, current performance models indicate that $10^{-9}$ contrasts can in fact be reached with current devices, as has been shown in the HCIT.

*3. VVC bandwidth.* To be useful for exoplanet observations, a coronagraph must reject starlight over a broad band; the Exo-C requirement is at least 20% bandwidth per individual device. Luckily, three distinct methods of achromatizing vortex coronagraphs are feasible: multi-layer vortex half-wave plate designs, twisted layer designs, and spectral polarization filtering. In the latter, the off band-center light is further rejected by a polarizer/quarter-wave-plate pair downstream of the vortex, and this technique has been used successfully in the HCIT. Additional work is needed on broadband multilayer masks.

Preliminary testing of vortex phase masks can be partially carried out using "standard" diagnostic devices such as polarizing microscopes, crossed-polarization transmission spectroscopy, and Mueller matrix imaging polarimetry, but the ultimate contrast performance tests will need to be carried out in a high contrast imaging testbed. This is especially true for broadband performance

tests, as the interaction of the spectral characteristics of the phase mask and of the wavefront control algorithms plays a crucial role. Testing individual vortex phase masks to high contrast is not particularly time-consuming, taking a few days per mask, but the switching time between coronagraph configurations in the test facility may be more significant (except in the case of the band-limited Lyot configuration, which is very similar to the VVC), and the testing of multiple masks also increases the necessary testing time. Thus, regular access to a high contrast imaging testbed is needed, on the order of a few months per year.

## 8.5  Focused Technology Needs for Exo-C

### 8.5.1  Development Needed for a 2017 Exo-C Program Start

We again note that WFIRST-AFTA technology development plans address increasing TRL for the DMs and LOWFS, as well as adding a "dynamic" contrast demonstration and imaging detector qualification. Additional technology development for all coronagraphs to improve broadband performance is desired.

*Coronagraphs.* Technology development funds are needed that support the simulation, design, fabrication, and testing of the masks and stops used in the HLC as well as the apodizers and masks for the PIAA to ensure that the Exo-C requirements, beyond the AFTA milestones, are achieved for HLC and PIAA. Also, additional funding for testing of the Vector Vortex (which is not included in the AFTA technology milestones) is needed to demonstrate Exo-C requirement performance.

For Exo-C, we will still need HLC demonstrations in the HCIT to validate models of the 2.2 λ/D simulated HLC IWA. We will also need to repeat the "dynamic" contrast demonstration that WFIRST-AFTA will perform but with the Exo-C telescope architecture and HLC, and to meet the more challenging Exo-C requirements (smaller IWA and higher contrast requirement).

Additional technology development should also be done for Exo-C's alternate coronagraph designs. A new round of PIAA mirrors should be procured for HCIT testing and to validate predicted performance, which may improve throughput over the current HLC design by a factor of two. Another design and fabrication cycle should go forward for the Vector Vortex coronagraph masks, including funding to achieve a <1 micron central defect, along with HCIT demonstrations toward Exo-C's performance requirements.

***Deformable mirrors.*** It would be beneficial to flight qualify an integrated DM and fine steering mirror system to help simplify the instrument optical layout by removing extra reflections and reducing volume.

Exo-C also would benefit from accurate models of DM actuator influence functions, thermal sensitivities, hysteresis, and development of high-fidelity calibration procedures.

The leading alternate technology to the fused silica facesheet with electrorestrictive actuator DMs are MEMS DMs. MEMS DMs need to advance laboratory demonstrations to the $10^{-9}$ level of contrast required by Exo-C. We also need MEMS DMs with less pointy influence functions, and less scalloping and print-through, as they cause undesirable diffraction effects that detract from the goal of reducing speckles and creating a dark hole. Smaller actuator pitch and improved surface quality are also desirable.

We need to establish lifetime performance requirements for the DMs and characterize them in their ability to meet these requirements (number of actuations expected and methods for accelerated lifecycle testing). For all candidate DMs, we need to understand actuator failure modes, performance impacts and mitigations from a systems perspective.

Two-DM wavefront control systems need to be demonstrated (also a goal of WFIRST-AFTA). System tests must include: 20% spectral bandwidths, 360° dark hold, and realistically low S/N photon rates.

***Wavefront control.*** Efficiency of the wavefront control system will ultimately drive the requirements for telescope thermal stability.

WFIRST-AFTA LOWFS technology development should be repeated with the Exo-C architecture.

***IFS.*** The PISCES prototype instrument aims to demonstrate the high contrast capability of the lenslet array. An assessment should be made in late 2016 as to whether additional development work will be needed.

***Binary systems.*** Additional support is needed to investigate what the best performing



LENSLETS            LENSLET FOCUS       DISPERSED LENSLET IMAGES        EXTRACTED DATA CUBE
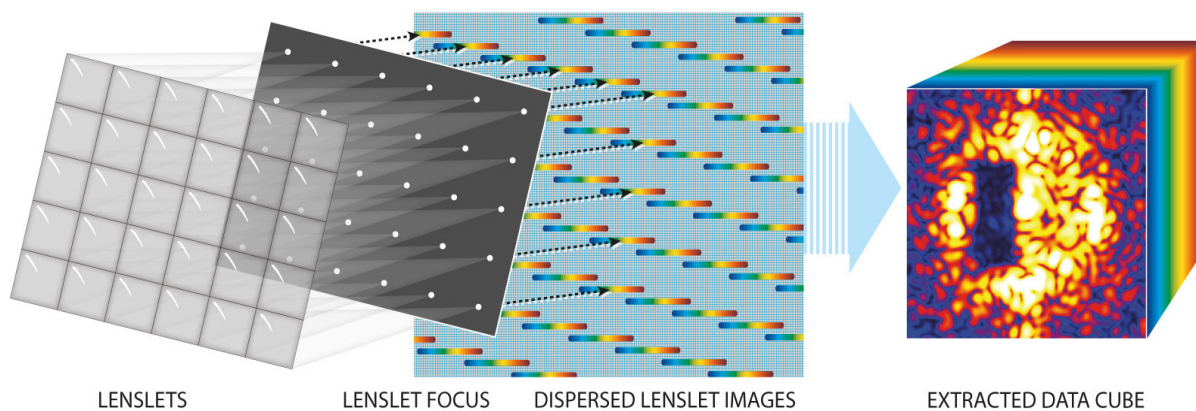
**Figure 8-8.** The lenslet array and the pinhole mask in the Exo-C IFS work together to focus and contain light. After the light passes through spectrograph optics, a spectrum for every spatial element in the instrument's field of view is produced (McEwain et al. 2013).

options are for management of exoplanet searches and characterization attempts around binary stars.

### 8.5.2 Technologies Desired for a 2020 Exo-C Program Start

*Detectors.* For the IFS detector, it is important to qualify a larger (2K×2K) EMCCD so that the IFS can perform wavefront sensing across the entire dark hole (a 1K×1K detector provides only partial coverage).

The IFS also would greatly benefit from future development of 4K×4K detectors which would be beneficial if a larger aperture is considered. The larger format devices would need to meet the same performance requirements as their smaller counterparts. This

includes QE, clock induced charge, dark current, flat fielding, and charge transfer efficiency. Validation of effective noise of than less than 0.0005 −e/pix/s in a simulated or prototype space environment would also be useful, as well as radiation testing these devices.

*Deformable mirrors.* Exo-C also would greatly benefit from the development and flight qualification of a 64×64 actuator DM. The improved wavefront control authority at higher spatial frequencies should allow for a larger dark hole and/or better contrast within a smaller dark hole. The DM devices will also require development of compact, low-power, low-complexity drive electronics and flight qualification, including radiation testing.

**Table 8-1.** Exo-C technology development plan.

| Category | Item(s) | Required (2017)/ Desired (2020) | Current Capability | AFTA Plan? (Poberezhskiy JPL Document) | ROM Time/Cost |
|---|---|---|---|---|---|
| DM | More actuators | Required: 48×48 (2017) Desired: 64×64 (2020) | 48×48 | 48×48 | 2 years >$2M to achieve 64 x 64 |
| DM | Flight electronics | Miniaturized (2017) ASIC (2020) | | Similar | 1 year $1M |
| DM | Environmental testing | Pass 0°C to+30°C and Launch Vibration (2017) | | | 1 year $1M |
| WFC | LOWFS | Required: 10 pm RMS wavefront sensing with ZWFS (2017) Desired: 5 pm RMS wavefront sensing with ZWFS (2020) Desired: Combine DM and FSM platform | Not yet demonstrated | <0.4 mas RMS per axis sensing with ZWFS | 1 year <$1M  1 year $1M |
| IFS | Detectors | Required: EMCCD with 0.0005 e/pix/s and read noise less than 1 e/pix/frame (2017 and 2020) Desired: 0.0001 e/pix/s | | 0.0001 e/pix/s and read noise less than 0.05 e/pix/frame | AFTA |
| IFS | Detectors | Required: 1K×1K EMCCD (2017) Desired: 2K×2K EMCCD or larger fromat (2020) | | 1K×1K EMCCD | 2 years >$2M |
| IFS | Lenslet array | Required: Preserve intrascene contrast at $10^3$ (2017) Desired: $10^4$ (2020), Desired: Increase number of lenslets and spectral resolution Desired: WFSC with IFS | $10^2$ contrast | PISCES (McEwain et al. 2013) | 1 year >$1M  1 year, $0.5M  2 years, $1M |

| Category | Item(s) | Required (2017)/ Desired (2020) | Current Capability | AFTA Plan? (Poberezhskiy JPL Document) | ROM Time/Cost |
|---|---|---|---|---|---|
| Coronagraph | HLC static | Required: $10^{-9}$ raw contrast at an angular separation of 2 λ/D (0.16″ at 550 nm) and 20% band in presence of jitter (2017) Desired: contrast: $5\times10^{-10}$ contrast, same IWA, 20% band with jitter (2020) | $2\times10^{-9}$ contrast at IWA of 3 λ/D, 20% bandwidth, in static system with linear mask. | $10^{-8}$ raw contrast at 550 nm narrowband | 2 years $1M |
| Coronagraph | PIAA static | Required: $10^{-9}$ raw contrast at IWA 2 λ/D, bandwidth 20%, in a dynamic system (2017) Desired: raw contrast: $5\times10^{-10}$ at IWA 2.0 λ/D, 20% bandwidth, in presence of jitter (2020) | $1e^{-8}$ at of 2 λ/D and 550 nm with 10% bandwidth in static system | $10^{-8}$ raw contrast at 550 nm, 10% band (with PIAACMC, a variant of PIAA) | 2 years, $1M Include hardware development, new mirrors (5 nm rms), apodizer (D/1000 shape) |
| Coronagraph | VVC static | Required: $10^{-9}$ raw contrast at an angular separation of 2 λ/D, (20% bandwidth, in presence of jitter (2017) Desired: contrast $10^{-9}$ IWA 1.7 λ/D, bandwidth 20% (2020) | $1e^{-8}$ at of 2 λ/D and 550 nm with 10% bandwidth in static system | $10^{-8}$ raw contrast at 550 nm narrowband | 2 years, $1M Include central defect, broadband mask |
| Coronagraph | All dynamic | Repeat all static tests with Exo-C worst case dynamic condition, requirement 0.8 RMS mas/axis | Not yet demonstrated, CBE 0.28 mas RMS/axis post FSM correction | Dynamic testing included, but performance range not specified (Poberezhskiy JPL Document). | 2 year $2M |
| Algorithm Development | ADI, CDI | Required: factor of 10 improvement in contrast Desired: factor of 30 | Factor of ~30, but under idealized conditions | TBD, but most likely factor of 10 | 1 year $500K |
| Binary Star | Demo | Required: Spillover light contrast $3\times10^{-8}$ at 8λ equivalent separation. (2017). Desired: $3e^{-9}$ achieved by mirror polishing or wavefront control | $10^{-7}$ at 8" by HST | None | 1 year $200K for WFC |

*The cost information contained in this document is of a budgetary and planning nature and is intended for informational purposes only. It does not constitute a commitment on the part of JPL and Caltech.*

# 9   Conclusion

The Exo-C Science and Technology Definition Team (STDT) was chartered in June 2013 by NASA's Exoplanet Exploration Program Office to develop a probe-class (not to exceed $1B) reference mission concept for direct exoplanet imaging and spectral characterization using a visible/NIR space telescope and internal coronagraph instrument.

The science goals outlined for the mission by the Exo-C STDT are to: (a) Spectrally characterize at least a dozen RV planets; (b) Search >100 nearby stars (including alpha Centauri) at multiple epochs for planets down ~$10^{-10}$ contrast—discovering and characterizing mini-Neptunes and smaller planets if they are present around nearby stars; and (c) Image the internal structures of hundreds of circumstellar disks. A modest-aperture coronagraph mission to address these goals was endorsed in the Electromagnetic Observations from Space panel report of the Astro2010 Decadal Survey.

Exo-C is a mission dedicated to exoplanet direct imaging. Nearly all of the 3 year mission time is devoted to imaging exoplanetary systems, just as Kepler focused on a single type of science observation. The study has defined an optimal design for achieving this science goal in a probe-scale mission. **The special engineering requirements of very high-contrast imaging are reflected throughout the mission design.** Relative to a general-purpose telescope, the choice of an unobscured telescope provides better throughput, better access to small λ/D inner working angles, better raw contrast and spectral bandwidth from high-contrast wavefront control, and relaxed pointing requirements. By avoiding a very fast telescope primary mirror and placing the instrument on the side of the telescope, induced polarization is reduced—thus enabling dual polarization wavefront control that maximizes the system throughput across the full wavelength range of interest. The mission

design puts a premium on system stability both passively (choice of an Earth-trailing orbit, large sunshade, engineering for structural stiffness, two stages of payload vibration isolation) and actively (30+ zone thermal control system for the telescope and instrument, precise pointing using a high-bandwidth fine steering mirror, low-order wavefront sensing/control, and mid-frequency wavefront control using large-format deformable mirrors). As a single-spacecraft pointed observatory, Exo-C has the agility to re-observe targets as many times as necessary to establish common proper motion of planetary candidates, follow planetary orbits and phase curves, and to maximize the completeness of searches for new planets.

The April 2014 interim report documented the work performed by the STDT and Design Team from June 2013 up to the midpoint of the mission study. This included definition of the science goals, trade studies of design options, the selection of a baseline design, and production of an initial technology needs assessment. Since the interim report, the study work proceeded along several lines: 1) Refining and updating the science case; 2) Improving the baseline design to reduce its mass and cost, relaxing requirements where possible; 3) Conducting a second iteration of design and optical performance modeling for the three remaining coronagraph options, now including the case of a binary star target; 4) Structural, thermal, optical modeling of the telescope wavefront stability that resulted in adjustments to the baseline design; 5) Working out the details of technology work needed in pre-Phase A; and 6) Finalizing the target list, science performance and yield estimates, and simulated science images and spectra.

The Exo-C final baseline design consists of an unobscured Cassegrain telescope with a 1.4 m primary, in an Earth-trailing orbit, and designed for a 3-year science mission lifetime. It carries a starlight suppression system (SSS) instrument capable of $10^{-9}$ raw contrast, between 2 and 20 λ/D, between 450–1000 nm, and spectral

resolution ranging from R=70, and consists of the following elements (in optical train order): fine-guidance and low-order wavefront sensor (FGS/LOWFS), wavefront control (WFC) system, coronagraph, an integral field spectrometer (IFS), and an imaging camera. The hybrid Lyot coronagraph is baselined for a 2017 project start, primarily because it provides the best demonstrated contrast, bandwidth, and polarization performance to date in testbed experiments on unobscured pupils. The PIAA and vector vortex coronagraphs have the potential to match the hybrid Lyot in these aspects and also provide better throughput and inner working angle performance. They remain options for a later project start.

Technology development work supported by the AFTA/WFIRST study is directly applicable to the needs of Exo-C. In addition to this, one to two years of hardware developments and laboratory demonstrations with unobscured pupils will be needed to make Exo-C's preferred coronagraphs flight-ready. This technology work would be responsive to the Astro2010 Decadal Survey's overall recommendation that NASA advance the technology needed for an eventual large mission to image habitable terrestrial exoplanets.

The Exo-C mission study serves as a proof-of-concept that a low-risk, cost-driven, $1B "probe-class" mission leveraging proven technologies is capable of ground-breaking exoplanet science. Exo-C would be major step toward directly revealing the planetary systems of nearby stars, with luck finding a planet as small as the Earth. Through its imaging surveys and spectral characterizations, Exo-C can provide an "Exoplanetary Grand Tour" of our immediate galactic neighborhood.

This final report caps 19 months of effort by the STDT and engineering design team to arrive at an optimal mission concept for an internal coronagraph. NASA headquarters will now evaluate it, perhaps towards a path to flight at the end of the decade—either as backup to the AFTA/WFIRST mission or as a potential mission to follow it. Many aspects of the Exo-C baseline design—particularly the choices made to minimize cost, and its thermal/mechanical configuration that yields high wavefront stability—provide a template for the design of larger-scale coronagraphic imaging missions that NASA may consider. It is our sincere hope that the results of this study will prove useful to the design of a future direct imaging mission for the study of habitable exoplanets.

# 10  Acknowledgements

Members of the Kepler project team provided helpful discussions on the stability achieved by their mission. We thank John Troelzsch, Denny Deutsch, and Michael Kaplan of Ball Aerospace; and Doug Caldwell and Jon Jenkins (NASA Ames) for engaging with the Exo-C team on this topic at our June 2014 meeting.

We thank Dennis Ebbets (Ball Aerospace) and Paul Scowen (ASU) for their suggestions on science priorities for a potential Exo-C auxiliary instrument.

# 11 References and Acronyms

## 11.1 References

Anglada-Escudé, G., M. Tuomi, et al. "A dynamically-packed planetary system around GJ 667C with three super-Earths in its habitable zone." *Astronomy & Astrophysics* 556, no. A126 (2013).

Ardila, D. et al. "A Resolved Debris Disk around the G2V Star HD 107146." *The Astrophysical Journal* 614, 147 (2004).

Bacon, R., Y. Copin, G. Monnet, Bryan W. Miller, J. R. Allington-Smith, M. Bureau, C. Marcella Carollo, Roger L. Davies, Eric Emsellem, Harald Kuntschner, Reynier F. Peletier, E. K. Verolme, P. Tim de Zeeuw, et al. "The SAURON project - I. The panoramic integral-field spectrograph." *Monthly Notices of the Royal Astronomical Society* 326, no.1 (September 2001): 23–35.

Barnet, C. D., Westphal, J. A., Beebe, R. F., and Huber, L.F. "Hubble Space Telescope observations of the 1990 Equatorial Disturbance on Saturn: Winds and Central Meridian Albedos." *Icarus* 100 (1992): 499–511.

Bastien, F.A., et al. "Radial velocity variations of photometrically quiet, chromospherically inactive Kepler stars: A link between RV jitter and photometric flicker." *The Astronomical Journal* 147, 29 (2014).

BATC presentation to STDT, "Ball Precision Telescope Heritage and Capabilities," December 13, 2013.

Bayard, D. S. "Advances in Precision Pointing Control for NASAs Spitzer Space Telescope." Proceedings of the 27th Annual AAS Rocky Mountain Guidance and Control Conference (2004).

Bean, Jacob L., Desert, Jean-Michel, Kabath, Petr, Stalder, Brian., Seager, Sara, et al. "The Optical and Near-infrared Transmission Spectrum of the Super-Earth GJ 1214b: Further Evidence for a Metal-rich Atmosphere." *The Astrophysical Journal* 743, Issue 1, article id. 92 (2011): 12 pp.

Belikov, R., Pluzhnik, E., Witteborn, F. C., Greene, T. P., Lynch, D. H., Zell, P. T., Schneider, G., Guyon, O., and Tenerelli, D. "EXCEDE Technology Development I: First demonstrations of high contrast at 1.2 λ/D for an Explorer space telescope mission." *Proc SPIE 8442-6* (2012), doi:10.1117/12.2024569, http://arxiv.org/abs/1407.4393.

Belikov, R., Pluzhnik, E., Witteborn, F. C., Greene, T. P., Lynch, D. H., Zell, P. T., and Guyon, O. "Laboratory demonstration of high-contrast imaging at inner working angles 2 λ/D and better." *Proc SPIE* 8151 (2011).

Belikov, R., Give'on, A., Kern, B., Cady, E., Carr, M., Shaklan, S., Balasubramanian, K., White, V., Echternach, P., Dickie, M., Trauger, J., Kuhnert, A., and Kasdin, N. J. "Demonstration of high contrast in 10% broadband light with the shaped pupil coronagraph." *Proc. SPIE* 6693, 6693-0Y (2007).

Belikov, R., Give'on, A., Savransky, D., Pueyo, L., Kern, B., Kasdin, J., "Demonstration of Synthetic Exo-earth Detection in the Lab with Speckle Subtraction Techniques." American Astronomical Society, AAS Meeting #211, #135.19; *Bulletin of the American Astronomical Society* 39 (2007a): pp. 975, http://adsabs.harvard.edu/abs/2007AAS...211113519B.

Belikov, R., Kasdin, N. J., and Vanderbei, R. J. "Diffraction-based Sensitivity Analysis of Apodized Pupil-Mapping Systems." *Astrophysical Journal* 652, Issue 1 (2006): 833–844.

Betremiuex and Kaltenegger 2013 (in review).

Borucki, William J., Agol, Eric, Fressin, Francois, Kaltenegger, Lisa, Rowe, Jason, et al. "Kepler-62: A Five-Planet System with Planets of 1.4 and 1.6 Earth Radii in

the Habitable Zone." *Science* 340, Issue 6132 (2013): 587–590.

Breckinridge, J. B., and B. R. Oppenheimer. "Polarization Effects in Reflecting Coronagraphs for White-Light Applications in Astronomy." *Astrophysical Journal* 600 (2004): 1091–1098.

Bryden, G., Beichman, C. A., Trilling, D. E., et al. "Frequency of Debris Disks around Solar-Type Stars: First Results from a Spitzer/MIP Survey." *The Astrophysical Journal* 636 (2006): 1098–1113.

Burrows, A. Scientific Return of Coronagraphic Exoplanet Imaging and Spectroscopy Using WFIRST, arXiv:1412.6097 (2014).

Cahoy, K.L., Marley, M.S., and Fortney, J.J. "Exoplanet albedo spectra and colors as a function of planet phase, separation, and metallicity." *The Astrophysical Journal* 724 (2010): 189–214.

Casertano, S., Lattanzi, M. G., Sozzetti, A., et al. "Double-blind test program for astrometric planet detection with Gaia." *Astronomy & Astrophysics* 482, no. 2 (2008): 699–729.

Charbonneau, David, Berta, Zachory K., Irwin, Jonathan, Burke, Christopher J., Nutzman, Philip, et al. "A super-Earth transiting a nearby low-mass star." *Nature* 462, Issue 7275 (2009): 891–894.

Chabrier, G., Baraffe, I., Selsis, F., et al. "Gaseous planets, protostars, and young brown dwarfs." *Protostars and Planets V* (2007): 623–638.

Clampin, M. et al. "The Extrasolar Planetary Imaging Coronagraph: Architectures of Extrasolar Systems." ASMC Study Report (2009). http://exep.jpl.nasa.gov/files/exep/asmc-clampin.pdf.

Deming, D., Seager, S., Winn, J., Miller-Ricci, E., Clampin, M., Lindler, D., and Ennico, K., "Discovery and characterization of super-Earths using an all-sky transit survey and follow-up by the James Webb Space Telescope." *Publications of the Astronomical Society of the Pacific* 121 no. 883 (2009): 952–967.

De Pontieu, B., et al. "The Interface Region Imaging Spectrograph (IRIS)." *Astro-ph*. (2014).

Deroo, P., Swain, M.R., and Green, R.O., "Spectroscopy of exoplanet atmospheres with the FINESSE Explorer mission." *Proc. SPIE*, 8442, 844241 (2012).

Des Marias D. et al. "Remote Sensing of Planetary Properties and Biosignatures on Extrasolar Terrestrial Planets." *Astrobiology* 2 (2002): 153–181.

Dumusque et al., "The Kepler-10 Planetary System Revisited by HARPS-N: A Hot Rocky World and a Solid Neptune-Mass Planet." *ApJ* 789, 154 (2014).

Eiroa, C., Marshall, J. P., Mora, A., Montesinos, B., Absil, O., Augereau, J. C., Bayo, A., Bryden, G., Danchi, W., del Burgo, C., Ertel, S., Fridlund, M., Heras, A. M., Krivov, A. V., Launhardt, R., Liseau, R., L¨ohne, T., Maldonado, J., Pilbratt, G. L., Roberge, A., Rodmann, J., Sanz-Forcada, J., Solano, E., Stapelfeldt, K., Th´ebault, P., Wolf, S., Ardila, D., Ar´evalo, M., Beichmann, C., Faramaz, V., Gonz´alez-Garc´ıa, B. M., Guti´errez, R., Lebreton, J., Mart´ınez-Arn´aiz, R., Meeus, G., Montes, D., Olofsson, G., Su, K. Y. L., White, G. J., Barrado, D., Fukagawa, M., Gr¨un, E., Kamp, I., Lorente, R., Morbidelli, A., M¨uller, S., Mutschke, H., Nakagawa, T., Ribas, I., and Walker, H. "DUst around NEarby Stars. The survey observational results." *Astronomy & Astrophysics* 555, no. A11 (2013).

Elkins-Tanton, Linda T. and Seager, Sara. "Ranges of Atmospheric Mass and Composition of Super-Earth Exoplanets." *The Astrophysical Journal* 685, Issue 2 (2008): 1237–1246.

Fortney, J., Marley, M., Saumon, D., Lodders, K. "Synthetic Spectra and Colors of Young Giant Planet Atmospheres: Effects of

Initial Conditions and Atmospheric Metallicity." *ApJ* 683, 1104-1116 (2008).

Give'on, A., Kern, B., Shaklan, S., Moody, D., and Pueyo, L. "Broadband wavefront correction algorithm for high-contrast imaging systems." *Proc. SPIE* 6691, 66910A (2007).

Greaves, J. S., Holland, W. S., Wyatt, M. C., Dent, W. R. F., Robson, E. I., Coulson, I. M., Jenness, T., Moriarty-Schieven, G. H., Davis, G. R., Butner, H. M., Gear, W. K., Dominik, C., and Walker, H. J. "Structure in the ϱ Eridani Debris Disk." *The Astrophysical Journal* 619 (2005): L187–L190.

Green, Joseph J., and Shaklan, S. B. "Optimizing coronagraph designs to minimize their contrast sensitivity to low-order optical aberrations." *Proc. SPIE* 5170 (2003): 25–37. doi: 10.1117/12.506485.

Green, J., et al. "Wide-Field InfraRed Survey Telescope (WFIRST) Final Report," arXiv 1208.4012 (2012).

Guyon, Olivier, Brian Kern, Andreas Kuhnert, Albert Niessner, K. Balasubramanian "Technology Development for Exoplanet Missions Technology Milestone Report: Phase-Induced Amplitude Apodization (PIAA) Technology Development, Milestone 1, Monochromatic Contrast Demonstration." JPL Document D-81778 (2014a), http://exep.jpl.nasa.gov/files/exep/PIAAMilestone1.pdf.

Guyon, Olivier, Brian Kern, Andreas Kuhnert, Albert Niessner "Technology Development for Exoplanet Missions Technology Milestone Report: Phase-Induced Amplitude Apodization (PIAA) Technology Development, Milestone 3, 10% Bandpass Contrast Demonstration." JPL Document D-93064 (2014b), http://exep.jpl.nasa.gov/technology/Guyon-PIAA-Milestone-3.pdf.

Guyon, O., Martinache, F. "How extremely large telescopes (ELTs) will acquire the first spectra of rocky habitable planets." *American Astronomical Society Meeting Abstracts* 221, no. 419.05 (2013).

Guyon, Olivier. "Limits of Adaptive Optics for High-Contrast Imaging." *The Astrophysical Journal* 629 (2005): 592–614. arXiv:astro-ph/0505086v2.

Guyon, Olivier, Taro Matsuo, and Roger Angel. "Coronagraphic Low Order Wave front Sensor: Principle and Application to a Phase-Induced Amplitude Coronagraph." *The Astrophysical Journal* 693 (2009):75–84. arXiv:0911.1301v1.

Handy, B. N., L. W. Acton, C. C. Kankelborg, C. J. Wolfson, D. J. Akin, M. E. Bruner, R. Caravalho, R. C. Catura, R. Chevalier, D. W Duncan, C. G. Edwards, C. N. Feinstein, S. L. Freeland, F. M. Friedlaender, C. H. Hoffmann, N. E. Hurlburt, B. K. Jurcevich, N. L. Katz, G. A. Kelly, J. R. Lemen, M. Levay, R. W. Lindgren, D. P. Mathur, S. B. Meyer, S. J. Morrison, M. D. Morrison, R. W. Nightingale, T. P. Pope, R. A. Rehse, C. J. Schrijver, R. A. Shine, L. Shing, K. T. Strong, T. D. Tarbell, A. M. Title, D. D. Torgerson, L. Golub, J. A. Bookbinder, D. Caldwell, P. N. Cheimets, W. N. Davis, E. E. Deluca, R. A. McMullen, H. P. Warren, D. Amato, R. Fisher, H. Maldonado, and C. Parkinson. "The transition region and coronal explorer." *Solar Physics* 187, no. 2 (1999): 229–260.

Hines, D. C., et al. "The Moth: an Unusual Circumstellar Structure Associated with HD 61005." *The Astrophysical Journal* 671, L165 (2007).

Hinz, P. "The Hunt for Observable Signatures of Terrestrial Planetary Systems (HOSTS): LBTI's Zodiacal Dust Survey." In *American Astronomical Society Meeting Abstracts* 221 (2013): #403.06.

Howard, A. and Fulton, B.J. (2015) to be submitted.

Howard, A., et al. "The Occurrence and Mass Distribution of Close-in Super-Earths,

Neptunes, and Jupiters." *Science* 330, 653 (2010).

Howard, Andrew W. "Observed Properties of Extrasolar Planets." *Science* 340, Issue 6132 (2013): 572–576.

Howard, Andrew W., Marcy, Geoffrey W., Bryson, Stephen T., Jenkins, Jon M., Rowe, Jason F., et al. *The Astrophysical Journal Supplement* 201, Issue 2, article id 15 (2012): 20 pp.

Hu, R. Ammonia, Water Clouds and Methane Abundances of Giant Exoplanets and Opportunities for Super-Earth Exoplanets, arXiv:1412.7582 (2014).

Ida, Shigeru and Lin, D. N. C. "Toward a Deterministic Model of Planetary Formation. II. The Formation and Retention of Gas Giant Planets around Stars with a Range of Metallicities." *The Astrophysical Journal* 616, Issue 1 (2004): 567–572.

Kalas, P., Graham, J. R., and Clampin, M. "A Planetary System as the Origin of Structure in Fomalhaut's Dust Belt" *Nature* 435 (2005): 1067–1070.

Kalas, P., Fitzgerald, M. P., and Graham, J. R., "Discovery of Extreme Asymmetry in the Debris Disk Surrounding HD 15115." *The Astrophysical Journal* 661, L85 (2007).

Karkoschka, E. "Spectrophotometry of the Jovian planets and Titan at 300–1000 nm wavelength, The methane spectrum." *Icarus* 111 (1994) 174–192.

Kasdin, N. J., Groff, T., Carlotti, A., and Vanderbei, R. "Space-based planet detection using two MEMS DMs and a shaped pupil." in *Society of Photo-Optical Instrumentation Engineers (SPIE) Conference Series* 8253 (2012).

Kelsall, T., Weiland, J. L., Franz, B. A., et al. "The COBE Diffuse Infrared Background Experiment Search for the Cosmic Infrared Background. II. Model of the Interplanetary Dust Cloud." *The Astrophysical Journal* 508 (1998): 44–73.

Kern, B., Guyon, O., Give'on, A., Kuhnert, A., Niessner, A., Martinache, F., and Balasubramanian, K. "Laboratory demonstration of phase induced amplitude apodization (PIAA) coronagraph with better than $10^{-9}$ contrast." *Proc. SPIE* 8864, 8864-26 (2013).

Kern, B. D., Guyon, O., Give'on, A., Kuhnert, A., and Niessner, A. "Laboratory testing of a Phase-Induced Amplitude Apodization (PIAA) coronagraph." *Proc. SPIE* 8151, (2011).

Koch, D., Borucki, W., Dunham, E., Geary, J., Gilliland, R., Jenkins, J., Latham, D., Bachtell, E., Berry, D., Deininger, W., R. Dureng, T. N., Gautier, Gillis, L., Mayer, D., Miller, C., Shafer, D., Sobeck, C., Stewart, C., and Weiss, M. "Overview and status of the Kepler Mission." Proceedings of the SPIE Conference 5487 on Optical, Infrared, and Millimeter Space Telescopes (2004).

Kreidberg, L., Bean, J. L., Desert, J.-M., Benneke, B., Deming, D., Stevenson, K. B., Seager, S., Berta-Thompson, Z., Seifahrt, A., and Homeier, D. "Clouds in the atmosphere of the super-Earth exoplanet GJ1214b." *Nature* 505 (2014): 69–72.

Kreidberg, L., Bean, J. L., Desert, J.-M., Benneke, B., Deming, D., Stevenson, K. B., Seager, S., Berta-Thompson, Z., Seifahrt, A., and Homeier, D. "Clouds in the atmosphere of the super-Earth exoplanet GJ1214b." *Nature* 505 (2014): 69–72.

Krist, J., Belikov, R., Pueyo, L., Mawet, D., Moody, D., Trauger, J., and Shaklan, S. "Assessing the performance limits of internal coronagraphs through end-to-end modeling." *Proc. SPIE* 8864, 88640P (2013), doi:10.1117/12.892772.

Krist, J., et al. "TDEM Technology Milestones 1 & 2 Results Reports: Assessing the performance limits of internal coronagraphs through end-to-end modeling." JPL Documents D-74425 and

D-74426 (2012) (available at exep.jpl.nasa.gov/technology).

Krist, J. E., Stapelfeldt, K. R., Bryden, G., and Plavchan, P. "Hubble Space Telescope Observations Observations of the HD 202628 Debris Disk." *The Astronomical Journal* 144, 45 (2012).

Krist, J., Belikov, R., Pueyo, L., Mawet, D., Moody, D., Trauger, J., and Shaklan, S. "Assessing the performance limits of internal coronagraphs through end-to-end modeling: a NASA TDEM study." *Proc. SPIE* 8151, 81510E (2011).

Krist, J., Pueyo, L., and Shaklan, S. "Practical numerical propagation of arbitrary wavefronts through PIAA optics." *Proc. SPIE* 7731, 77314N (2010).

Krist, J. "PROPER: an optical propagation library for IDL." *Proc. SPIE* 6675, 66750P (2007).

Krist, J. "Coronagraphs on the Hubble Space Telescope." *Exoplanet Detection with Coronagraph*, Jet Propulsion Laboratory, California Institute of Technology (2006), http://exep.jpl.nasa.gov/TPF/Coronagraph_PDFs/CWP2006_15_Krist_pp83-85.pdf.

Krist, J. E., Ardila, D. R., Golimowski, D. A., Clampin, M., Ford, H. C., Illingworth, G. D., Hartig, G. F., Bartko, F., Ben´ıtez, N., Blakeslee, J. P., Bouwens, R. J., Bradley, L. D., Broadhurst, T. J., Brown, R. A., Burrows, C. J., Cheng, E. S., Cross, N. J. G., Demarco, R., Feldman, P. D., Franx, M., Goto, T., Gronwall, C., Holden, B., Homeier, N., Infante, L., Kimble, R. A., Lesser, M. P., Martel, A. R., Mei, S., Menanteau, F., Meurer, G. R., Miley, G. K., Motta, V., Postman, M., Rosati, P., Sirianni, M., Sparks, W. B., Tran, H. D., Tsvetanov, Z. I., White, R. L., and Zheng, W. "Hubble Space Telescope Advanced Camera for Surveys Coronagraphic Imaging of the AU Microscopii Debris Disk." *The Astronomical Journal* 129 (2005): 1008–1017.

Kuchner, M. J., and Holman, M. J. "The Geometry of Resonant Signatures in Debris Disks with Planets." *The Astrophysical Journal* 588 (2003): 1110–1120.

Lagrange, A.-M., Bonnefoy, M., Chauvin, G., et al. "A Giant Planet Imaged in the Disk of the Young Star beta Pictoris." *Science* 329, 57 (2010).

Larkin, James, Matthew Barczys, Alfred Krabbe, Sean Adkins, Ted Aliado, Paola Amico, George Brims, Randy Campbell, John Canfield, Thomas Gasaway, Allan Honey, Christof Iserlohe, Chris Johnson, Evan Kress, David LaFreniere, Ken Magnone, Nick Magnone, Michael McElwain, Juleen Moon, Andreas Quirrenbach, Gunnar Skulason, Inseok Song, Michael Spencer, Jason Weiss, and Shelley Wright. "OSIRIS: A diffraction limited integral field spectrograph for Keck." *New Astronomy Reviews* 50, no. 4 (2006): 362–364.

Lawson, P.R., Seager, S., Stapelfeldt, K., Brenner, M., Lisman, D., Siegler, N., Unwin, S., Warfield, K., "An analysis of technology gaps and priorities in support of probe-scale coronagraph and starshade missions," *Proc. of SPIE* 9143, 91432Q (2014), doi:10.1117/12.2054939.

Lawson, P. R., Belikov, R., Cash, W., Clampin, M., Glassman, T., Kasdin, N. J., Kern, B. D., Lyon, R., Mawet, D., Moody, D., Samuele, R., Serabyn, E., Sirbu, D., and Trauger, J. "Survey of experimental results in high-contrast imaging for future exoplanet missions." *Proc. SPIE* 8864, 8864-1F (2013).

Lawson, P. R. "Exoplanet Exploration Program Technology Plan, Appendix: 2012." JPL Document D-77698 (2013). http://exep.jpl.nasa.gov/files/exep/2012Appendix_Fall.pdf.

Leger, A., Rouan, D., Schneider, J., Barge, P., Fridlund, M., et al. "Transiting exoplanets from the CoRoT space mission. VIII. CoRoT-7b: the first super-Earth with

measured radius." *Astronomy and Astrophysics* 506, Issue 1 (2009): 287–302.

Lindegren, L., Lammers, U., Hobbs, D., et al. "The astrometric core solution for the Gaia mission." *Astronomy & Astrophysics* 538, A78 (2012).

Jack J. Lissauer, Daniel C. Fabrycky, Eric B. Ford, William J. Borucki, Francois Fressin, Geoffrey W. Marcy, Jerome A. Orosz, Jason F. Rowe, Guillermo Torres, William F. Welsh, Natalie M. Batalha, Stephen T. Bryson, Lars A. Buchhave, Douglas A. Caldwell, Joshua A. Carter, David Charbonneau, Jessie L. Christiansen, William D. Cochran, Jean-Michel Desert, Edward W. Dunham, Michael N. Fanelli, Jonathan J. Fortney, Thomas N. Gautier III, John C. Geary, Ronald L. Gilliland, Michael R. Haas, Jennifer R. Hall, Matthew J. Holman, David G. Koch, David W. Latham, Eric Lopez, Sean McCauliff, Neil Miller, Robert C. Morehead, Elisa V. Quintana, Darin Ragozzine, Dimitar Sasselov, Donald R. Short, and Jason H. Steffen "A closely packed system of low-mass, low-density planets transiting Kepler-11." *Nature* 470 (2011): 53–58.

Lopez, Eric, and Fortney, J. J. "How Thermal Evolution and Photo-Evaporation Sculpt Kepler's Sub-Neptunes and Super-Earths." *American Astronomical Society*, DPS meeting #45, #200.08. (2013).

Luger R., Barnes R., Lopez E., Fortney J., Jackson B., and Meadows V. "Habitable Evaporated Cores: Transforming Mini-Neptunes into Super-Earths in the Habitable Zones of M Dwarfs." *Astrobiology* 15, 1 (2015): 57–88.

Lyon, R. G., Clampin, M., Petrone, P., Mallik, U., Madison, T., and Bolcar, M. R. "High contrast vacuum nuller testbed (VNT) contrast, performance, and null control." *Proc. SPIE* 8442, 8442-08 (2012).

Marcy, G., Butler, R. P., Fischer, D., Vogt, S., Wright, J. T., Tinney, C. G., and Jones, H. R. A. "Observed Properties of Exoplanets:

Masses, Orbits, and Metallicities." *Progress of Theoretical Physics Supplement*, No. 158 (2005): 24–42.

Marcy, Geoffrey W., Isaacson, Howard, Howard, Andrew W., Rowe, Jason F., Jenkins, Jon M., et al. "Masses, Radii, and Orbits of Small Kepler Planets: The Transition from Gaseous to Rocky Planets." *The Astrophysical Journal Supplement* 210, 2, article id. 20 (2014): 70 pp.

Marley, M.S., et al. "On the luminosity of young Jupiters." *The Astrophysical Journal* 655 (2007): 541–549.

Marley, M., Lupu, R., Lewis, N., Line, M., Morley, C., Fortney, J. A Quick Study of the Characterization of Radial Velocity Giant Planets in Reflected Light by Forward and Inverse Modeling, arXiv: 1412.8440 (2014).

Marois, C., et al. "Extrasolar planets: A giant surprise." *Nature* 468 (2010): 1048–1049.

Marois, C., Zuckerman, B., Konopacky, Q., et al. "Images of a fourth planet orbiting HR 8799" *Nature* 468 (2010): 1080–1083.

Marois, C., Macintosh, B., and Verian, J-P. "Exoplanet imaging with LOCI processing: photometry and astrometery with the new SOSIE pipeline." *Proc. SPIE* 7736 (2010).

Martin-Fleitas, J., Mora, A., Sahlmann, J., et al. "Enabling Gaia observations of naked-eye stars." *Proc. SPIE* 9143, 91430Y (2014).

Mawet et al., *Proc. SPIE* 8442, 04 (2012).

McEwain, M., Perrin, M., Gong, Q., Wilkins, A., Stapelfeldt, K., Woodgate, B., Brandt, T., Heap, S., Hilton, G., Kruk, J., Moody, D., Trauger, J. "PISCES: An integral field spectrograph to advance high contrast imaging technologies." Techniques and Instrumentation for Detection of Exoplanets VI, edited by Stuart Shaklan, *Proc. of SPIE* 8864, 88641O (2013), doi: 10.1117/12.2024385

Mendillo, C. B., et al. "Flight demonstration of a milliarcsecond pointing system for direct

exoplanet imaging." *Applied Optics* 51, no. 29 (2012).

Misra et al. 2014 (in review).

Mouillet, D., Larwood, J. D., Papaloizou, J. C. B., and Lagrange, A. M. "A planet on an incline orbit as an explanation for the warp in the beta Pictoris disc." *MNRAS* 292 (1997): 896–904.

N'Diaye, M., Kjetil, D., Caillat, A., Costille, A., Fusco, T., Jolivet, A., Madec, F., Mugnier, L., Baptiste, P., Sauvage, J., Soummer, R., Vigan, A., Wallace, J.K., "Design optimization and lab demonstration of ZELDA: a Zernike sensor for near-coronagraph quasi-static measurements," *Proc. SPIE, Adaptive Optics Systems IV* 9148, 91485H (2014), doi:10.1117/12.2056818.

N'Diaye, M., Dohlen, K., and Paul, B. "Calibration of quasi-static aberrations in exoplanet direct imaging instruments with a Zernike phase-mask sensor." *Astronomy & Astrophysics* 29 (2013). arXiv:1305.5143v2.

Nesvorny, D., Jenniskens, P., Levison, H. F., Bottke, W. F., Vokrouhlick´y, D., and Gounelle, M. "Cometary Origin of the Zodiacal Cloud and Carbonaceous Micrometeorites. Implications for Hot Debris Disks." *The Astrophysical Journal* 713, no. 2 (2010): 816–836.

Oberg, K. I., Murray-Clay, R., and Bergin, E. A. *The Astrophysical Journal Letters* 743, L16 (2011).

Oppenheimer, B. and Hinkley, S. "High-contrast observations in optical and infrared astronomy." *Annual Review of Astronomy and Astrophysics* 47 (2009): 253–289.

Perrin, M. et al. "Gemini Planet Imager Polarimetry of the Circumstellar Ring around HR 4796A." *AAS* 225, 330.05 (2015).

Perryman, M., Hartman, J. Bakos, G. A., and Lindegren, L. "Astrometric exoplanet detection with Gaia." *ApJ* 797, 14 (2014).

Poberezhskiy, I. "Major Advances in WFIRST/AFTA Coronagraph Technology." ExoPlanet Exploration Program Newsletter, Issue 14, October (2014)

Poberezhskiy, I. "WFIRST-AFTA Coronagraph Technology Development Plan," JPL D-81964.

Pollack, James B., Olenka Hubickyj, Peter Bodenheimer, Jack J. Lissauer, Morris Podolak, and Yuval Greenzweig. "Formation of the Giant Planets by Concurrent Accretion of Solids and Gas." *Icarus* 124, no. 1 (1996): 62–85.

Roberge, A., Chen, C. H., Millan-Gabet, R., Weinberger, A. J., Hinz, P. M., Stapelfeldt, K. R., Absil, O., Kuchner, M. J., and Bryden, G. "The Exozodiacal Dust Problem for Direct Observations of Exo-Earths." *Publications of the Astronomical Society of the Pacific* 124 (2012): 799–808.

Robinson, T., Meadows, V., Crisp, D. "Detecting Oceans on Extrasolar Planets Using the Glint Effect," *ApJ*, 721, 67 (2010).

Robinson, T., et al. "Detection of Ocean Glint and Ozone Absorption Using LCROSS Earth Observations." *ApJ*, 787, 171 (2014).

Sato, M. and Hansen, J. "Jupiter's atmospheric composition and cloud structure deduced from absorption bands in reflected sunlight." *J. Atmos. Sci.*, 36, 1133 (1979).

Schneider, G., Weinberger, A. J., Becklin, E. E., Debes, J. H., and Smith, B. A. "STIS Imaging of the HR 4796A Circumstellar Debris Ring." *The Astronomical Journal* 137, no. 5 (2009): 3–61.

Serabyn, E., Mawet, D., Trauger, J. T., Moody, M., Liewer, K., Krist, J. E., and Kern, B. D. "High-contrast imaging with the vortex coronagraph." *Proc. SPIE* 8864, 8864-32 (2013).

Shao, M., et al. "DAVINCI, a dilute aperture visible nulling coronagraph instrument." *Proc. SPIE* 7013, 789767 (2008).

Sharkey, J. P., G. S. Nurre, G. A. Beals, and J. D. Nelson. "A chronology of the on-orbit pointing control system changes on the Hubble Space Telescope and associated pointing improvements." AIAA-92-4618-CP.

Stahl, H. Philip, Todd Henrichs, Alexander Luedtke, and Miranda West. "Update to single-variable parametric cost models for space telescopes." *Optical Engineering* 52(9), 091805 (2013). http://dx.doi.org/10.1117/1.OE.52.9.091805.

Stapelfeldt, K. "The Scientific requirements for extremely large telescopes." *Proceedings of the International Astronomical Union Symposium* 232 (2006): 149–158.

Su, K. Y. L., Rieke, G. H., Stapelfeldt, K. R., et al. "The Debris Disk around HR 8799." *The Astrophysical Journal* 705 (2009): 314–327.

Sudarsky, D., Burrows, A., Hubeny, I., and Li, A. "Phase Functions and Light Curves of Wide-Separation Extrasolar Giant Planets." *ApJ* 627, 520-533 (2005).

Sumi, T. et al. "A Cold Neptune-Mass Planet OGLE-2007-BLG-368Lb: Cold Neptunes Are Common." *ApJ*, 710, 1641-1653 (2010).

Trauger, J., Moody, D., Gordon, B., Krist, J., and Mawet, D. "Complex apodization Lyot coronagraphy for the direct imaging of exoplanet systems: design, fabrication, and laboratory demonstration." *Proc. SPIE* 8442, 8442-4Q (2012), http://wfirst.gsfc.nasa.gov/science/sdt_public/spie/886412.pdf.

Trauger, J., et al. "ACCESS: a concept study for the direct imaging and spectroscopy of exoplanetary systems." *Proc. SPIE* 7731, 773128 (2010).

Trauger, J., Traub, W., "A laboratory demonstration of the capability to image an Earth-like extrasolar planet." *Nature* 446 (2007), doi:10.1038/nature05729.

Trauger, J., et al. "A space Coronagraph Concept for direct imaging and spectroscopy of Exoplanetary SystemS (ACCESS)." *ASMC Study Report* (2009). http://exep.jpl.nasa.gov/files/exep/access_compiled_report_public_090610.pdf.

Weisskopf, M., Aldcroft, T., Bautz, M., Cameron, R., Dewey, D., Drake, J., Grant, C., Marshall, H., and Murray, S. "An Overview of the Performance of the Chandra X-ray Observatory." *Experimental Astronomy*, 16, no. 1 (2003): 1–68.

WFIRST-AFTA Science Definition Team Final Report (2013). http://wfirst.gsfc.nasa.gov/science/sdt_public/wfirst-afta_sdt_final_report_rev1_130523.pdf.

## 11.2  Acronyms

| | |
|---|---|
| ACCESS | Actively-Corrected Coronagraphs for Exoplanetary System Studies |
| ACE | Ames Coronagraph Experiment |
| ACS | attitude control system |
| ADCS | Attitude Determination and Control Subsystem |
| ADI | angular difference imaging |
| AFTA | Astrophysics Focused Telescope Asset |
| ALMA | Atacama Large Millimeter/ submillimeter Array |
| AOI | angle-of-incidence |
| AOX | Adaptive Optics Associates/Xinetics |
| APRA | Astrophysics Research and Analysis |
| ARC | Ames Research Center |
| ASMCS | Astrophysics Strategic Mission Concept Studies |
| AU | astronomical unit |
| BCA | bus control assembly |
| BOE | basis of estimate |
| CAD | computer-aided design |
| CADRe | Cost Analysis Data Requirement |
| CATE | Cost Appraisal and Technical Evaluation |
| CBE | current best estimate |
| CCD | charge coupled device |
| CDI | coherence difference imaging |
| CG | center of gravity |
| CHARIS | Coronagraphic High Angular Resolution Imaging Spectrograph |
| CLOWFS | Coronagraphic Low Order Wavefront Sensor |
| CMOS | complementary metal–oxide–semiconductor |
| CNC | computer numerical control |
| CoRoT | COnvection ROtation et Transits |
| CSS | coarse Sun sensor |
| CTE | coefficient of thermal expansion |

| | |
|---|---|
| CVD | chemical vapor deposited |
| CVZ | continuous viewing zone |
| DM | deformable mirror |
| DMC | Data Management Center |
| DOF | degree of freedom |
| DSN | Deep Space Network |
| ECB | Exo-C control box |
| EDU | Engineering Design Unit |
| EE | encircled energy |
| E-ELT | European Extremely Large Telescope |
| ELT | Extremely Large Telescope |
| EMCCD | electron multiplying charge coupled device |
| ENF | excess noise factor |
| EOL | end-of-life |
| EOS | Electromagnetic Observations from Space |
| EPD | entrance pupil diameter |
| EPDS | Electrical Power and Distribution Subsystem |
| EPIC | Extrasolar Planetary Imaging Coronagraph |
| ESA | European Space Agency |
| ESPRESSO | Echelle SPectrograph for Rocky Exoplanet and Stable Spectroscopic Observations |
| EXCEDE | EXoplanetary Circumstellar Environments and Disk Explorer |
| ExEP | Exoplanet Exploration Program |
| FEM | finite element model |
| FGS | fine-guidance sensor |
| FPA | focal-plane array |
| FOV | field-of-view |
| FMD | flight management system |
| FPC | Flight Planning Center |
| FS | flight segment |
| FSM | fine-steering mirror |
| FSW | flight software |
| FWHM | Full-width, half-maximum |
| Galex | Galaxy Evolution Explorer |
| GDS | ground data system |

| | | | | |
|---|---|---|---|---|
| GMT | Giant Magellan Telescope | | OSIRIS | OH-Suppressing InfraRed Imaging Spectrograph |
| GPI | Gemini Planet Imager | | OTA | optical telescope assembly |
| GS | Ground Segment | | OVC | optical vortex coronagraph ( |
| HCIT | High-Contrast Imaging Testbed | | OWA | outer working angle |
| HGA | high-gain antenna | | PCA | principal component analysis |
| HST | Hubble Space Telescope | | PDI | polarization difference imaging |
| IB | inner barrel | | PDR | Preliminary Design Review |
| IBA | inner barrel assembly | | PEC | precision external clock |
| ICE | instrument control electronics | | PECO | Pupil mapping Exoplanet Coronagraphic Observer |
| IFS | integral field spectrograph | | PEL | Power Equipment List |
| IMU | inertial measurement unit | | PIAA | phase-induced amplitude apodization |
| IR | infrared | | | |
| IRU | inertial reference unit | | PID | proportional-integral-derivative |
| IWA | inner working angle | | PISCES | Prototype Imaging Spectrograph for Coronagraphic Exoplanet Studies |
| JPL | Jet Propulsion Laboratory | | | |
| JWST | James Webb Space Telescope | | | |
| LBTI | Large Binocular Telescope Interferometer | | PLATO | Planetary Transits and Oscillations of stars |
| LGA | low-gain antenna | | PM | primary mirror |
| LOCI | locally optimized combination of images | | PMA | primary mirror assembly |
| | | | PMB | primary mirror bipods |
| LOWFS | low-order wavefront sensor | | PPE | payload processing electronics |
| LV | launch vehicle | | PPMZWFS | Pupil Plane Mach-Zehnder Wavefront Sensor |
| M | magnification | | | |
| M | mirror | | PSF | point spread function |
| MEL | Master Equipment List | | PSS | Project Scheduling Service |
| MIRI | Mid InfraRed Instrument | | PSS | primary mirror support structure |
| MIT | Massachusetts Institute of Technology | | PSS | Project Scheduling Service |
| | | | QE | quantum efficiency |
| MMO | Mission Management Office | | RBA | rigid body actuator |
| MOC | Mission Operations Center | | RCS | reaction control system |
| MOS | mission operations system | | RF | radio frequency |
| NASA | National Aeronautics and Space Administration | | RMS | root mean square |
| | | | RV | radial velocity |
| NICM | NASA Instrument Cost Model | | RWA | reaction wheel assembly |
| NIRCam | Near Infrared Camera | | SAT | Strategic Astrophysics Technology |
| NIRSpec | Near InfraRed Spectrograph | | | |
| OAP | off-axis parabola | | SBIR | Small Business Innovation Research |
| OB | outer barrel | | | |
| OBA | outer barrel assembly | | S/C | spacecraft |
| OPZ | operational pointing zone | | | |

| | | | | |
|---|---|---|---|---|
| SCExAO | Subaru Coronagraphic Extreme Adaptive Optics | TDI | time-delayed integration |
| SDI | spectral difference imaging | TESS | Transiting Exoplanet Survey Satellite |
| SFE | surface figure error | TMT | Thirty Meter Telescope |
| SM | secondary mirror | TRL | technology readiness level |
| S/N | signal-to-noise | TWTA | traveling wave tube amplifier |
| SNR | signal-to-noise ratio | ULE | ultra-low expansion |
| SO | Science Office | UV | ultraviolet |
| SOC | Science Operations Center | VLT | Very Large Telescope |
| SPHERE | Spectro-polarimetric High-contrast Exoplanet Research | WBS | Work Breakdown Structure |
| SSR | solid-state recorder | WFC | wavefront control |
| SSS | starlight suppression system | WFE | wavefront error |
| STB | system test bed | WFIRST | Wide-Field Infrared Survey Telescope |
| STDT | Science and Technology Definition Team | WFSC | wavefront sensing and control |
| STOP | structural, thermal, optical, performance | WISE | Wide-field Infrared Survey Explorer |
| TCE | telescope control electronics | ZLOWS | Zernike Low-order Wavefront Sensor |
| TCS | thermal control subsystem | ZWFS | Zernike Wavefront Sensor |
| TDEM | Technology Development for Exoplanet Missions | | |

# B   Architecture Trades

## B.1   Payload Trades

The focus of the JPL design team for the first 9 months was to conduct and complete the primary trade studies that drive the general mission architecture. The JPL design team was established and met in July 2013 and generated a detailed trade list that would be assessed for the interim report. The focus of the design team for the interim report was to establish a baseline and complete the trades necessary to have the system hold together technically. After the interim report, the design team focused on refining the design through detailed structural, thermal, and optical performance (STOP) modeling as documented in §5.10. The first trades that were conducted were related to the optical architecture and design. All mechanical and thermal trades were conducted once the optical architecture yielded a system that maximized performance and efficiency. Each of the major functional engineering areas

had related trades that progressed to more detail at the subsystem and assembly levels. Many of the trades were coupled and contained a large trade space, such as the pointing control architecture and the S/C bus trade. Table B.1-1 contains a full listing of the trades and their current status. This section provides the details of the major trades, the rationale, and the recommended solution. The design team conducted trades that affected the payload, spacecraft, and mission-level aspects.

### B.1.1   Optical

### B.1.1.1   Obscured versus Unobscured Configuration

This section lays out considerations for comparing the merits/impacts of obscured versus unobscured aperture forms for a coronagraph instrument. For this section, only technical and performance aspects were examined, independent of cost and schedule considerations.

**Table.B.1-1.** Completed trades.

| Trade | Outcome |
|---|---|
| Telescope obscured vs. Unobscured | Unobscured |
| Telescope design | Cassegrain |
| Low CTE glass vs. silicon carbide (SiC) | Low CTE glass |
| Orbit | Earth-trailing |
| Aperture size | 1.4 meter |
| High-gain antenna (HGA) | Fixed |
| Isolators: between reaction wheel assembly (RWA) and S/C, and again between spacecraft and payload | Two passive layers |
| Deformable mirror (DM) | 48×48 |
| Instrument bench location: lateral vs. behind PM | Lateral |
| Low-order wavefront sensor (LOWFS) design | Zernike Low-order Wavefront Sensor (ZLOWS) |
| Spacecraft bus | Kepler type |
| Solar array configuration: Fixed vs. articulated | Fixed |
| Mission lifetime | 3 years |
| Pointing architecture | Isolation, flight management system (FMS), payload, and spacecraft interface |
| Spectral measurement technique | Integral field spectrometer (IFS) |
| Telescope stability—thermal architecture | Heater control on barrel, assembly, PM and SM mirror assemblies, flat solar panel w/ sunshield that extends to the end of the barrel |
| Secondary mirror configuration | Actuated secondary |
| Aft metering structure configuration | Integrated inner barrel assembly |
| Instrument architecture | Fine-guidance sensor (FGS), LOWFS, Coronagraph, filters, IFS |

### B.1.1.1.1 Summary and Recommendation

From a performance perspective, the use of an ***unobscured telescope form for a coronagraph is preferred***. The two main factors involved in determining this were collecting area and integration time, both of which significantly favored the unobscured form. Five other factors were examined (polarization influence, fabrication complexity, structural considerations, optical design complexity, and binary target performance) that either yielded no net distinction or only very weakly favored one form over the other.

### B.1.1.1.2 Study Assumptions

For quantitative comparison purposes, a point design was selected, including:

- Primary mirror diameter=1.5 m
- Secondary mirror diameter=0.15 m
- Lyot blocking diameter=90% (equivalent to 0.075 m in the entrance aperture)
- System focal ratio=f/30
- Wavelength=500 nm
- Detector pixel dimension=13 microns

The obscured form was taken to be symmetrical, with a vane support approach[*]:

- Number of vanes=4 (to provide minimum perturbation to point spread function (PSF) structure)
- Vane width=0.0375 m (1/4 of secondary aperture dimension)
- Lyot blocking dimension=0.075 m (same equivalent dimension as for primary aperture)

Figure B.1-1 is a scale representation of the entrance apertures and the equivalent Lyot masks for the selected properties.

---

[*] The vane approach was selected to provide best properties for control of diffraction effects by making diffracting elements co-planar, and hence of more uniform effect at the Lyot mask.
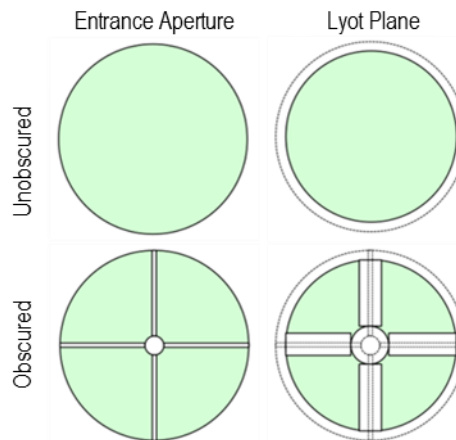


**Figure B.1-1.** Entrance aperture and equivalent Lyot masks. The green shaded areas are the light-collecting regions.

### B.1.1.1.3 Assessment of Factors

The collecting area, integration time, and binary target performance factors were evaluated quantitatively for the listed properties. A search on prior art was performed to consider the implications of polarization influence, while the other three factors were examined based on engineering experience.

#### Collecting Area

A straightforward calculation was performed of the effective collecting area, as defined by the Lyot mask equivalent in the entrance aperture.

Unobscured form collecting area A (unobscured)=$\pi*(R-a)^2$

where

R=aperture radius=0.75 m

a=effective Lyot aperture radius difference at entrance aperture=0.075 m

→ A (unobscured)=1.43 m$^2$

The obscured form collecting area was calculated as A(obscured)=$\pi*[(R-a)^2-(r+a)^2]-N*(w+2a)*(R-r-2a)-e$

where R and a are as above, and

r=obscuration radius=0.075 m

N=number of secondary supports=4

w=support width=0.0375 m

e=correction accounting for simplification of geometry where strut masks meet the

inner and outer mask diameters=0 (i.e., negligible by inspection in this geometry)

→ A (obscured)=0.97 m$^2$

***The collecting area for the unobscured case is 1.48× that of the obscured case.***

### Integration Time

All else being equal, integration time is affected by the collecting area (as calculated above), and how the PSF at the detector distributes target energy (photons) across the sensor pixels.

For purposes of comparison, a pupil function model was created in CodeV and evaluated for encircled energy (EE) for the collecting area geometries described above (see Figure B.1-2).
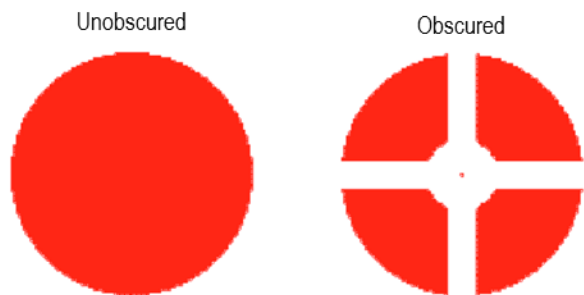


| Energy [%] | Circle Diameter [micron] | | | Circle Area [microns sq.] | | |
|---|---|---|---|---|---|---|
| | Unobs | Obs | Obs/Unobs | Unobs | Obs | Obs/Unobs |
| 10 | 6.045 | 7.872 | 1.30 | 27.80 | 48.67 | 1.70 |
| 20 | 10.171 | 12.888 | 1.27 | 81.25 | 130.45 | 1.61 |
| 30 | 12.860 | 17.819 | 1.39 | 129.89 | 249.38 | 1.92 |
| 40 | 15.735 | 23.352 | 1.48 | 194.46 | 428.29 | 2.20 |
| 50 | 18.840 | 42.269 | 2.24 | 278.77 | 1403.24 | 5.03 |
| 60 | 21.905 | 53.946 | 2.46 | 376.86 | 2285.64 | 6.07 |
| 70 | 25.396 | 67.912 | 2.67 | 506.55 | 3622.28 | 7.15 |
| 80 | 31.416 | 103.147 | 3.28 | 775.16 | 8356.08 | 10.78 |
| 90 | 64.947 | 171.226 | 2.64 | 3312.90 | 23026.55 | 6.95 |

**Figure B.1-2.** Encircled energy data. The data are listed by both circle diameter and circle area, and the ratio of obscured to unobscured listed. Ratio>1 favors the unobscured form; the data show that the relative performance of the unobscured form is substantially better.

By examining the encircled energy level and measurement (linear dimension or collecting area) of interest, the relative spot size between the cases can be determined by the ratio columns "Obs/Unobs." (Note: the results in the 80% row likely represents a grid-sampling artifact in the analysis and should not be used in this comparison.)

A plot of the %EE versus diameter results (Figure B.1-3) provides some insight into the relative behaviors.
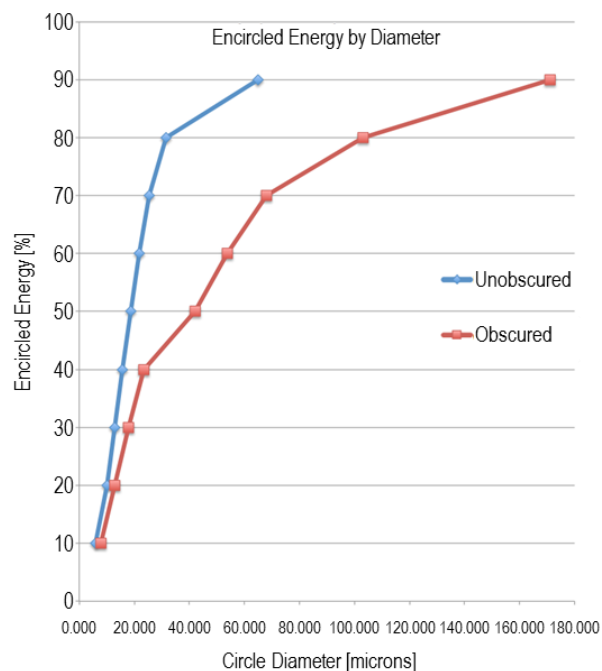


**Figure B.1-3.** Encircled energy plot, by diameter. Beyond 40% EE the obscured form PSF spreads energy farther from the core, requiring a larger area to collect the same energy.

From this, it is clear that for metrics <40% EE there is little distinction between the two forms. However, the diffraction effects in the obscured case spread the remaining energy over a larger distance, which requires larger areas to collect the same amount of energy as the unobscured case.

To provide a physical interpretation, the encircled energy results of Figure B.1-2 were converted into equivalent pixel units as shown in Table B.1-2.

In physical terms, the "pixels readout" columns indicate the number of pixels collecting the signal photons for an optimum placement of the PSF on the array. It can be clearly seen that above the 40% EE level the obscured form PSF spreads energy out over

**Table B.1-2.** Detector pixels involved for encircled energy levels. Larger pixel readout sizes for the obscured form at levels above 40% EE mean substantially fewer photons/pixel/second, and thus either lower per-pixel signal-to-noise ratio (SNR) or longer integration times to achieve performance comparable to the unobscured form.

| | Circle Diameter (Pixels) | | Circle Area (Pixels) | | Pixels Readout | |
|---|---|---|---|---|---|---|
| Energy % | Unobscured | Obscured | Unobscured | Obscured | Unobscured | Obscured |
| 10 | 0.47 | 0.61 | 0.17 | 0.29 | 1×1 | 1×1 |
| 20 | 0.78 | 0.99 | 0.48 | 0.77 | 1×1 | 1×1 |
| 30 | 0.99 | 1.37 | 0.77 | 1.48 | 1×1 | 2×2 |
| 40 | 1.21 | 1.80 | 1.15 | 2.53 | 2×2 | 2×2 |
| 50 | 1.45 | 3.25 | 1.65 | 8.30 | 2×2 | 4×4 |
| 60 | 1.69 | 4.15 | 2.23 | 13.52 | 2×2 | 5×5 |
| 70 | 1.95 | 5.22 | 3.00 | 21.43 | 2×2 | 6×6 |
| 80 | 2.42 | 7.93 | 4.59 | 49.44 | 3×3 | 8×8 |
| 90 | 5.00 | 13.17 | 19.60 | 136.25 | 5×5 | 14×14 |

significantly more pixels, resulting in a lower SNR condition. Roughly speaking, in order to recapture a SNR equivalent to the unobscured case would then require increased integration periods proportional to the area ratio. Taking the 70% energy level as a significant metric (the effective core of the distribution), the signal from a point object (i.e., a planet) would cover an area of 21 pixels for the obscured form as compared to just 3 for the unobscured. This gives an approximate 7× difference in the photons/second incident on each pixel for all else being equal. Even lowering the metric to the 40% energy level, the ratio still favors the unobscured form by a factor of 2.2

Considering then the two main influences together (collecting area and PSF size), for the same target and performance metrics **the unobscured form provides for integration times 3–10× shorter than the obscured form**. While this factor can be somewhat tuned by the geometry of the obscuration and the blocking ratio at the Lyot mask, the net effect remains that the obscured form will always require a significantly longer integration time than the unobscured.

### Polarization Influence

Due to the variation in reflectivity with angle of incidence as a function of polarization and wavelength, light reflecting at any angle other than normal incidence picks up a polarization signature (and in practice, at normal incidence as

well due to variations in depositions of coatings.) In a situation where that angle varies over the beam area, i.e., on a curved surface, then large-scale pupil apodization takes place. This effect is discussed in *The Astrophysical Journal* article "Polarization Effects in Reflecting Coronagraphs for White-Light Applications in Astronomy" by (Breckinridge and Oppenheimer 2004), where the authors caution that coronagraph performances at contrast levels as low as $10^{-8}$ may be compromised by scattering induced by this phenomena. Figure B.1-4 illustrates this apodization effect due to the primary mirror alone.

The effect is most pronounced for the decentered portion of a powered element (i.e., the unobscured aperture form) as it exhibits as a gradient across the pupil. However, it also exists in the obscured form, appearing as a radial apodization. Beyond the low-frequency apodization effects, real-world, non-ideal properties of materials and processes will introduce scattering from higher spatial frequency polarization and wavelength-dependent variations. The more deterministic effects due to geometry can be calculated and presumably mitigated, likely slightly more easily for the obscured form than the unobscured. The more difficult problem of the scattering effects will be common to both forms, resulting in no net distinction between the obscured and unobscured forms for this factor.
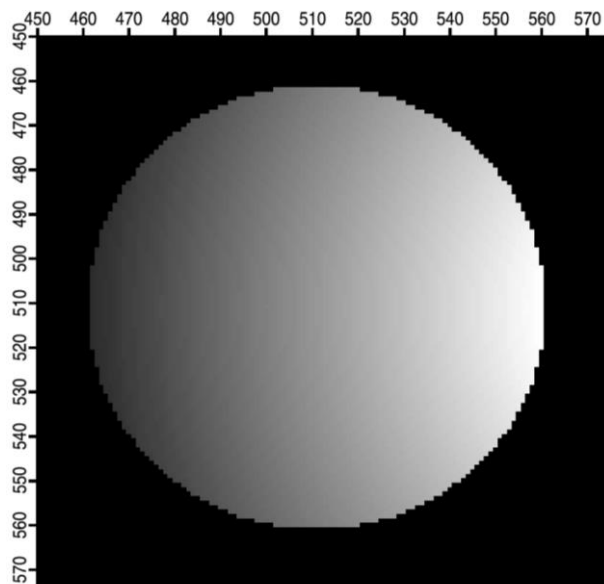
**Figure B.1-4.** Pupil apodization due to polarization effects induced by a perfectly deposited, isotropic, ideal silver thin film on a perfect parabolic surface. The surface represents an f/1.5 primary that is one half of the mirror diameter off-axis. The grey scale ranges from 99.9% to 98.9% reflectivity, with the maximum transmittance toward the parabola's axis at right.

The remaining four factors, where distinctions exist, are of minor influence and do not change the conclusion indicated by the two main factors:

Fabrication complexity of the primary mirror is virtually identical for the two forms given the state-of-the-art in manufacturing of large optical elements (dominated by advances in substrate generating techniques, computer numerically controlled (CNC) machining, and optical testing).

Structural considerations in the relative alignment stability between the primary and secondary mirrors are effectively the same for the two forms, although the unobscured form may permit the use of a structure of slightly lower mass.

Optical design complexity of the rest of the instrument is slightly higher for the unobscured form as it must preserve the unobscured beam path to retain its performance advantage. The obscured form is free to make use of either obscured or unobscured components, giving it a slight relative benefit.

Binary target performance was evaluated for an equal magnitude companion star at a separation of 8 arcsec. Using simplified models that assumed idealized conditions (and no vanes for the obscured form), the relative PSF level at this separation was computed. Both forms gave a result of approximately $5\times10^{-8}$ over the region around the primary star, with the obscured form trending 15–20% higher than the unobscured. The effect of the vanes in the obscured form would be to create a cross-shaped flare in the PSF centered on the companion star; it is assumed that observations would be planned with the telescope rolled to move these flares out of the region of the primary star, and thus would be a likely insignificant effect. Extending the analysis to include the influence of real-world, non-ideal properties in the fabrication of the optical elements is expected to yield virtually identical impacts for the two forms, thus binary target performance is considered a non-discriminator.

### B.1.1.1.4   Conclusion

Overall, the unobscured form is favored over the obscured form due to its advantages in greater collecting area, more compact PSF, and consequently significantly shorter integration times for otherwise equivalent systems.

### B.1.1.2   Instrument Bench Configuration

### B.1.1.2.1   Summary

Two basic configurations were examined to accommodate the coronagraph instrument: "aft," which places the instrument bench parallel to and behind the telescope primary mirror plane, and "lateral," which places it parallel and offset to the telescope axis. The lateral configuration was selected for its ability to fulfill all desired functions while providing for best overall performance with a minimum total count and lowest angles of incidence on critical optical surfaces.

### B.1.1.2.2   Packaging Design Constraints

A nominal point design for layout and packaging was selected based on inputs from technical experts and established instrument requirements:

- Telescope diameter=1.5 m, unobscured aperture
- Pupil image diameter=64 mm (to match candidate DM unit). Note: subsequently changed to 48 mm after the study reported in this section was completed. This change does not significantly affect study results.
- F/# at coronagraph mask=f/30
- Imaging detector field-of-view=1 arcmin
- Imaging detector 1000×1000, 13 micron pixels

Remaining configuration considerations were the placement of FGS/LOWFS and IFS modules. The FGS/LOWFS functions by sensing the light from the target star, so it had to package in an area that permits the starlight to reach it (i.e., by field or wavefront splitting

of the starlight energy before it is removed from the light path). The IFS shares the science focal plane (by beamsplitting or mirror mechanism), so it had to package in that vicinity. Another configuration consideration was the ability to incorporate an auxiliary instrument (of yet to be defined properties) without requiring significant redesign of the system to accommodate it.

Initially two variations of the aft configuration were examined. The first ("Aft1," see Figure B.1-5) constrained the optical elements to fit within a footprint no larger than that of the telescope primary and secondary mirrors combined. This required multiple high angle-of-incidence (AOI) fold mirrors, which were identified as risks to the instrument performance; every extra optical surface would reduce the total energy reaching
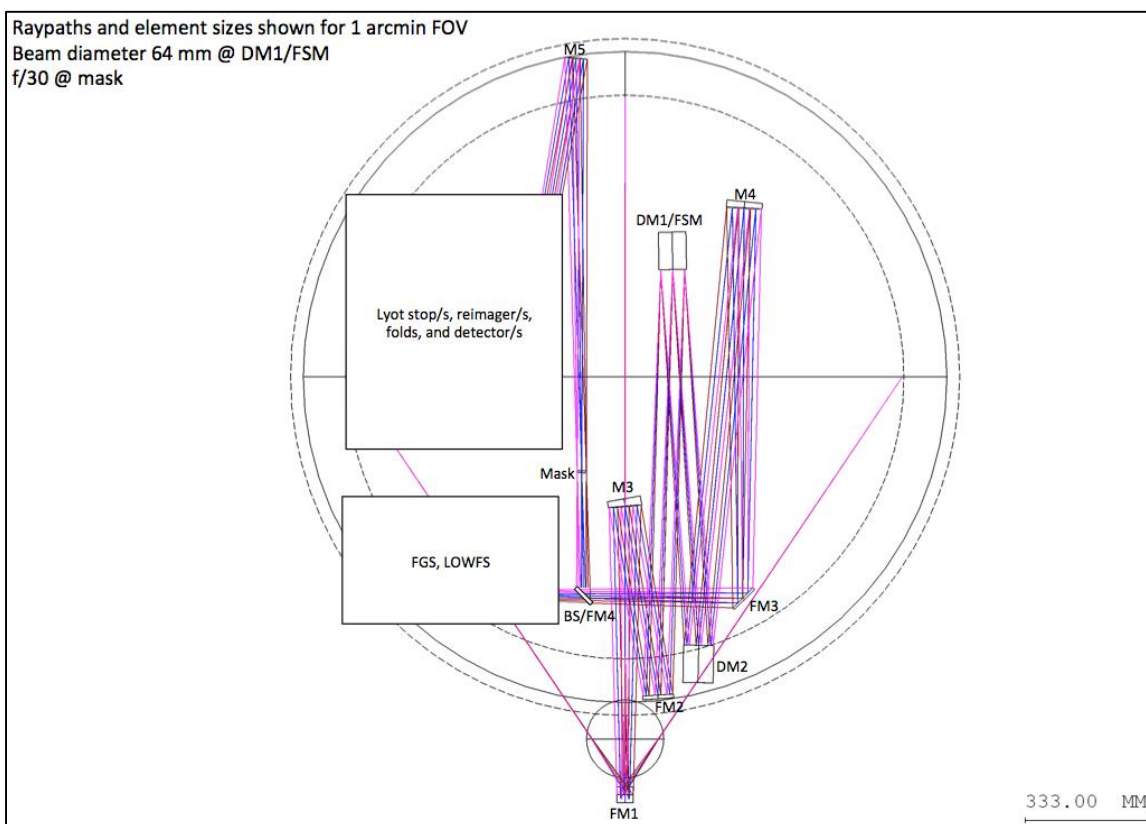


**Figure B.1-5.** "Aft1" configuration end view. Identified issues with this configuration were: 1) The presence of four fold mirrors. Every extra reflection reduces the total throughput to the imaging detector; further, every extra surface/element is another source of wavefront error and scattering. 2) The AOI is steep on three of these elements (FM1, FM3, and FM4). Steep AOIs introduce significant polarization effects, which may adversely impact coronagraph performance. 3) This configuration has limited lateral zones available to the FGS/LOWFS and IFS modules; packaging these might require folding the light path out-of-plane.

the detectors, and high AOIs would introduce polarization effects that could limit the contrast achieved. This configuration was also restricted in volume and could not fit an auxiliary instrument without going to another layer. Accounting for a second instrument layer would require creating more space between the spacecraft and the primary mirror, which would introduce a significant ripple effect in mechanical, thermal, dynamics, and controls.

The second aft configuration ("Aft2," Figure B.1-6) expanded the available volume beyond the limits of the telescope mirror footprints, which was permitted as mechanical packaging activities had been performed that showed the presumed launch vehicle capacity was larger than assumed for the Aft1 variation. Doing so allowed the long optical paths (required to satisfy the quantitative constraints) to be packaged with fewer fold mirrors. The detector positions were placed near the periphery of the volume to provide the shortest paths to presumptive thermal control radiators. This variation required only two fold mirrors, although one still had a high AOI (the first fold following the telescope secondary required to redirect light 90° into the instrument plane).

### Configuration 3: Lateral

Since the spacecraft available volume had been identified to be significantly larger than the telescope, it was recognized that sufficient clearance existed so that the instrument could be placed alongside the primary-secondary path, rather than 90° from it (see Figure B.1-7). With nothing behind the primary mirror, this configuration can mount as close as possible against the spacecraft, making a minimum stack height.

This configuration (Figure B.1-8) addressed the issues identified in Aft1 and Aft2:

1. Fold mirror count reduced from two down to zero. The long throws made possible by the available volume allowed the design to be packaged using the absolute minimum element count to implement the instrument functions.
2. All sensitive elements have low AOIs. With the first fold mirror (identified as FM1 in the Aft variations) eliminated in this configuration, M6 has the highest AOI, but it follows the coronagraph elements so any polarization effect from it would have effectively no impact on instrument performance.
3. Significant clear volumes, more so than Aft2, exist in this plane to accommodate the FGS/LOWFS, IFS, and an auxiliary instrument.

This configuration was developed further to include mechanism representations to visualize clearances around the light paths. In the process of sketching out the filter wheel mechanism (Figure B.1-9), it became apparent that a second filter wheel would be needed to perform all desired functions while keeping the wheel diameter manageable, hence the presence of "Filter Set 1" and "Filter Set 2" ahead of the imaging detector.
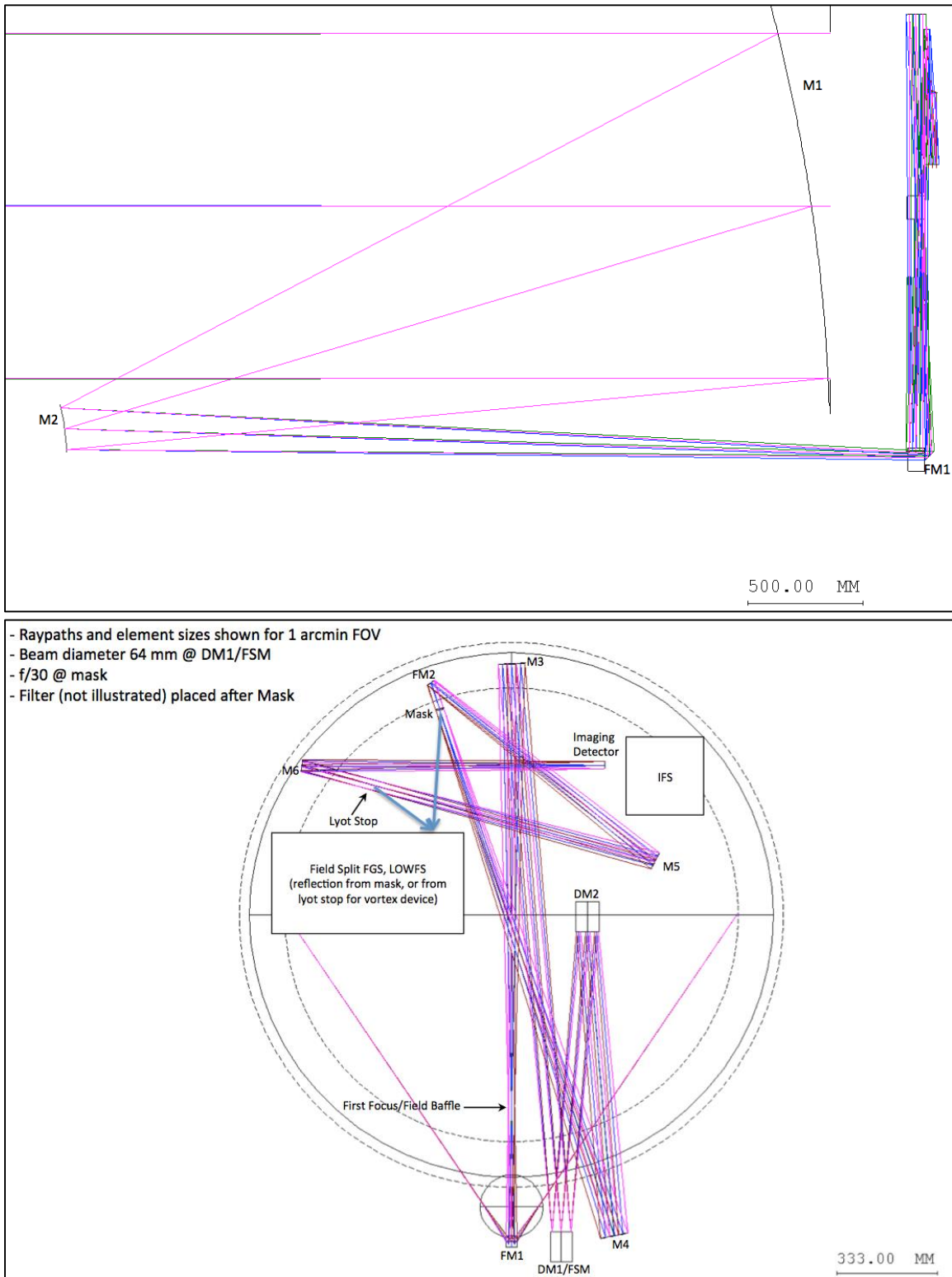
**Figure B.1-6.** "Aft2" configuration side and end view. This configuration addressed most of the issues identified in Aft1: 1) Fold mirror count reduced from four down to two. Of these, the second fold (FM2) follows the Lyot stop so it would have effectively no impact on coronagraph performance other than its throughput reduction. 2) All sensitive elements have low AOIs, other than FM1 (unavoidable). 3) Significant clear volumes exist in this plane to accommodate the FGS/LOWFS, IFS, and a TBD auxiliary instrument.
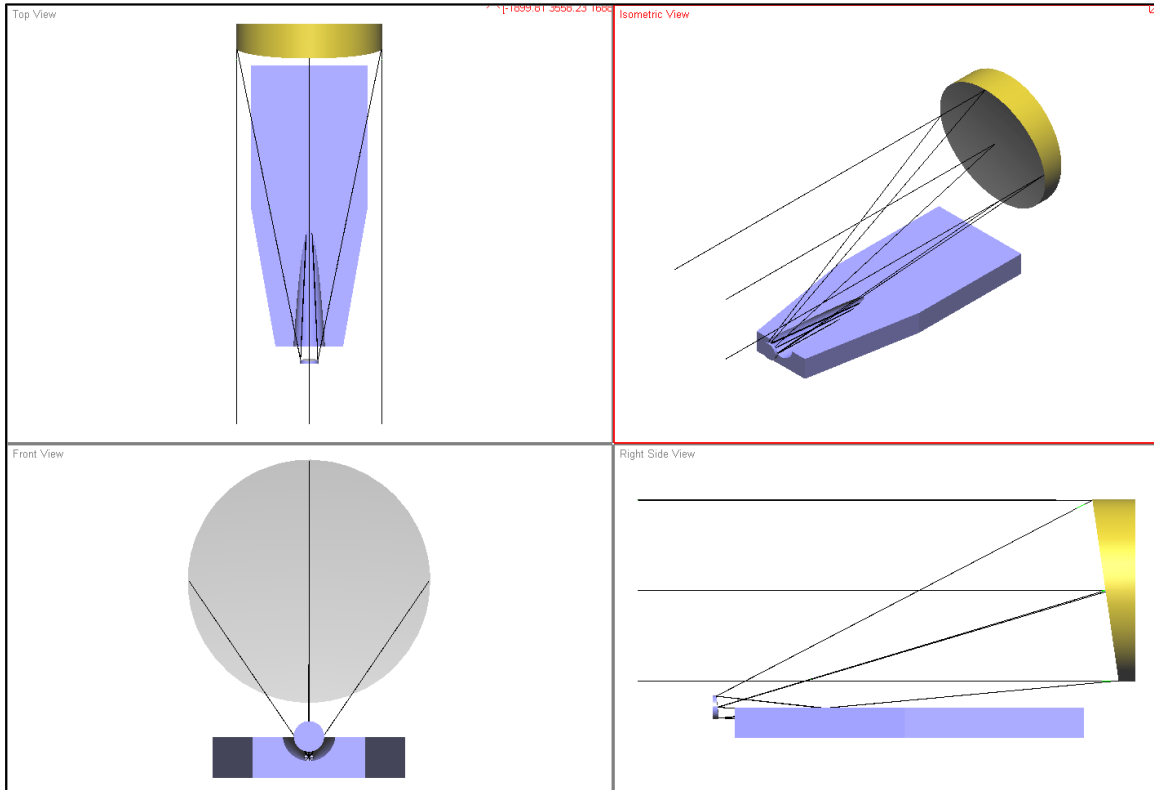
**Figure B.1-7.** "Lateral" configuration. The instrument bench was placed parallel to the telescope primary-secondary axis, which eliminated the need for an initial 90˚ fold mirror and provided ample volume for packaging the optical system.
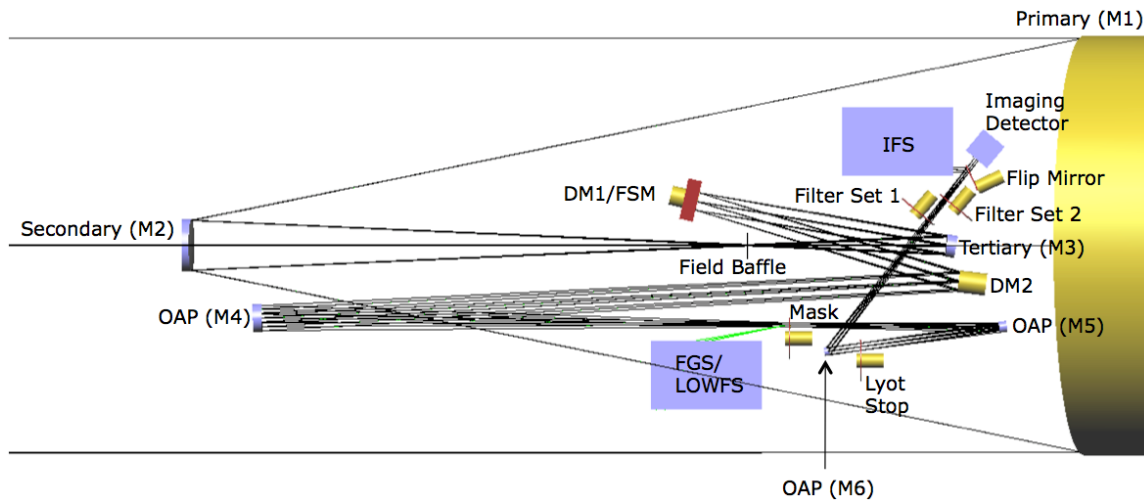


**Figure B.1-8.** "Lateral" configuration, top view. This configuration resolves issues identified in the Aft forms: (1) Fold mirrors are eliminated. (2) All sensitive elements have low AOIs. (3) Significant clear volumes exist in this plane to accommodate the FGS/LOWFS, IFS, and an auxiliary instrument.
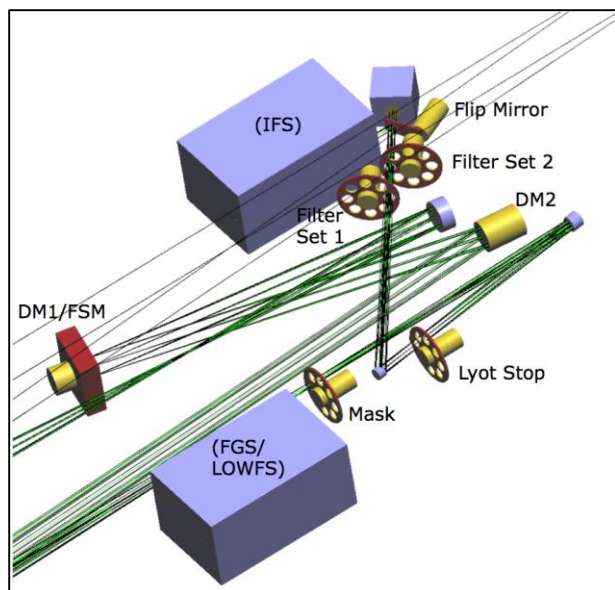
**Figure B.1-9.** "Lateral" configuration, detail of mechanism and subassembly allocations, isometric view. The eight-slot wheel capacity was defined by the minimum slot diameter to pass the light beam and the maximum wheel diameter that would package into the allocated mechanical envelope; this resulted in the use of two filter wheels to provide sufficient slots to carry a presumed complement of filters.

### Conclusion

The lateral configuration concept satisfies all identified constraints and addresses all issues raised. Of all design options studied, it has the best properties for meeting instrument performance requirements by minimizing the number of optical surfaces and the AOI on critical elements.

### B.1.1.3    Aperture Size

#### B.1.1.3.1    Summary and Recommendation

This section summarizes the internal trade that set the baseline clear aperture. Since science only improves with aperture size, available resources set the upper limit. Of those, mass is not a limitation because we have ample mass margin with respect to the launch vehicle capability. Because of that, cost is the dominant driver for the upper limit of the aperture size. The current baseline is set at 1.4 m.

#### B.1.1.3.2    Introduction of Trade

This trade sets the clear aperture size of the observatory, and therefore the size of the primary mirror. The primary mirror is approximately 5 cm in radius larger than the clear aperture for figuring and coating purposes.

The science performance clearly increases with aperture size, since it increases the light collected. More important, the clear aperture size for a coronagraph sets the inner working angle (IWA). This in turn directly affects the number of known radial velocity (RV) exoplanets for which Exo-C is able to obtain spectra, and also the number of Super-Earths that Exo-C would be capable of detecting.

#### B.1.1.3.3    Assessment of Factors

#### Integration Time

The integration time needed per target decreases as the clear aperture diameter increases. This can therefore be traded with lifetime, or throughput. Thus, this is not that strong a driver toward larger aperture size.

#### Inner Working Angle

The IWA requirement is $2\,\lambda/D$. Since the detectors and system throughput will limit the short wavelengths, this is fixed at ~450 nm. Hence, an increase in diameter directly affects how close to the star we can detect or characterize exoplanets. There is no other parameter to trade for diameter, as there is with integration time, and hence the IWA becomes a very strong driver. Figure B.1-10 shows the number of known RV exoplanets that can be characterized as a function of clear aperture diameter. Note that the cutoff is set at 0.8 μm so that, for these exoplanets, a spectrum from 0.45 to 0.8 microns would be measured.

From the diagram, there is a modest gain in going from 1.3 m to 1.5 m. There is little advantage in going from 1.5 m to 1.8 m since there is a flattening in that part of the accumulated targets. It would require apertures larger than 1.8 m to dramatically increase the known RV planets that we can observe.

#### Detections

Neptune to Jupiter sized planets are expected to be detectable around a few hundred nearby stars using an aperture range between 1.1 and

Known RV Planets vs. 2λ/D @ λ = 0.8 μm
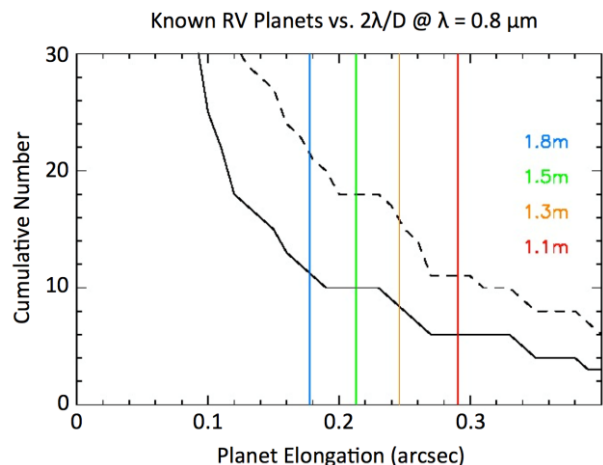
**Figure B.1-10.** Cumulative number of known RV planets Exo-C can measure with different aperture diameters. Below 1.3 m, the presumptive science return would be minimal. Exo-C can measure the spectra of 10 known RV planets at 0.45–0.8 microns. The dashed line represents the cumulative number of known RV planets vs. separation from the parent star. The solid line only counts those with V mag ≤29, which is measurable by Exo-C. The vertical lines shows the sensitivity vs. clear aperture diameter, indicating a small plateau around our current baseline of 1.5 m.

1.8 m; however, that is not the case for Super-Earths. Table B.1-3 shows the number of Super-Earth planets (two Earth radii) we may expect to be detectable. This assumes a maximum of 10 days of integration time.

The table shows that for Super-Earths, 1.3-m and 1.5-m diameter apertures have comparable yields; however, at 1.1 m the sample drops to only four objects, which is below our current minimum baseline science requirement of 10. Hence, we adopt a minimum aperture diameter of 1.3 m for our science floor.

**Table B.1-3**. Expected number of Super-Earth-sized planets detectable as a function of their orbital distance and telescope aperture diameter. Exo-C can probe for Super Earth-sized planets around 1 AU separation around 10 Hipparcos stars (values in black). This will hold true even if the clear aperture diameter decreases a little. Super-Earths could be accessed in a substantially larger target sample if contrasts better than $10^{-9}$ could be achieved (values in red).

| Orb Rad (AU) | 1.1m | 1.3m | 1.5m | 1.8m | Delta Mag |
|---|---|---|---|---|---|
| 1 | 4 | 10 | 10 | 17 | 22.6 |
| 2 | 16 | 25 | 39 | 61 | 24.1 |
| 3 | 17 | 35 | 46 | 66 | 25 |

### B.1.1.3.4    Resources Needed

#### Mass

With a clear aperture diameter of 1.4 m, our current best estimate (CBE) wet mass for the observatory is 1089 kg. A low cost intermediate class launch vehicle has a launch capability calculated at 3580 kg for an Earth-trailing orbit. This gives considerable mass margin to Exo-C. Within the range of apertures being evaluated, mass will not drive the aperture choice.

#### Cost

Not surprisingly, cost is the main resource restriction for aperture size. Early in this design process, Exo-C commissioned a study through JPL's Advanced Projects Design Team on aperture cost sensitivity using an earlier coronagraph mission study as a starting point. The study showed that a more complicated 1.5 m telescope with 5 years of operations was just above the Exo-C $1B target. A reduction from 1.5m to 1.4m as well as simplifications in the payload thermal, mechanical and jitter control designs; a more cost effective high-heritage commercial bus; and a reduction in operational life would later prove the answer in getting the baseline design cost below $1B). A summary of the baseline desing cost estimate is provided in Appendix A. Designs with 1.3 m and 1.1 m apertures came in soundly below the target in the JPL Advanced Projects Design Team study. As a result of this study, apertures larger than 1.5 m were not considered as credibly below the $1B requirement.

### B.1.1.3.5    Conclusion

Given the results of the JPL Advanced Projects Design Team study and the reality of the Kepler mission—1.4 m primary mirror and 4.5 years of leading edge exoplanet discoveries for a total cost of ~$750M FY15—Exo-C decided to baseline a 1.4 m primary mirror aperture.

### B.1.1.4    Instrument Architecture

#### B.1.1.4.1    Summary

A single-path instrument with selectable elements (to provide coverage over the full waveband) is baselined at this time to support initial STOP (structural, thermal, optical, performance) modeling activities. The FGS uses reflections off the starlight rejection element to maximize the fine-steering mirror (FSM) control loop rate at no impact to the science path. Spectral content is evaluated with a field spectrometer to provide the most efficient use of observing time.

#### B.1.1.4.2    Background

Recent mission concept studies (e.g., Actively-Corrected Coronagraphs for Exoplanetary System Studies (ACCESS), DaVinci, Pupil mapping Exoplanet Coronagraphic Observer (PECO), EXoplanetary Circumstellar Environments and Disk Explorer (EXCEDE)) have documented the base coronagraphic functional approaches, with attributes, limitations, and commonalities (Lawson 2013). In summary:

There are five primary approaches, of which three (Lyot, shaped pupil, and vector vortex) share a virtually identical configuration (distinguished by the nature of the element placed in the mask plane). These three, plus the fourth (phase-induced amplitude apodization), once past the coronagraphic implementation, can have identical backends. The fifth form (visible nuller) is unique in almost all aspects, and, while not represented in the following discussion of backend options, was also considered as a coronagraph approach for this mission.

There are three areas where options are considered: science path, FGS function path, and spectrometer path. While there are multiple options for implementing each area, a single architecture needed to be identified to promote the initial analysis activity. This section describes the options considered, and the rationale for the baseline selections made.

#### B.1.1.4.3    Science Path

Once past the coronagraphic elements, all of the starlight rejection will have occurred, leaving a straightforward camera system to create a field image. The performance assumption made is that, based on wavelength-dependent effects, multiple discrete images in several wavebands would be required to preserve the nominal contrast ratio across a broad band. These multiple images can be captured through either multi-path/simultaneous observation or single-path/sequential observation.

Observing efficiency would be maximized if data from all wavebands of interest were collected simultaneously. However, wavefront control can only provide adequate correction over approximately 20% bandwidths, so this would require four coronagraph paths from the first DM back to the detector, each path being effectively an independent instrument as illustrated in Figure B.1-12.

Preserving the necessary conjugate relationship between the primary mirror and the FSM to control pointing and beamwalk effects in all paths would require either equal optical distances, or unique pupil reimaging optics, in each path. The technical impact of this would be extra surfaces in each path, and consequently more opportunities for energy loss and wavefront degradations (from surface figure deformations and/or alignment perturbations). While both of these effects could be mitigated to some degree (i.e., more efficient coatings in narrow bands, DM correction capabilities), what would be unavoidable is the mass/cost impact of implementing such a system. While some variations exist that could eliminate some components (e.g., focusing all four paths to a single detector), this impact was considered to be undesirable, and this option was set aside.

The alternative to the above would be the single-path system (Figure B.1-13). Acquisition of data over the full waveband would require mechanisms to switch waveband-specific
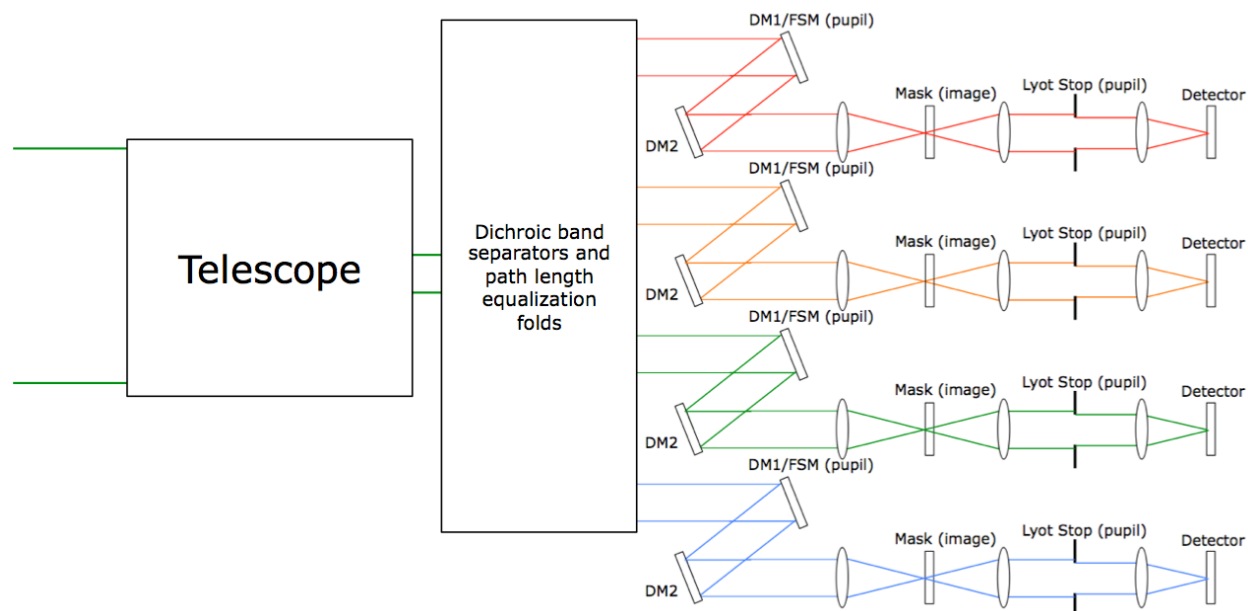
**Figure B.1-12.** Multiple path option. The dichroic separators and path length equalizers split the collected light into four wavebands and channel each band to a dedicated coronagraphic system. This approach would provide efficient use of observing time, but would require significant mass and volume to implement.
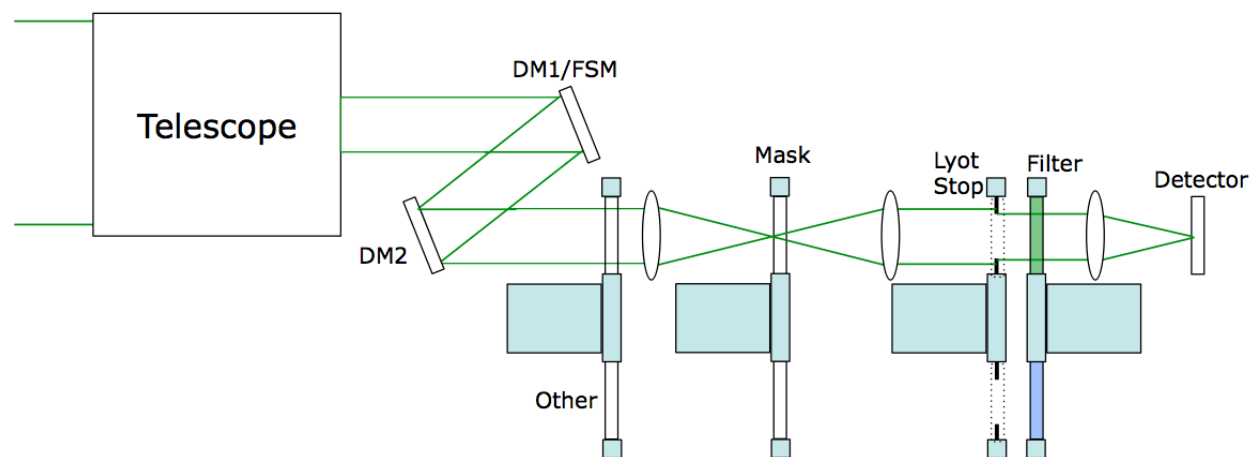


**Figure B.1-13.** Single path option. In this simplified representation, mechanisms switch-in band-specific elements for each of four sequential observations, with the full waveband covered by four narrower wavelength regions. This approach would take somewhat over four times longer than the multi-path option to make a full observation, but is considered more practical to implement.

components and repeating observing runs four times. These components would be spectral filters, Lyot stops, masks, and other beam conditioning elements (e.g., apodizers, polarizers) as needed, depending on the coronagraphic approach being implemented.

Implementing the single-path option would require several mechanisms; in the ideal case, they would all be copies of a single design to minimize costs. It is expected that packaging, mass, and total costs would be, in aggregate, minimized with this option. So, while the multiple-path option would provide optimum use of observing time, practical considerations (component costs, integration costs, mass) weighed in favor of *the single-path option, so it was baselined for the initial STOP analysis at this time.*

### B.1.1.4.4  Fine-guidance Path

The desired ideal would be to use the target starlight as the control for the fine-guidance function (control of the fine-steering mirror). Since this starlight would not be accessible past the coronagraphic elements, it must be acquired ahead of, or within, that zone. Further, since the role of the FGS would be to sense any perturbations of the optical path leading to the key coronagraphic element, acquiring that light as close as possible to the mask would be optimum.

This path also had two main options: amplitude splitting of the starlight wavefront (sees the entire telescope field-of-view), or field splitting (sees only the target star).

Amplitude splitting would be accomplished by placing a beamsplitter plus compensator in the optical path as the last elements prior to the mask, as either a dedicated function (transmits to the mask and reflects to the FGS) or an optical path fold (reflects to the mask and transmits to the FGS). The latter form would provide the minimum perturbation to the science wavefront and should be considered the preferred means if implementing this option (Figure B.1-14).

The primary issue with this option would be that the FGS path "steals" light from the science path. A broadband beamsplitter could be specified in almost any desired R/T ratio, for example 90/10 so that there would be only a 10% reduction in the science path. However, the consequences would be twofold: 1) 10% longer observing times to acquire the same number of photons on the science path, and 2) a slow FGS loop rate since it would take longer to acquire a centroid signal at the appropriate SNR. This issue could be mitigated by using band-specific dichroic beamsplitters on a switching mechanism that would reflect a selected 20% science waveband and transmit the remaining 80% of the waveband light to the FGS. Note that this bandwidth ratio does not represent the energy ratios in each path; that will depend on the star spectral type and which 20% bandwidth is currently in effect.

Another issue would be that the science path, in reflection off the beamsplitter, becomes sensitive to perturbations of that element that the FGS would not detect. This is



**Amplitude Split**
- Splitting element either wideband or dichroic, followed by compensator
- Splitter close to mask with few extra components minimizes errors due to non-common paths
- Option available to place reimager past first focus to control PSF size on detector, but requires adding more non-common mode components to path.
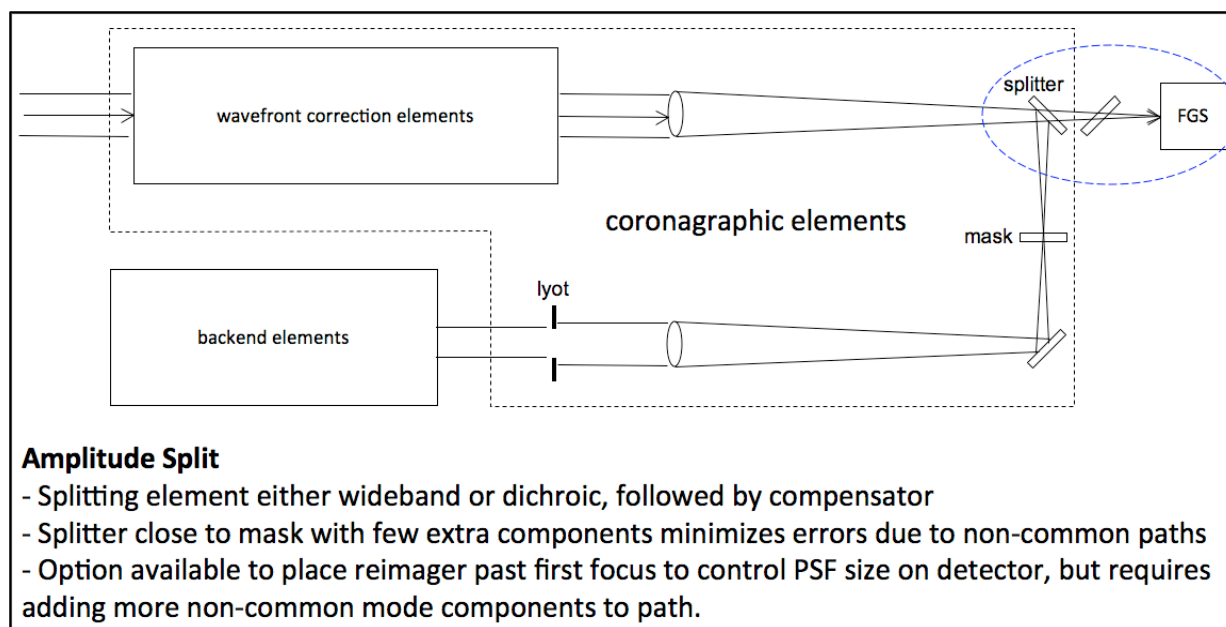
**Figure B.1-14.** FGS via amplitude splitting. This approach provides the full telescope field-of-view to the FGS at the cost of reduced throughput to the science path. Several potential non-common mode effects between the FGS and science paths exist and would need to be well-controlled in order for the system-pointing requirements to be satisfied.

part of a larger issue of non-common mode influences between the FGS path and the science path. Whatever option or implementation is selected, these non-common mode effects will need to be identified and reduced to tolerable levels by choice of configuration, materials, and thermal controls.

The second option for directing light into the FGS path would be to use a field splitting approach by using the light from the center of the field, i.e., the rejected target star light. This would resolve the primary issue with amplitude splitting in that there would be no loss of light in the science path, with the full amount of light from the target star available to the FGS.

For coronagraphs that function by blocking the light at the mask (Lyot, shaped pupil), the blocking area would be made reflective, and the star light reimaged to the FGS detector (Figure B.1-15).

In the vector vortex coronagraph the mask would transmit the rejected target star light, but by virtue of the vortex function, its energy would appear at the edge of the beam. Making the Lyot aperture reflective, the star light would be redirected and focused onto the FGS

detector (Figure B.1-16).

Note that in both of these field-splitting forms starlight would only reach the FGS detector once the system had been reasonably well aligned to the mask. Thus, the initial acquisition function would need to be implemented via other means. A two-step acquisition process is visualized: First, by using spacecraft sensors (star trackers) registered to the instrument line-of-sight, point the spacecraft to get the target star within the field-of-view of the science path. Second, by using the image of the target star on the imaging detector, update the FSM to get the starlight centered on the mask. From that point, the FGS would take command of the FSM to set and hold the desired pointing. The only operational difference between this and the amplitude splitting option would be that since the FGS would have the same field-of-view as the science path in the amplitude splitting case, the science path would not be needed in the FSM control loop, as the FGS would see the target star directly from the spacecraft pointing initially.

From the above, there is no significant



**Field Split (1)**
- Use target starlight reflected from occulting disc of mask
- Focal length of reimager element/s selected to provide desired PSF sampling on detector
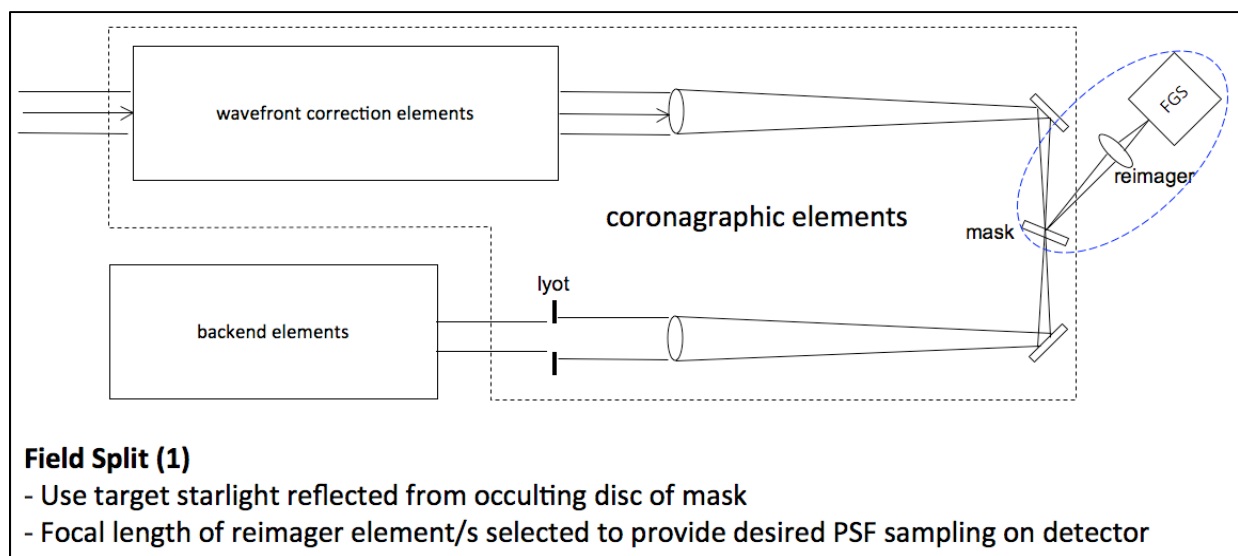
**Figure B.1-15.** FGS via field splitting at coronagraph mask. Once the system is well-enough aligned using information from the imaging detector, the target starlight is picked up by the FGS for the pointing control function. This option makes use of 100% of the starlight with no throughput loss in the science path. Non-common mode effects are reduced due to the more integrated mask+FGS relationship. Note that the fold element is not required for this option, but is illustrated only to be schematically similar to Figure B.1-14 for comparison.

**Field Split (2)**
- Viable only for Vortex Coronagraph; uses vortexed target starlight reflected from lyot aperture
- Focal length of focusing element/s selected to provide desired PSF sampling on detector
- Non-common elements in path do not impair performance; system detects characteristics of vortexed starlight, predominately a function of target star image registration to mask

**Figure B.1-16.** FGS via field splitting at Lyot stop (vector vortex only).Similar in concept and operation to that shown in Figure B.1-15, except it makes use of the unique property of the vector vortex coronagraph operation that puts the target starlight at the edge of the Lyot stop where it can be redirected with high efficiency to the FGS with no impact to the science path. This option functions without non-common mode effects, making for a simple implementation.

distinction between the two options leading up to acquiring the FGS signal. The primary distinction, and clear advantage, is that the field-splitting option collects virtually 100% of the rejected starlight, with no impact to the science path. Based on this, ***the field splitting option for FGS is baselined***.

### B.1.1.4.5   Spectrometer Path

Once a stabilized high-contrast scene has been established, spectral measurements will be performed for both target identification and target characterization functions. The basic spectral resolution requirement (R) to perform these functions was identified to be R~70. While the simplest concept would be to have multiple wheels carrying multiple filters that could be moved in and out of the path, it is clear that it would take impractically long to acquire a full spectrum of data at the resolution required.

A more practical solution would be to use a spectrometer as shown in Figure B.1-17 that either shares (via beamsplitting) or diverts (via an actuated flip mirror) the science field-of-view (the annular zone bounded by the inner working angle of the shortest wavelength and the outer working angle of the longest).

While a point spectrometer would be relatively simple to implement for this function, acquiring the spectra of only a single point at a time would take an inordinate amount of time to cover the entire field. A practical approach would be to use an IFS. Such a device would collect spectral information for almost every feature within the field-of-view simultaneously, providing for the most efficient use of observing time.

Implementation of an IFS would have significant mission benefits. Its detector could perform as a reduced-capacity backup in the event of a failure of the imaging detector. It
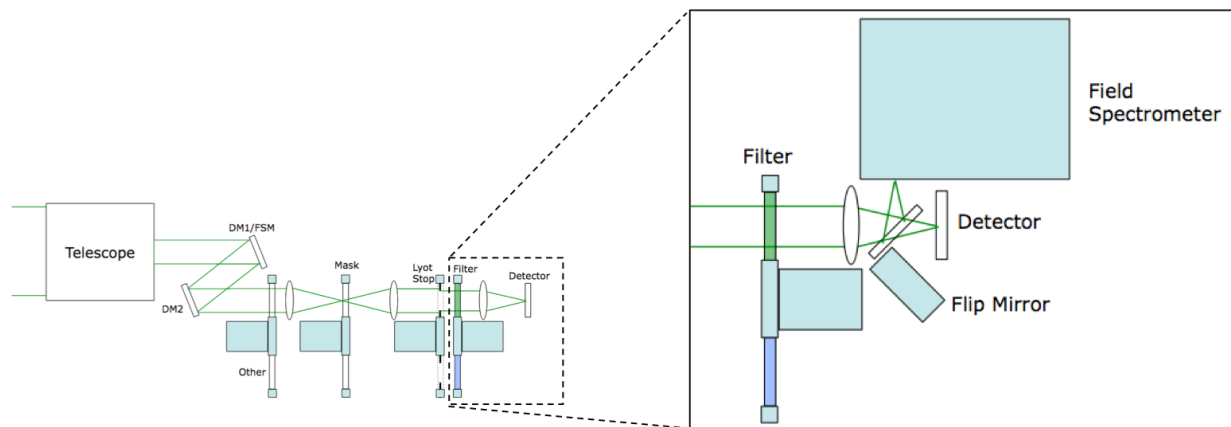
**Figure B.1-17.** Spectrometer implementation. Once the coronagraph establishes that features of interest exist around a target star, the light is directed into a spectrometer that analyzes the spectral content with a resolution R ~ 70 across the waveband. While a static solution exists (a beamsplitter near the detector), observing efficiency in each mode is maximized by the use of a mechanism that either passes the light to the detector or flips in a mirror to reflect it to the spectrometer.

also provides spectral diversity information within a single observing period, in addition to its primary function of full-field spectrographic measurement. ***For these reasons, the integral field spectrometer is baselined.***

### B.1.1.5    Coronagraph

Five coronagraph approaches have been identified for evaluation and comparison in this application. They all have common functional sections: wavefront sensing and control (WFSC), followed by starlight suppression (coronagraph), and finally imaging.

The first and last sections are, to first order, the same for all the approaches. The WFSC section consists of an FSM, DM pair, and simple mirrors (flats and off-axis parabolas (OAPs)) as needed to create pupil images on each of these elements of the appropriate size. The imaging section includes filters, lenses, and other elements to fulfill various desired capabilities (waveband limits, calibration functions, imaging functions, etc.).

While there are other minor differences (e.g., how the starlight is sensed for the WFS area), the primary distinctions in the five approaches is in the coronagraph section. A high-level outline of each of the approaches is provided below:

#### B.1.1.5.1    Lyot/Hybrid-Lyot

This is the classical coronagraph form. After the WFSC section, light from the target star is focused on an occulting disc (mask) that blocks the majority of the starlight while passing virtually all of the light from the surrounding region. In the hybrid variation, a metal and dielectric coating is applied to the mask to provide improved suppression of the starlight at the focal plane. A Lyot mask placed at a downstream pupil image blocks the bulk of the diffracted starlight from the edge of the pupil, and the beam, now with the starlight effectively removed, passes on to the imaging section (Trauger 2012).

#### B.1.1.5.2    Vector Vortex

This approach is structurally identical to the Lyot approach, except the occulting mask is replaced by a structured phase plate that induces a complex phase pattern onto the wavefront. The effect of that pattern is to diffract the starlight to the periphery of the wavefront at a downstream pupil image where it is blocked by the Lyot stop. The nature of the phase plate is such that only light centered on the plate experiences this effect; light from the surrounding region propagates through and is passed by the Lyot stop to be imaged at the focal plane (Serabyn 2013).

### B.1.1.5.3    Shaped Pupil

This approach is essentially identical to the Lyot, except an amplitude mask is located in a pupil plane before the light reaches the occulting mask. The amplitude mask shapes the energy distribution in the focal plane to suppress diffracted light effects. Implementation comes at a throughput cost as effective masks typically have transmission efficiencies around 25–50% (Kasden 2012).

### B.1.1.5.4    Phase-induced Amplitude Apodization

This is another technique for reshaping the energy distribution in the beam to suppress diffraction effects. It uses additional elements in the optical train to induce beam apodization ahead of the occulting mask, and a second set of additional elements following the Lyot stop to unwrap the apodization in order to provide good imaging across the outer working angle (OWA) (Kern 2013).

### B.1.1.5.5    Visible Nuller

This approach is structurally different from the four others. Rather than focusing the light to a coronagraph mask, the wavefront is split, phase shifted, and interferometrically recombined to create a regular pattern of destructive interference across the field of view. The system is aligned to place the target star in one of these zones to null its light; multiple observations made with rotations of the null pattern around this point reveal any objects of interest at the target star (Lyon 2012).

### B.1.1.5.6    Coronagraph PROPER Modeling

The predicted science return of each coronagraph (e.g., the number of planets potentially characterized within a given amount of time) is dependent on the contrast that can be achieved. Because of the effects of optical aberrations and wavefront control, the contrast cannot be reliably determined via analytical methods. It requires end-to-end numerical modeling of the optical system including realistic errors on each surface and wavefront control with DMs.

In this study, a realistic numerical model of the optical system was constructed using the PROPER library for IDL (Krist 2007) which propagates a wavefront from surface to surface using angular spectrum and Fresnel algorithms. The telescope and coronagraph layouts were translated into an unfolded (linear) format. Each surface had simulated phase (polishing) and amplitude (coating) errors applied representative of that sort of optic (i.e., primary mirror, secondary, flat, OAP, etc.), based on power spectral density curves for similar real optics. Coronagraphic masks had no errors, and the PIAA optics had negligible (5 nm RMS) wavefront errors.

In the absence of wavefront errors the coronagraphs were designed to provide contrasts of $\sim 10^{-9}$ or better. Scattering from optical aberrations included in the broadband models degraded contrasts to $10^{-5}$–$10^{-4}$, depending on radius (Figure B.1-18). For the non-VNC coronagraphs, wavefront control using the two DMs was exercised on a DM model composed of measured influence functions. The Electric Field Conjugation (EFC; Giveon et al. 2007) algorithm was used to determine the DM settings necessary to create a dark annulus around the star in which the scattered light was nulled. For practical reasons, the electric fields at the image plane at multiple wavelengths computed by PROPER were used as inputs to EFC rather than deriving them from indirect sensing, as would be done in reality. As an iterative algorithm, EFC was run until the mean contrast inside the dark hole region converged to a minimum. Note that the size of the dark hole can be configured to all or just a portion of the region over which the coronagraph controls diffraction; in most cases improved contrast can be obtained by controlling scattering over a smaller region.

The dark hole for each coronagraph was generated for a static system. To determine the impact on contrast of pointing jitter and a finite diameter star, offsets of the star from its default location were simulated without any additional wavefront control. An offset was
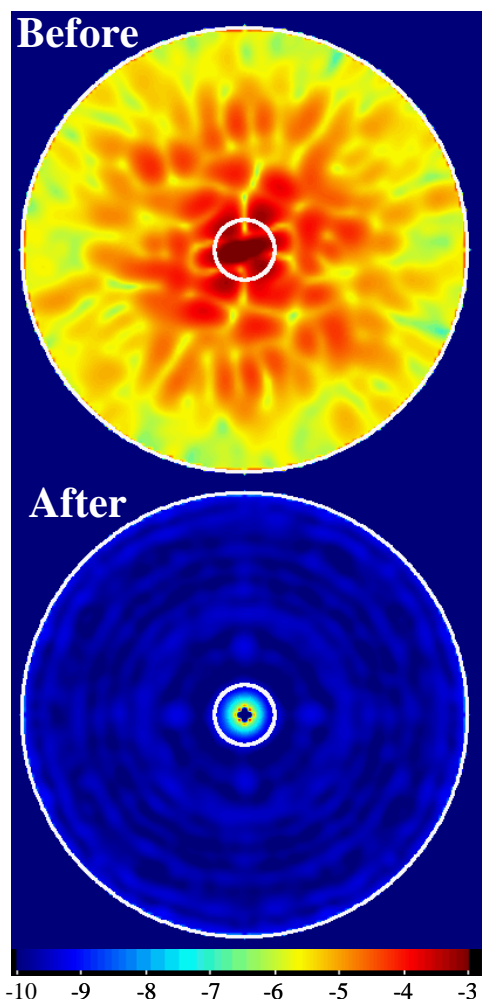
**Figure B.1-18.** HLC broadband contrast before (top) and after (bottom) wavefront control using EFC and the PROPER model. $\log_{10}$(contrast) is given. The white circles are r=2.2 and 16 λ/D.

generated by adding a wavefront tilt to the primary mirror and propagating the wavefront through the system, obtaining a contrast map at the end. A grid of contrast maps for a couple hundred offsets was generated. The maps were then averaged together with weights defined by the Gaussian jitter profile convolved with a 1.0 mas top-hat function representing a finite-diameter star. Jitters of 0.4 and 0.8 mas RMS were simulated.

The contrast maps, planet PSF properties, and transmission curves produced by these simulations were used for the science metrics.

## Shaped Pupil Coronagraph (SPC)

The shaped pupil mask was a series of concentric rings, and was provided as an image file by Robert Vanderbei (Princeton). It was placed in the reimaged pupil location where a Lyot stop would be in the HLC and VVC. In an unaberrated, 20% broadband system it controls diffraction over an r=3.8-22 λ/D annulus with a transmission of 21% (angular λ/D radian units in this section are referenced to λ=550 nm; 1 λ/D=76 mas). EFC was run on the PROPER model for an r=3.3-22 λ/D dark hole, and the resulting contrast (Figure B.1-19) was ~$10^{-8}$ at 4 λ/D and ~$2\times10^{-9}$ beyond 5 λ/D. Because it does not rely on a focal plane mask as part of its diffraction control and only on the pupil mask, the shaped pupil is highly insensitive to pointing jitter, so those effects were not modeled.
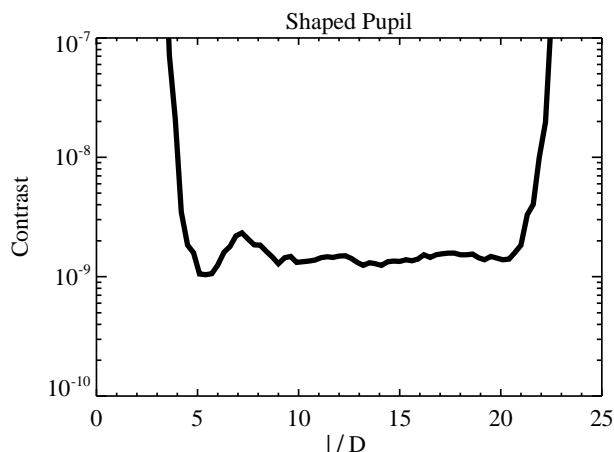


**Figure B.1-19.** Azimuthal mean contrast curve for the shaped pupil coronagraph after wavefront control over λ=495–605 nm. Neither jitter nor a finite star has been included.

## Hybrid Lyot Coronagraph (HLC)

The HLC is a combination of a focal plane mask, Lyot stop, and DMs patterns. Together these control diffraction over a limited field (in this case, out to r=16.5 λ/D with an inner working angle of 2.2 λ/D). Image files of these components were provided by Dwight Moody (JPL). The focal plane mask, which modulates both amplitude and phase, was provided as complex-valued arrays for multiple wavelengths to account for the wavelength-

dependent properties of the nickel and dielectric coatings. EFC was run over an r = 0.6–16.5 λ/D field, and then jitter was added as previously described. At 2.2 λ/D the contrast was $7\times10^{-10}$ for 0.4 mas RMS jitter and $2\times10^{-9}$ for 0.8 mas (Figure B.1-20). Beyond 3 λ/D the contrast is $<4\times10^{-10}$ out to 15 λ/D even with 0.8 mas jitter.
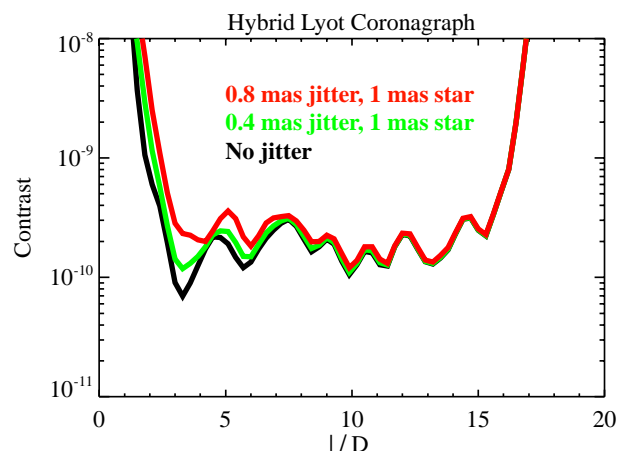


**Figure B.1-20.** Azimuthal mean contrast curves for the hybrid Lyot coronagraph after wavefront control over λ = 495–605 nm.

### Vector Vortex Coronagraph (VVC)

The VVC consists of a focal plane phase mask and a simple clear-aperture Lyot stop. The vortex focal plane mask used here was of charge four (i.e., it imparted a spiral ramp of four waves over a 360º azimuth). A 10 μm diameter opaque spot at the center of the mask was included that, in the real world, would block the confusion region at the center caused by fabrication alignment errors. The mask provided 50% transmission at r=1.8 λ/D. The Lyot stop was a 90% clear diameter aperture with 81% transmission.

A three-layer mask was assumed that provided a broadband contrast of $10^{-8}$ (a five-layer mask would provide $<10^{-10}$, but that was deemed too low in TRL to evaluate here). To improve the contrast caused by the residual chromatic leakage a polarizer was included, reducing throughput by an additional 50%.

EFC was run on the PROPER VVC model for an r=1.2–21.0 λ/D dark hole. The resulting contrast (Figure B.1-21) with 0.4 mas jitter

was ~$10^{-9}$ at 1.8 λ and below that further out. The deep contrast demonstrates that the coronagraph designs, not the telescope aberrations, limit the contrast in these simulations.
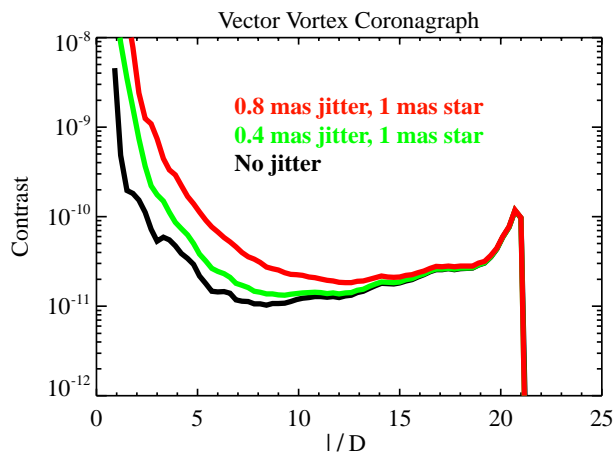


**Figure B.1-21.** Azimuthal mean contrast curves for the vector vortex coronagraph after wavefront control over λ=495–605 nm.

### Phase Induced Amplitude Apodization (PIAA)

The PIAA coronagraph configuration as specified by Rus Belikov (NASA/Ames) was defined as beam remapping functions that represented the phase-induced amplitude apodization (PIAA) optics, a binary post-apodizer mask composed of a series of concentric rings, a hard-edge opaque focal plane occulter, and inverse remapping functions. A PIAA layout specific to this telescope was not defined, so the ACCESS (Trauger, et. al. 2010) layout was used instead. This has the advantage that it is the same layout used to evaluate the same PIAA configuration in the Technology Development for Exoplanet Missions (TDEM) coronagraph modeling study.

The specified PIAA design allowed for an arbitrary focal plane mask size, with trade-offs between contrast, jitter sensitivity, and throughput at the inner working angle. The system was evaluated using a mask that provided 50% transmission at r=2.1 λ/D. Due to large angle diffraction generated by the binary post-apodizer, a field stop masked everything outside of r=18.3 λ/D. Aperture

stops on the reverse mapping optics, together with the post-apodizer, provided a net transmission of 71%.

EFC was run on the PIAA model for a dark hole size of r=0.9–18.3 λ/D. The resulting contrast (Figure B.1-22) was ~$10^{-8}$ at r=2.1 λ/D and $10^{-9}$ or below beyond r=3 λ/D. There was low sensitivity to jitter.
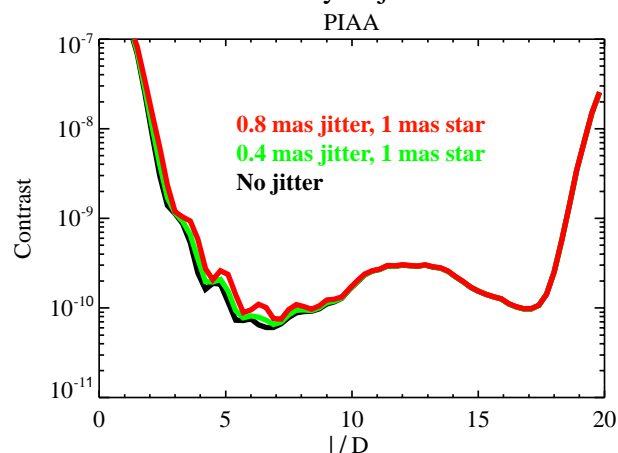


**Figure B.1-22.** Azimuthal mean contrast curves for the vector vortex coronagraph after wavefront control over λ=495–605 nm.

### *Visible Nuller*

The Visible Nulling Coronagraph (VNC) achieves starlight rejection via interferometric nulling. The telescope pupil is split into four nonoverlapping subapertures. These apertures are then interfered two at a time, first in the X-direction, and then in the Y-direction, in order to achieve a two-dimensional null pattern on the sky. Figure B.1-23 shows the arrangement of the sub-apertures. This arrangement reflects the dilute aperture nulling mission concept outlined for DAVINCI (Shao et. al. 2008).

For this simulation, the optical layout consisted of the first three telescope optics (primary, secondary and collimator) used for simulation of the other coronagraph concepts, followed by ~40 optics custom to the VNC design. One arm of the nuller houses the DM. This is a segmented DM with hexagonal segments spaced 520 µm apart. Each segment is supported on three actuators, enabling control of its piston, tip, and tilt. The nuller produces four dark beams and four bright
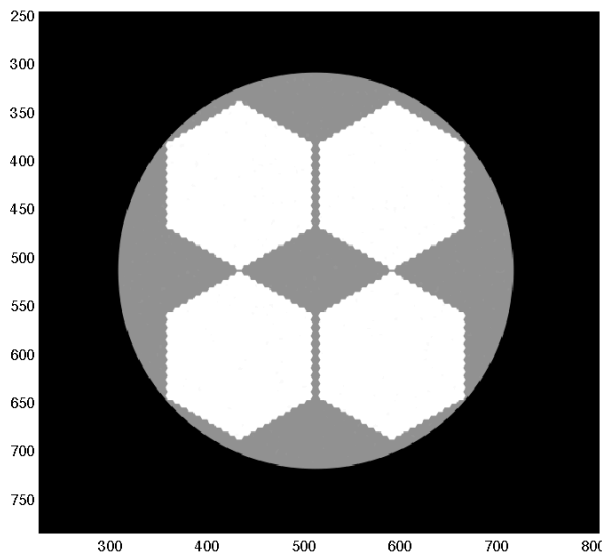


**Figure B.1-23.** Arrangement of VNC sub-apertures on DM and telescope pupil.

beams. The bright beams are used for star tracking and wavefront control, while the dark beams are coherently combined before injection into an array of single mode fibers. There is one fiber for each DM segment. The fibers are used to filter the wavefront of the corresponding DM segments, as well as modulate the intensity of each segment for deep nulling.

The wavefront control for nulling consisted of the following steps: 1) For each pair of beams being nulled, measure the dependence of light coupling from a DM segment to its corresponding fiber as a function of segment tip and tilt, 2) deliberately tip/tilt a DM segment in each arm of the nuller in order to match its intensity to the intensity of the corresponding segment in the other arm, and 3) introduce piston offsets in each DM segment so that the phase difference between segments in the two arms equals pi (half a wavelength at the center wavelength). The errors in the intensity ratio and phase difference determine the level of nulling achievable. For contrast ~$10^{-10}$, phase differences ~0.1 nm, and intensity balance ~0.1% are needed. The simulation was able to control phase to the desired accuracy but intensity matching was limited to ~0.2% due

mainly to coarse granularity in simulation of the DM segments. This resulted in contrast $\sim 5 \times 10^{-10}$–$5 \times 10^{-9}$. The baseline separation of 0.636 meter enables a very small IWA $\sim 1\,\lambda/D$, while the OWA is limited by the acceptance angle of the fibers, $\sim 24\,\lambda/D$. Figure B.1-24 shows the 2-dimensional contrast achieved in this range for a single visit by the VNC.

The null pattern of the VNC limits the contrast in directions corresponding to the X/Y orientation of the sub-apertures. 360° coverage is achieved by rotating the pupil injected into the VNC over a 90° range. Figure B.1-25 illustrates the median radial contrast for this
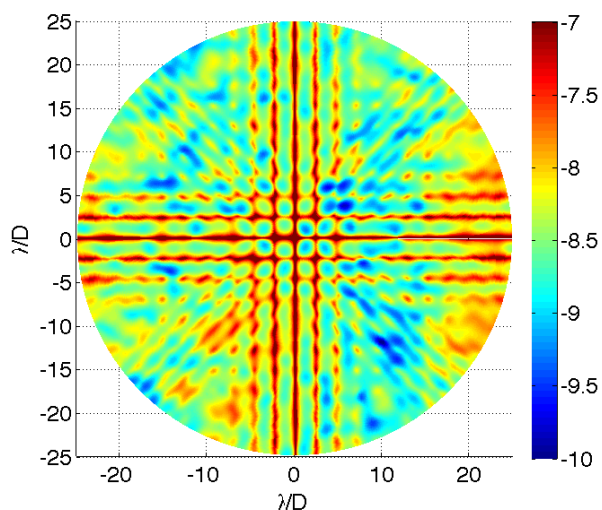


**Figure B.1-24.** VNC 2D contrast for 0 jitter.
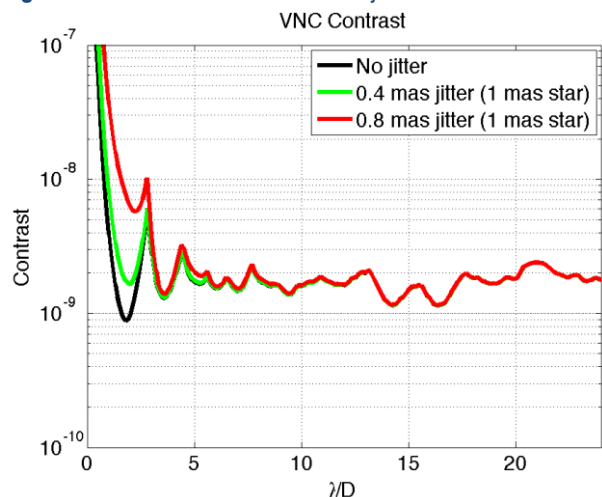


**Figure B.1-25.** VNC median radial contrast with ideal transmission.

ideal case, as well as for the case of 0.4 and 0.8 mas jitter (with 1 mas star).

### B.1.1.5.7  Coronagraph Architecture Downselect

Each of the approaches outlined provides different performances such as IWA, OWA, throughput, bandwidth, contrast, as well as varying levels of complexity, and technology readiness level (TRL). Carrying a design and performing analyses for all five approaches would exceed the resources available to this task; in order to narrow the field for the work going forward, the capabilities of each of the approaches (both as demonstrated to date in laboratory testing and as projected for flight implementation) was collected as shown in Table B.1-4.

A weighted trade of these capabilities and other factors was performed, and relative scores assigned to each approach. After all considerations were taken into account, the hybrid Lyot approach was ranked as first choice and hence baseline for this mission, while the vector vortex and PIAA approaches scored a very close second and third respectively. The vector vortex approach has an architecture that is highly compatible with the hybrid Lyot, and will be carried as the prime alternate in case the hybrid Lyot does not achieve its projected flight levels of performance in future testing. In the meantime, progress made on the PIAA by other studies will be monitored and compared against developments for the vector vortex. Should it become necessary to pursue one of these alternate approaches, the trade for these two will be reevaluated at that time and a final selection made.

**Table B.1-4.** Performance summary of the coronagraph architecture options. The columns "Flight" are the projected capabilities of the architectures, while "Lab" columns contain performance numbers that have been shown to date in laboratory testing. The difference between the two columns provides an indication of the relative maturity of the technology, and the relative amount of development work remaining for each.

| Coronagraph Architecture | | Option 1 Hybrid Lyot | | Option 2 Vector Vortex | | Option 3 Shaped Pupil | | Option 4 PIAA | | Option 5 Visible Nuller (Davinci) | |
|---|---|---|---|---|---|---|---|---|---|---|---|
| | | Flight | Lab | Flight | Lab | Flight | Lab | Flight | Lab | Flight | Lab |
| IWA | λ/D | 2.2 | 3 | 2.2 | 2 | 3 | 4 | 2.1 | 2 | 1 | 3 |
| OWA | λ/D | 16 | 15 | 20 | 7 | 21 | ~20 | 18 | 4 | 24 | N/A |
| Bandpass | % | 20 | 20 | 20 | 10 | 20 | 10 | 20 | 10 | 20 | 10 |
| Contrast (floor) | | 1.E-10 | 1.E-09 | 5.E-12 | 9.E-09 | 8.E-10 | 2.E-09 | 3.E-11 | 1.E-08 | 2.E-09 | 2.0E-06 |
| AZ Coverage | degrees | 360 | 180 | 360 | 180 | 360 | ~90 | 360 | 180 | 90 | N/A |
| Throughput: Pupil x Reflectivity | % | 37 | - | 33 | - | 17 | - | 49 | - | 18 | - |

### B.1.1.6 Low-order Wavefront Sensor

#### B.1.1.6.1 Summary

Although each coronagraph design has different sensitivities to wavefront drift, all coronagraph designs will require a LOWFS in a closed loop with DMs to maintain contrast levels of $10^{-9}$ for the duration of the typical exposure. Three LOWFS architectures were examined in detail and the Zernike Wavefront Sensor (ZWFS) was chosen as the baseline method for the Exo-C probe mission.

#### B.1.1.6.2 Introduction

It has been shown by Green and Shaklan (2003) that coronagraphs designed for $10^{-9}$ contrast and small inner working angles are sensitive to low-order wavefront drift as small as a few 10s of picometers. Maintaining this level of stability during the exposure requires a dedicated sensor that feeds the wavefront error signal back to a DM, which is actuated to correct the drift. The dominant contributors to loss of contrast are focus, astigmatism, coma, trefoil, and spherical aberrations. These are also the dominant terms arising from figure and rigid body drift of individual optical elements due to thermal settling.

#### B.1.1.6.3 LOWFS Trade

Many wavefront sensors have been developed over the years, but most are not suited for the photon-limited regime of a probe-class coronagraph (Guyon 2005). After rejecting the unsuitable designs, three candidates remained:

the Pupil Plane Mach-Zehnder Wavefront Sensor (PPMZWFS) (Guyon 2005), Coronagraphic Low-order Wavefront Sensor (CLOWFS) (Guyon et al. 2009), and the ZWFS (N'Diaye 2013). Each sensor has its strengths and weaknesses. PPMZWFS is a good match for visible nuller coronagraphs where ample light is available in one arm of the nuller for wavefront sensing; however, it is the most complex and most sensitive to photon noise and misalignment. The CLOWFS design is the simplest and has the capability to sense the misalignment of the central starlight with the coronagraph mask. It is only suitable, however, to coronagraphs that employ an occulter at an image plane to block the central starlight. Additionally, it is not clear that the CLOWFS offers the same level of sensitivity to wavefront error (WFE) drift provided by the ZWFS, beyond tip and focus. While no LOWFS has been demonstrated at this level of performance needed for Exo-C, the trade selected the ZWFS for further study due to its simplicity, performance, and compatibility with the selected coronagraphs. The high-level discriminators in the study are summarized in Table B.1-5. A detailed description of the proposed ZWFS implementation is presented in §5.5.5.

### B.1.1.7 Primary Mirror Material Options

This section summarizes the trade study performed to determine the primary mirror material for the Exo-C mission study.

**Table B.1-5.** LOWFS candidates and discriminators.

| Sensor | Coronagraph Compatibility | Astigmatism, Coma, Trefoil, Spherical | Alignment Tolerance | Sensitivity to Photon Noise |
|---|---|---|---|---|
| PPMZWFS | Visible Nuller | Yes | Poor | 2 |
| CLOWFS | PIAA, Shaped Pupil | Maybe | Best | 1 |
| ZWFS | Hybrid Lyot, PIAA, Vector Vortex, Shaped Pupil, Visible Nuller | Yes | Good | 1 |

Primary mirror material options include:

1. SiC options
   a. Active
      i. Piezo-actuated SiC with nanolaminate
   b. Passive with cladding
      i. Chemical vapor deposited (CVD) SiC
      ii. Plasma-ion assisted deposition Si
2. Glass options
   a. Low CTE glass
   b. Zerodur

### B.1.1.7.1   Factors Involved in Determination

1. Wavefront Error (favors glass)
2. Wavefront Drift
3. Thermal Settling Time (favors SiC)
4. Mass (favors SiC)
5. Maturity/Risk (favors glass)
6. Cost (favors glass)

### B.1.1.7.2   Study Assumptions

- Primary mirror diameter=1.5 m
- Mission cost <$1B (including technology development)
- Zonal heating of primary mirror WFE <1 nm RMS (including DMs and a LOWFS)
- Wavefront stability <0.1 nm RMS (including DMs and a LOWFS)

### B.1.1.7.3   Summary and Recommendation

The design team favors a glass primary mirror design (low CTE glass or Zerodur) over SiC (piezo-actuated or passive) given the constraints and assumptions of this mission study. The flight heritage and low thermal expansivity of a glass primary mirror are deemed more important design factors than the lower mass and shorter settling time of SiC. Among the glass options, the design team favors low CTE glass over Zerodur due to its slightly lower mass in designs with flight heritage (fused core versus open back).

### B.1.1.7.4   Assessment of Factors

The first four factors (WFE, wavefront drift, thermal settling time, and mass) were evaluated based on engineering handbook data, prior mission studies, and prior technology demonstrations. The last two factors (maturity/risk and cost) were examined based on engineering experience.

#### Wavefront Error

The science requirements for this mission study specify an overall system WFE of <1 nm root mean square (RMS) including two DMs and a LOWFS. In addition, the overall system wavefront stability must be <0.1 nm RMS over the duration of each science observation. (To characterize Earth-like planets would require wavefront stability <0.01 nm RMS) Spectroscopy observations can have durations ≥48 hrs. The primary mirror WFE achievable for each trade space option is summarized in Table B.1-6.

**Table B.1-6.** Wavefront error achievable for each trade space option. Note that the WFE of the primary mirror is upstream of the DMs and LOWFS, and can be partially compensated.

| Primary Mirror Material | Wavefront Error (nm RMS) |
|---|---|
| Piezo-actuated SiC with nanolaminate | 15 |
| Passive SiC | 0.2–2 |
| Low CTE glass | 0.1 |
| Zerodur | 0.1 |

#### Wavefront Drift

Next, the dynamic wavefront stability of each trade space option is discussed. The wavefront stability of both a glass and SiC primary mirror can be actively controlled with zonal heater control. However, due to SiC's higher coefficient of thermal expansion (CTE), an order of

magnitude higher-precision thermal control system is required for the same level of wavefront stability as glass, even at temperatures as low as 180 K, see Figure B.1-26.

### Thermal Settling Time

Approximate values for the thermal settling time of each trade space option are summarized in Table B.1-7.

**Table B.1-7.** Thermal settling time. For the SiC trade space options, settling times are estimated from prior laboratory experiments and analysis of ~1-m diameter SiC mirrors. The settling time for low CTE glass and Zerodur are estimated from prior analysis for the WFIRST trade study.

| Primary Mirror Material | Thermal Settling Time |
|---|---|
| Piezo-actuated SiC with nanolaminate | ~30 minutes |
| Passive SiC | ~30 minutes |
| Low CTE glass | ~2 hours |
| Zerodur | ~2 hours |

### Mass

The mass of each trade space option is summarized in Table B.1-8.

Low CTE glass is typically used in NASA missions and its front and back are fused on a core. Zerodur mirrors are typically used in European missions. They are open-backed and pocketed, which leads to a heavier mirror for the same stiffness.

**Table B.1-8.** Mass. SiC is significantly lighter and stiffer than glass. For piezo-actuated SiC, the mass of electronics and actuators would be ~5–10 kg/m$^2$ in addition to that listed for the mirror alone.

| Primary Mirror Material | Mass (kg/m$^2$) |
|---|---|
| Piezo-actuated SiC with nanolaminate | ~ 10–15 |
| CVD SiC | ~ 25 |
| Low CTE glass | ~ 40 |
| Zerodur | ~ 50 |

### Maturity/Risk

The TRL level of each trade space option is summarized in Table B.1-9. The TRL levels are best estimates based on the collective experience and engineering judgment of the team. The cost to mature technology to flight readiness levels must be included in the overall mission cost of $1B. Technical maturity is a strong driver for this trade study due to the proposed 2017 start date for Exo-C.
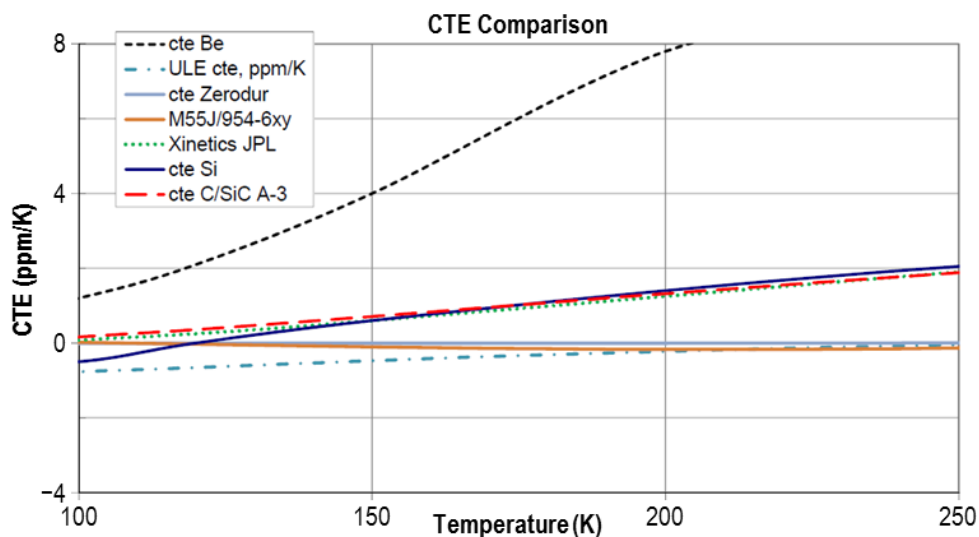


**Figure B.1-26.** Thermal expansivity of various optical and structural materials (Green et al. 2012). The modest power requirements (<50 W) to maintain the primary mirror at 290 K are more than compensated by the low thermal expansion capability of low CTE glass and Zerodur.

**Table B.1-9.** Maturity. Although SiC optics have been flown on several missions, they have been either substantially smaller than 1.5 m in diameter or the surface finish has not been adequate for coronagraph missions. While small SiC optics with either SiC or Si cladding have been polished to sub-nm surface roughness, the process has not been demonstrated on 1.5-m class optics.

| Primary Mirror Material | TRL Level |
|---|---|
| Piezo-actuated SiC with nanolaminate | 6 |
| (CVD) SiC | 3 |
| Low CTE glass | 9 |
| Zerodur | 9 |

### Cost

Requests for cost information were not sent out for the three viable options; recent surveys suggest, however, that SiC is likely to cost significantly more than Glass, and Zerodur is likely to have a marginally lower cost than low CTE glass.

### B.1.1.7.5    Conclusion

Although SiC is an attractive technology for the benign thermal environment of either Earth-trailing or L2 orbits, overall, glass is favored over SiC due to the cost risk and schedule risk required to mature SiC mirror technology to flight readiness levels. The lower mass and faster settling time of SiC are deemed less important design factors than cost and maturity. Among the glass options, low CTE glass is favored over Zerodur due to its slightly lower mass in designs with flight heritage.

### B.1.2    Mechanical

The design of the telescope is a result of the standard mechanical configuration design and analysis process. No mechanical trades have been conducted. The mechanical design, up to this point, has been largely driven by optical design decisions and considerations. For example, the decision to move the instrument bench to the side of the inner barrel led to the elimination of the Aft Metering Structure and the Secondary Support Tower. Additionally, the decision was made to have an articulated secondary mirror, instead of a stationary

mirror, due to alignment and ground-to-orbit structural effects.

### B.1.3    Thermal

### B.1.3.1    Introduction

The thermal design team performed two trade studies, the first investigated active vs. passive thermal control approaches, and the second investigated alternative approaches to solar shielding. The objective of both trade studies was to minimize thermal settling time and maximize wavefront (WFE) stability. Two spacecraft maneuvers were used as representative input disturbances to the thermal control system. These maneuvers were a 45° pitch relative to the orbital plane, and a 30° roll around the boresight. A visual depiction of each maneuver is presented in §5.10, Figures 5.10-1 and 5.10-2, respectively.

A lightweight PM finite element model (FEM), shown in Figure B.1-27, was developed in order to measure the thermal settling time and WFE changes in response to each representative thermal input disturbance. The thermal model is described in §5.6.
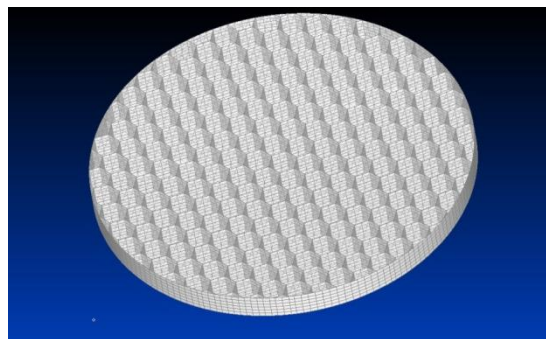


**Figure B.1-27.** 1.4-m low CTE glass primary mirror finite element model.

### B.1.3.2    Trade #1: Heater Controller Design

In order to characterize the relationship between heater controller design complexity and optical performance, four different heater controller designs were implemented.

1. Proportional-integral-derivative (PID) heater control on barrel, PM, and SM
2. PID heater control on barrel only

3. Constant heater power on barrel, PM and SM

4. No heater power

The location of heater zones and temperature sensors was the same across all configurations. To achieve each heater configuration, a symbol manager was used to place heater zones in one of three modes: PID Control, Constant Heat Flux, and Inactive.

The PM surface figure error (SFE) in response to a representative 45° pitch maneuver is shown for each design configuration in Figure B.1-28. Most notably, the two PID control approaches have significantly shorter settling times (~2–3 hours) than the constant and no heater power approaches (~10–20 hours). The current operations plan allows up to 4–5 hours of thermal settling time per maneuver for each new science target.

The SFE stability (the derivative of each curve in Figure B.1-28) must be kept small (less than 10s of picometers) during each science observation in order to maintain the required coronagraph instrument contrast. The designs without PID control (constant heater power and no heater power) have significant PM SFE drift after 20+ hours. This trade study
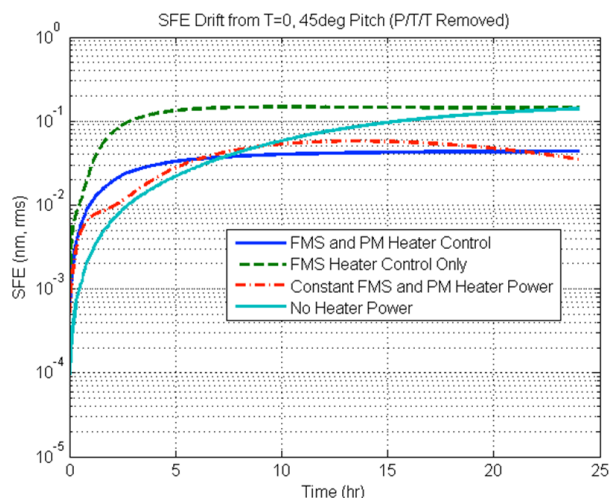


**Figure B.1-28.** Comparison of total SFE for 45° pitch maneuver (starting with SFE=0 at T=0). The two PID heater control approaches have significantly shorter settling times (~2–3 hours) than the constant and no heater power approaches (~10–20 hours).

rules out passive and constant heater power thermal designs. Therefore, Option 1 above (PID control on the telescope barrel assembly, PM, and SM) was chosen for the Exo-C baseline thermal design. A detailed performance analysis of the baseline design is presented in §5.11.

### B.1.3.3 Trade #2: Solar Shielding Design

To characterize the relationship between solar shielding and optical performance, three solar shielding designs were studied, shown in Figure B.1-29.

Each solar shielding design was subjected to a representative 45° pitch, and 30° roll maneuver with PID heater control on the barrel assembly, PM, and SM.

The team started out by investigating a double barrel design, shown in Figure B.1-29a, where the inner barrel is actively thermally controlled and the outer barrel is a passive barrier to the Sun. Both barrels were wrapped in multi-layer insulation (MLI). The passive outer barrel, however, was too heavy and lengthened the thermal transients in response to a maneuver, because of its large thermal inertia.

Next, the team investigated a Kepler-like thermal shielding approach, shown in Figure B.1-29b, in which a layer of MLI, called an MLI tent, was stretched between the solar panels and the barrel assembly, thereby replacing the more bulky outer barrel. This design significantly reduced both the mass and thermal transient time but did not achieve the required contrast stability of 1e-10 over a maneuver. After analyzing the design, it was determined that the dihedral angle of the solar panels and the rounded MLI-tent (both of which were inherited design features from Kepler) were optimized for Kepler's specific science objective of viewing many stars in one area in the sky for months at a time. Exo-C, however, will observe targets one at a time, and needs to maintain contrast stability through a pitch about the orbital plane (to go from a calibration to target star) and a roll
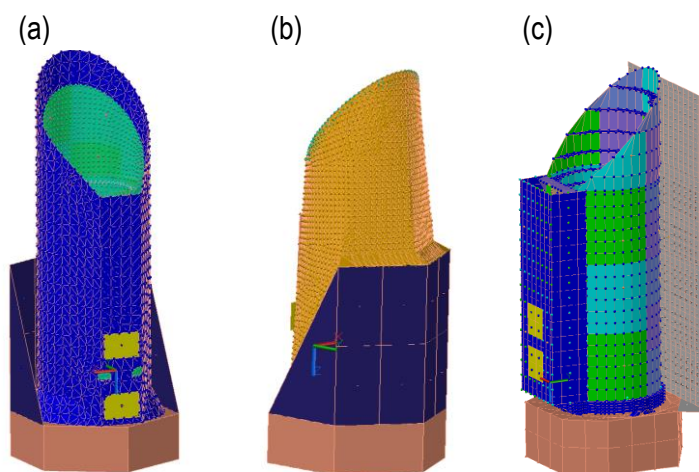
| Solar Shielding Trade Study | Outer Barrel | MLI-tent | Flat solar panel |
|---|---|---|---|
| Mass | ✕ | ✔ | ✔ |
| Fast recovery from thermal transient | ✕ | ✔ | ✔ |
| Contrast stability at steady state | ✔ | ✔ | ✔ |
| Contrast stability over 30 degree roll and 45 degree pitch | Not analyzed | ~2-5 e-9 stability | >1e-10 stability |

**Figure B.1-29.** Three different sunshield configurations: (a) passive outer barrel, (b) Kepler like MLI-tent, and (c) flat solar panel.

about the telescope boresight (to resolve the planet from the background noise).

The preceding analysis lead the design team to investigate a flat solar panel design, which allows the heat load on the barrel to remain symmetric before and after a roll of +15° to −15° about the Sun vector. This performance case, which is studied in detail in §5.11 meets the Exo-C requirement of 1e-10 contrast stability.

## B.2    Mission and S/C Trades

### B.2.1    Earth-trailing vs. L2 Orbit Trade

This section lays out considerations for comparing science capability and cost associated with an observatory located in an Earth-trailing orbit versus a halo orbit at about the Earth-Sun L2 Lagrange point. For this study, the mission's science capability was assessed as a function of sky accessibility and target availability. In addition, model-based cost estimation was used to determine engineering and operation cost differences to access and maintain the two orbits.

The initial examination of this trade suggests that there is no significant increase in target availability or data return capability for a L2-orbiting spacecraft over an Earth-trailing spacecraft. As a result, the major driver for orbit selection will be determined by the overall mission cost. Due to increased operations for orbital maintenance, L2 orbit requires additional navigation costs that the Earth-trailing orbit does not. Therefore, the Earth-trailing orbit is recommended as the baseline orbit for the Exo-C Probe study.

### B.2.1.1    Approach to Study the Trade

The orbital trade study was broken up into two parts to better understand the effects of choosing an L2 halo versus an Earth-trailing orbit. To assess the science drivers for the various orbits, visibility, and target scheduling for Spitzer (Earth-trailing) and the James Webb Space Telescope (JWST) (L2 halo) were compared based on their viewing constraints. This provided a better understanding of the portions of the sky that will be visible

throughout the mission either from the L2 halo orbit or from the Earth-trailing orbit.

To better understand the engineering and cost ramifications of choosing one orbit over the other, a sample spacecraft architecture was selected and examined using JPL's institutional cost models. Small variations to the telecom and propulsion subsystems were changed based on requirements levied by the orbit selected. From there, an overall mission cost was produced for each orbit and compared.

### B.2.1.2 Earth-trailing and L2 Halo Orbits Characteristics

#### Earth-trailing Orbit

Earth-trailing orbit is a heliocentric orbit where a spacecraft is provided a very low positive characteristic energy, allowing the spacecraft to barely escape the Earth's sphere of influence. Once in heliocentric space, the spacecraft will continue to drift away from the Earth at a rate of roughly 0.11 AU per year. Table B.2-1 describes various characteristics for an Earth-trailing orbit that drive the spacecraft design, while Figure B.2-1 provides a visual depiction of the orbit. Figure B.2-2 depicts the Earth's location within the Exo-C viewing zone.

**Table B.2-1.** Earth-trailing orbit characteristics.

| Parameter | Value |
|---|---|
| Launch Characteristic Energy | 0.4 km2/s2 |
| Max Distance from Earth | 0.33 AU (after 3 years) |
| Orbital Maintenance Delta V | 0 m/s |

#### L2 Halo Orbit

The L2 halo orbit is an actively controlled orbit in which the spacecraft maintains a stable orbit at about the L2 Lagrange point. This particular orbit provides an ideal viewing platform, allowing an observatory to access the entire sky as it rotates around the Sun. Though the orbit maintains a constant distance from the Earth for communication, it also requires constant orbit maintenance, including frequent maneuvers for stability. Table B.2-2 and

Figure B.2-3 provide orbit characteristics and a visual depiction of the L2 halo orbit.

**Table B.2-2.** L2 halo orbit characteristics.

| Parameter | Value |
|---|---|
| Launch Characteristic Energy | 0.5 km2/s2 |
| Max Distance from Earth | 1500000 km |
| Orbital Maintenance Delta V | 150 m/s |
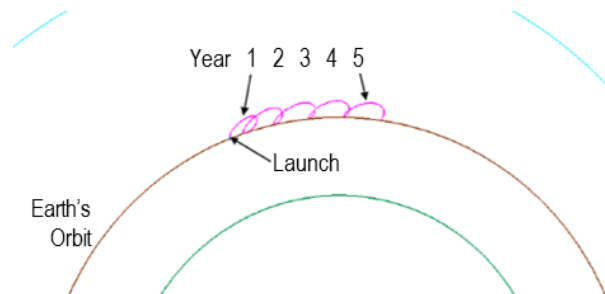


**Figure B.2-1.** Depiction of an Earth-trailing orbit.
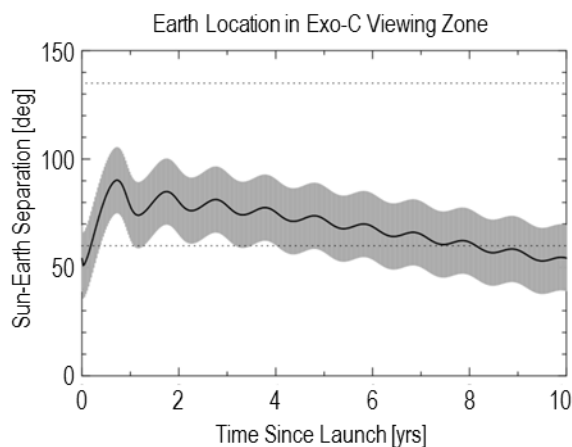


**Figure B.2-2.** Earth location in Exo-C viewing zone for Earth-trailing orbit.
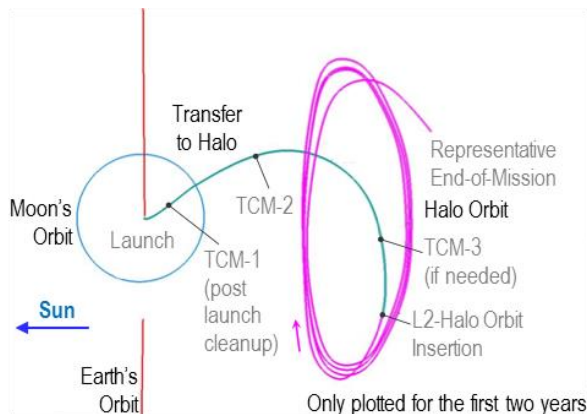


**Figure B.2-3.** Depiction of sample L2 halo orbit.

### B.2.1.3   Science Target Selection and Visibility

With regard to sky accessibility and periods of target availability, an Earth-trailing orbit has comparable advantages to an L2 orbit. Models for comparison of visibility and target scheduling for these two orbits include Spitzer, which has an Earth-trailing orbit, and JWST, which will have an L2 halo orbit. The two telescopes have comparable target viewing windows and sky availability.

In Earth-trailing orbit, the operational pointing zone (OPZ) of an astronomical telescope migrates at a rate of ~1° per day such that the entire sky is visible during the year. However, the number of days in which a target will be visible is a strong function of that target's ecliptic latitude. Within 10° of the ecliptic poles, targets are visible year round in the continuous viewing zone (CVZ). From ±80° ecliptic latitude, targets are visible for a single extended period of time, which decreases with decreasing absolute latitude. At ecliptic latitudes below 60°, the viewing zones break into two shorter periods per year, down to a target on the ecliptic plane, which will be visible for approximately 75 days, twice a year. For our exoplanet targets, we would therefore be able to schedule observations at least 6 months apart, which would be important for phase-dependent measurements. For targets near the poles, there would be a lot more flexibility in scheduling revisits and orbital phase sampling.

For comparison, JWST can observe targets in the ecliptic plane for approximately 53 continuous days, twice a year. Targets within 45° of the ecliptic have two visibility windows per year. There are larger continuous visibility periods above 45°, and these periods culminate in continuous accessibility within 5° of the ecliptic poles.

Targets on the ecliptic are susceptible to zodiacal light, and they have their viewing windows truncated by the presence of the Solar System's planet (including the Earth), which can drift into the OPZ from the sunward direction for an Earth-trailing spacecraft in the first few years of the mission. This problem will not affect a telescope at L2, which is shielded against the Sun, Moon, and Earth, and which will only have to avoid planets at larger distances from the Sun than the Earth. Spitzer's policy was to avoid the Earth by at least 7° when it was in the OPZ, which can heavily truncate available observing periods for targets on or near the ecliptic plane. All other Solar System planets had a 0.5° zone of avoidance. For the Exo-C design, we may need an even tighter avoidance constraint. For Spitzer, the Earth was in the OPZ in the first two years of the mission, dwelling near the inner edge of the OPZ for 160 days in year one and for 132 days in year two. Its largest excursion into the OPZ was a few degrees. However, even at these times, targets beyond the 7° Earth avoidance zone were visible and operations continued. Having the Earth enter the OPZ will only affect targets near the ecliptic, which is already an undesirable region due to zodiacal light, and should not affect overall observing strategies for extrasolar planet observations, since the target stars will be widely distributed across the sky.

### B.2.1.4   Spacecraft Considerations for the Orbits

Both the Earth-trailing and L2 halo orbits have unique considerations required when designing spacecraft. For the Earth-trailing case, communication is the driving engineering hurdle, while the L2 halo case requires a more capable propulsion system. For both orbits, subsystems-specific upgrades are required to a "standard" spacecraft bus designed for Earth orbit in order to meet mission requirements. For comparison purposes, we assumed a standard spacecraft bus consists of deep space capable avionics, attitude determination and control, power, structure and thermal that would be used independent of the orbit selected. From there, communication and propulsion capabilities are added to the bus, depending on mission requirements for the selected orbit. Model-based costs were developed using cost models

to differentiate the overall bus costs associated with each orbit.

### Communication Variations

Due to the drift rate of the Earth-trailing orbit, communication is a major consideration to meet the science needs of the mission. As the observatory drifts farther from Earth, the data rate capability of the system decreases at a rate proportional to the distance squared. To meet the new distances and provide the data rates necessary for the science mission, the frequency used and radio frequency power output must be designed to meet the data rate requirements at the maximum distance from the Earth. For design reference, the Kepler mission utilized a redundant Ka-band communication system, using a 35 W amplifier and a body-mounted 0.85 m HGA. This communication system provides sufficient data rates for the Exo-C mission at maximum expected distances in an Earth-trailing orbit.

In comparison, the L2 halo orbit always remains fixed, and relatively close to Earth (1,500,000 km). This allows the spacecraft to employ a much simpler unamplified S-band system to meet the communication needs of the mission.

### Propulsion Variations

Propulsion systems are used in space missions for a number of reasons, including trajectory corrections, maintaining a steady orbit, or for desaturating the reaction wheels due to rotational rate build-up from reorientation of the spacecraft. As a result, observatories in both the L2 halo and Earth trailing orbits require a propulsion system for one or more of these reasons.

For the L2 halo orbit, the propulsion system is required to perform all three of the above operations, including, "clean-up" discrepancies in the launch vehicle's original trajectory, injection maneuvers, and minor but consistent halo orbit maintenance. These maneuvers are substantial, requiring a fairly

capable propulsion system to move the observatory around.

The Earth-trailing orbit is substantially easier to access and maintain. Since the orbit is effectively a heliocentric, uncontrolled orbit, there are no additional maneuvers required outside the initial launch vehicle injection burn. As a result, the only propulsion system required by the mission is for spacecraft orientation, including reaction wheel desaturations. These maneuvers are quite small, requiring a very small propulsion system.

### B.2.1.5    Cost Trades Discussion

To assess the cost impacts of the two orbits, sample missions were examined using the JPL Institutional Cost Models. A baseline mission concept was developed and used for both the L2 halo and Earth-trailing orbit to ensure that only changes due to the orbit selection affected the cost. From there, orbit-specific spacecraft and operations variations were applied to compare the cost differences.

The Earth-trailing option was estimated to be between $10M and $20M cheaper than the L2 halo option. The major savings for this option is due to the navigation support associated with maintaining the Halo orbit. This requires a fully staffed navigation team throughout the life of the mission to analyze the current orbit of the spacecraft, plan, and perform correction maneuvers when appropriate. Since the Earth-trailing orbit requires no additional maintenance maneuvers, this team can be substantially reduced to almost nothing. All other variations, including the propulsion and communication trades, effectively cancel each other out.

### B.2.1.6    Summary and Conclusion

The initial examination of Earth-trailing versus L2 halo orbit trade suggests that the Earth-trailing orbit is the low-cost option with minimal impact to target visibility and selection for the Exo-C probe study. As a result, it is recommended that the baseline

option moving forward should be an Earth-trailing orbit.

### B.2.2   S/C Architecture

This section lays out considerations for the comparison of contractor-built "off-the-shelf" spacecraft buses versus a custom designed bus.

The initial examination of this trade space suggests that a mission based around a contractor-built spacecraft bus is likely the lowest-cost mission. Of the missions examined, Kepler and Spitzer seem to draw the most similarities to the Exo-C mission, including payload size, power generation, communication and propulsive capability. An architecture utilizing one of these types of buses will likely provide the lowest cost and least risk option for the Exo-C mission.

#### B.2.2.1   Potential Vendor Buses

NASA has recently conducted a range of observatory missions that used commercially built buses. Of these missions the Kepler and Spitzer space telescopes share the most similarities to the Exo-C mission. Both of these spacecraft are good analogies due to their mission class, payload size, and observatory orbit.

To assess the capability of meeting the Exo-C mission requirements, a set of guidelines was developed using mission and instrument requirements defined for the study. These guidelines allowed for the comparison of a variety of potential observatory buses, including the Kepler and Spitzer buses to determine the required modifications needed to meet the mission objectives.

##### B.2.2.1.1   Guidelines for Comparison

- Payload Mass: 923 kg
- Payload Power: 742 W
- Attitude Control: 30 arcsec per axis

- Stability: 0.1 arcsec per axis for 1000 sec
- Delta V Capability: 50 m/s
- Downlink Capability: 2Mbps

##### B.2.2.1.2   Potential Bus Product Lines

Table B.2-3 provides a summary of the Kepler and Spitzer bus capabilities. Both buses require minor modifications to increase payload and power capabilities to accommodate the Exo-C payload. Both missions employed a similar overall mission architecture to that being proposed for the Exo-C mission, including overall mission life, observing scheme, and target orbit. As a result, either bus would be favored moving forward toward the development of the Exo-C mission.

#### B.2.2.2   Conclusion

Due to the existence of "product lines," commercial buses are likely to be the lowest cost option for developing the Exo-C spacecraft bus. Of the many observatory missions examined during this trade study, the Kepler and Spitzer missions carry the highest amount of heritage for the overall mission architecture. As a result, buses developed based on these missions will likely be the lowest cost and least risky options moving forward for Exo-C.

### B.2.3   Mission Lifetime and Operations

#### B.2.3.1   Summary

An initial examination of the trade relating the increase in mission cost due to mission life vs. additional science acquired suggests that there is potentially a significant increase in overall mission cost for an incremental increase in overall science. Though increased mission life will provide for additional observations and an increased cadence, baselining the longer mission will result in additional technical requirements as well as an increase in

**Table B.2-3.** Summary of key parameters for commercial buses that could meet the science objectives of Exo-C.

| Bus | Target Orbit | Payload Mass | Available Power | Propulsive Capability | Downlink Capability | Pointing Capability |
|---|---|---|---|---|---|---|
| Kepler | Earth Trailing | 478 kg | 807 W | ~50 m/s | 4.3 Mbps | 0.75 arcsec |
| Spitzer | Earth Trailing | 403 kg | 413 W | ~150 m/s | 2.2 Mbps | 5 arcsec |

operations cost. As a result, it has been determined that the mission will baseline an overall mission life of 3 years, but will carry consumables for 5 years to allow for a potential extended mission.

### B.2.3.2   Introduction

To first order, the mission lifetime trade exchanges cost for additional observations. Additional observations serve to increase the size of the surveys and can improve the quality of measured parameters. For example, better orbital parameters may be obtained by measuring a longer portion of an orbit. If a planet has a 12-year orbit, then the fit of that orbit will have significant improvements as the length of the mission increases to a larger fraction of that orbit.

The drivers for increasing lifetime are consumables, tougher end-of-life (EOL) requirements, and operations cost. We will assume that all the parts and reliability will stay the same, since Exo-C is a Class-B mission, regardless of the lifetime. Of these, the operations cost is the dominant factor, since we plan to have consumables for 5 years, regardless of the planned lifetime. This ensures that we have the capability to extend the mission later on, and adds margin to the consumables.

The lifetime trade space is between 3 and 5 years. The 3-year minimum is set by the minimum science observations levied on the mission. The 5-year maximum is set by the program office's requirement that Exo-C be a Class-B mission. Although there are exceptions, missions longer than 5 years will tend toward the higher reliability Class-A requirements. Since these are the two extremes, we have selected these two as the only possible options for the trade space.

### B.2.3.3   Increase in Science

There are two scientific benefits to increasing the lifetime of the coronagraph mission. First, lifetime increases the number of observations, and second, it improves the timing or cadence

at which measurements can be made. We will address each separately in the following subsections.

### B.2.3.3.1   Additional Observations

Table B.2-4 shows the number of science targets for each of the two lifetime options. The additional known RV targets that are added in the longer lifetime are dimmer, since the brighter targets were done first. Because of that, the increase in this category is only five targets. The other science categories do not suffer from the same problem, so they scale more proportionally to lifetime. We also left 6 months to be determined later in the study, or be used by other science categories.

### B.2.3.3.2   Improved Cadence

The improvement in the cadence is much harder to assess and would have to be modeled properly in order to determine the benefits to measuring long orbital periods over 5 years, compared to the 3-year baseline mission lifetime. In addition, a statistical model would have to be used with typical orbital periods that we are going to observe. If the typical orbital periods are short compared to the lifetime, then increased lifetime will be less beneficial.

### B.2.3.4   Resources Needed

The affected resources needed to change the lifetime from 3 to 5 years are cost and consumables. In addition, the requirements specified at EOL become more stringent. We address each of these in the next subsections.

### B.2.3.4.1   Consumables

The current baseline is to carry 5 years of consumables, regardless of mission lifetime. Given the $1B cost of these concepts, any future mission would represent a significant asset to NASA so carrying enough propellant to support operations through the typical expected life of the commercial bus, regardless of the time required to meet the mission's primary science goals, would be sensible. As often happens, the spacecraft could be repurposed to a different mission once the

**Table B.2-4.** This table shows the number of science targets for the 3- and 5-year options (center and right columns, respectively). The last column shows the difference between the two cases.

| Science Type | Visits | | Science Observation | | Total Mission Time | Visits | Science | Total Mission Time | Delta |
|---|---|---|---|---|---|---|---|---|---|
| | No. of targets | Ave No. of visits | Ave. Integration time/visit | Total Observe time per Science Type | Total Mission Time | No. of targets | Total Observe time per Science Type | Total Mission Time | No. of targets |
| | $N\_target$ | $N\_visit$ | $t\_I$ (hrs) | $T\_Obs$ (days) | $T\_M$ (days) | $N\_target$ | $T\_Obs$ (days) | $T\_M$ (days) | $N\_target$ |
| **Planet characterizations** | | | | | | | | | |
| Spectroscopy of Known Exoplanets (known from RV and exo-C survey) | 20 | 1 | 200 | 167 | 193 | 25 | 104 | 136 | 5 |
| Multi color photometry of Known Exoplanets (known from RV and exo-C survey) | 20 | 1 | 20 | 17 | 43 | 30 | 25 | 64 | 10 |
| **Planet discovery surveys** | | | | | | | | | |
| Survey nearby stars for super-Earths within the habitable zone | 20 | 6 | 20 | 100 | 150 | 40 | 200 | 300 | 20 |
| Search for giant planets around nearby stars | 140 | 3 | 20 | 350 | 525 | 200 | 500 | 750 | 60 |
| **Disk Imaging Surveys** | | | | | | | | | |
| Detection survey in RV planet systems | 60 | 1 | 12 | 30 | 40 | 120 | 60 | 80 | 60 |
| Known debris disks within 40 pc | 60 | 1 | 6 | 15 | 24 | 100 | 25 | 40 | 40 |
| Young debris disks from WISE | 100 | 1 | 6 | 25 | 40 | 300 | 75 | 119 | 200 |
| Nearby protoplanetary disks | 80 | 1 | 6 | 20 | 32 | 200 | 50 | 79 | 120 |
| Total on-orbit ops time | | | | 723 | 1045 | | 1039 | 1568 | |
| Initial On-Orbit Checkout (days) | | | | | 60 | | | 60 | |
| Total (days) | | | | | 1105 | | | 1628 | |
| Total (years) | | | | | 3.0 | | | 4.5 | |

science goals of its original mission are reached. Hence, there is no change in the consumables that Exo-C would carry.

### B.2.3.4.2 Operating Costs

Based on Kepler actual operations costs, Exo-C is budgeting just under $20M FY15 per year plus 30% cost reserves. This means that adding 2 years to the current 3-year baseline mission, would increase operations costs by about $50M.

### B.2.3.4.3 End-of-Life Requirements

Several other requirements, such as the solar panel output, are set at mission EOL. For this concept, EOL is defined as the end of the primary science mission—3 years. Any subsequent missions will make the best use of the spacecraft's resources available at that time, and most can compensate operationally for degradations below performance levels required for the primary mission.

### B.2.3.5 Conclusion

The lifetime trade is fundamentally a trade between additional costs and additional observations. The additional $50M in cost for a 5-year mission represents a significant increase and would impact other elements of the mission concept in order to meet the $1B total mission cost cap. This impact to the baseline design is not seen as a worthwhile tradeoff against the improvement in science created by an additional 2 years of observations. Accordingly, the recommended baseline design life is 3 years, with consumables sized for 5 years.

### B.2.4 Solar Array and High Gain

This section summarizes the trade study performed to determine the HGA configuration: articulated vs. body-fixed. HGA options include:

A. Articulated

B. Body fixed

Factors involved in determination include:

1. Cost (favors fixed)
2. Mass (favors fixed)
3. Induced dynamics (favors fixed)

### B.2.4.1 Evaluation of Factors

*1. Cost.* Based on hardware data in JPL's institutional cost models, a body-fixed antenna

offers \$5.2M hardware-only savings (including margin) compared to a gimbaled system. Testing and pointing control software costs will further increase this.

*2. Mass.* A body-fixed antenna offers 9.7 kg mass savings compared to a gimbaled system.

*3. Dynamics Environment.* An articulated antenna is expected to introduce dynamics into the system, even when not pointed, and therefore will require additional isolation. This will either affect payload performance or require additional cost and/or mass to isolate the associated dynamic disturbances.

# D Target List

| Star Name | V (mag) | Dist. (pc) | RA, Dec | Band | Integration (hrs) | Visits | Known RV Target | New Planet Survey | HZ? | Disk Program |
|---|---|---|---|---|---|---|---|---|---|---|
| eps Eridani | 3.73 | 3.2 | 3.5 h -8.5° | V | 84.1 | 1 | phot,spec | Earth | * | RV,HZ |
| eps Eridani | 3.73 | 3.2 | 3.5 h -8.5° | R | 1.9 | 1 | phot,spec | | | |
| eps Eridani | 3.73 | 3.2 | 3.5 h -8.5° | I | 13.1 | 1 | phot,spec | | | DD |
| eps Eridani | 3.73 | 3.2 | 3.5 h -8.5° | z | 8.6 | 1 | phot,spec | | | |
| GJ 832 | 8.67 | 5 | 21.6 h -49.0° | V | 195.2 | 1 | phot | | | |
| GJ 832 | 8.67 | 5 | 21.6 h -49.0° | R | 22.7 | 1 | phot | | | |
| GJ 832 | 8.67 | 5 | 21.6 h -49.0° | I | 182.8 | 1 | phot,spec | | | |
| GJ 832 | 8.67 | 5 | 21.6 h -49.0° | z | 16.1 | 1 | phot | | | |
| 55 Cnc | 5.95 | 12.3 | 8.9 h 28.3° | V | 12 | 1 | phot | | | RV |
| 55 Cnc | 5.95 | 12.3 | 8.9 h 28.3° | R | 385.1 | 1 | phot,spec | | | |
| 55 Cnc | 5.95 | 12.3 | 8.9 h 28.3° | I | 215.6 | 1 | phot,spec | | | |
| 55 Cnc | 5.95 | 12.3 | 8.9 h 28.3° | z | 14.3 | 1 | phot | | | |
| beta Pic | 3.86 | 19.4 | 5.8 h -50.9° | V | 103.2 | 1 | phot,spec | Saturn | | HZ |
| beta Pic | 3.86 | 19.4 | 5.8 h -50.9° | R | 95.8 | 1 | phot,spec | | | |
| beta Pic | 3.86 | 19.4 | 5.8 h -50.9° | I | 107.9 | 1 | phot,spec | | | DD |
| beta Pic | 3.86 | 19.4 | 5.8 h -50.9° | z | 8.1 | 1 | phot | | | |
| GJ 433 | 9.81 | 8.9 | 11.6 h -31.5° | R | 165.7 | 1 | phot | | | |
| GJ 433 | 9.81 | 8.9 | 11.6 h -31.5° | I | 29.6 | 1 | phot | | | |
| GJ 433 | 9.81 | 8.9 | 11.6 h -31.5° | z | 110.3 | 1 | phot | | | |
| mu Ara | 5.15 | 15.5 | 17.7 h -50.2° | V | 142.1 | 1 | phot,spec | | | RV |
| mu Ara | 5.15 | 15.5 | 17.7 h -50.2° | R | 66.2 | 1 | phot,spec | | | |
| mu Ara | 5.15 | 15.5 | 17.7 h -50.2° | I | 44.9 | 1 | phot,spec | | | |
| mu Ara | 5.15 | 15.5 | 17.7 h -50.2° | z | 421.8 | 1 | phot,spec | | | |
| HD 142 | 5.70 | 25.7 | 0.1 h -48.9° | R | 115.6 | 1 | phot | | | |
| HD 99492 | 7.53 | 18 | 11.4 h 3.0° | V | 99.2 | 1 | phot | | | |
| HD 99492 | 7.53 | 18 | 11.4 h 3.0° | R | 41.1 | 1 | phot | | | |
| HD 99492 | 7.53 | 18 | 11.4 h 3.0° | I | 24 | 1 | phot | | | |
| HD 99492 | 7.53 | 18 | 11.4 h 3.0° | z | 97.2 | 1 | phot | | | |
| HD 217107 | 6.18 | 19.9 | 23.0 h -1.6° | V | 13 | 1 | phot | | | |
| HD 217107 | 6.18 | 19.9 | 23.0 h -1.6° | R | 8 | 1 | phot | | | |
| HD 217107 | 6.18 | 19.9 | 23.0 h -1.6° | I | 415.1 | 1 | phot,spec | | | |
| GJ 849 | 10.37 | 8.6 | 22.2 h -3.4° | R | 180.1 | 1 | phot | | | |
| GJ 849 | 10.37 | 8.6 | 22.2 h -3.4° | I | 45.8 | 1 | phot | | | |
| GJ 849 | 10.37 | 8.6 | 22.2 h -3.4° | Z | 169.4 | 1 | phot | | | |
| HD 134987 | 6.46 | 26.2 | 15.2 h -24.7° | V | 30.4 | 1 | phot | | | |
| HD 134987 | 6.46 | 26.2 | 15.2 h -24.7° | R | 19.3 | 1 | phot | | | |
| HD 134987 | 6.46 | 26.2 | 15.2 h -24.7° | I | 14.8 | 1 | phot | | | |
| 47 Uma | 5.04 | 14.1 | 11.0 h 40.4° | V | 109.9 | 1 | phot,spec | Saturn | | RV |
| 47 Uma | 5.04 | 14.1 | 11.0 h 40.4° | R | 24.6 | 1 | phot,spec | | | |
| 47 Uma | 5.04 | 14.1 | 11.0 h 40.4° | I | 17.6 | 1 | phot,spec | | | |
| HD 190360 | 5.71 | 15.9 | 20.1 h 29.9° | V | 192.4 | 1 | phot,spec | | | RV |
| HD 190360 | 5.71 | 15.9 | 20.1 h 29.9° | R | 90.4 | 1 | phot,spec | | | |
| HD 190360 | 5.71 | 15.9 | 20.1 h 29.9° | I | 58.8 | 1 | phot,spec | | | |
| HD 150706 | 7.03 | 28.2 | 16.5 h 79.8° | V | 144.5 | 1 | phot | | | |
| HD 150706 | 7.03 | 28.2 | 16.5 h 79.8° | R | 99.7 | 1 | phot | | | |
| HD 150706 | 7.03 | 28.2 | 16.5 h 79.8° | I | 82.7 | 1 | phot | | | |
| HD 154345 | 6.74 | 18.6 | 17.0 h 47.1° | V | 24 | 1 | phot | | | |
| HD 154345 | 6.74 | 18.6 | 17.0 h 47.1° | R | 14.4 | 1 | phot | | | |
| HD 154345 | 6.74 | 18.6 | 17.0 h 47.1° | I | 10.6 | 1 | phot | | | |
| HD 87883 | 7.55 | 18.2 | 10.1 h 34.2° | V | 66.5 | 1 | phot | | | |
| HD 87883 | 7.55 | 18.2 | 10.1 h 34.2° | R | 27.6 | 1 | phot | | | |

| Star Name | V (mag) | Dist. (pc) | RA, Dec | Band | Integration (hrs) | Visits | Known RV Target | New Planet Survey | HZ? | Disk Program |
|---|---|---|---|---|---|---|---|---|---|---|
| ups And | 4.10 | 13.5 | 1.6 h 41.4° | V | 17.9 | 1 | phot,spec | Saturn | | RV,HZ |
| HD 39091 | 5.67 | 18.3 | 5.6 h -79.5° | V | 365.9 | 1 | phot,spec | | | RV |
| HD 62509 | 1.14 | 10.4 | 7.8 h 28.0° | V | 6.4 | 1 | phot,spec | Neptune | | RV |
| HIP 8102 | 3.50 | 3.6 | 1.7 h -14.1° | V | 98.8 | 2 | | Earth | * | HZ |
| HIP 32349 | -1.46 | 2.6 | 6.8 h -15.3° | V | 0.1 | 2 | | Earth | | |
| HIP 37279 | 0.37 | 3.5 | 7.7 h 5.2° | V | 5.6 | 2 | | Earth | | HZ |
| HIP 97649 | 0.76 | 5.1 | 19.8 h 8.9° | V | 5.6 | 2 | | Earth | | HZ |
| HIP 71681 | 1.33 | 1.2 | 14.7 h -59.2° | V | 99.2 | 3 | | Earth | * | HZ |
| HIP 71683 | 0.01 | 1.3 | 14.7 h -59.2° | V | 9.3 | 3 | | Earth | * | |
| HD 20794 | 4.27 | 6 | 3.3 h -42.9° | V | 8.4 | 1 | | superEarth | | RV,HZ |
| HIP 3821 | 3.44 | 6 | 0.8 h 57.8° | V | 7.8 | 2 | | superEarth | * | HZ |
| HIP 19849 | 4.43 | 5 | 4.3 h -6.3° | V | 6.8 | 2 | | superEarth | | HZ |
| HIP 84405 | 4.32 | 5.9 | 17.3 h -25.4° | V | 8.3 | 2 | | superEarth | | HZ |
| HIP 88601 | 4.03 | 5.1 | 18.1 h 2.5° | V | 6.1 | 2 | | superEarth | | HZ |
| HIP 99240 | 3.56 | 6.1 | 20.1 h -65.8° | V | 9 | 2 | | superEarth | | HZ |
| HIP 108870 | 4.69 | 3.6 | 22.1 h -55.2° | V | 95.7 | 2 | | superEarth | | HZ |
| HIP 104214 | 5.21 | 3.5 | 21.1 h 38.7° | V | 82.4 | 2 | | superEarth | | |
| gamma Cephei | 3.22 | 14.1 | 23.7 h 77.6° | V | 62.8 | 1 | | Neptune | | RV,HZ |
| 61 Vir | 4.74 | 8.6 | 13.3 h -17.7° | V | 67 | 1 | | Neptune | | RV |
| HD 102365 | 4.88 | 9.2 | 11.8 h -39.5° | V | 94.3 | 1 | | Neptune | | RV |
| HIP 1599 | 4.23 | 8.6 | 0.3 h -63.1° | V | 29.9 | 2 | | Neptune | | |
| HIP 2021 | 2.79 | 7.5 | 0.4 h -76.7° | V | 7.8 | 2 | | Neptune | | HZ |
| HIP 12777 | 4.11 | 11.1 | 2.7 h 49.2° | V | 46.9 | 2 | | Neptune | | |
| HIP 14632 | 4.05 | 10.5 | 3.2 h 49.6° | V | 9.8 | 2 | | Neptune | | |
| HIP 17378 | 3.54 | 9 | 3.7 h -8.2° | V | 4.7 | 2 | | Neptune | | |
| HIP 22449 | 3.19 | 8.1 | 4.8 h 7.0° | V | 6.9 | 2 | | Neptune | | HZ |
| HIP 24608 | 0.08 | 13.1 | 5.3 h 46.0° | V | 5.6 | 2 | | Neptune | | HZ |
| HIP 27072 | 3.60 | 8.9 | 5.7 h -21.6° | V | 4.8 | 2 | | Neptune | | |
| HIP 27913 | 4.40 | 8.7 | 5.9 h 20.3° | V | 39.5 | 2 | | Neptune | | |
| HIP 28103 | 3.72 | 14.9 | 5.9 h -13.8° | V | 9.5 | 2 | | Neptune | | HZ |
| HIP 44127 | 3.14 | 14.5 | 9.0 h 48.0° | V | 7 | 2 | | Neptune | | HZ |
| HIP 46853 | 3.18 | 13.5 | 9.5 h 51.7° | V | 6.9 | 2 | | Neptune | | HZ |
| HIP 57632 | 2.13 | 11 | 11.8 h 14.6° | V | 2.9 | 2 | | Neptune | | |
| HIP 57757 | 3.60 | 10.9 | 11.8 h 1.8° | V | 8.7 | 2 | | Neptune | | HZ |
| HIP 61317 | 4.25 | 8.4 | 12.6 h 41.4° | V | 29.9 | 2 | | Neptune | | |
| HIP 61941 | 2.74 | 11.7 | 12.7 h -0.6° | V | 8.5 | 2 | | Neptune | | HZ |
| HIP 64394 | 4.25 | 9.1 | 13.2 h 27.9° | V | 34.5 | 2 | | Neptune | | |
| HIP 67927 | 2.68 | 11.4 | 13.9 h 18.4° | V | 8.5 | 2 | | Neptune | | HZ |
| HIP 69673 | -0.05 | 11.3 | 14.3 h 19.2° | V | 5.6 | 2 | | Neptune | | HZ |
| HIP 72659 | 4.59 | 6.7 | 14.9 h 19.1° | V | 42.4 | 2 | | Neptune | | |
| HIP 77257 | 4.42 | 12.1 | 15.8 h 7.4° | V | 28.8 | 2 | | Neptune | | |
| HIP 77952 | 2.85 | 12.4 | 15.9 h -62.6° | V | 8.5 | 2 | | Neptune | | HZ |
| HIP 78072 | 3.84 | 11.2 | 15.9 h 15.7° | V | 8 | 2 | | Neptune | | HZ |
| HIP 81693 | 2.80 | 10.7 | 16.7 h 31.6° | V | 7.7 | 2 | | Neptune | | HZ |
| HIP 86032 | 2.07 | 14.9 | 17.6 h 12.6° | V | 8.1 | 2 | | Neptune | | HZ |
| HIP 86974 | 3.42 | 8.3 | 17.8 h 27.7° | V | 8.8 | 2 | | Neptune | | HZ |
| HIP 89937 | 3.58 | 8.1 | 18.4 h 72.7° | V | 8.9 | 2 | | Neptune | | HZ |
| HIP 91262 | 0.03 | 7.7 | 18.6 h 38.8° | V | 5.6 | 2 | | Neptune | | HZ |
| HIP 96100 | 4.68 | 5.8 | 19.5 h 69.7° | V | 8.1 | 2 | | Neptune | | HZ |
| HIP 98036 | 3.71 | 13.7 | 19.9 h 6.4° | V | 8.9 | 2 | | Neptune | | HZ |
| HIP 102422 | 3.41 | 14.3 | 20.8 h 61.8° | V | 78.7 | 2 | | Neptune | | HZ |
| HIP 105199 | 2.46 | 15 | 21.3 h 62.6° | V | 24.3 | 2 | | Neptune | | |
| HIP 105858 | 4.22 | 9.3 | 21.4 h -64.6° | V | 30.5 | 2 | | Neptune | | |
| HIP 107556 | 2.83 | 11.9 | 21.8 h -15.9° | V | 8.4 | 2 | | Neptune | | HZ |

| Star Name | V (mag) | Dist. (pc) | RA, Dec | Band | Integration (hrs) | Visits | Known RV Target | New Planet Survey | HZ? | Disk Program |
|---|---|---|---|---|---|---|---|---|---|---|
| HIP 109176 | 3.77 | 11.7 | 22.1 h 25.3° | V | 7.3 | 2 | | Neptune | | HZ |
| HIP 113368 | 1.16 | 7.7 | 23.0 h -28.4° | V | 0.6 | 2 | | Neptune | | |
| HIP 5336 | 5.17 | 7.5 | 1.1 h 54.9° | V | 64.8 | 2 | | Neptune | | |
| HIP 15457 | 4.85 | 9.1 | 3.3 h 3.4° | V | 87.6 | 2 | | Neptune | | |
| alf Ari | 2.01 | 20.2 | 2.1 h 23.5° | V | 8.5 | 1 | | Saturn | | RV |
| 7 CMa | 3.91 | 19.8 | 6.6 h -18.7° | V | 74.8 | 1 | | Saturn | | RV |
| tau Boo | 4.49 | 15.6 | 13.8 h 17.5° | V | 42.1 | 1 | | Saturn | | RV |
| HIP 746 | 2.27 | 16.8 | 0.2 h 59.1° | V | 8.2 | 2 | | Saturn | | HZ |
| HIP 8796 | 3.42 | 19.4 | 1.9 h 29.6° | V | 9.3 | 2 | | Saturn | | HZ |
| HIP 8903 | 2.65 | 18 | 1.9 h 20.8° | V | 8.4 | 2 | | Saturn | | HZ |
| HIP 9007 | 3.70 | 17.9 | 1.9 h -50.4° | V | 7.3 | 2 | | Saturn | | HZ |
| HIP 10644 | 4.87 | 10.8 | 2.3 h 34.2° | V | 61.9 | 2 | | Saturn | | |
| HIP 12843 | 4.46 | 14.2 | 2.8 h -17.4° | V | 29.6 | 2 | | Saturn | | |
| HIP 14879 | 3.85 | 14.2 | 3.2 h -27.0° | V | 7.8 | 2 | | Saturn | | HZ |
| HIP 16852 | 4.30 | 14 | 3.6 h 0.4° | V | 23 | 2 | | Saturn | | |
| HIP 17651 | 4.20 | 17.6 | 3.8 h -22.8° | V | 8.5 | 2 | | Saturn | | HZ |
| HIP 21421 | 0.86 | 20.4 | 4.6 h 16.5° | V | 2.7 | 2 | | Saturn | | |
| HIP 23693 | 4.72 | 11.7 | 5.1 h -56.5° | V | 45.6 | 2 | | Saturn | | |
| HIP 23835 | 5.00 | 15.4 | 5.1 h 18.6° | V | 85.5 | 2 | | Saturn | | |
| HIP 24813 | 4.71 | 12.6 | 5.3 h 40.1° | V | 45.1 | 2 | | Saturn | | |
| HIP 32362 | 3.36 | 18 | 6.8 h 12.9° | V | 7.3 | 2 | | Saturn | | HZ |
| HIP 35550 | 3.53 | 18.5 | 7.3 h 22.0° | V | 6.7 | 2 | | Saturn | | HZ |
| HIP 36366 | 4.18 | 18.1 | 7.5 h 31.8° | V | 8.5 | 2 | | Saturn | | HZ |
| HIP 36850 | 1.58 | 15.6 | 7.6 h 31.9° | V | 0.8 | 2 | | Saturn | | |
| HIP 39757 | 2.81 | 19.5 | 8.1 h -23.7° | V | 8.5 | 2 | | Saturn | | HZ |
| HIP 40702 | 4.07 | 19.6 | 8.3 h -75.1° | V | 8.6 | 2 | | Saturn | | HZ |
| HIP 44248 | 3.96 | 16.1 | 9.0 h 41.8° | V | 7.7 | 2 | | Saturn | | HZ |
| HIP 46509 | 4.60 | 17.3 | 9.5 h -1.2° | V | 72.3 | 2 | | Saturn | | |
| HIP 46651 | 3.60 | 18.8 | 9.5 h -39.5° | V | 6.6 | 2 | | Saturn | | HZ |
| HIP 47592 | 4.94 | 15 | 9.7 h -22.1° | V | 84.4 | 2 | | Saturn | | |
| HIP 50954 | 4.01 | 16.2 | 10.4 h -74.0° | V | 7.7 | 2 | | Saturn | | HZ |
| HIP 51459 | 4.83 | 12.8 | 10.5 h 56.0° | V | 54.7 | 2 | | Saturn | | |
| HIP 54872 | 2.53 | 17.9 | 11.2 h 20.5° | V | 4.5 | 2 | | Saturn | | |
| HIP 59072 | 4.14 | 19.8 | 12.1 h -63.4° | V | 84.9 | 2 | | Saturn | | HZ |
| HIP 59199 | 4.00 | 14.9 | 12.1 h -23.3° | V | 7.7 | 2 | | Saturn | | HZ |
| HIP 64241 | 4.32 | 17.8 | 13.2 h 17.5° | V | 48.7 | 2 | | Saturn | | |
| HIP 65109 | 2.73 | 18 | 13.3 h -35.3° | V | 8.6 | 2 | | Saturn | | HZ |
| HIP 68933 | 2.05 | 18 | 14.1 h -35.6° | V | 2.9 | 2 | | Saturn | | |
| HIP 70497 | 4.05 | 14.5 | 14.4 h 51.9° | V | 8.6 | 2 | | Saturn | | HZ |
| HIP 71284 | 4.47 | 15.8 | 14.6 h 29.7° | V | 39.1 | 2 | | Saturn | | |
| HIP 71908 | 3.19 | 16.6 | 14.7 h -63.0° | V | 9.8 | 2 | | Saturn | | HZ |
| HIP 71957 | 3.88 | 18.3 | 14.7 h -4.3° | V | 7.8 | 2 | | Saturn | | HZ |
| HIP 73695 | 4.76 | 12.5 | 15.1 h 47.7° | V | 49.2 | 2 | | Saturn | | |
| HIP 76829 | 4.64 | 17.4 | 15.7 h -43.3° | V | 76.7 | 2 | | Saturn | | |
| HIP 77760 | 4.62 | 15.9 | 15.9 h 42.5° | V | 51.1 | 2 | | Saturn | | |
| HIP 80686 | 4.91 | 12.1 | 16.5 h -69.9° | V | 62.3 | 2 | | Saturn | | |
| HIP 82396 | 2.29 | 19.5 | 16.8 h -33.7° | V | 2.3 | 2 | | Saturn | | |
| HIP 82860 | 4.89 | 15.3 | 16.9 h 65.1° | V | 77.7 | 2 | | Saturn | | |
| HIP 84893 | 4.39 | 17.4 | 17.4 h -20.9° | V | 51.7 | 2 | | Saturn | | |
| HIP 89962 | 3.25 | 18.5 | 18.4 h -1.1° | V | 7.9 | 2 | | Saturn | | HZ |
| HIP 93825 | 4.20 | 17.3 | 19.1 h -36.9° | V | 8.5 | 2 | | Saturn | | HZ |
| HIP 95501 | 3.36 | 15.5 | 19.4 h 3.1° | V | 8 | 2 | | Saturn | | HZ |
| HIP 102485 | 4.15 | 14.7 | 20.8 h -24.7° | V | 8.5 | 2 | | Saturn | | HZ |
| HIP 104887 | 3.73 | 20.3 | 21.2 h 38.0° | V | 7.4 | 2 | | Saturn | | HZ |

| Star Name | V (mag) | Dist. (pc) | RA, Dec | Band | Integration (hrs) | Visits | Known RV Target | New Planet Survey | HZ? | Disk Program |
|---|---|---|---|---|---|---|---|---|---|---|
| HIP 112447 | 4.20 | 16.3 | 22.8 h 12.2° | V | 8.5 | 2 | | Saturn | | HZ |
| HIP 116771 | 4.12 | 13.7 | 23.7 h 5.6° | V | 8.5 | 2 | | Saturn | | HZ |
| HIP 5862 | 4.96 | 15.1 | 1.3 h -44.5° | V | 91.4 | 2 | | Saturn | | |
| HIP 7918 | 4.96 | 12.7 | 1.7 h 42.6° | V | 50.3 | 2 | | Saturn | | |
| HIP 7981 | 5.24 | 7.5 | 1.7 h 20.3° | V | 76.7 | 2 | | Saturn | | |
| HIP 15371 | 5.24 | 12 | 3.3 h -61.5° | V | 72.2 | 2 | | Saturn | | |
| HIP 25278 | 5.00 | 14.4 | 5.4 h 17.4° | V | 60.1 | 2 | | Saturn | | |
| HIP 29271 | 5.09 | 10.2 | 6.2 h -73.2° | V | 48.1 | 2 | | Saturn | | |
| HIP 56997 | 5.34 | 9.6 | 11.7 h 34.2° | V | 72.8 | 2 | | Saturn | | |
| HIP 86036 | 5.24 | 14.2 | 17.6 h 61.9° | V | 88.3 | 2 | | Saturn | | |
| HIP 99461 | 5.31 | 6 | 20.2 h -35.9° | V | 78.8 | 2 | | Saturn | | |
| HD 27442 | 4.44 | 18.2 | 4.3 h -58.7° | V | 40.3 | 1 | | Jupiter | | RV |
| HIP 2072 | 3.94 | 23.8 | 0.4 h -42.3° | V | 7.8 | 2 | | Jupiter | | HZ |
| HIP 2081 | 2.37 | 26 | 0.4 h -41.7° | V | 22.5 | 2 | | Jupiter | | |
| HIP 9236 | 2.84 | 22 | 2.0 h -60.4° | V | 7.8 | 2 | | Jupiter | | HZ |
| HIP 12706 | 3.47 | 24.4 | 2.7 h 3.2° | V | 6.5 | 2 | | Jupiter | | HZ |
| HIP 14576 | 2.12 | 27.6 | 3.1 h 41.0° | V | 8.2 | 2 | | Jupiter | | HZ |
| HIP 19893 | 4.20 | 20.5 | 4.3 h -50.5° | V | 49.4 | 2 | | Jupiter | | |
| HIP 21770 | 4.45 | 20.2 | 4.7 h -40.1° | V | 41.2 | 2 | | Jupiter | | |
| HIP 23875 | 2.79 | 27.4 | 5.1 h -4.9° | V | 30.1 | 2 | | Jupiter | | |
| HIP 27288 | 3.54 | 21.6 | 5.8 h -13.2° | V | 6.4 | 2 | | Jupiter | | HZ |
| HIP 27628 | 3.12 | 26.7 | 5.8 h -34.2° | V | 6.8 | 2 | | Jupiter | | HZ |
| HIP 28360 | 1.90 | 24.9 | 6.0 h 44.9° | V | 3.6 | 2 | | Jupiter | | |
| HIP 39903 | 4.76 | 20 | 8.2 h -60.7° | V | 67.9 | 2 | | Jupiter | | |
| HIP 42913 | 1.95 | 24.7 | 8.7 h -53.3° | V | 3.8 | 2 | | Jupiter | | |
| HIP 46733 | 3.67 | 23.8 | 9.5 h 63.1° | V | 6.5 | 2 | | Jupiter | | HZ |
| HIP 49669 | 1.40 | 24.3 | 10.1 h 12.0° | V | 1.9 | 2 | | Jupiter | | |
| HIP 53910 | 2.37 | 24.4 | 11.0 h 56.4° | V | 8.2 | 2 | | Jupiter | | HZ |
| HIP 55642 | 4.00 | 23.7 | 11.4 h 10.5° | V | 7.7 | 2 | | Jupiter | | HZ |
| HIP 55705 | 4.08 | 25.2 | 11.4 h -16.3° | V | 55.7 | 2 | | Jupiter | | |
| HIP 58001 | 2.44 | 25.5 | 11.9 h 53.7° | V | 19.8 | 2 | | Jupiter | | |
| HIP 59774 | 3.32 | 24.7 | 12.3 h 57.0° | V | 6.9 | 2 | | Jupiter | | HZ |
| HIP 60965 | 2.94 | 26.6 | 12.5 h -15.5° | V | 7.7 | 2 | | Jupiter | | HZ |
| HIP 61084 | 1.64 | 27.1 | 12.5 h -56.9° | V | 8.8 | 2 | | Jupiter | | |
| HIP 61174 | 4.31 | 18.3 | 12.5 h -15.8° | V | 28.9 | 2 | | Jupiter | | |
| HIP 62956 | 1.77 | 25.3 | 12.9 h 56.0° | V | 3 | 2 | | Jupiter | | |
| HIP 65378 | 2.27 | 26.3 | 13.4 h 54.9° | V | 16.5 | 2 | | Jupiter | | |
| HIP 65477 | 4.01 | 25.1 | 13.4 h 55.0° | V | 7.7 | 2 | | Jupiter | | HZ |
| HIP 66249 | 3.38 | 22.7 | 13.6 h 0.6° | V | 6.8 | 2 | | Jupiter | | HZ |
| HIP 67153 | 4.23 | 19.4 | 13.8 h -33.0° | V | 8.5 | 2 | | Jupiter | | HZ |
| HIP 69701 | 4.08 | 22.2 | 14.3 h -6.0° | V | 8.6 | 2 | | Jupiter | | HZ |
| HIP 71075 | 3.02 | 26.6 | 14.5 h 38.3° | V | 7.2 | 2 | | Jupiter | | HZ |
| HIP 72622 | 2.75 | 23.2 | 14.8 h -16.0° | V | 9.8 | 2 | | Jupiter | | HZ |
| HIP 76267 | 2.24 | 23 | 15.6 h 26.7° | V | 5.1 | 2 | | Jupiter | | |
| HIP 77070 | 2.63 | 22.7 | 15.7 h 6.4° | V | 9.9 | 2 | | Jupiter | | HZ |
| HIP 77622 | 3.71 | 21.6 | 15.8 h 4.5° | V | 7.4 | 2 | | Jupiter | | HZ |
| HIP 78527 | 4.00 | 21 | 16.0 h 58.6° | V | 35.8 | 2 | | Jupiter | | |
| HIP 80331 | 2.74 | 28.2 | 16.4 h 61.5° | V | 8.6 | 2 | | Jupiter | | HZ |
| HIP 83000 | 3.20 | 28 | 17.0 h 9.4° | V | 6.8 | 2 | | Jupiter | | HZ |
| HIP 84012 | 2.42 | 27.1 | 17.2 h -14.3° | V | 20 | 2 | | Jupiter | | |
| HIP 84143 | 3.33 | 22.5 | 17.2 h -42.8° | V | 6.8 | 2 | | Jupiter | | HZ |
| HIP 84379 | 3.13 | 23 | 17.3 h 24.8° | V | 7.1 | 2 | | Jupiter | | HZ |
| HIP 86742 | 2.75 | 25.1 | 17.7 h 4.6° | V | 7.8 | 2 | | Jupiter | | HZ |
| HIP 90496 | 2.81 | 24 | 18.5 h -24.6° | V | 7.7 | 2 | | Jupiter | | HZ |

| Star Name | V (mag) | Dist. (pc) | RA, Dec | Band | Integration (hrs) | Visits | Known RV Target | New Planet Survey | HZ? | Disk Program |
|---|---|---|---|---|---|---|---|---|---|---|
| HIP 92043 | 4.19 | 19.2 | 18.8 h 20.5° | V | 8.5 | 2 | | Jupiter | | HZ |
| HIP 93506 | 2.61 | 27 | 19.0 h -28.1° | V | 8.6 | 2 | | Jupiter | | HZ |
| HIP 93747 | 2.99 | 25.5 | 19.1 h 13.9° | V | 7.6 | 2 | | Jupiter | | HZ |
| HIP 96441 | 4.48 | 18.3 | 19.6 h 50.2° | V | 39.1 | 2 | | Jupiter | | |
| HIP 102488 | 2.48 | 22.3 | 20.8 h 34.0° | V | 8.5 | 2 | | Jupiter | | HZ |
| HIP 104858 | 4.49 | 18.5 | 21.2 h 10.0° | V | 40 | 2 | | Jupiter | | |
| HIP 107089 | 3.76 | 21.2 | 21.7 h -76.6° | V | 7.3 | 2 | | Jupiter | | HZ |
| HIP 114996 | 3.98 | 23.1 | 23.3 h -57.8° | V | 7.7 | 2 | | Jupiter | | HZ |
| gamma Leo | 1.98 | 39.9 | 10.3 h 19.8° | V | 6 | 1 | | | | RV |
| HIP 75458 | 3.29 | 31 | 15.4 h 59.0° | V | 6.6 | 1 | | | | RV,HZ |
| nu Oph | 3.34 | 46.2 | 18.0 h -8.2° | V | 12 | 1 | | | | RV |
| omi UMa | 3.42 | 55 | 8.5 h 60.7° | V | 12 | 1 | | | | RV |
| eps Tau | 3.53 | 45 | 4.5 h 19.2° | V | 12 | 1 | | | | RV |
| eps CrB | 4.13 | 68 | 16.0 h 26.9° | V | 12 | 1 | | | | RV |
| kappa And | 4.14 | 52 | 23.7 h 44.3° | V | 12 | 1 | | | | RV |
| 91 Aqr | 4.25 | 45.9 | 23.3 h -8.9° | V | 12 | 1 | | | | RV |
| HD 66141 | 4.38 | 78 | 8.0 h 2.3° | V | 12 | 1 | | | | RV |
| tau Gem | 4.42 | 98 | 7.2 h 30.2° | V | 12 | 1 | | | | RV |
| HD 60532 | 4.39 | 25.3 | 7.6 h -21.7° | V | 12 | 1 | | | | RV |
| HD 110014 | 4.66 | 90 | 12.7 h -6.0° | V | 12 | 1 | | | | RV |
| HD 11977 | 4.70 | 67 | 1.9 h -66.4° | V | 12 | 1 | | | | RV |
| ksi Aql | 4.72 | 56 | 19.9 h 8.5° | V | 12 | 1 | | | | RV |
| 11 Com | 4.74 | 89 | 12.3 h 17.8° | V | 12 | 1 | | | | RV |
| kappa CrB | 4.82 | 30.5 | 15.9 h 35.7° | V | 12 | 1 | | | | RV |
| 42 Dra | 4.83 | 97 | 18.4 h 65.6° | V | 12 | 1 | | | | RV |
| 70 Vir | 4.97 | 18 | 13.5 h 13.8° | V | 12 | 1 | | | | RV |
| 11 UMi | 5.02 | 122 | 15.3 h 71.8° | V | 12 | 1 | | | | RV |
| HD 19994 | 5.08 | 22.6 | 3.2 h -0.8° | V | 12 | 1 | | | | RV |
| HD 33564 | 5.09 | 20.9 | 5.4 h 79.2° | V | 12 | 1 | | | | RV |
| ome Ser | 5.23 | 84 | 15.8 h 2.2° | V | 12 | 1 | | | | RV |
| 14 And | 5.22 | 79 | 23.5 h 39.2° | V | 12 | 1 | | | | RV |
| HD 47536 | 5.26 | 123 | 6.6 h -31.7° | V | 12 | 1 | | | | RV |
| 75 Cet | 5.36 | 81 | 2.5 h -1.0° | V | 12 | 1 | | | | RV |
| HD 147513 | 5.38 | 12.8 | 16.4 h -38.8° | V | 12 | 1 | | | | RV |
| HR 810 | 5.40 | 17.2 | 2.7 h -49.2° | V | 12 | 1 | | | | RV |
| HD 81688 | 5.41 | 86 | 9.5 h 45.6° | V | 12 | 1 | | | | RV |
| HD 59686 | 5.45 | 97 | 7.5 h 17.1° | V | 12 | 1 | | | | RV |
| HD 122430 | 5.48 | 135 | 14.0 h -26.6° | V | 12 | 1 | | | | RV |
| 51 Peg | 5.46 | 15.6 | 23.0 h 20.8° | V | 12 | 1 | | | | RV |
| omi CrB | 5.51 | 83 | 15.3 h 29.6° | V | 12 | 1 | | | | RV |
| HD 10647 | 5.52 | 17.4 | 1.7 h -52.3° | V | 12 | 1 | | | | RV |
| 18 Del | 5.52 | 75 | 21.0 h 10.8° | V | 12 | 1 | | | | RV |
| 81 Cet | 5.66 | 93 | 2.6 h -2.6° | V | 12 | 1 | | | | RV |
| HD 136352 | 5.65 | 14.8 | 15.4 h -47.7° | V | 12 | 1 | | | | RV |
| HD 142 | 5.70 | 25.7 | 0.1 h -48.9° | V | 12 | 1 | | | | RV |
| HD 192310 | 5.72 | 8.9 | 20.3 h -27.0° | V | 12 | 1 | | | | RV |
| HD 89744 | 5.74 | 39.4 | 10.4 h 41.2° | V | 12 | 1 | | | | RV |
| HD 30562 | 5.77 | 26.4 | 4.8 h -4.3° | V | 12 | 1 | | | | RV |
| HD 16417 | 5.79 | 25.8 | 2.6 h -33.4° | V | 12 | 1 | | | | RV |
| 4 Uma | 4.61 | 78 | 8.7 h 64.3° | V | 12 | 1 | | | | RV |
| HD 104985 | 5.80 | 97 | 12.1 h 76.9° | V | 12 | 1 | | | | RV |
| HD 3651 | 5.88 | 11.1 | 0.7 h 21.3° | V | 12 | 1 | | | | RV |
| HD 2952 | 5.93 | 114 | 0.6 h 54.9° | V | 12 | 1 | | | | RV |
| 6 Lyn | 5.88 | 56 | 6.5 h 58.2° | V | 12 | 1 | | | | RV |

| Star Name | V (mag) | Dist. (pc) | RA, Dec | Band | Integration (hrs) | Visits | Known RV Target | New Planet Survey | HZ? | Disk Program |
|---|---|---|---|---|---|---|---|---|---|---|
| HD 169830 | 5.91 | 36.6 | 18.5 h -28.2° | V | 12 | 1 | | | | RV |
| HD 120084 | 5.91 | 101 | 13.7 h 78.1° | V | 12 | 1 | | | | RV |
| HD 210702 | 5.94 | 55 | 22.2 h 16.0° | V | 12 | 1 | | | | RV |
| HD 38529 | 5.94 | 39.3 | 5.8 h 1.2° | V | 12 | 1 | | | | RV |
| HD 69830 | 5.95 | 12.5 | 8.3 h -11.4° | V | 12 | 1 | | | | RV |
| HR 8799 | 5.95 | 39.4 | 23.1 h 21.1° | V | 12 | 1 | | | | RV |
| HD 38858 | 5.97 | 15.2 | 5.8 h -3.9° | V | 12 | 1 | | | | RV |
| HD 167042 | 5.95 | 50 | 18.2 h 54.3° | V | 12 | 1 | | | | RV |
| HD 139357 | 5.98 | 118 | 15.6 h 53.9° | V | 12 | 1 | | | | RV |
| HD 5608 | 6.00 | 56 | 1.0 h 34.0° | V | 12 | 1 | | | | RV |
| Vega | 0.03 | 7.7 | 18.6 h 38.8° | I | 6 | 1 | | | | DD |
| Fomalhaut | 1.16 | 7.7 | 23.0 h -28.4° | I | 6 | 1 | | | | DD |
| Beta Leo | 2.13 | 11 | 11.8 h 14.6° | I | 6 | 1 | | | | DD |
| Alpha CrB | 2.24 | 23 | 15.6 h 26.7° | I | 6 | 1 | | | | DD |
| Beta Uma | 2.37 | 24.4 | 11.0 h 56.4° | I | 6 | 1 | | | | DD |
| Iota Cen | 2.73 | 18 | 13.3 h -35.3° | I | 6 | 1 | | | | DD |
| Gam Boo | 3.02 | 26.6 | 14.5 h 38.3° | I | 12 | 1 | | | | DD |
| HD 13161 | 3.00 | 38.9 | 2.2 h 35.0° | I | 12 | 1 | | | | DD |
| Delta Uma | 3.32 | 24.7 | 12.3 h 57.0° | I | 12 | 1 | | | | DD |
| Zeta Lep | 3.54 | 21.6 | 5.8 h -13.2° | I | 12 | 1 | | | | DD |
| Tau Ceti | 3.50 | 3.6 | 1.7 h -14.1° | I | 12 | 1 | | | | DD |
| Eta Lep | 3.72 | 14.9 | 5.9 h -13.8° | I | 12 | 1 | | | | DD |
| Gam oph | 3.75 | 31.5 | 17.8 h 2.7° | I | 12 | 1 | | | | DD |
| HD 2262 | 3.94 | 23.8 | 0.4 h -42.3° | I | 12 | 1 | | | | DD |
| 30 Mon | 3.90 | 37.5 | 8.4 h -2.1° | I | 12 | 1 | | | | DD |
| HD 188228 | 3.95 | 32.2 | 20.0 h -71.1° | I | 12 | 1 | | | | DD |
| Gam Tri | 4.00 | 34.4 | 2.3 h 33.8° | I | 12 | 1 | | | | DD |
| HD 135379 | 4.07 | 30.6 | 15.3 h -57.2° | I | 12 | 1 | | | | DD |
| Eps Cep | 4.19 | 26.2 | 22.3 h 57.0° | I | 12 | 1 | | | | DD |
| Lambda boo | 4.18 | 30.4 | 14.3 h 46.1° | I | 12 | 1 | | | | DD |
| HD 1581 | 4.23 | 8.6 | 0.3 h -63.1° | I | 12 | 1 | | | | DD |
| Eta CrV | 4.31 | 18.3 | 12.5 h -15.8° | I | 12 | 1 | | | | DD |
| HD 22484 | 4.30 | 14 | 3.6 h 0.4° | I | 12 | 1 | | | | DD |
| Sigma boo | 4.47 | 15.8 | 14.6 h 29.7° | I | 12 | 1 | | | | DD |
| HD 87696 | 4.49 | 28.2 | 10.1 h 35.2° | I | 12 | 1 | | | | DD |
| HD 139664 | 4.64 | 17.4 | 15.7 h -43.3° | I | 12 | 1 | | | | DD |
| 61 Vir | 4.74 | 8.6 | 13.3 h -17.7° | I | 12 | 1 | | | | DD |
| HD 33262 | 4.72 | 11.7 | 5.1 h -56.5° | I | 12 | 1 | | | | DD |
| HR 7012 | 4.78 | 28.6 | 18.8 h -63.1° | I | 12 | 1 | | | | DD |
| HD 27045 | 4.92 | 28.9 | 4.3 h 20.6° | I | 12 | 1 | | | | DD |
| Rho Vir | 4.88 | 36.3 | 12.7 h 10.2° | I | 12 | 1 | | | | DD |
| HD 28355 | 5.01 | 48.9 | 4.5 h 13.0° | I | 12 | 1 | | | | DD |
| 70 Vir | 4.97 | 18 | 13.5 h 13.8° | I | 12 | 1 | | | | DD |
| HD 165908 | 5.07 | 15.6 | 18.1 h 30.6° | I | 12 | 1 | | | | DD |
| HD 19994 | 5.08 | 22.6 | 3.2 h -0.8° | I | 12 | 1 | | | | DD |
| HD 20807 | 5.24 | 12 | 3.3 h -61.5° | I | 12 | 1 | | | | DD |
| HD 48682 | 5.25 | 16.7 | 6.8 h 43.6° | I | 12 | 1 | | | | DD |
| HD 88215 | 5.30 | 27.7 | 10.2 h -11.2° | I | 12 | 1 | | | | DD |
| HD 25457 | 5.38 | 18.8 | 4.0 h 0.3° | I | 12 | 1 | | | | DD |
| HD 10647 | 5.52 | 17.4 | 1.7 h -52.3° | I | 12 | 1 | | | | DD |
| HD 30495 | 5.50 | 13.3 | 4.8 h -15.1° | I | 12 | 1 | | | | DD |
| HD 207129 | 5.58 | 16 | 21.8 h -46.7° | I | 12 | 1 | | | | DD |
| HD 72905 | 5.64 | 14.4 | 8.7 h 65.0° | I | 12 | 1 | | | | DD |
| HD 221756 | 5.56 | 80 | 23.6 h 40.2° | I | 12 | 1 | | | | DD |

| Star Name | V (mag) | Dist. (pc) | RA, Dec | Band | Integration (hrs) | Visits | Known RV Target | New Planet Survey | HZ? | Disk Program |
|---|---|---|---|---|---|---|---|---|---|---|
| HD 28226 | 5.71 | 47.1 | 4.5 h 21.6° | I | 12 | 1 | | | | DD |
| HD 38206 | 5.73 | 75 | 5.7 h -17.4° | I | 12 | 1 | | | | DD |
| HD 142 | 5.70 | 25.7 | 0.1 h -48.9° | I | 12 | 1 | | | | DD |
| HR 4796 | 5.78 | 73 | 12.6 h -38.1° | I | 12 | 1 | | | | DD |
| HD 38529 | 5.94 | 39.3 | 5.8 h 1.2° | I | 12 | 1 | | | | DD |
| HD 11413 | 5.94 | 77 | 1.8 h -49.8° | I | 12 | 1 | | | | DD |
| HD 71043 | 5.89 | 70 | 8.4 h -51.9° | I | 12 | 1 | | | | DD |
| HD 80950 | 5.87 | 82 | 9.3 h -73.3° | I | 12 | 1 | | | | DD |
| HD 38858 | 5.97 | 15.2 | 5.8 h -3.9° | I | 12 | 1 | | | | DD |
| HR 8799 | 5.95 | 39.4 | 23.1 h 21.1° | I | 12 | 1 | | | | DD |
| HD 110897 | 5.95 | 17.4 | 12.7 h 39.3° | I | 12 | 1 | | | | DD |
| HD 76151 | 6.00 | 17.4 | 8.9 h -4.6° | I | 12 | 1 | | | | DD |
| EP Eri | 6.05 | 10.3 | 2.9 h -11.2° | I | 12 | 1 | | | | DD |
| HD 206860 | 5.95 | 17.9 | 21.7 h 14.8° | I | 12 | 1 | | | | DD |
| HD 216435 | 6.04 | 32.6 | 22.9 h -47.4° | I | 12 | 1 | | | | DD |
| HD 69830 | 5.95 | 12.5 | 8.3 h -11.4° | I | 12 | 1 | | | | DD |
| HD 166 | 6.13 | 13.7 | 0.1 h 29.0° | I | 12 | 1 | | | | DD |
| HD 111786 | 6.14 | 67 | 12.9 h -25.3° | I | 12 | 1 | | | | DD |
| HD 30422 | 6.18 | 56 | 4.8 h -27.9° | I | 12 | 1 | | | | DD |
| HR 9 | 6.19 | 39.4 | 0.1 h -22.9° | I | 12 | 1 | | | | DD |
| HD 119124 | 6.32 | 25.3 | 13.7 h 50.5° | I | 12 | 1 | | | | DD |
| HD 35850 | 6.31 | 27 | 5.5 h -10.1° | I | 12 | 1 | | | | DD |
| HD 52265 | 6.30 | 29 | 7.0 h -4.6° | I | 12 | 1 | | | | DD |
| HD 45184 | 6.39 | 21.9 | 6.4 h -27.2° | I | 12 | 1 | | | | DD |
| HD 82943 | 6.53 | 27.5 | 9.6 h -11.9° | I | 12 | 1 | | | | DD |
| HD 1461 | 6.46 | 23.2 | 0.3 h -7.9° | I | 12 | 1 | | | | DD |
| HD 7590 | 6.59 | 23.2 | 1.3 h 42.9° | I | 12 | 1 | | | | DD |
| HD 8907 | 6.66 | 34.8 | 1.5 h 42.3° | I | 12 | 1 | | | | DD |
| HD 73350 | 6.72 | 24 | 8.6 h -5.2° | I | 12 | 1 | | | | DD |
| HD 202628 | 6.75 | 24.4 | 21.3 h -42.7° | I | 12 | 1 | | | | DD |
| HD 53143 | 6.80 | 18.3 | 7.0 h -60.7° | I | 12 | 1 | | | | DD |
| HD 141569A | 7.12 | 116 | 15.8 h -2.1° | I | 12 | 1 | | | | DD |
| HD 181327 | 7.04 | 52 | 19.4 h -53.5° | I | 12 | 1 | | | | DD |
| HD 187897 | 7.13 | 35.1 | 19.9 h 7.5° | I | 12 | 1 | | | | DD |
| HD 107146 | 7.01 | 27.5 | 12.3 h 16.5° | I | 12 | 1 | | | | DD |
| HD 105 | 7.53 | 39.4 | 0.1 h -40.2° | I | 12 | 1 | | | | DD |
| HD 377 | 7.59 | 39.1 | 0.1 h 6.6° | I | 12 | 1 | | | | DD |
| HD 92945 | 7.72 | 21.4 | 10.7 h -28.9° | I | 12 | 1 | | | | DD |
| HD 104860 | 7.91 | 45.5 | 12.1 h 66.3° | I | 12 | 1 | | | | DD |
| HD 32297 | 8.14 | 112 | 5.0 h 7.5° | I | 12 | 1 | | | | DD |
| HD 61005 | 8.22 | 35.4 | 7.6 h -31.8° | I | 12 | 1 | | | | DD |
| AU Mic | 8.63 | 9.9 | 20.8 h -30.7° | I | 12 | 1 | | | | DD |
| HIP 82673 | 4.38 | 75 | 16.9 h 10.2° | V | 12 | 1 | | | | DD |
| HIP 53954 | 4.41 | 38.9 | 11.0 h 20.2° | V | 12 | 1 | | | | DD |
| HIP 58484 | 4.90 | 111 | 12.0 h -77.8° | V | 12 | 1 | | | | DD |
| HIP 79653 | 5.12 | 118 | 16.3 h -46.6° | V | 12 | 1 | | | | DD |
| HIP 90806 | 5.13 | 68 | 18.5 h -17.6° | V | 12 | 1 | | | | DD |
| HIP 7943 | 5.64 | 84 | 1.7 h 35.2° | V | 12 | 1 | | | | DD |
| HIP 7965 | 5.59 | 119 | 1.7 h 68.0° | V | 12 | 1 | | | | DD |
| HIP 64053 | 5.70 | 100 | 13.1 h -52.5° | V | 12 | 1 | | | | DD |
| HIP 62576 | 5.78 | 93 | 12.8 h 27.6° | V | 12 | 1 | | | | DD |
| HIP 72552 | 5.80 | 98 | 14.8 h 28.6° | V | 12 | 1 | | | | DD |
| HIP 58720 | 5.88 | 106 | 12.0 h -68.8° | V | 12 | 1 | | | | DD |
| HIP 61558 | 5.88 | 69 | 12.6 h -4.2° | V | 12 | 1 | | | | DD |

| Star Name | V (mag) | Dist. (pc) | RA, Dec | Band | Integration (hrs) | Visits | Known RV Target | New Planet Survey | HZ? | Disk Program |
|---|---|---|---|---|---|---|---|---|---|---|
| HIP 83478 | 5.92 | 77 | 17.1 h 13.6° | V | 12 | 1 | | | | DD |
| HIP 27713 | 5.96 | 99 | 5.9 h -9.0° | V | 12 | 1 | | | | DD |
| HIP 43620 | 6.01 | 92 | 8.9 h -55.4° | V | 12 | 1 | | | | DD |
| HIP 115806 | 5.99 | 111 | 23.5 h 25.2° | V | 12 | 1 | | | | DD |
| HIP 4366 | 6.10 | 78 | 0.9 h 27.2° | V | 12 | 1 | | | | DD |
| HIP 26395 | 6.09 | 63 | 5.6 h -10.2° | V | 12 | 1 | | | | DD |
| HIP 60183 | 6.19 | 94 | 12.3 h -64.2° | V | 12 | 1 | | | | DD |
| HIP 92676 | 6.18 | 82 | 18.9 h -47.6° | V | 12 | 1 | | | | DD |
| HIP 94140 | 6.26 | 93 | 19.2 h 66.0° | V | 12 | 1 | | | | DD |
| HIP 15987 | 6.39 | 108 | 3.4 h -34.1° | V | 12 | 1 | | | | DD |
| HIP 25453 | 6.40 | 92 | 5.4 h 6.9° | V | 12 | 1 | | | | DD |
| HIP 76234 | 6.36 | 108 | 15.6 h -38.7° | V | 12 | 1 | | | | DD |
| HIP 35567 | 6.56 | 71 | 7.3 h -55.7° | V | 12 | 1 | | | | DD |
| HIP 36624 | 6.54 | 81 | 7.5 h 38.9° | V | 12 | 1 | | | | DD |
| HIP 47115 | 6.56 | 80 | 9.6 h -63.0° | V | 12 | 1 | | | | DD |
| HIP 60561 | 6.60 | 91 | 12.4 h -71.4° | V | 12 | 1 | | | | DD |
| HIP 105169 | 6.61 | 105 | 21.3 h -74.7° | V | 12 | 1 | | | | DD |
| HIP 118027 | 6.57 | 91 | 23.9 h 83.2° | V | 12 | 1 | | | | DD |
| HIP 20472 | 6.93 | 87 | 4.4 h 11.4° | V | 12 | 1 | | | | DD |
| HIP 30088 | 6.67 | 99 | 6.3 h -12.0° | V | 12 | 1 | | | | DD |
| HIP 36837 | 6.65 | 115 | 7.6 h -25.9° | V | 12 | 1 | | | | DD |
| HIP 63839 | 6.64 | 99 | 13.1 h -63.6° | V | 12 | 1 | | | | DD |
| HIP 74553 | 6.66 | 100 | 15.2 h 43.0° | V | 12 | 1 | | | | DD |
| HIP 95574 | 6.70 | 116 | 19.4 h -13.4° | V | 12 | 1 | | | | DD |
| HIP 100526 | 6.66 | 72 | 20.4 h 54.7° | V | 12 | 1 | | | | DD |
| HIP 104430 | 6.66 | 101 | 21.2 h 0.2° | V | 12 | 1 | | | | DD |
| HIP 107919 | 6.65 | 70 | 21.9 h 11.1° | V | 12 | 1 | | | | DD |
| HIP 118133 | 6.65 | 95 | 24.0 h 11.5° | V | 12 | 1 | | | | DD |
| HIP 63236 | 6.76 | 111 | 13.0 h -66.0° | V | 12 | 1 | | | | DD |
| HIP 75953 | 6.81 | 108 | 15.5 h 34.5° | V | 12 | 1 | | | | DD |
| HIP 96610 | 6.78 | 101 | 19.6 h -64.1° | V | 12 | 1 | | | | DD |
| HIP 114031 | 6.76 | 106 | 23.1 h 15.0° | V | 12 | 1 | | | | DD |
| HIP 21238 | 6.81 | 71 | 4.6 h 43.0° | V | 12 | 1 | | | | DD |
| HIP 22013 | 6.92 | 118 | 4.7 h 22.9° | V | 12 | 1 | | | | DD |
| HIP 27259 | 6.82 | 95 | 5.8 h -35.8° | V | 12 | 1 | | | | DD |
| HIP 45667 | 6.89 | 94 | 9.3 h -39.0° | V | 12 | 1 | | | | DD |
| HIP 74359 | 6.87 | 113 | 15.2 h 10.2° | V | 12 | 1 | | | | DD |
| HIP 107585 | 6.84 | 97 | 21.8 h -3.4° | V | 12 | 1 | | | | DD |
| HIP 13063 | 6.92 | 106 | 2.8 h 55.6° | V | 12 | 1 | | | | DD |
| HIP 18863 | 6.93 | 113 | 4.0 h 0.8° | V | 12 | 1 | | | | DD |
| HIP 26062 | 6.95 | 114 | 5.6 h 24.6° | V | 12 | 1 | | | | DD |
| HIP 42197 | 6.97 | 83 | 8.6 h 42.6° | V | 12 | 1 | | | | DD |
| HIP 59502 | 6.98 | 101 | 12.2 h -62.5° | V | 12 | 1 | | | | DD |
| HIP 82069 | 7.02 | 108 | 16.8 h -25.4° | V | 12 | 1 | | | | DD |
| HIP 110786 | 6.98 | 78 | 22.4 h -10.8° | V | 12 | 1 | | | | DD |
| HIP 2496 | 7.07 | 107 | 0.5 h -0.2° | V | 12 | 1 | | | | DD |
| HIP 7699 | 7.08 | 47.6 | 1.7 h -55.6° | V | 12 | 1 | | | | DD |
| HIP 14479 | 7.06 | 79 | 3.1 h 30.5° | V | 12 | 1 | | | | DD |
| HIP 15902 | 7.12 | 102 | 3.4 h 28.7° | V | 12 | 1 | | | | DD |
| HIP 76223 | 7.17 | 105 | 15.6 h -59.2° | V | 12 | 1 | | | | DD |
| HIP 94491 | 7.10 | 62 | 19.2 h -25.1° | V | 12 | 1 | | | | DD |
| HIP 15922 | 7.29 | 119 | 3.4 h 11.0° | V | 12 | 1 | | | | DD |
| HIP 16876 | 7.28 | 119 | 3.6 h -28.2° | V | 12 | 1 | | | | DD |
| HIP 74144 | 7.24 | 81 | 15.2 h -37.5° | V | 12 | 1 | | | | DD |

| Star Name | V (mag) | Dist. (pc) | RA, Dec | Band | Integration (hrs) | Visits | Known RV Target | New Planet Survey | HZ? | Disk Program |
|---|---|---|---|---|---|---|---|---|---|---|
| HIP 84881 | 7.26 | 118 | 17.3 h -44.6° | V | 12 | 1 | | | | DD |
| HIP 59397 | 7.33 | 113 | 12.2 h -55.6° | V | 12 | 1 | | | | DD |
| HIP 62209 | 7.35 | 99 | 12.8 h -69.0° | V | 12 | 1 | | | | DD |
| HIP 78533 | 7.41 | 116 | 16.0 h -36.5° | V | 12 | 1 | | | | DD |
| HIP 99892 | 7.33 | 73 | 20.3 h -15.7° | V | 12 | 1 | | | | DD |
| HIP 18297 | 7.40 | 119 | 3.9 h 9.2° | V | 12 | 1 | | | | DD |
| HIP 42994 | 7.48 | 111 | 8.8 h 48.9° | V | 12 | 1 | | | | DD |
| HIP 55570 | 7.47 | 111 | 11.4 h -19.4° | V | 12 | 1 | | | | DD |
| HIP 59282 | 7.39 | 104 | 12.2 h -57.7° | V | 12 | 1 | | | | DD |
| HIP 70441 | 7.44 | 110 | 14.4 h -46.8° | V | 12 | 1 | | | | DD |
| HIP 75134 | 7.36 | 66 | 15.4 h -53.7° | V | 12 | 1 | | | | DD |
| HIP 81971 | 7.46 | 92 | 16.7 h 2.3° | V | 12 | 1 | | | | DD |
| HIP 109497 | 7.42 | 105 | 22.2 h 57.9° | V | 12 | 1 | | | | DD |
| HIP 4630 | 7.53 | 110 | 1.0 h 40.2° | V | 12 | 1 | | | | DD |
| HIP 66837 | 7.56 | 77 | 13.7 h -17.0° | V | 12 | 1 | | | | DD |
| HIP 75158 | 7.43 | 74 | 15.4 h -5.2° | V | 12 | 1 | | | | DD |
| HIP 7805 | 7.61 | 67 | 1.7 h -59.0° | V | 12 | 1 | | | | DD |
| HIP 13682 | 7.71 | 116 | 2.9 h 4.0° | V | 12 | 1 | | | | DD |
| HIP 23632 | 7.63 | 99 | 5.1 h 18.3° | V | 12 | 1 | | | | DD |
| HIP 25998 | 7.70 | 109 | 5.5 h -46.3° | V | 12 | 1 | | | | DD |
| HIP 50945 | 7.64 | 116 | 10.4 h -67.9° | V | 12 | 1 | | | | DD |
| HIP 68781 | 7.64 | 113 | 14.1 h -49.9° | V | 12 | 1 | | | | DD |
| HIP 102880 | 7.61 | 120 | 20.8 h 22.7° | V | 12 | 1 | | | | DD |
| HIP 33227 | 7.66 | 86 | 6.9 h 3.2° | V | 12 | 1 | | | | DD |
| HIP 74923 | 7.70 | 116 | 15.3 h -25.0° | V | 12 | 1 | | | | DD |
| HIP 87325 | 7.77 | 107 | 17.8 h 7.2° | V | 12 | 1 | | | | DD |
| HIP 91272 | 7.70 | 87 | 18.6 h -3.4° | V | 12 | 1 | | | | DD |
| HIP 103048 | 7.66 | 70 | 20.9 h -52.7° | V | 12 | 1 | | | | DD |
| HIP 26625 | 7.79 | 81 | 5.7 h 12.0° | V | 12 | 1 | | | | DD |
| HIP 61593 | 7.83 | 96 | 12.6 h -34.9° | V | 12 | 1 | | | | DD |
| HIP 95938 | 7.82 | 55 | 19.5 h 35.1° | V | 12 | 1 | | | | DD |
| HIP 3092 | 3.28 | 32.4 | 0.7 h 30.9° | V | 6.7 | 1 | | | | HZ |
| HIP 4436 | 3.87 | 39.8 | 0.9 h 38.5° | V | 7.3 | 1 | | | | HZ |
| HIP 5364 | 3.45 | 38 | 1.1 h -9.8° | V | 6.7 | 1 | | | | HZ |
| HIP 6537 | 3.59 | 34.9 | 1.4 h -7.8° | V | 7.4 | 1 | | | | HZ |
| HIP 10064 | 3.00 | 38.9 | 2.2 h 35.0° | V | 7.3 | 1 | | | | HZ |
| HIP 10670 | 4.00 | 34.4 | 2.3 h 33.8° | V | 7.7 | 1 | | | | HZ |
| HIP 13254 | 4.20 | 37 | 2.8 h 38.3° | V | 8.5 | 1 | | | | HZ |
| HIP 14668 | 3.81 | 34.6 | 3.2 h 44.9° | V | 7.8 | 1 | | | | HZ |
| HIP 17440 | 3.85 | 29.9 | 3.7 h -63.2° | V | 7.8 | 1 | | | | HZ |
| HIP 18907 | 3.90 | 35.9 | 4.1 h 6.0° | V | 7.3 | 1 | | | | HZ |
| HIP 19747 | 3.86 | 35.3 | 4.2 h -41.7° | V | 7.7 | 1 | | | | HZ |
| HIP 21594 | 3.87 | 33.7 | 4.6 h -13.7° | V | 7.7 | 1 | | | | HZ |
| HIP 26366 | 4.09 | 36 | 5.6 h 9.3° | V | 8.5 | 1 | | | | HZ |
| HIP 27654 | 3.85 | 34.9 | 5.9 h -19.1° | V | 7.8 | 1 | | | | HZ |
| HIP 28358 | 3.72 | 38.6 | 6.0 h 54.3° | V | 7.3 | 1 | | | | HZ |
| HIP 32607 | 3.30 | 29.6 | 6.8 h -60.1° | V | 6.9 | 1 | | | | HZ |
| HIP 35350 | 3.58 | 30.9 | 7.3 h 16.5° | V | 6.7 | 1 | | | | HZ |
| HIP 36046 | 3.79 | 36.9 | 7.4 h 27.8° | V | 7.8 | 1 | | | | HZ |
| HIP 41307 | 3.90 | 37.5 | 8.4 h -2.1° | V | 7.3 | 1 | | | | HZ |
| HIP 41312 | 3.77 | 33 | 8.4 h -65.9° | V | 7.8 | 1 | | | | HZ |
| HIP 43109 | 3.38 | 39.6 | 8.8 h 6.4° | V | 6.5 | 1 | | | | HZ |
| HIP 44382 | 4.00 | 38.3 | 9.0 h -65.6° | V | 7.7 | 1 | | | | HZ |
| HIP 45336 | 3.88 | 34.8 | 9.2 h 2.3° | V | 7.3 | 1 | | | | HZ |

| Star Name | V (mag) | Dist. (pc) | RA, Dec | Band | Integration (hrs) | Visits | Known RV Target | New Planet Survey | HZ? | Disk Program |
|---|---|---|---|---|---|---|---|---|---|---|
| HIP 45688 | 3.82 | 38.3 | 9.3 h 36.8° | V | 7.4 | 1 | | | | HZ |
| HIP 47508 | 3.52 | 40 | 9.7 h 9.9° | V | 6.6 | 1 | | | | HZ |
| HIP 48319 | 3.81 | 35.6 | 9.8 h 59.0° | V | 7.3 | 1 | | | | HZ |
| HIP 48455 | 3.88 | 38 | 9.9 h 26.0° | V | 7.7 | 1 | | | | HZ |
| HIP 49841 | 3.61 | 34.5 | 10.2 h -11.6° | V | 7.4 | 1 | | | | HZ |
| HIP 50191 | 3.85 | 31.1 | 10.2 h -41.9° | V | 7.3 | 1 | | | | HZ |
| HIP 51986 | 3.84 | 26.8 | 10.6 h -47.8° | V | 7.3 | 1 | | | | HZ |
| HIP 53229 | 3.83 | 29.1 | 10.9 h 34.2° | V | 7.8 | 1 | | | | HZ |
| HIP 53253 | 3.79 | 29.1 | 10.9 h -57.1° | V | 7.8 | 1 | | | | HZ |
| HIP 56343 | 3.54 | 39.8 | 11.6 h -30.1° | V | 6.6 | 1 | | | | HZ |
| HIP 57363 | 3.65 | 39 | 11.8 h -65.3° | V | 6.6 | 1 | | | | HZ |
| HIP 61932 | 2.17 | 39.9 | 12.7 h -47.0° | V | 8.1 | 1 | | | | HZ |
| HIP 63125 | 2.88 | 35.2 | 12.9 h 38.3° | V | 8.6 | 1 | | | | HZ |
| HIP 63608 | 2.79 | 33.6 | 13.0 h 11.0° | V | 7.6 | 1 | | | | HZ |
| HIP 63613 | 3.62 | 27.9 | 13.0 h -70.5° | V | 7.4 | 1 | | | | HZ |
| HIP 68895 | 3.28 | 31 | 14.1 h -25.3° | V | 6.8 | 1 | | | | HZ |
| HIP 69732 | 4.18 | 30.4 | 14.3 h 46.1° | V | 8.6 | 1 | | | | HZ |
| HIP 74395 | 3.41 | 36 | 15.2 h -51.9° | V | 6.4 | 1 | | | | HZ |
| HIP 74666 | 3.49 | 37.3 | 15.3 h 33.3° | V | 6.7 | 1 | | | | HZ |
| HIP 74824 | 4.07 | 30.6 | 15.3 h -57.2° | V | 7.7 | 1 | | | | HZ |
| HIP 75695 | 3.68 | 34.3 | 15.5 h 29.1° | V | 6.5 | 1 | | | | HZ |
| HIP 79882 | 3.23 | 32.6 | 16.3 h -3.3° | V | 6.8 | 1 | | | | HZ |
| HIP 80000 | 4.02 | 39.5 | 16.3 h -49.8° | V | 8.6 | 1 | | | | HZ |
| HIP 81833 | 3.50 | 33.3 | 16.7 h 38.9° | V | 6.6 | 1 | | | | HZ |
| HIP 85340 | 4.17 | 25.5 | 17.4 h -23.8° | V | 8.5 | 1 | | | | HZ |
| HIP 86263 | 3.54 | 32.3 | 17.6 h -14.6° | V | 6.7 | 1 | | | | HZ |
| HIP 87108 | 3.75 | 31.5 | 17.8 h 2.7° | V | 7.4 | 1 | | | | HZ |
| HIP 87261 | 3.21 | 38.6 | 17.8 h -37.0° | V | 6.8 | 1 | | | | HZ |
| HIP 87585 | 3.75 | 34.5 | 17.9 h 56.9° | V | 7.3 | 1 | | | | HZ |
| HIP 88635 | 2.99 | 29.7 | 18.1 h -29.6° | V | 7.2 | 1 | | | | HZ |
| HIP 88771 | 3.73 | 26.6 | 18.1 h 9.6° | V | 7.4 | 1 | | | | HZ |
| HIP 90139 | 3.84 | 36.5 | 18.4 h 21.8° | V | 7.8 | 1 | | | | HZ |
| HIP 90568 | 4.13 | 38.7 | 18.5 h -48.9° | V | 8.5 | 1 | | | | HZ |
| HIP 93805 | 3.43 | 37.9 | 19.1 h -3.1° | V | 6.8 | 1 | | | | HZ |
| HIP 93864 | 3.31 | 37.3 | 19.1 h -26.3° | V | 6.6 | 1 | | | | HZ |
| HIP 94376 | 3.07 | 29.9 | 19.2 h 67.7° | V | 6.9 | 1 | | | | HZ |
| HIP 94779 | 3.76 | 38.1 | 19.3 h 53.4° | V | 7.8 | 1 | | | | HZ |
| HIP 95168 | 3.93 | 38.9 | 19.4 h -16.2° | V | 7.8 | 1 | | | | HZ |
| HIP 95853 | 3.77 | 37.2 | 19.5 h 51.7° | V | 7.4 | 1 | | | | HZ |
| HIP 98495 | 3.95 | 32.2 | 20.0 h -71.1° | V | 7.8 | 1 | | | | HZ |
| HIP 100064 | 3.58 | 32.5 | 20.3 h -11.5° | V | 6.5 | 1 | | | | HZ |
| HIP 101769 | 3.63 | 30.9 | 20.6 h 14.6° | V | 6.5 | 1 | | | | HZ |
| HIP 101772 | 3.11 | 30.1 | 20.6 h -46.7° | V | 6.8 | 1 | | | | HZ |
| HIP 106481 | 4.02 | 37.9 | 21.6 h 45.6° | V | 8.6 | 1 | | | | HZ |
| HIP 107354 | 4.16 | 34.2 | 21.7 h 25.6° | V | 8.5 | 1 | | | | HZ |
| HIP 109427 | 3.55 | 28.3 | 22.2 h 6.2° | V | 6.5 | 1 | | | | HZ |
| HIP 109857 | 4.19 | 26.2 | 22.3 h 57.0° | V | 8.5 | 1 | | | | HZ |
| HIP 110960 | 3.65 | 28.2 | 22.5 h 0.0° | V | 6.5 | 1 | | | | HZ |
| HIP 111169 | 3.77 | 31.5 | 22.5 h 50.3° | V | 7.4 | 1 | | | | HZ |
| HIP 112623 | 3.49 | 39.5 | 22.8 h -50.7° | V | 6.5 | 1 | | | | HZ |
| HIP 112724 | 3.54 | 35.4 | 22.8 h 66.2° | V | 6.6 | 1 | | | | HZ |
| HIP 112748 | 3.48 | 32.5 | 22.8 h 24.6° | V | 6.6 | 1 | | | | HZ |
| HIP 113638 | 4.12 | 33.4 | 23.0 h -51.2° | V | 8.5 | 1 | | | | HZ |
| HIP 116584 | 3.82 | 26.4 | 23.6 h 46.5° | V | 7.8 | 1 | | | | HZ |

| Star Name | V (mag) | Dist. (pc) | RA, Dec | Band | Integration (hrs) | Visits | Known RV Target | New Planet Survey | HZ? | Disk Program |
|---|---|---|---|---|---|---|---|---|---|---|
| HD 163296 | 6.85 | 140 | 17.9 h -20.0° | R | 6 | 1 | | | | YSO |
| AB AUR | 7.05 | 140 | 4.9 h 30.6° | R | 6 | 1 | | | | YSO |
| MWC 480 | 7.62 | 140 | 5.0 h 29.8° | R | 6 | 1 | | | | YSO |
| MWC 758 | 8.27 | 140 | 5.5 h 25.3° | R | 6 | 1 | | | | YSO |
| UX ORI | 8.70 | 140 | 5.1 h -2.2° | R | 6 | 1 | | | | YSO |
| CQ TAU | 10.00 | 140 | 5.6 h 24.7° | R | 6 | 1 | | | | YSO |
| HD 142666 | 8.82 | 140 | 15.9 h -22.0° | R | 6 | 1 | | | | YSO |
| FU ORI | 9.60 | 140 | 5.8 h 9.1° | R | 6 | 1 | | | | YSO |
| TY CRA | 9.39 | 140 | 19.0 h -35.1° | R | 6 | 1 | | | | YSO |
| T TAU | 9.30 | 140 | 4.4 h 19.5° | R | 6 | 1 | | | | YSO |
| SZ 68 | 10.22 | 140 | 15.8 h -33.7° | R | 12 | 1 | | | | YSO |
| RU LUP | 9.60 | 140 | 15.9 h -36.2° | R | 12 | 1 | | | | YSO |
| SZ 19 | 10.90 | 140 | 11.1 h -76.4° | R | 12 | 1 | | | | YSO |
| T CHA | 11.86 | 140 | 12.0 h -78.6° | R | 12 | 1 | | | | YSO |
| CV CAR | 10.48 | 140 | 10.8 h -56.1° | R | 12 | 1 | | | | YSO |
| RW AUR | 9.60 | 140 | 5.1 h 30.4° | R | 12 | 1 | | | | YSO |
| HP TAU | 14.90 | 140 | 4.6 h 22.9° | R | 12 | 1 | | | | YSO |
| UX TAU | 10.80 | 140 | 4.5 h 18.2° | R | 12 | 1 | | | | YSO |
| RY LUP | 9.90 | 140 | 16.0 h -39.6° | R | 12 | 1 | | | | YSO |
| GLASS F | 11.01 | 140 | 11.1 h -76.6° | R | 12 | 1 | | | | YSO |
| GQ LUP | 11.40 | 140 | 15.8 h -34.3° | R | 12 | 1 | | | | YSO |
| S CRA | 10.49 | 140 | 19.0 h -35.0° | R | 12 | 1 | | | | YSO |
| R CRA | 11.92 | 140 | 19.0 h -35.0° | R | 12 | 1 | | | | YSO |
| DR TAU | 10.50 | 140 | 4.8 h 17.0° | R | 12 | 1 | | | | YSO |
| CS CHA | 11.69 | 140 | 11.0 h -76.4° | R | 12 | 1 | | | | YSO |
| SZ CHA | 12.68 | 140 | 11.0 h -76.7° | R | 12 | 1 | | | | YSO |
| SZ 82 | 11.90 | 140 | 15.9 h -36.1° | R | 12 | 1 | | | | YSO |
| 035120+3154W | 11.90 | 140 | 3.9 h 32.1° | R | 12 | 1 | | | | YSO |
| DS TAU | 11.90 | 140 | 4.8 h 29.4° | R | 12 | 1 | | | | YSO |
| V1331 CYG | 11.96 | 140 | 21.0 h 50.4° | R | 12 | 1 | | | | YSO |
| BP TAU | 10.70 | 140 | 4.3 h 29.1° | R | 12 | 1 | | | | YSO |
| V826 TAU | 12.07 | 140 | 4.5 h 18.0° | R | 12 | 1 | | | | YSO |
| 042916+1751 | 12.10 | 140 | 4.5 h 18.0° | R | 12 | 1 | | | | YSO |
| V827 TAU | 12.18 | 140 | 4.5 h 18.3° | R | 12 | 1 | | | | YSO |
| AS 205 | 12.05 | 140 | 16.2 h -17.4° | R | 12 | 1 | | | | YSO |
| DN TAU | 11.50 | 140 | 4.6 h 24.2° | R | 12 | 1 | | | | YSO |
| TW HYA | 10.50 | 54 | 11.0 h -33.3° | R | 12 | 1 | | | | YSO |
| EX LUP | 8.50 | 140 | 16.1 h -39.7° | R | 12 | 1 | | | | YSO |
| HARO1 14 | 12.30 | 140 | 16.5 h -24.1° | R | 12 | 1 | | | | YSO |
| GK TAU | 13.00 | 140 | 4.6 h 24.4° | R | 12 | 1 | | | | YSO |
| IK LUP | 12.13 | 140 | 15.7 h -33.2° | R | 12 | 1 | | | | YSO |
| DK TAU | 11.90 | 140 | 4.5 h 26.0° | R | 12 | 1 | | | | YSO |
| HD 163296 | 6.85 | 140 | 17.9 h -20.0° | I | 6 | 1 | | | | YSO |
| AB AUR | 7.05 | 140 | 4.9 h 30.6° | I | 6 | 1 | | | | YSO |
| MWC 480 | 7.62 | 140 | 5.0 h 29.8° | I | 6 | 1 | | | | YSO |
| MWC 758 | 8.27 | 140 | 5.5 h 25.3° | I | 6 | 1 | | | | YSO |
| UX ORI | 8.70 | 140 | 5.1 h -2.2° | I | 6 | 1 | | | | YSO |
| CQ TAU | 10.00 | 140 | 5.6 h 24.7° | I | 6 | 1 | | | | YSO |
| HD 142666 | 8.82 | 140 | 15.9 h -22.0° | I | 6 | 1 | | | | YSO |
| FU ORI | 9.60 | 140 | 5.8 h 9.1° | I | 6 | 1 | | | | YSO |
| TY CRA | 9.39 | 140 | 19.0 h -35.1° | I | 6 | 1 | | | | YSO |
| T TAU | 9.30 | 140 | 4.4 h 19.5° | I | 6 | 1 | | | | YSO |
| SZ 68 | 10.22 | 140 | 15.8 h -33.7° | I | 12 | 1 | | | | YSO |
| RU LUP | 9.60 | 140 | 15.9 h -36.2° | I | 12 | 1 | | | | YSO |

| Star Name | V (mag) | Dist. (pc) | RA, Dec | Band | Integration (hrs) | Visits | Known RV Target | New Planet Survey | HZ? | Disk Program |
|---|---|---|---|---|---|---|---|---|---|---|
| SZ 19 | 10.90 | 140 | 11.1 h -76.4° | I | 12 | 1 | | | | YSO |
| T CHA | 11.86 | 140 | 12.0 h -78.6° | I | 12 | 1 | | | | YSO |
| CV CAR | 10.48 | 140 | 10.8 h -56.1° | I | 12 | 1 | | | | YSO |
| RW AUR | 9.60 | 140 | 5.1 h 30.4° | I | 12 | 1 | | | | YSO |
| HP TAU | 14.90 | 140 | 4.6 h 22.9° | I | 12 | 1 | | | | YSO |
| UX TAU | 10.80 | 140 | 4.5 h 18.2° | I | 12 | 1 | | | | YSO |
| RY LUP | 9.90 | 140 | 16.0 h -39.6° | I | 12 | 1 | | | | YSO |
| GLASS F | 11.01 | 140 | 11.1 h -76.6° | I | 12 | 1 | | | | YSO |
| GQ LUP | 11.40 | 140 | 15.8 h -34.3° | I | 12 | 1 | | | | YSO |
| S CRA | 10.49 | 140 | 19.0 h -35.0° | I | 12 | 1 | | | | YSO |
| R CRA | 11.92 | 140 | 19.0 h -35.0° | I | 12 | 1 | | | | YSO |
| DR TAU | 10.50 | 140 | 4.8 h 17.0° | I | 12 | 1 | | | | YSO |
| CS CHA | 11.69 | 140 | 11.0 h -76.4° | I | 12 | 1 | | | | YSO |
| SZ CHA | 12.68 | 140 | 11.0 h -76.7° | I | 12 | 1 | | | | YSO |
| SZ 82 | 11.90 | 140 | 15.9 h -36.1° | I | 12 | 1 | | | | YSO |
| 035120+315W | 11.90 | 140 | 3.9 h 32.1° | I | 12 | 1 | | | | YSO |
| DS TAU | 11.90 | 140 | 4.8 h 29.4° | I | 12 | 1 | | | | YSO |
| V1331 CYG | 11.96 | 140 | 21.0 h 50.4° | I | 12 | 1 | | | | YSO |
| BP TAU | 10.70 | 140 | 4.3 h 29.1° | I | 12 | 1 | | | | YSO |
| V826 TAU | 12.07 | 140 | 4.5 h 18.0° | I | 12 | 1 | | | | YSO |
| 042916+1751 | 12.10 | 140 | 4.5 h 18.0° | I | 12 | 1 | | | | YSO |
| V827 TAU | 12.18 | 140 | 4.5 h 18.3° | I | 12 | 1 | | | | YSO |
| AS 205 | 12.05 | 140 | 16.2 h -17.4° | I | 12 | 1 | | | | YSO |
| DN TAU | 11.50 | 140 | 4.6 h 24.2° | I | 12 | 1 | | | | YSO |
| TW HYA | 10.50 | 54 | 11.0 h -33.3° | I | 12 | 1 | | | | YSO |
| EX LUP | 8.50 | 140 | 16.1 h -39.7° | I | 12 | 1 | | | | YSO |
| HARO1 14 | 12.30 | 140 | 16.5 h -24.1° | I | 12 | 1 | | | | YSO |
| GK TAU | 13.00 | 140 | 4.6 h 24.4° | I | 12 | 1 | | | | YSO |
| IK LUP | 12.13 | 140 | 15.7 h -33.2° | I | 12 | 1 | | | | YSO |
| DK TAU | 11.90 | 140 | 4.5 h 26.0° | I | 12 | 1 | | | | YSO |